

SRS AND PLASMA STUDIES WITH RUBY LASER

By
D. MADHAVAN



DEPARTMENT OF PHYSICS

INDIAN INSTITUTE OF TECHNOLOGY KANPUR

JUNE 1975

TH
PHY/1975/D
m2648
PHY
1975
D
MAD

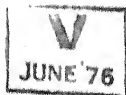
SRS

SRS AND PLASMA STUDIES WITH RUBY LASER

A Thesis Submitted
In Partial Fulfilment of the Requirements
for the Degree of
DOCTOR OF PHILOSOPHY

By
D. MADHAVAN

to the
DEPARTMENT OF PHYSICS
INDIAN INSTITUTE OF TECHNOLOGY KANPUR
JUNE 1975



I.I.T. KANPUR
CENTRAL LIBRARY
No. A 46003.

Thesis
530.44
M264

FEB 1976

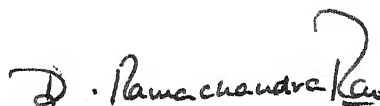
PHY-1975-ID-MAD-SRS

TO

DEAR SHITYA

CERTIFICATE

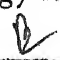
This is to certify that the thesis entitled 'SRS and Plasma Studies Using Ruby Laser' is the original work of Sri D. Madhavan carried out under my supervision and the same has not been submitted elsewhere for a degree.



D. Ramachandra Rao
Professor
Department of Physics
Indian Institute of Technology Kanpur

June 25, 1975.

POST GRADUATE OFFICE

This thesis has been approved
for the award of the Degree of
Doctor of Philosophy (Ph.D.)
in accordance with the
regulations of the Indian
Institute of Technology Kanpur
Dated: 12/2/76 

ACKNOWLEDGEMENTS

I am very grateful to Professor D. Ramachandra Rao for his guidance throughout this work. He has been an extremely understanding friend and guide, for which I will ever be indebted to him. I am equally thankful to Professor P. Venkateswarlu for his constant interest in me and my work throughout my stay at this Institute. My thanks are due to Professor T. S. Jaseja for having introduced me to the field of lasers, during his stay at this Institute.

Professor V. Subba Rao and his students have been generous in lending almost anything I needed at all times. It is a pleasure to thank them, especially him for his personal interest in me. I am very grateful to Dr. N. A. Narasimham and Dr. R. N. Dixit of the Spectroscopy Division, BARC, Bombay for their kindness and help in obtaining densitometer traces of my spectra. My thanks are due to Professor T.M. Srinivasan, Dr. R. K. Ray and the staff of the Low Temperature Laboratory for their munificent supply of liquid nitrogen without which a greater part of this work would have been impossible. I thank Mr. J. N. Sharma and his colleagues for their ready help in Glass Blowing. Thanks are due to Professor M. V. George and members of the Chemistry laboratory for frequent help by providing organic compounds needed and above all for the plentiful supply of ice, indispensable for the experiments.

I acknowledge with thanks the help rendered by my friend and colleague, Dr. M. K. Dheer during some part of this work. My sincere thanks go to my colleagues, Shri Bansilal, U. V. Kumar and Dr. Rama Sastry for their considerable and ready help during this work. Thanks are also due to Shri H. Jagannath, A. Sivaram, D. Narayana Rao, Sundaram, M. S. Ansari, Radhakrishna Murthy and N. V. G. Swamy. Some of them have been of much help in getting the thesis ready in time. I acknowledge the help rendered by my friends Drs. Dayal Saran, K. N. Swamy Rao, K. V. Subbaram and S. Aravamudan. Shri Kuldip Singh Ubhey has been of much help with the mechanical and other odd jobs arising during the work. I thank him for his services that too always with a smile.

Shri Durga Singh Rawat has always been ready with his help, be it a crisis or a celebration. I cannot thank him enough for his help.

I thank Mrs. Rukmini and Mr. Nihal Ahmad for typing this thesis. Thanks are also due to Mr. B.B. Srivastava and A.K. Ganguly for preparing the drawings in time.

Financial assistance, for carrying out the experimental work, from our Institute, NBS and INSA grants are gratefully acknowledged.

I would like to put on record with gratitude the help I received from Mr. V. S. Narayana. Thanks are also due to Mr. R. S. Nigam for help in polishing the optical components. Lastly, I am extremely thankful to Mr. H. K. Panda for the cyclostyling of the thesis.

I am ever indebted to my parents for their love and care bestowed on me. I would be failing in my duty if I do not express my deep sense of gratitude and thanks to my wife Lalitha, who has been extremely patient, forbearing and loving during all this trying times.

TABLE OF CONTENTS

Page

List of Figures	xi
List of Tables	xiv
Preface	xv
Synopsis	xviii

Part ICHAPTER I: STIMULATED RAMAN SCATTERING

I.1	Introduction	2
I.2	Spontaneous Raman Scattering	4
I.3.1	Stimulated Raman Scattering (SRS)	6
I.3.2	SRS theory	8
I.3.3	Anomalies in SRS	12
I.3.4	Townes' theory of SRS	17
I.4	Nonlinear optics and SRS	26
I.4.1	Nonlinear susceptibilities	26
I.4.2	Coupled wave equations	34
I.4.3A	Nonlinear susceptibility third order in electric field	38
I.4.3B	Frequency dependence of $\chi^{(3)}$	39
I.4.3C	Two-photon absorption	43
I.4.3D	Intensity dependent changes in refractive index	44
I.4.4A	Self focussing and SRS	45
I.4.4B	Anti-Stokes rings	50

I.4.4C Anomalous broadening	52
I.4.4D Verification of SRS theory	53
I.4.5 Coupled mode analysis of SRS	53
I.4.5A Raman type susceptibilities	54
I.4.5B Harmonic oscillator model	57
I.4.5C Coupling between vibrational and light waves in a Raman media	57
I.4.5D Coupling between Stokes and anti-Stokes waves	61
References	65

CHAPTER II: THERMOSPECTRUM OF SRS IN LIQUIDS

II.1 , Introduction	70
II.2 Wave interaction in nonlinear media	73
II.3 Experimental	81
II.4 Results	85
II.5 Calculations	91
II.6 Results of other workers	92
II.6.1 Biscar, Braunstien and Gratch	92
II.6.2 Heumann, Trinks and others	96
II.6.3 Piekara's theory	97
II.7 Discussion	100
II.7A Our Results	100
II.7B Comments on the results of other workers	112
II.8 Conclusions	119
References	122

Part II

Page

CHAPTER III: MODELS OF WATER STRUCTURE AND IR AND
RAMAN SPECTRUM OF WATER

III.1	Introduction	125
III.2	Models of water structure	126
III.3	Water solute models	133
III.4	IR and Raman spectrum of water	
III.4A	Assignments and temperature effects	135
III.4B	Effect of electrolytes	151
	References	154

CHAPTER IV: STIMULATED RAMAN SCATTERING IN H₂O
AND D₂O

IV.1	Introduction	156
IV.2	Experimental	158
IV.3	Earlier reported results	
IV.3A	Colles, Walrafen and Wecht	161
IV.3B	Rahn, Maier and Kaiser	164
IV.3C	Ved Prakash, Dheer and Jaseja	165
IV.4	Our results	166
IV.5	Discussion	173
IV.6	Conclusions	180
	References	182

Part III

	Page
<u>CHAPTER V: LASER PRODUCED PLASMAS AND THEIR</u> <u>DIAGNOSTICS</u>	
V.1 Introduction	184
V.2 Laser produced breakdown in gases	187
V.2.1 Ionization mechanism	187
V.2.2 Dynamics of plasma expansion	192
V.3 LPP from solid targets	196
V.4 Plasma diagnostics	200
V.4.1 Probe measurements	200
V.4.2 Measurement of electron density and temperature	201
V.5 Plasma spectroscopy	205
V.5.1 Introduction	205
V.5.2 Local thermodynamic equilibrium (LTE)	208
V.5.3 Radiation from plasma	215
V.5.4 Plasma effects	222
V.5.4A Lowering of ionization potential	222
V.5.4B Advance of series limit	223
V.5.5 Line broadening	225
V.6. Spectroscopic method of measuring parameters	232
V.6.1 Temperature measurement	233
V.6.1A Line intensity ratio	233
V.6.1B Line to continuum intensity ratio	236
V.6.1C Relative continuum intensity ratio	238

V.6.2	Density measurements	240
V.6.2A	Absolute intensity measurements	240
V.6.2B	From Stark widths of lines	241
V.6.2C	Advance of series limit	243
	References	244

CHAPTER VI: SPECTROSCOPIC INVESTIGATIONS OF LASER GENERATED PLASMA FROM SOLID TARGETS

VI.1.1	Introduction	252
VI.1.2	Earlier spectroscopic investigations of LPP	254
VI.2	Experimental	260
VI.3	Results	262
VI.3.1	Physical characteristics of the plasma	262
VI.3.2	Spectra	263
VI.3.3	Temperature and density evaluation from the spectra.	269
VI.4	Discussion	277
VI.5	Time-domain studies	286
VI.5.1	Introduction	286
VI.5.2	Experimental	287
VI.5.3	Results and discussion	289
VI.6	Conclusions	294
	References	298
	Appendix 1	322
	Appendix 2	325
	Appendix 3	326
	List of publications	

LIST OF FIGURES

	Page
I.1 Schematic representation of the Raman scattering processes.	5
I.2 Stokes gain in a Benzene Raman amplifier as a function of cell length.	16
I.3 Dispersion curves for optical and acoustic phonons.	21
I.4 Wave-vector diagram for the generation of Stokes and anti-Stokes waves.	22
I.5 Schematic illustrating the frequency dependence of resonant two-photon processes.	42
I.6 Energy level scheme for the quantum treatment of SRS.	55
II.1 Experimental set up of Maker and Terhune used to study the generation of $\omega_0 + \Delta$ from ω_0 and $\omega_0 - \Delta$.	78
II.2 The dependence of signal at $\omega_0 + \Delta$ on cell thickness in the experimental set up Fig. II.1.	79
II.3 Our experimental set up	84
II.4 Thermospectrum of the 8050Å line of benzene in a cell length of 30 cms.	87
II.5 Thermospectrum of the 8050Å line of benzene in a cell length of 12 cms.	88
II.6 Thermospectrum of the 8069Å line of Toluene in a cell length of 30 cms.	89

II.7	Thermospectrum of the 8659 ⁰ Å line of cyclohexane in a cell length of 30 cms.	90
III.1	Five molecular water structure model of C ₂ symmetry.	128
III.2	A typical Raman spectrum recording of H ₂ O	138
III.3	The spontaneous valence band contour of H ₂ O along with the four gaussian components.	148
IV.1	Spontaneous and SRS profiles in H ₂ O, D ₂ O and HDO obtained by Colles, Walrafen and Wecht.	162
IV.2a	Our spontaneous Raman contours of the valence band of H ₂ O at 20°C and 65°C.	167
IV.2b	Our spontaneous Raman contour of the valence band of D ₂ O at 28°C and 65°C.	168
IV.2c	Superposition of the experimental valence band contours of H ₂ O and D ₂ O at two different temperatures.	169
IV.3	Prism spectra of the SRS in H ₂ O and D ₂ O.	170
IV.4	Grating spectra of the SRS in H ₂ O and D ₂ O	171
IV.5	Densitometer traces of our SRS spectra in H ₂ O and D ₂ O along with those of Colles, Walrafen and Wecht.	172
VI.1	Spectra of laser generated plasma from CaF ₂	302
VI.2	Spectra of laser generated plasma from CaF ₂ (plasma imaged onto spectrograph slit).	303
VI.3	Spectra of laser generated plasma from SrF ₂ .	304
VI.4	Spectra of laser generated plasma from SrF ₂ (plasma imaged onto spectrograph slit).	305

VI.5	Spectra of laser generated plasma from Aluminium.	306
VI.6	Spectra of laser generated plasma from Aluminium (plasma imaged onto spectrograph slit).	307
VI.7	Spectra of laser generated plasma from CaF_2 (in air) at different distances from the target surface.	308
VI.8	Boltzman Plot of AlI,II and III lines.	309
VI.9	Densitometer trace of the CaF_2 plasma spectrum in air (along the central continuum).	310
VI.10	Densitometer trace of the CaF_2 plasma spectrum in air (slightly above the central continuum)	311
VI.11	Densitometer trace of the CaF_2 plasma spectrum in vacuum.	312
VI.13 A,B	Densitometer trace of the CaF_2 plasma spectrum in air taken at different distances from target surface.	314
VI.14	Densitometer trace of Aluminium plasma spectrum in vacuum.	316
VI.15	Densitometer trace of Aluminium plasma spectrum in air, along with Aluminium arc lines.	317
VI.16	Densitometer trace of Aluminium plasma spectrum in vacuum.	318
VI.17	Oscilloscope traces of the laser pulse.	319
VI.18	Oscilloscope traces of the plasma emission from different Aluminium lines (Target in air).	320
VI.19	Oscilloscope traces of the plasma emission from different Aluminium lines (Target in vacuum).	321

LIST OF TABLES

	Page
I.1 Stokes and anti-Stokes emission angles.	25
II.1 Our calculated product of thermal period and length for different liquids.	93
II.2 Our experimental and theoretical thermal periods.	107
II.3 Observed thermal periods of other workers and our calculated periods.	113
II.4 Experimental thermal periods and hypersonic velocities for four liquids.	117
III.1 Vapour, liquid and ice phase frequencies of the valence Raman bands in H_2O , D_2O , HDO.	144
III.2 The four gaussian components obtained by Walrafen from the IR and Raman contours of the valence band in H_2O , D_2O and HDO.	154
VI.1 Electron densities obtained from different CaI and II lines (from Fig. VI.10).	300
VI.2 Temperature, density and intensity of lines at different distances from target surface (from Fig. VI.13A and 13B).	301

PREFACE

Giant pulse solid-state lasers, ever since their discovery have been extensively used for studying various nonlinear phenomenon arising due to interaction of these intense radiation with matter. Some of them, which are already well studied are: Efficient Harmonic generation, Frequency mixing, Stimulated molecular scattering such as Stimulated Raman, Brillouin, Rayleigh etc. scattering, Two-photon absorption processes, Parametric interaction leading to tunable high power light sources, Saturable absorption which is usefully employed in laser Q-switching, dyes, Intensity dependent refractive index leading to self-focusing of intense light beams in a medium, ... and others. All the above processes comprise a new field named 'Nonlinear Optics'. The earlier studies have used laser pulses of duration of few msecs in normal mode to tens of nsec in giant pulse mode operation of the laser. Presently, extremely short laser pulses of duration of a few psecs are being employed to study the interaction of radiation and matter.

Stimulated Raman scattering (SRS) has been extensively studied over the past decade or more, both with giant and ultra short laser pulses. More recently the thermal spectrum of SRS in liquids has attracted the interest of a few groups. This has led to the interesting discovery of fine-period intensity variations of SRS with temperature. Though several theories are proposed, the phenomenon is not completely understood and there

241

is scope for further experimental investigation. We have carried out experimental investigations of thermospectrum of SRS in liquids and have proposed an alternate mechanism which seems to explain the existing results.

Water, because of its complex structure, has been the subject of extensive IR and Raman studies over the past several decades. Due to the large line-widths and low intensity of the Raman modes, SRS was not successfully observed in water in the early investigations. More recently, a few investigations are reported on the SRS of H_2O and D_2O , using both psec and nsec laser pulses. However, some discrepancies exist in the observed results. It was felt that a study of SRS in H_2O and D_2O using the 50ns pulse width of our giant pulse ruby laser could possibly resolve the existing discrepancies. Our investigations have led to correcting some error in the reported results and give a cohesive picture to the existing results.

More recently high power solid state and also CO_2 lasers have been used to produce dense, high temperature plasma at the surface of solid targets. In continuation of our work using giant pulse ruby laser, it was felt instructive to undertake spectroscopic investigations of laser generated plasmas at solid target surfaces, using the existing spectroscopic facilities (in visible and ultraviolet) in our laboratory. The studies yield spatial distribution of the plasma parameters such as

electron temperatures and densities. The effect of atmosphere on the target-plasma formation is inferred. Time profiles of the plasma emission are also carried out under conditions of crater formation in the target.

A brief, chapterwise description of the thesis is given in the following synopsis.

SYNOPSIS

This thesis, written in three parts, presents the results of some investigations of the Thermospectrum of SRS in liquids (Part 1: Chapters I and II), SRS in H_2O and D_2O (Part 2: Chapters III and IV) and Spectroscopic investigation of laser generated plasma from solid targets (Part 3: Chapters V and VI).

Chapter I is a brief review of SRS phenomenon. The susceptibilities χ^3 and the coupled mode analysis of non-linear interactions are introduced. These are used in the next chapter. Chapter II presents our experimental results and discussions on the thermospectrum of SRS in liquids Benzene, Toluene and Cyclohexane. The intensities of the 1st and 2nd Stokes components are observed to show periodic variation with temperature of a fine period of the order of $0.5-1^\circ C$, in the temperature range $20-30^\circ C$. For an explanation of this, consider the generation of the 2nd Stokes wave E_{-2} by the mixing of the laser, 1st Stokes and 1st anti-Stokes waves E_0 , E_{-1} and E_{+1} through the third order nonlinear susceptibility χ^3 . The following expression for the intensity of the wave E_{-2} is obtained by solving the coupled-wave equations in the parametric approximation:

$$S(\omega_0 - 2\Delta, L) = \frac{n_{-2}}{n_0} \frac{S(\omega_0, 0)}{l_r^2} \left[\frac{\sin \frac{\Delta k L}{2}}{\frac{\Delta k}{2}} \right]^2 \quad (1)$$

where $\frac{1}{l_r^2} = \frac{2k_{-2}}{\epsilon - 2} \left| \times^3 E_{-1} E_{+1}^* \right|^2$

and $\Delta k = k_0 + k_{-1} - k_{+1} - k_{-2}$ is the wave-vector mismatch among the participating waves, L being the Raman cell length. Eqn. (1) shows that the intensity varies periodically with change in the argument $\Delta k L / 2$. The periodic variation of the Raman intensity with length L has been verified by Maker and Terhune.

Our thermospectra is interpreted as the periodic variation resulting from a change in Δk through a change of temperature of the liquid; the period corresponds to a change in the argument

$$\delta (\Delta k L / 2) = \pi \quad (2)$$

From the available refractive index data we have calculated the thermal periods from eqn. (2). Our experimental periods in Benzene and Toluene are 1/3rd the calculated value and is interpreted as being due to the superposition of three spectra with the calculated period but shifted w.r.t each other. Such a possibility is attributed to the existence of intense light filaments in these liquids. Whereas in Cyclohexane, which is non-self-focussing, the experimental period agrees with the calculated period. The reciprocal dependence

of thermal period on length as evidenced from eqn. (2) is verified in Benzene in which we have obtained nearly three times larger period when the cell length is reduced to 1/3rd.

Our calculated periods are also compared with similar experimental results reported by two other groups. We find favourable agreement assuming again a superposition of triple-spectra. The available experimental data do not corroborate the only alternate theory of lattice resonance mechanism suggested by Piekara.

In Part 2, Chapter III presents a brief summary of the spontaneous Raman spectra of H_2O and D_2O vis-a-vis the existing models for water structure, notably the continuum as against the mixture models. The Raman spectra of the valence band of H_2O and D_2O show very broad contours often resolvable into more than one component and hence are interesting for SRS studies. Our experimental results of the SRS of the valence band of H_2O and D_2O and their interpretation is described in Chapter IV. The spectra show a somewhat reduced but nevertheless broad bands. The resolvable components agree with the component positions predicted by Walrafen of Bell Telephone Labs., based on analysis of his experimentally obtained spontaneous profiles. Our results are interpreted in terms of a two-species model of water structure suggested by Walrafen in terms of Hydrogen-bonded and non-Hydrogen-bonded water molecules. Also, our results have

cleared a discrepancy found in one of the reported results and thus bring the existing experimental data on the SRS of H_2O and D_2O into conformity with Walrafen's two-species model.

In Part 3, Chapter V contains an introduction to the field of laser produced plasmas, particularly their spectroscopic diagnosis with relevant formulae. Chapter VI presents our results on the time and space evolution of plasma generated when the laser radiation is focussed on solid targets. The laser output is estimated to be 4J contained in 2-3 pulses of about 50 nsec each. The targets employed are CaF_2 , SrF_2 , Aluminium and Carbon. The plasma is imaged onto the spectrograph slit by means of a lens and spectra taken with target in air and also in vacuum (1μ). The spectra show continuum confined to plasma core at target surface and line emission from up to doubly ionized species. Presence of higher ionization could not be verified due to lack of vacuum UV facilities. The doubly ionized lines are considerably broad and extend very little beyond the continuum the neutral lines extend to the full height of the spectrum and are also weaker. In vacuum the doubly ionized species increase in intensity at the cost of neutral lines.

Plasma temperatures (T_e) are estimated from ratio of line intensities from two different ionic species obtained from densitometric traces of spectra. Electron densities (n_e) are estimated from linewidths using pressure broadening

cleared a discrepancy found in one of the reported results and thus bring the existing experimental data on the SRS of H_2O and D_2O into conformity with Walrafen's two-species model.

In Part 3, Chapter V contains an introduction to the field of laser produced plasmas, particularly their spectroscopic diagnosis with relevant formulae. Chapter VI presents our results on the time and space evolution of plasma generated when the laser radiation is focussed on solid targets. The laser output is estimated to be 4J contained in 2-3 pulses of about 50 nsec each. The targets employed are CaF_2 , SrF_2 , Aluminium and Carbon. The plasma is imaged onto the spectrograph slit by means of a lens and spectra taken with target in air and also in vacuum (1μ). The spectra show continuum confined to plasma core at target surface and line emission from up to doubly ionized species. Presence of higher ionization could not be verified due to lack of vacuum UV facilities. The doubly ionized lines are considerably broad and extend very little beyond the continuum the neutral lines extend to the full height of the spectrum and are also weaker. In vacuum the doubly ionized species increase in intensity at the cost of neutral lines.

Plasma temperatures (T_e) are estimated from ratio of line intensities from two different ionic species obtained from densitometric traces of spectra. Electron densities (n_e) are estimated from linewidths using pressure broadening

data and values of $5 \times 10^{17} - 5 \times 10^{18} \text{ cm}^{-3}$ are obtained. Though CaII/CaI ratio gives relatively low temperatures of the order of 13000-15000 °K, the presence of CaIII and more particularly FIII indicate temperatures in the range 50000-60000 °K. T_e is observed to be higher with the target in vacuum. Several lines show highly asymmetrical self-reversal with the absorption peak shifted towards red. Measurement of intensities and estimation of T_e and n_e at different distances from the target surface indicates recombination of the ionized species and increasing concentration of neutrals beyond a mm or two from the surface.

Time profiles of lines from different ionizations are visually monitored on a CRO screen with the plasma probed at different distances from the target surface. A luminous front velocity of the order of 10^7 cms/sec is indicated. Continuum is negligible beyond 1 mm from the surface. The peaks of continuum, II and III ionization lines are hardly resolved, that of I being slightly delayed. With the laser beam focussed on the same spot from pulse to pulse, the peaks of the time profiles gradually occur earlier and the initial rise becomes steeper. This is interpreted as due to higher velocities and temperature resulting from plasma confinement within the deep crater that is formed on the surface after several pulses.

PART 1

CHAPTER I AND II

THERMOSPECTRUM OF SRS IN LIQUIDS

CHAPTER I

STIMULATED RAMAN SCATTERING

I.1 Introduction

The discovery of coherent optical sources have led to a renewal of intense activity in the field of Raman scattering and a greater portion of earlier results have been reinvestigated by making use of the improved sensitivity and resolution of Laser Raman Spectrometers.¹ On the other hand, the intense radiations from pulsed solid state lasers such as Q-switched ruby and Nd-glass lasers, have led to the observation of a variety of interesting phenomenon arising from the non-linear interactions of these intense radiations with matter. Some of these are Harmonic generation, non-linear mixing of waves, self-focussing of light beams, parametric interactions, non-linear saturation processes, multiphoton processes and the like. These non-linear processes are presented in several review papers.²⁻⁹ The interaction of the intense light beams from

lasers with matter tend to excite various degrees of freedom of both the matter and the radiation field. At certain threshold intensities instabilities set in which transfer energy very rapidly from the light beam to other electromagnetic or mechanical modes of the systems. In particular, the excitation of coherent molecular vibrations and generation of optical phonons by the interaction of intense light beams with matter is of particular interest as they lead to the observation of Stimulated Raman Scattering. Light wave also couples to other excitation waves such as acoustic waves, plasma waves, spin waves etc., leading to stimulated emission of radiation at the difference frequency between the laser frequency and the frequency of each one of the excitation waves.^{9a} Coupling to the acoustic waves gives rise to stimulated Brillouin scattering and coherent generation of intense hypersonic waves which has already been extensively studied¹⁰⁻¹³ parallel with the stimulated Raman scattering. Stimulated inelastic^{14,15} and elastic¹⁶⁻¹⁸ Rayleigh scattering have also been observed, thus contributing to the increasingly complex interaction of intense laser light with matter. In this thesis we confine ourselves to the discussion of stimulated Raman scattering. The phenomenon is amply reviewed in several papers.¹⁹⁻²¹ The concept of Raman susceptibility and the theory of coupled mode analysis are considered in some detail in this chapter as it is particularly relevant to our experimental work on thermospectrum of SRS dealt with in the next chapter.

I.2. Spontaneous Raman Scattering

The quantum theoretical picture of spontaneous Raman emission is a two-photon scattering in which a photon $h \nu_L$ of the exciting radiation is absorbed and a photon $h \nu_s$ at the Raman frequency is emitted, the difference in energy $h (\nu_L - \nu_s)$ is compensated by transition of the scattering molecule from the initial ground level to an excited vibrational level.

The quantum process is schematically shown in Fig. I.1a. The frequency $\nu_s = \nu_L - \nu_{10}$ is called the Stokes radiation. If the molecule is already in an excited state, it is possible for an incident photon $h \nu_L$ to be absorbed and a photon $h \nu_a$ emitted, the molecule making a transition to the ground vibrational level. This is shown in Fig. I.1b. The frequency

$\nu_a = \nu_L + \nu_{10}$ is called the anti-Stokes. In general if $h \nu_{10} \gg kT$, the scattering medium has very few molecules in the excited vibrational state and hence except for very small vibrational shifts or rotational transitions the anti-Stokes emission is, in general, absent or very weak in the ordinary Raman scattering. Transitions from the ground vibrational state $v = 0$ to excited vibrational states $v = 1, 2, 3 \dots$ results in Stokes lines shifted from laser line by frequencies ν_{01} , ν_{02} , $\nu_{03} \dots$ etc. These are not equally spaced but get closer together away from the exciting line due to the anharmonicity of the molecular oscillations. The spontaneous Raman scattering lacks phase coherence between successive photon emissions.

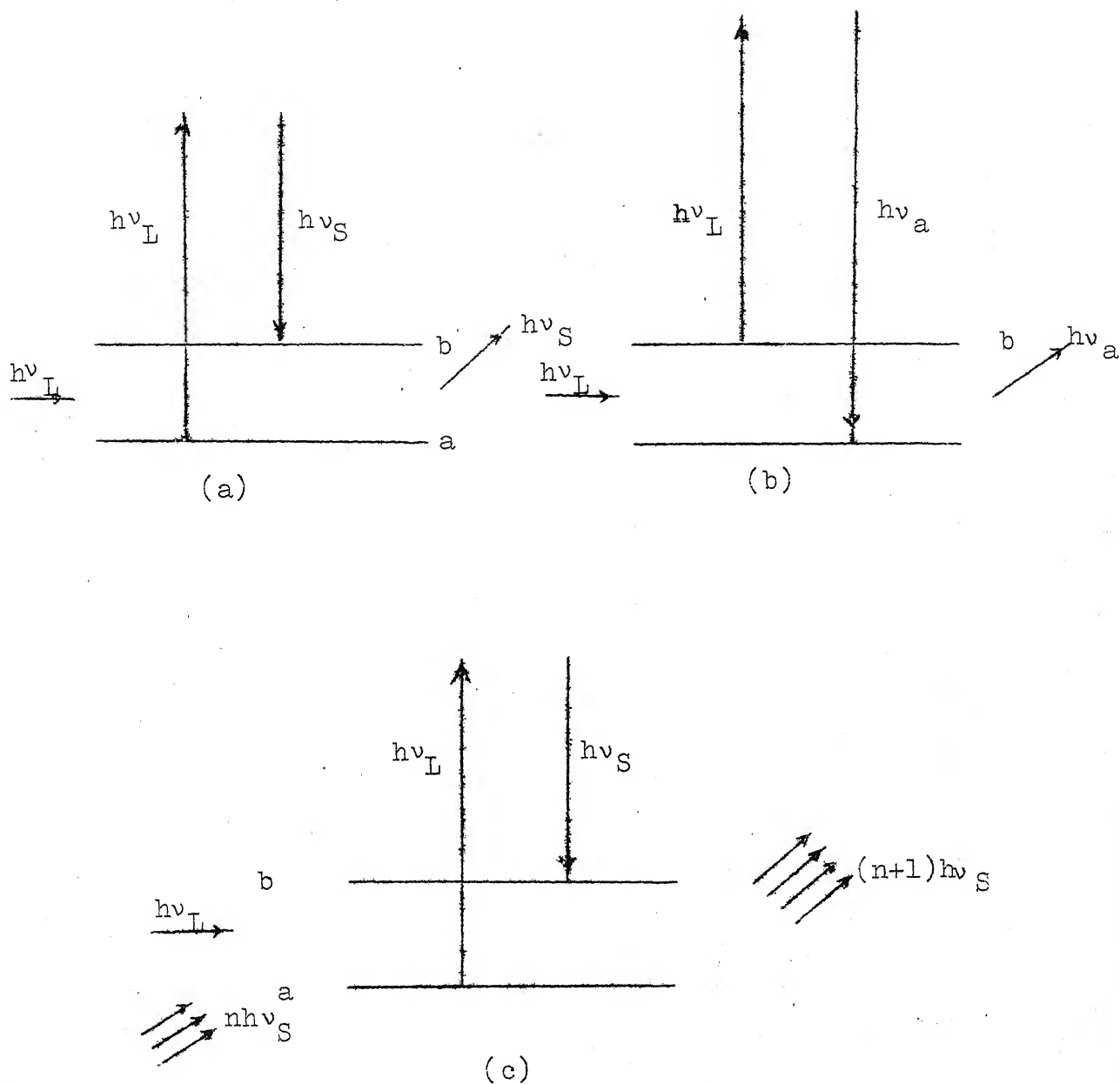


Fig. 1.1. Schematic representation of the Raman scattering processes. a) spontaneous stokes emission, b) spontaneous anti-Stokes emission, and c) stimulated Stokes emission (From Ref. 19)

In classical theory the harmonic oscillator at the vibrational frequency give rise to a polarizability at a shifted frequency from the incident frequency and hence to radiation at the shifted frequencies giving rise to a Raman spectrum. Only those vibrational modes of the system appear in Raman spectrum or are said to be Raman active, which produce a change in the molecular polarizability. The strength of the Raman scattering is given in terms of total or differential Raman scattering cross-section. The spontaneous Raman scattering is well documented in literature.²²

I.3.1 Stimulated Raman Scattering (SRS)

SRS was discovered accidentally by Woodbury and Ng²³ in 1962 while working on a Q-switched ruby laser. The possibility of generating giant pulses from a ruby laser by Q-switching technique was just then recently proposed²⁴ and demonstrated²⁵ by Hellwarth. While studying the detailed output characteristics of ruby laser, Q-switched by using a nitrobenzene kerr-cell, they found that the laser emitted a strong radiation at 7670\AA , in addition to the normally emitted ruby laser light at 6943\AA . This radiation is shifted from the ruby laser frequency by an amount 1345 cm^{-1} which corresponds to the totally symmetric vibrational frequency of nitrobenzene molecule. The experiment was repeated with different liquids²⁷ placed inside the cavity of the ruby laser in which the Q-switching was accomplished using a KDP Pockell-Cell. With each of the liquids different frequencies

were emitted which were shifted from the ruby laser frequency by an amount corresponding to a strong vibrational frequency of the liquid. Induced fluorescence from a real level was ruled out because of the high intensity of the emitted radiation as against the very small or zero absorption in the liquids at the ruby laser frequency.²⁶

It was conclusively proved that the new radiation observed was stimulated Raman scattering from the liquids when excited by the intense ruby laser light. A theory of SRS was immediately proposed by Hellwarth.^{28,29} The radiation emitted had all the characteristics of a laser and hence aptly called a 'Raman Laser'. The stimulated Raman scattering bears the same analogy to spontaneous Raman scattering that the stimulated (Laser) emission bears to spontaneous fluorescence and can be treated on same lines. The fundamental difference between the stimulated processes in ordinary and Raman lasers, is that for the generation of coherent Raman radiation there is no need for the material to possess population inversion. Following the accidental discovery of SRS in nitrobenzene, the same was observed in several liquids,²⁷⁻³⁰ solids³¹ (diamond and calcite) and gases³² (Hydrogen). The linewidths of SRS lines were observed to be very narrow, especially in hydrogen, oxygen and nitrogen, essentially determined by instrumental width ($\sim 0.2 \text{ cm}^{-1}$). In organic liquids, such as benzene, the observed linewidths were about 0.5 cm^{-1} in comparison to the normal Raman linewidths of 2.5 cm^{-1} .

I.3.2 SRS Theory:

The stimulated Raman scattering process is schematically illustrated in Fig. I.1c. A light wave at frequency ν_s is incident on the scattering medium along with the incident radiation at frequency ν_L . In the presence of the wave at frequency ν_s , the Raman scattering at $\nu_s = \nu_L - \nu_{10}$ is stimulated and each Raman transition adds a photon to the wave at ν_s and depletes one photon from the exciting radiation at ν_L , the molecule being excited by the quantum $h(\nu_L - \nu_s) = h\nu_v$. Thus the wave at ν_s is amplified at the cost of the exciting wave at ν_L .

Even before the discovery of the SRS, Javan³³ has discussed the possibility of a two level Raman maser without any quantum state available near the frequency of the exciting radiation. The quantum mechanical treatment of ordinary Raman process involves the calculation of matrix elements which involve a large number of intermediate states and consequently renders the calculation very difficult. Alternatively, a phenomenological theory of SRS is presented through the rate equations using transition probabilities.^{29,34} Process of emission of Stokes photon is characterized by a rate proportional to $n_L(n_s + 1)$. The reverse process in which a photon at ν_s is absorbed and one at laser energy ν_L emitted, has a rate proportional to $(n_L + 1)n_s$.

Considering the process of Raman scattering into a single mode at ν_s from the exciting wave at ν_L , the net rate of emission of photons into Stokes wave is given by

$$-\frac{dn_L}{dt} = \frac{dn_S}{dt} = DP_i n_L (n_S + 1) - DP_f n_S (n_L + 1) \quad I.1$$

$$= D [n_L P_i - n_S P_f + n_L n_S (P_i - P_f)] \quad I.1a$$

where D is a proportionality constant to be determined, while P_i and P_f are the probabilities of finding the molecule in the ground state i and excited vibrational state f respectively.

In ordinary Raman scattering $n_S \ll 1$ and the photon decay is given by

$$n_L(z) = n_L(0) \exp\left(\frac{-DP_i}{c} z\right) = n_L(0) \exp(-\beta z) \quad I.2$$

In actual scattering experiments one has to consider all the modes p at the Stokes frequency that lie within the natural line-width $\Delta\nu$ of the transition. The scattering crosssection per unit volume (σ) for emission into the totality of these modes is therefore given by

$$\sigma = p\beta = \frac{8\pi \nu_s^2 DP_i \Delta\nu V}{c^4} \quad I.3$$

σ can be directly measured as the ratio of the number of the Stokes photons emitted per second per unit volume of medium to the incident photon flux (quanta/sec-cm²). A quantity more often used in practice is the differential scattering crosssection per molecule

$$\left(\frac{d\sigma}{d\Omega}\right)_{\text{mol}} = \frac{1}{2} \frac{\sigma}{4\pi N} = \frac{DP_i v_s^2 V \Delta\nu}{NC^4} \quad \text{I.4}$$

where N is the density of scattering molecules and the factor $\frac{1}{2}$ is due to the fact that the scattering in a given direction has two polarizations.

The stimulated Raman scattering is described by the third term in eqn. I.1a and is the dominant term for $n_L, n_s \gg 1$. The increase in Stokes intensity can be obtained from

$$\frac{dn_s}{dz} = \left[\frac{D}{C} (P_i - P_f) \right] n_s n_L \quad \text{I.5}$$

The Stokes intensity grows with an exponential gain per unit length

$$g \text{ (cm}^{-1}\text{)} = \frac{D}{C} (P_i - P_f) n_L$$

$$= \left(\frac{d\sigma}{d\Omega}\right) \left(\frac{C^3}{v_s \Delta\nu}\right) \left[1 - \exp\left(\frac{-h\nu_v}{kT}\right) \right] \left(\frac{n_L}{V}\right) \quad \text{I.6}$$

where eqn. I.4 is made use of and $P_f/P_i = \exp\left(\frac{-h\nu_v}{kT}\right)$ is substituted in which ν_v is the vibrational frequency. From eqn. I.6 it is clear that the Stokes gain is positive for a system in thermal-equilibrium since $\exp\left(\frac{-h\nu_v}{kT}\right) \ll 1$. The system can be assumed to be in thermal equilibrium during the short (10^{-8} secs) duration of the laser pulse as the equilibrium is not drastically altered by the relatively small number of Raman transitions even with the intense laser pulses.^{21,29} Analogous to laser theory a threshold condition can be obtained for the 'Raman Laser' at which the gain at Stokes frequency exceeds the single pass loss

in the medium (γ) and the threshold laser photon density is obtained from

$$gL = \gamma \quad \text{I.7}$$

$$\left(\frac{n_L}{V}\right) = \frac{\gamma}{L} \left(\frac{v^2 \Delta v}{c^3}\right) \frac{1}{\left(\frac{d\sigma}{d\Omega}\right) (1 - \exp \frac{-h\nu}{kT})} \quad \text{I.8}$$

$$I_L^{th} = \frac{Cn_L}{V} = \frac{\gamma}{L} \left(\frac{v^2 \Delta v}{c^3}\right) \frac{1}{\left(\frac{d\sigma}{d\Omega}\right)} \quad \text{I.9}$$

since $\exp \left(\frac{-h\nu}{kT}\right) \ll 1$. I_L^{th} is the threshold laser intensity (photon/cm² sec.).

On similar lines one could consider anti-Stokes emission for which eqn. I.1 and I.5 become

$$\frac{dn_a}{dt} = Dn_L (n_a + 1) P_f - Dn_a (n_L + 1) P_i \quad \text{I.10}$$

$$\left(\frac{dn_a}{dt}\right)_{stim} = D (P_f - P_i) n_L n_a \quad \text{I.11}$$

From eqn. I.11 it is clear that under thermal equilibrium there is no positive gain and the anti-Stokes wave is attenuated.

Hellwarth,²⁹ on similar lines, obtains a gain coefficient for Stokes emission

$$g_\beta \text{ (cm}^{-1}\text{)} = \frac{I_\alpha \sigma_{\alpha\beta} \lambda_\beta^4}{C_\beta} \left[1 - \exp \frac{h(\nu_\alpha - \nu_\beta)}{kT}\right] \quad \text{I.12}$$

where α and β refer to laser and Stokes modes respectively, $\sigma_{\alpha\beta}$ is the scattering crosssection in cm² per steradian per unit wave length per volume of matter, λ_β is the Stokes wavelength

in cms. For nitrobenzene,²⁹ with $\sigma_{\alpha\beta} = 2.3 \text{ cm}^2$, γ_{loss} (round pass) = 0.5 and $L = 5 \text{ cms}$ we get for the threshold intensity $I_L^{\text{th}} = 10 \text{ MW/cm}^2$. Such large intensities are only possible with high power solid state lasers and this is the reason for SRS being observed only with giant pulse ruby lasers.

From eqn. I.9 it is seen that the Raman gain is the largest and SRS threshold least for the vibration which has the largest cross-section per line-width, in accordance with laser theory. In experiments with liquids CS_2 , C_6H_6 and CCl_4 whose spontaneous intensities are in the ratio 5:4:1 and half widths are 1.0, 2.5 and 2.0 cm^{-1} respectively, the SRS threshold is least for CS_2 and highest for CCl_4 .

I.3.3 Anomalies in SRS:

Though we have seen that the theory of Raman scattering gives a reasonably good explanation of stimulated Raman effect, in practice the observed characteristics of SRS show quite a few anomalies which cannot be directly explained on the basis of ordinary Raman scattering. It is these anomalies which make SRS interesting per-se and have made it a subject of considerable study in the field of nonlinear optics. These anomalies are listed below:

1. In the first experiments with the liquid or crystal outside the laser cavity,³⁷ concentric rings of different colours were observed on a screen behind the cell. These were soon

identified as the anti-Stokes radiations emitted at different angles to the laser direction. Liquid N_2 , O_2 etc.³⁵ also show anti-Stokes emission whereas at these low temperatures one could hardly expect any population at the excited vibrational levels and hence no anti-Stokes emission. The anti-Stokes radiations are generated with exponential gain along particular directions to the laser axis, by a nonlinear interaction of the laser and stimulated Stokes radiations.³⁷ More of this later.

2. The SRS spectrum consists of a series of Raman lines both on the Stokes and anti-Stokes sides and these are separated from the exciting laser line by exact multiples of the fundamental vibrational frequency. These are not overtones of the fundamental corresponding to transitions from $v=0$ to $v=1, 2, 3$ etc. and vice versa, because of the anharmonicity in the molecular oscillation. Further, these overtones in the ordinary Raman scattering are extremely weak whereas the higher order stimulated Stokes and anti-Stokes lines have intensities comparable to the first Stokes line. These lines at $\nu_L \pm n\nu_v$ (n being an integer) are referred to as the 'SRS ladder'. The 1st Stokes line itself acts as the exciting line giving rise to its own Stokes and anti-Stokes lines which are the second Stokes ($\nu_L - 2\nu_v$) and the laser line (ν_L) respectively. Thus each successive Stokes line acts as the exciting line to generate the next higher order Stokes line and also the lower one. Each step of this chain process has a threshold just as for the

primary Stokes generation. Each higher order anti-Stokes line is generated from the previous anti-Stokes line in the same manner as the first anti-Stokes from the laser line. The higher order lines can also be generated by a nonlinear mixing of the existing SR components and these processes generally possess no threshold but may have to satisfy certain phase matching conditions. However, it is observed that when the exciting laser intensity exceeds the threshold for the generation of the 1st Stokes line, the whole SRS ladder appears in the SRS spectrum.

3. It is observed that invariably only one (or sometimes two) of the vibrational frequencies of the substance appears in different orders in the SRS spectrum. The modes which are polarized and correspond to a totally symmetric vibration are the ones to appear strongly in SRS; for, it is these modes which have the largest Raman cross-section and small line-width and hence the smallest SRS threshold according to eqn. I.9. It is characteristic of Boson statistics that once a stimulated process occurs first, it grows and takes over from other competing processes. Thus spectroscopically SRS does not add any new information to the Raman spectra of the medium.

4. In many SRS spectrum from liquids such as CS_2 , benzene and toluene, the SRS Stokes and anti-Stokes lines exhibit considerable broadening extending upto 100 cm^{-1} , often with asymmetry where the maximum is shifted by as much as 10 cm^{-1} to absolute higher frequency.³⁵ The broadening may also show a fine structure of a few cm^{-1} .

5. The broad anti-Stokes emission often exhibited a sharp absorption corresponding to the spontaneous anti-Stokes frequency.³¹ This induced anti-Stokes absorption is termed 'Inverse Raman Effect'.³⁸ The normal Raman spectrum of the sample can be obtained in absorption by providing a strong continuum by passing the laser beam through a cell of toluene (for example) before it enters the sample.³⁹

6. The threshold laser power for SRS is observed⁴⁰ to be two orders of magnitude smaller than the theoretical estimate from eqn. I.9 or I.12, after careful measurement of Raman scattering crosssections.⁴¹ The experimentally observed gain is found to be 25 times greater than the theoretical gain.²⁹ The anomalously high gain was initially attributed to multimode structure of the exciting laser,⁴² but subsequently it is conclusively proved that the gain is independent of mode structure.⁴³⁻⁴⁵ The gain is large enough (typically $g=3 \text{ cm}^{-1}$) for the SRS to be essentially a single pass effect and feedback is not essential,⁴⁵ except for short lengths.⁴⁶ The Raman output shows a sudden discontinuity at the threshold value.⁴⁵ This is shown in Fig. I.2.

7. The SRS in liquids show a threshold both in the incident laser power and in the cell length.

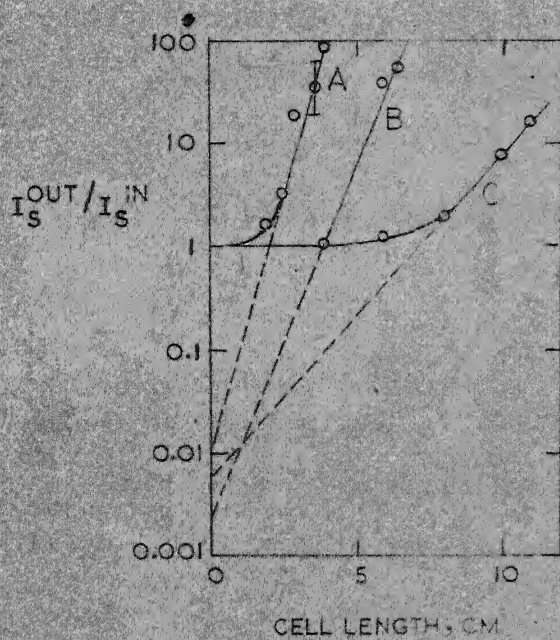


FIG. 1.2 STOKES GAIN IN A BENZENE RAMAN AMPLIFIER
VS CELL LENGTH A>B>C ARE DIFFERENT
LASER INTENSITIES (REPRODUCED FROM REF. 46.)

I.3.4 Townes' Theory of SRS

The previous quantum mechanical treatment in terms of the number of photons in the laser and Raman modes has the disadvantage that phase information is completely lost by specifying the photon number as a consequence of the uncertainty principle. Many of the nonlinear effects observed at high intensities are found to depend sensitively on phase matching between different participating waves. At large photon numbers as are usually found in lasers and Raman lasers, all the processes could be conveniently dealt with from classical or semiclassical point of view.

In the classical model first proposed by Townes and co-workers,^{47,48} the Raman medium is to be taken as consisting of N harmonic oscillators per unit volume. Each molecular oscillator is characterised by its position z and vibrational displacement co-ordinate X . The equation of motion for an oscillator is given by:

$$\frac{d^2 X(z,t)}{dt^2} + \gamma \frac{dX}{dt}(z,t) + \omega_v^2 X(z,t) = \frac{F(z,t)}{m} \quad \text{I.13}$$

where γ is a phenomenological damping constant giving rise to a spontaneous Raman linewidth $\Delta\nu = \gamma/2\pi$, ω_v is the (undamped) oscillator frequency and $F(z,t)$ is a driving force, which can be derived from the interaction energy of the molecules in an electric field.

The molecular polarizability α is a function of the vibrational co-ordinate and hence varies at the vibrational frequency. To a first approximation in the vibrational co-ordinate it could be written as:

$$\alpha(X) = \alpha_0 + \alpha_1 X \text{ where } \alpha_1 = \left(\frac{\partial \alpha}{\partial X}\right)_0 \quad \text{I.14}$$

The electrostatic stored energy density is

$$W = \frac{1}{2} \epsilon E^2 \text{ where } \epsilon = 1 + N\alpha(X) \quad \text{I.15}$$

$$\text{and } F = \frac{1}{N} \frac{\partial W}{\partial X} = \frac{1}{2} \alpha_1 E^2 \quad \text{I.16}$$

To study the stimulated Raman generation, it is necessary to consider fields at the frequencies of both laser and Raman waves. If E_0 is the electric field at laser frequency ω_0 of wave vector k_0 and E' the field at the Raman shifted frequency $\omega' = \omega_0 \pm \omega_v$, of wave vector k' , the total electric field can be written as:

$$E = E_0 \cos(\omega_0 t - k_0 Z) + E' \cos(\omega' t - k' Z + \phi') \quad \text{I.17}$$

Considering terms in E^2 at the difference frequency, we obtain from eqn. I.13, 16 and 17.

$$X = \frac{E_0 E' \alpha_1}{2m\gamma(\omega_0 - \omega')} \sin[(\omega_0 - \omega')t - (k_0 - k')Z - \phi'] \quad \text{I.18}$$

Time averaged power flow per unit volume P' , into the Raman wave E' , is given by $N \left\langle \frac{d\mu}{dt} \cdot E' \right\rangle$ where the induced dipole moment $\mu = \alpha_1 X E$

$$P' = \frac{N\alpha_1^2}{8m\gamma} \frac{\omega'}{\omega_0 - \omega'} (E_0 \cdot E')^2 \quad I.19$$

It is at once apparent that $P' > 0$ for $\omega_0 - \omega' > 0$ (Stokes wave) and $P' < 0$ for $\omega_0 - \omega' < 0$ (anti-Stokes wave), ie. in the direct Raman process described by Fig. I.1, there can be positive gain only for Stokes wave as already seen in Chapter I.3.2. The fractional power gain per unit length (a) for Stokes wave should exceed the fractional loss per unit length (b), which gives the threshold condition on laser intensity

$$E_0^2 > \frac{bcm\gamma}{\pi N\alpha_1^2} \frac{\omega_v}{\omega_s} \quad I.20$$

In a typical case $a=10 \text{ cm}^{-1}$ for a laser power 10^2 MW/cm^2 . If $b=0.1 \text{ cm}^{-1}$, the threshold power would be 1 MW/cm^2 .

For possible gain at the anti-Stokes wave also, we should consider all three fields together

$$E = E_0 \cos(\omega_0 t - k_0 Z) + E_s \cos[(\omega_0 - \omega_v)t - k_s Z + \varphi_s] \\ + E_a \cos[(\omega_0 + \omega_v)t - k_a Z + \varphi_a] \quad I.21$$

Following the same steps as above, the average power gains per unit volume for Stokes and anti-Stokes waves are given by:

$$P_s = \frac{N\alpha_1^2 \omega_s}{8m\gamma \omega_v} [(E_0 \cdot E_s)^2 + (E_0 \cdot E_a) (E_0 \cdot E_s) \cos((2k_0 - k_s - k_a)Z + \varphi_s + \varphi_a)] \\ P_a = \frac{N\alpha_1^2 \omega_s}{8m\gamma \omega_v} [-(E_0 \cdot E_a)^2 - (E_0 \cdot E_a) (E_0 \cdot E_s) \cos((2k_0 - k_s - k_a)Z + \varphi_s + \varphi_a)] \quad I.22$$

The first term in each is the same as eqn. I.19. Usually $E_s > E_a$ and in that case there can be gain at anti-Stokes radiation if $2k_o = k_s + k_a$ and the phase $\varphi_s + \varphi_a = \pi$. Under these conditions the power gain at Stokes frequency is reduced from its value given by eqn. I.19. The gain at anti-Stokes wave exists only in the presence of Stokes wave.

The generation of anti-Stokes wave E_a may be interpreted as caused by a modulation of the input radiation E_o due to the variation of refractive index at the vibrational frequency ω_v resulting from the coherent molecular vibrations set up by E_o and E_s . Such a modulation produces side bands on any radiation present,⁴⁸ and hence if the threshold condition on E_o for the generation of E_s is met then the whole SRS ladder referred to earlier may be generated without further threshold. Because of the relatively flat slope of the ω_v vs k_v of the optical phonons it is always possible to find a matching momentum k_v of the optical phonon regardless of the direction in which the Stokes wave travels. (See dispersion diagram for optical phonons in Fig. I.3) Hence the momentum matching condition for Stokes wave generation

$$k_o - k_s = k_v \quad \text{I.23}$$

is satisfied over a wide range of directions of the Stokes wave. Hence the Stokes wave is emitted diffusely with a peak in the direction of the laser radiation.

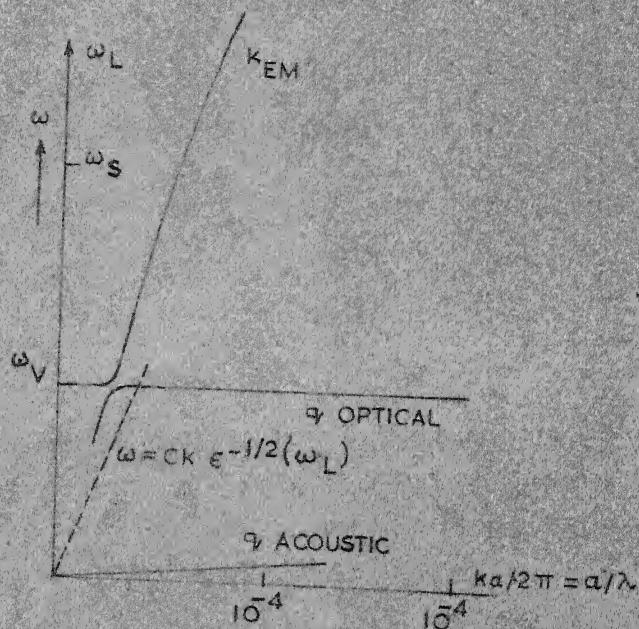


FIG. 1.3 THE ACOUSTIC AND OPTICAL PHONON DISPERSION CURVES

(From Ref; 19)

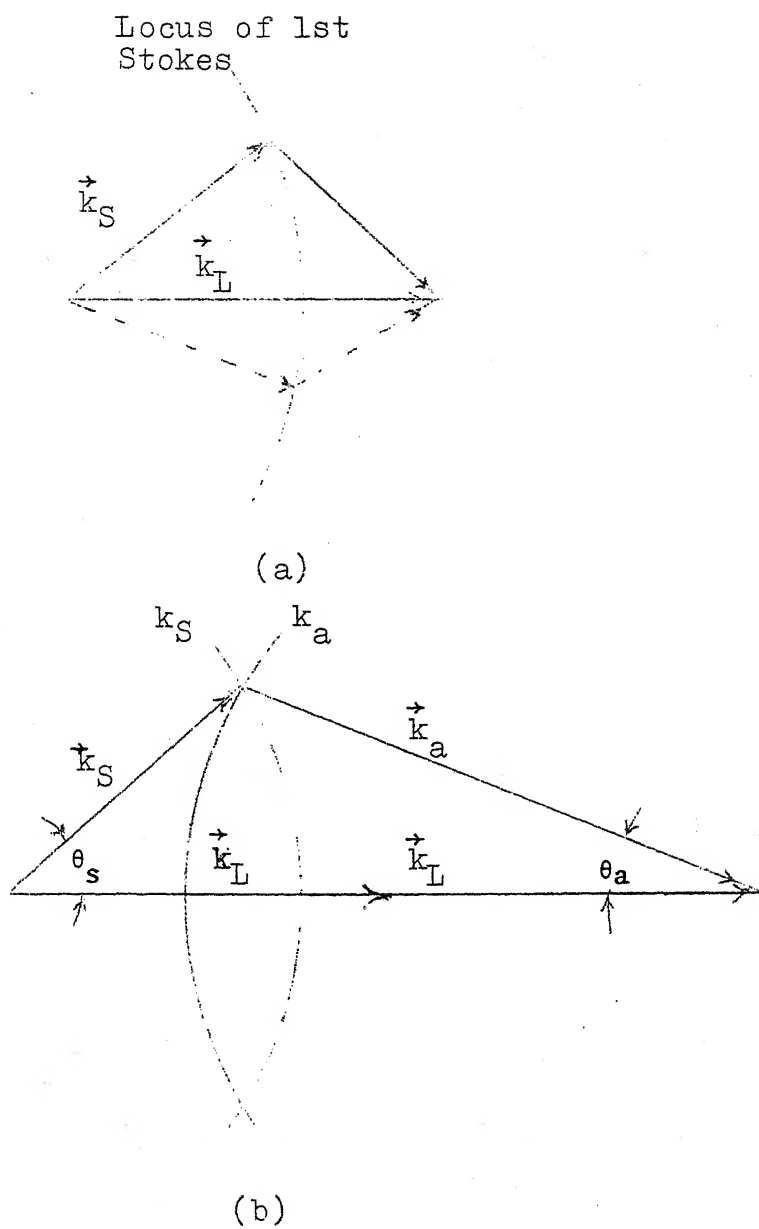


Fig. I.4. Wave-vector diagram for the generation of
 (a) Stokes wave and (b) anti-Stokes wave.

The momentum matching condition

$$2k_0 = k_a + k_s \quad \text{I.24}$$

for the generation of the anti-Stokes wave is not easily met, except for specific relative directions of k_s and k_a . Fig. I.4 shows the direction of momentum matching for (a) the Stokes generation and (b) the anti-Stokes generation. As $|k_a|$ and $|k_s|$ are fixed by their frequencies the resulting direction for the anti-Stokes wave is determined by the intersection of the loci of k_a and k_s from either end of k_0 . The half cone angle θ_a along which anti-Stokes waves are emitted is given by^{47,48}

$$\theta_a^2 = \frac{1}{n} \frac{\omega_s}{\omega_a} [(\Delta n_a - \Delta n_s) + \frac{\omega_v}{\omega_0} (\Delta n_a + \Delta n_s)] \quad \text{I.25}$$

where $n=n(\omega_0)$ =Index of refraction at ω_0 , $\Delta n_a=n(\omega_a)-n(\omega_0) > 0$ and $\Delta n_s=n(\omega_0)-n(\omega_s) > 0$. The Stokes direction corresponding to the momentum-matching condition (I.24) occurs at an angle

$$\theta_s = \frac{\omega_a}{\omega_s} \theta_a \quad \text{I.26}$$

The momentum-matching condition cannot be satisfied when k_0 and k_s are in the same direction. Hence anti-Stokes generation was not observed in the early experiments on SRS with the Raman medium placed inside the laser cavity where the exciting radiation will be orders of magnitude stronger.

The field E_{-2} at frequency $\omega_0 - 2\omega_v$ can be generated from E_s , diffusely, with power proportional to $E_{-2}^2 E_s^2$ in a process identical to the generation of E_s from E_0 . The process has a

threshold condition on E_s . In addition it can be produced through a modulation of E_s by the oscillation in the dielectric constant due to E_0 and E_s , giving a power proportional to $E_0(E_s)^2 E_{-2}$. This process requires a momentum matching condition.

$$k_0 - k_s = k'_s - k_{-2} \quad \text{I.27}$$

where k_s , k'_s correspond to same frequency ω_s but may have different directions. This process has a greater probability when the Raman medium is outside the laser cavity. Eqn. I.27 cannot usually be satisfied with k_0 and k_s in the same direction, such as when the Raman medium is inside the laser cavity.

Radiation at $\omega_0 + 2\omega_v$ is produced without threshold by vibrational modulation of ω_a and is emitted in a direction satisfying

$$k_0 - k_s = k_2 - k_a \quad \text{I.28}$$

The angle between k_2 and laser direction is of the order of $2\theta_a$. Similar mechanisms generate the 'SRS Ladder'. The anti-Stokes cone angles and the Stokes matching angles of several orders for several liquids are shown in Table I.1.

The anti-Stokes cone generation has been extensively studied by Garmire⁵⁰⁻⁵² and also by Chiao and Stoicheff.⁵³ These studies clearly show sharp absorption in the Stokes radiation along directions corresponding to matching angles for the generation of $\omega_0 + n\omega_v$ and $\omega_0 - 2\omega_v$.⁵³ These absorption rings are due to a reduction in gain for Stokes waves participating in

Class I stokes and anti-stokes emission angles (θ_n) according to eqn. I.24 and I.27. Absorption angles (α_n) according to eqn. I.26. Experimental class II emission angles (ϕ_n) are also given.

Liquid	Order n	Class I			Class II		
		θ_n (Theo)	θ_n (Exp)	α_n (Theo)	α_n (Exp)	ϕ_n (Exp)	(10 ⁻²)
Benzene	-2	5.5	5.4 \pm .2	2.3	2.3 \pm .2	3.8	
	1	2.57	2.58 \pm .04	2.95	3.0 \pm .2	3.25	
	2	5.06	5.1 \pm .2	3.24	3.2 \pm .2	6.0	
	3	7.50	7.3 \pm .2	3.54		8.5	
Toluene	-2	5.5				3.8	
	1	2.58		2.97	2.9 \pm .2	3.0	
	2	5.10				5.6	
	3	7.57					
Carbon disulfide	1	2.35	2.2 \pm .2			3.3	
	2	4.64	4.7 \pm .2			6.05	
	3	6.88	7.2 \pm .2			7.8	
Nitrobenzene	-2	9.6				6.5	
	1	4.3	4.17 \pm .1			5.8	
	2	8.5				10.1	
Acetone	1	4.0	3.6 \pm .6			5.7	
	2	8.0				9.8	
Cyclohexane	1	4.3	4.0 \pm .6			5.2	

This table is reproduced from Ref. 51.

anti-Stokes generation according to eqn. I.22a and these occur along Stokes matching angle θ_s (eqn. I.26). Emission rings of second Stokes radiation at frequency $\omega_0 - 2\omega_{\text{pr}}$ have also been observed.⁵³

It has been experimentally demonstrated that the phase-matched anti-Stokes emission can be generated more strongly by tilting the liquid cell in order to increase feedback for Stokes waves along the matching direction θ_s for a more efficient generation of anti-Stokes radiation.⁵⁴

The phenomenon of SRS and its anomalies are intimately associated with various nonlinear processes, as will be shown shortly. A nonlinear susceptibility third order in electric field strength describes both SRS and many of these related nonlinear processes. In the next and subsequent chapters the concept of nonlinear susceptibility is presented, which is generally applicable in any treatment of nonlinear optics.

I.4 NONLINEAR OPTICS AND SRS

I.4.1 Nonlinear Susceptibilities

The propagation of an EM wave through a material produces changes in the spatial and temporal distribution of electric charges. The effect can be characterized by a constitutive relation between the induced polarization (ie. dipole moment per unit volume) and the electric field strength. The polarization can in general be expressed as a series in powers of the electric field strength such as

$$P = \chi_1 \cdot E + \chi_2 : EE + \chi_3 : EEE + \dots$$

I.29

where $P=P(z,t)$ and $E=E(z,t)$. This expansion may also contain terms including time derivatives and in the most general case should include the magnetic field strength also. The first term in right hand side is the usual linear term and gives rise to the index of refraction ($\chi_1 \sim 10^{-1}$). The second term which is second order in electric field has components at zero and second harmonic 2ω of an incident monochromatic wave of frequency ω ($\chi_2 \sim 10^{-9}$). It also leads to terms with sum and difference frequencies when the incident field has two frequency components. If one of the applied fields is a d.c field, this term describes a change in the linear refractive index with applied d.c. fields and is the well known electro-optic effect. The third term which is third order in electric field strength gives rise to several effects such as third harmonic generation ($\chi_3 \sim 10^{-15}$), Kerr and second order electro-optic effect ($\chi_3 \sim 10^{-11}$). Intensity dependent refractive index, two-photon absorption, Stimulated Raman Effect etc. The polarizability χ_n is, in general, a Tensor of order $(n + 1)$. Symmetry operations of the medium leaves the polarization unchanged and this places certain restrictions on the tensor elements of χ_n . In general there are certain overall permutation symmetry inherent in the constitutive relations. These are dealt with at length by Butcher.⁵⁵ Several extensive works on nonlinear optics introduce the nonlinear polarization phenomenologically and obtain a detailed

quantum mechanical derivation for the susceptibilities.^{6,8,9}
In general it is better to deal with the polarization and fields in term of their fourier components.

The electric field associated with a plane wave will be represented in terms of its fourier frequency components as follows:

$$E(z,t) = E(0,z) + \frac{1}{2} \sum_{m=-N}^N E(\omega_m, z) \exp[i(k_m z - \omega_m t)] \quad I.30$$

Since $E(z,t)$ is real, we can write

$$E(-\omega_m, z) = E^*(\omega_m, z), \quad \omega_{-m} = -\omega_m, \quad k_{-m} = -k_m^* \quad \text{and} \quad k_m = \frac{n_m \omega_m}{C} \quad I.31$$

$n_m = n_{-m}^* = k_m \frac{1}{\omega_m}$ is the linear refractive index of the medium at frequency ω_m .

The nonlinear polarization will likewise be assumed to be expandable in terms of its harmonic components:

$$P^{NL}(z,t) = P^{NL}(0,z) + \frac{1}{2} \sum_{m=-M}^M P^{NL}(\omega_m, z) \exp(-i\omega_m t) \quad I.32$$

where $M \geq N$, since $P^{NL}(z,t)$ can have new frequencies other than in $E(z,t)$. There is no explicit term of the form $\exp(ik_m z)$ in conformity with the assumption that $P^{NL}(\omega_m, z)$ is a general function of the applied fields as in eqn. I.29.

The lowest order nonlinear polarization which is generated at the sum or difference frequency of two electric fields at frequencies ω_1 and ω_2 is given by:

$$P_i^{(2)}(\omega_1 + \omega_2, z) = D \chi_{2ijk}[-(\omega_1 + \omega_2), \omega_1, \omega_2] E_j(\omega_1) E_k(\omega_2) \exp[i(k_1 + k_2)z] \quad \text{I.33}^\dagger$$

$$P_i^{(2)}(\omega_1 - \omega_2, z) = D \chi_{2ijk}[-(\omega_1 - \omega_2), \omega_1, -\omega_2] E_j(\omega_1) E_k^*(\omega_2) \exp[i(k_1 - k_2)z] \quad \text{I.34}$$

where i, j, k refer to the co-ordinate axes x, y, z and summation over repeated indices is assumed. The ordering of the frequencies in χ_{ijk} indicate their association with their corresponding co-ordinate ie. $(\omega_1 \pm \omega_2)$ with i , ω_1 with j and ω_2 with k . The induced polarization $P_i^{(2)}(\omega_1 + \omega_2, z)$ gives rise to a wave at frequency $\omega_3 = (\omega_1 + \omega_2)$ whose field amplitude could be obtained from Maxwell's equations in which $P_i^{NL}(\omega_3, z)$ is used as the source term. Thus the nonlinear polarizability in eqn. I.33 couples the three waves ω_1, ω_2 and $\omega_3 = \omega_1 + \omega_2$ and leads to changes in the field amplitudes $E(\omega)$, which are, for this reason, assumed to be slowly varying along the propagation direction z .

The overall permutation symmetry can be stated⁵⁵ as that, the polarizability is invariant under pair wise permutation of the frequency and the corresponding co-ordinate taken together ie. $\chi_{ijk}(-\omega_3, \omega_1, \omega_2)$ remains invariant under pair wise interchange of $i3, ji$ and $k2$

$$\text{ex. } \chi_{ijk}(-\omega_3, \omega_1, \omega_2) = \chi_{ikj}(-\omega_3, \omega_2, \omega_1) \quad \text{I.35}$$

$$\chi_{ijk}(-\omega_3, \omega_1, \omega_2) = \chi_{jik}(\omega_1, -\omega_3, \omega_2) \quad \text{I.36}$$

[†]The susceptibilities χ_{ijk} of different authors differ by constant factors which make comparisons rather confusing in view of the different expressions used for the field amplitudes. Definition of D in eqns. I.33 and 34 and clarification

Equation I.36 holds when damping is zero. χ is related to χ^* through the relation

$$\chi_{ijk}(-\omega_3, \omega_1, \omega_2) = \chi_{ijk}^*(\omega_3, -\omega_1, -\omega_2) \quad \text{I.37}$$

consequence of time reversal symmetry is

$$\chi_{ijk}(-\omega_3, \omega_1, \omega_2) = \chi_{ijk}(\omega_3, -\omega_1, -\omega_2) \quad \text{I.38}$$

In medium with inversion symmetry, as χ_2 's are subject to the same symmetry properties as the medium they remain unaltered, whereas the polarization changes sign and hence we have

$$-P_2 = \chi_2 (-E) (-E) = P_2 \text{ hence } P_2 = 0$$

The detailed expression for the nonlinear susceptibilities have been obtained by several authors from a time dependent perturbation treatment.^{6,8,56} These expressions for the nonlinear susceptibilities show that they have resonant frequency denominators and the resonant terms obviously dominate the non-resonant terms. These resonances play a vital role as will be brought out subsequently. The nonlinear susceptibilities can be derived for a simple anharmonic oscillator model^{8,9,57,58} which clearly brings out the resonant denominators in the expression for the susceptibilities.

Consider a one-dimensional anharmonic oscillator with damping,⁸ driven by two electric fields at frequencies ω_1 and ω_2 :

$$\ddot{x} + \Gamma \dot{x} + \omega_0^2 x + Vx^2 = \frac{e}{m} [E_1 \exp(-i\omega_1 t) + E_2 \exp(-i\omega_2 t) + c.c.] \quad I.39$$

Because of the anharmonic term Vx^2 , one expects solutions for x with frequencies $2\omega_1, 2\omega_2, \omega_1 \pm \omega_2$. Written explicitly

$$x = q_1 \exp(-i\omega_1 t) + q_2 \exp(-i\omega_2 t) + q_1^{(2)} \exp(-i2\omega_1 t) + q_2^{(2)} \exp(-i2\omega_2 t) \\ + q_{12}^+ \exp[-i(\omega_1 + \omega_2)t] + q_{12}^- \exp[-i(\omega_1 - \omega_2)t] \quad I.40$$

We can solve for q 's either by an iterative process starting from the linear approximation or substitute eqn. I.40 in I.39, collect terms of like-exponent and solve the resultant equations. The linear solution is

$$q_1 = x(\omega_1) = \frac{(e/m)E_1}{D(\omega_1)} \quad I.41$$

$$\text{where} \quad D(\omega_1) = D^*(-\omega_1) = (\omega_0^2 - \omega_1^2 - i\Gamma\omega_1) \quad I.42$$

The linear susceptibility at ω_1 is obtained from

$$P^L(\omega_1) = \chi^L(\omega_1) E_1 \exp(-i\omega_1 t) + c.c. = Ne[x(\omega_1) \exp(-i\omega_1 t) + c.c.] \quad I.43$$

$$\therefore \chi^L(\omega_1) = \frac{Ne^2/m}{D(\omega_1)} \quad I.44$$

Substituting the linear terms in Vx^2 we get the second order solutions:

$$x(2\omega_1) = \frac{-(e^2/m^2)V E_1^2}{D^2(\omega_1)D(2\omega_1)} \quad I.45$$

$$x(\omega_1 - \omega_2) = \frac{-(e^2/m^2)V E_1 E_2^*}{D(\omega_1)D^*(\omega_2)D(\omega_1 - \omega_2)} \quad I.46$$

At resonance ie $\omega_1 - \omega_2 \sim \omega_0$ this term predominates and leads to the next higher order terms with frequencies $(\omega_1 - 2\omega_2)$, $(2\omega_1 - \omega_2)$, ω_1 , ω_2 etc. The resulting fourth rank susceptibilities can be written as:

$$\begin{aligned} x_3^{NL}(\omega_2) &= x_3^{NL}(\omega_2 = \omega_2 + \omega_1 - \omega_1) = \frac{N(e^4/m^3)V^2}{D^2(\omega_2)|D(\omega_1)|^2 D^*(\omega_1 - \omega_2)} \\ &= x_3^{NL*}(\omega_1 = \omega_1 + \omega_2 - \omega_2) \end{aligned} \quad \text{I.47}$$

$$\begin{aligned} \text{and } x_3^{NL}(2\omega_1 - \omega_2) &= x_3^{NL}[(2\omega_1 - \omega_2) = \omega_1 + \omega_1 - \omega_2] \\ &= \frac{N(e^4/m^3)V^2}{D^2(\omega_1)D^*(\omega_2)D(2\omega_1 - \omega_2)D(\omega_1 - \omega_2)} \end{aligned} \quad \text{I.48}$$

at resonance $\omega_1 - \omega_2 = \omega_0$ and since $\omega_1 \gg \omega_0$, $D(\omega_1 - \omega_2)$ is purely imaginary and the other denominators are real. We have

$$x_3^{NL}(\omega_2) = - \frac{iN(e^4/m^3)V^2}{r\omega_0(\omega_1^2 - \omega_0^2)^2 (\omega_2^2 - \omega_0^2)^2} \quad \text{I.49}$$

The three dimensional problem can be similarly dealt with⁹ by writting eqn. I.39 as

$$\ddot{x}_i + \Gamma \dot{x}_i + \omega_0^2 x_i + \sum_{jk} V_{ijk} x_j x_k = \frac{e}{m} E_i \quad \text{I.50}$$

$$\text{Linear response } x_i(\omega_1) = \frac{(e/m)E_i(\omega_1)}{D_i(\omega_1)}$$

Considering two driving frequencies ω_1 and ω_2

$$P^{NL}(\omega) = 4\pi N e x(\omega) \quad \text{I.51}$$

$$P_i^{NL}(\omega_1 + \omega_2) = \sum_{jk} \left\{ \chi_{ijk}[-(\omega_1 + \omega_2), \omega_1, \omega_2] E_j(\omega_1) E_k(\omega_2) + \chi_{ijk}[-(\omega_1 + \omega_2), \omega_2, \omega_1] E_j(\omega_2) E_k(\omega_1) \right\} \quad I.52$$

where

$$\chi_{ijk}[-(\omega_1 + \omega_2), \omega_1, \omega_2] = - \frac{4\pi N e^3 V_{ijk}}{m^2 D_i(\omega_1 + \omega_2) D_j(\omega_1) D_k(\omega_2)} \quad I.53$$

for $\chi_{ijk}[-(\omega_1 + \omega_2), \omega_2, \omega_1]$ interchange 1 and 2 in eqn. I.53

similarly

$$\chi_{ijk}[-(\omega_1 - \omega_2), \omega_1, -\omega_2] = \frac{4\pi N e^3 V_{ijk}}{m^2 D_i(\omega_1 - \omega_2) D_j(\omega_1) D_k^*(\omega_2)} \quad I.54$$

Writing with the earlier notation by replacing $\omega_3 = \omega_1 + \omega_2$, we can show the following permutation symmetry relation:

$$\chi_{ijk}(-\omega_3, \omega_1, \omega_2) = \chi_{ikj}(-\omega_3, \omega_2, \omega_1)$$

but $\chi_{ijk}(-\omega_3, \omega_1, \omega_2) = \chi_{jik}(-\omega_1, \omega_3, -\omega_2)$ only if $D = D^*$ ie. damping is zero. These hold good also for $\omega_3 = \omega_1 - \omega_2$ etc. These equations are the same as eqn. I.35 and I.36.

These permutation symmetry leads to the important result that both the linear electro-optic effect and optical rectification depend on the same coefficient:

Linear electro-optic susceptibility is described by $\chi_{ijk}(-\omega, 0, \omega)$

Optical rectification susceptibility is described by $\chi_{jik}(0, -\omega, \omega)$

The result follows immediately from eqn. I.36.

The second order nonlinear susceptibility $\chi_{ijk}(-2\omega, \omega, \omega)$ describing second harmonic generation is symmetric in the last two suffixes and has the same symmetry properties as the piezoelectric constants d_{mn} where m runs from 1 to 3 and n from 1 to 6 where the usual contraction is used with $n=1$ to 6 representing xx, yy, zz, yz, zx and xy respectively. These coefficients are tabulated by Cady⁵⁹ and Nye.⁶⁰

I.4.2 Coupled-wave equations:

The two steps in the analysis of a nonlinear interaction of matter and radiation are: (1) to obtain the induced polarization at a frequency ω due to the radiations present at other frequencies. A similar polarization is derived for each of the frequencies in terms of the other fields. This has been briefly done in Chapter I.4.1. (2) the next step would be to use the polarization as a source term in the Maxwell's equations to obtain the development of the corresponding fields generated, which were assumed in step 1. A self-consistent solution of the resultant set of coupled differential equations for the fields would complete the analysis attempted.

Considering as before the mixing of two frequencies at ω_1 and ω_2 , we will be interested in the field equations for $E(\omega_1)$, $E(\omega_2)$ and $E(\omega_3 = \omega_1 \pm \omega_2)$. The Maxwell's equations in a non magnetic medium are:

$$\nabla \times H = \frac{1}{C^2} (\sigma E + \frac{\partial D}{\partial t}) \quad I.55$$

$$\nabla \times E = - \frac{\partial H}{\partial t} \quad I.56$$

These two equations give the wave equation:

$$\nabla \times \nabla \times E + \frac{\sigma}{C^2} \frac{\partial E}{\partial t} + \frac{1}{C^2} \frac{\partial^2 D}{\partial t^2} = 0 \quad I.57$$

Where σ is the conductivity of the medium which we can generally omit except when we have to explicitly include losses in the equations as when dealing with oscillatory conditions.

$$D = \epsilon E + 4\pi P^{NL} \quad I.58$$

using $\nabla \times \nabla \times E = \nabla(\nabla \cdot E) - \nabla^2 E$ and since $\nabla \cdot E = 0$, we have

$$\nabla^2 E = \frac{\epsilon}{C^2} \frac{\partial^2 E}{\partial t^2} + \frac{4\pi}{C^2} \frac{\partial^2 P^{NL}}{\partial t^2} \quad I.59$$

The travelling wave expression for the fields are taken to be

$$\begin{aligned} E_i^{(\omega_1)}(z, t) &= \frac{1}{2} [E_1(z) \exp i(k_1 z - \omega_1 t) + c.c] \\ E_k^{(\omega_2)}(z, t) &= \frac{1}{2} [E_2(z) \exp i(k_2 z - \omega_2 t) + c.c] \\ E_j^{(\omega_3)}(z, t) &= \frac{1}{2} [E_3(z) \exp i(k_3 z - \omega_3 t) + c.c] \end{aligned} \quad I.60$$

The relationship among the three frequencies for the interaction under consideration is $\omega_3 = \omega_1 + \omega_2$. The field amplitudes $E_1(z)$ etc., are slowly varying function of z due to the nonlinearities as described earlier. If $P^{NL} = 0$, the solution of these

equations are that of the uncoupled plane-travelling waves independent of each other with constant field amplitudes.

The polarization at the frequency ω_3 can be written as:

$$P_j^{NL}(\omega_3, z) = \frac{1}{2} \chi_{jik}(-\omega_3, \omega_1, \omega_2) \times E_{1i}(z) E_{2k}(z) \exp[i(k_1 + k_2)z] + c.c \quad I.61$$

As there are no variations in x and y directions we have

$$\nabla^2 E_j^{\omega_3}(z, t) = -\frac{\partial^2}{\partial z^2} E_j^{\omega_3}(z, t) = \frac{1}{2} \frac{\partial^2}{\partial z^2} [E_{3j}(z) \exp i(k_3 z - \omega_3 t) + c.c] \quad I.62$$

in carrying out the differentiation, we can neglect the second order differential as the variation of the amplitudes are small per wavelength.

$$\text{ie.} \quad \frac{dE_{3j}}{dz} k_3 \gg \frac{d^2 E_{3j}}{dz^2} \quad I.63$$

hence I.62 gives

$$\nabla^2 E_j^{\omega_3}(z, t) = -\frac{1}{2} [k_3^2 E_{3j}(z) - 2ik_3 \frac{dE_{3j}(z)}{dz}] \exp i(k_3 z - \omega_3 t) + c.c \quad I.64$$

eqn. I.59 gives

$$\begin{aligned} & \left[\frac{k_3^2}{2} E_{3j}(z) - ik_3 \frac{dE_{3j}(z)}{dz} \right] \exp i(k_3 z - \omega_3 t) + c.c \\ & = \left(\frac{i\omega_3 \sigma_3}{c^2} + \frac{\omega_3^2 \epsilon_3}{c^2} \right) \left[\frac{E_{3j}}{2} \exp i(k_3 z - \omega_3 t) + c.c \right] \\ & \quad - \frac{\partial^2}{\partial t^2} \left[\frac{4\pi}{c^2} P^{NL}(\omega_3, z, t) \right] \quad I.65 \end{aligned}$$

$$\begin{aligned}
\text{since } \frac{\epsilon_3 \omega_3^2}{c^2} &= k_3^2, \\
-ik_3 \frac{dE_j(z)}{dz} \exp ik_3 z &= \frac{i\omega_3 \sigma_3}{2c^2} E_{3j} \exp ik_3 z \\
&+ \frac{4\pi \omega_3^2}{c^2} \frac{1}{2} x_{jik}(-\omega_3, \omega_1, \omega_2) E_{1i}(z) E_{2k}(z) \exp i(k_1 + k_2)z \quad \text{I.66}
\end{aligned}$$

$$\begin{aligned}
\text{ie. } \frac{dE_{3j}(z)}{dz} &= -\frac{\sigma_3}{2c n_3} E_{3j}(z) + i \frac{2\pi \omega_3}{c n_3} x_{jik}(-\omega_3, \omega_1, \omega_2) E_{1i}(z) E_{2k}(z) \\
&\times \exp i(k_1 + k_2 - k_3)z \quad \text{I.67}
\end{aligned}$$

after having obtained the final equation, we will henceforth do away with the term with σ and also omit the explicit dependence on z for ease of writing. We have:

$$\frac{dE_{3j}}{dz} = \frac{2\pi i \omega_3}{c n_3} x_{jik}(-\omega_3, \omega_1, \omega_2) E_{1i} E_{2k} \exp i(k_1 + k_2 - k_3)z \quad \text{I.68}$$

$$\frac{dE_{1i}}{dz} = \frac{2\pi i \omega_1}{c n_3} x_{ijk}(-\omega_1, \omega_3, -\omega_2) E_{3j} E_{2k}^* \exp i(k_3 - k_2 - k_1)z \quad \text{I.69}$$

$$\frac{dE_{2k}^*}{dz} = -\frac{2\pi i \omega_2}{c n_2} x_{kij}(-\omega_2, -\omega_1, \omega_3) E_{1i} E_{3j}^* \exp i(k_1 - k_3 + k_2)z \quad \text{I.70}$$

These are the equations which form the starting point of most of the calculations. From the permutation and time-reversal symmetries it is clear that the susceptibilities in the three equations are equal and hence can be replaced by a single notation. Further, we can also dispense with the co-ordinate indices and can write the equation in terms of the amplitudes. The general solution can be written as:

$$\frac{dE_3}{dz} = \frac{2\pi i \omega_3}{Cn_3} P_2^{NL}(\omega_3, z) \exp(-ik_3 z) \quad I.71$$

and $P_2^{NL}(\omega_3, z)$ could be written down for the particular type of interaction in which $\omega_3 = 2\omega$ or $\omega_1 \pm \omega_2$ etc.

I.4.3A Nonlinear Susceptibility third order in Electric Field

This is the lowest order nonlinearity in media with inversion symmetry and they can be considered in a manner analogous to the consideration of χ_2 in Chapter I.4.1 and 4.2. The third order nonlinear polarizability is a fourth rank tensor subject to the same symmetry properties as the medium (in addition to the inherent permutation symmetries). The nonzero coefficients of χ_3 have been tabulated for the 32 crystallographic point groups.⁶¹ In what follows we will not stress the tensorial nature and these are amply dealt with in standard works.^{6,8}

The different effects arising through the third order polarization have been dealt with in some detail and the corresponding susceptibilities experimentally obtained by Maker and Terhune.⁶² Different processes arise from different components of the same nonlinear, complex susceptibility tensor. Bloembergen reviews the various effects arising from χ_3 in the light of their influence on SRS. Complete quantum mechanical expressions have been derived for χ_3 also.^{6,8,9,56,83}

The general expression for the third order polarization at frequency ω_4 in terms of the electric fields at frequencies ω_1 , ω_2 and ω_3 , subject to the frequency relation $\omega_4 = \omega_1 + \omega_2 - \omega_3$ can be written as:

$$P_{lmno}^{(3)}(\omega_4, z) = D \chi_{lmno}(-\omega_4, \omega_1, \omega_2, -\omega_3)$$

$$\times E_m(\omega_1) E_n(\omega_2) E_o(\omega_3)^* \exp i(k_1 + k_2 - k_3)z$$

I.72

I.4.3B Frequency dependence of χ_3^\dagger

In the absence of any induced nonlinear effects, a material is assumed to be transparent in the visible and absorb strongly in the infrared and ultraviolet. This is taken to be the normal dispersion characteristics of the medium. In the presence of strong incident fields such as that of a laser radiation the material medium exhibits a new set of resonances which is described by the resonant denominators of the nonlinear susceptibilities and these resonances can be observed when a continuum is incident on the medium in the presence of the intense laser radiation.

Each of the twenty four terms in the expression for χ_3 contain three energy denominators.^{55,56} Two of these denominators contain only one of the frequencies of the participating electric fields. χ_3 effects associated with these single frequency resonances reflect the intensity dependence of the

[†]Equations in Chapter I.4.3 closely follow references 3, 6 and 62.

corresponding first order (linear) resonances. The third denominator involves two of the frequencies in the electric field spectrum. These denominators require the existence of an excited state having same parity as the ground state and separated by the ground state by either the sum or difference of the two frequencies. Resonances associated with these states correspond to simultaneous absorption of two photons or to absorption of one photon with the simultaneous emission of another photon at a different frequency. This last process can be recognized as the Raman effect.

The 24 terms in the expression can be divided into resonant and non-resonant terms with terms corresponding to the two-photon and difference frequency resonances separately shown.

The nonlinear polarization induced at the frequency ω in the presence of the laser field of frequency ω_L and the incident field at frequency ω can be written down as follows,^{3,62} by putting $\omega_4 = \omega_1 = \omega$ and $\omega_2 = \omega_3 = \omega_L$ in eqn. I.72

$$P_{lmno}^{(3)}(\omega, z) = D\chi_{lmno}(-\omega, \omega, \omega_L, -\omega_L) E_m(\omega) E_n(\omega_L) E_o^*(\omega_L) \exp(ik_z z) \quad \text{I.73}$$

where

$$\begin{aligned} D\chi_{lmno}(-\omega, \omega, \omega_L, -\omega_L) = & 6\chi_{lmno}^{NR}(-\omega, \omega, \omega_L, -\omega_L) \\ & + \chi_{lomo}^t(-\omega, -\omega_L, \omega, \omega_L) \frac{\Gamma_t}{\omega_t - (\omega + \omega_L) - i\Gamma_t} \\ & + \chi_{lnmo}^r(-\omega, \omega_L, \omega, -\omega_L) \left[\frac{\Gamma_r}{\omega_r - (\omega - \omega_L) - i\Gamma_r} + \frac{\Gamma_r}{\omega_r - (\omega_L - \omega) + i\Gamma_r} \right] \end{aligned} \quad \text{I.74}$$

The resonant nonlinear susceptibilities χ_3^t and χ_3^r are of the same form and given by

$$\chi_{31mno}^s(\omega_1, \omega_2, \omega_3, \omega_4) = \frac{\epsilon_0^{NL}}{4\hbar\Gamma_s} \langle g | \alpha_{1m}(\omega_1, \omega_2) | s \rangle \langle g | \alpha_{no}(-\omega_3, -\omega_4) | s \rangle^* \quad I.75$$

$$\langle g | \alpha_{1m}(\omega_i, \omega_j) | s \rangle \equiv \frac{e}{\hbar} \sum_b \left[\frac{\langle g | x_1 | b \rangle \langle b | x_m | s \rangle}{\omega_b' + \omega_i} + \frac{\langle g | x_m | b \rangle \langle b | x_1 | s \rangle}{\omega_b' + \omega_j} \right] \quad I.76$$

where g and s refer to the ground and resonant states and $\hbar\omega_b'$ is the energy of the intermediate state b , L is the local field correction factor $(n+2)^4/81$ which leads to high values of χ_3 in high index materials. $\langle g | \alpha_{1m}(\omega_1, \omega_2) | s \rangle$ are the polarizability matrix elements for the molecular transition involved ($\sim 10^{-24} \text{ cm}^3$) and as $\Gamma_r \sim 10^{11} \text{ rad/sec}$, χ_3^r for molecular vibrational transitions are of the order of $10^{-13} \text{ cm}^3/\text{erg}$. With $\Gamma_t \sim 10^{13} \text{ rad/sec}$, χ_3^t for electronic transitions have about the same value as χ_3^r . Values of χ_3^{NR} are two orders smaller.⁶

In eqn. I.74 the second term represents absorption at frequency ω_1 when $\omega_t = \omega_1 + \omega_L$. This is a two-photon process. The third term represents absorption at ω_2 when $\omega_r = \omega_2 - \omega_L$ and emission (because of negative imaginary susceptibility) at ω_3 when $\omega_r = \omega_L - \omega_3$. The last two refer to anti-Stokes absorption and Stokes emission respectively in the primary SRS process already discussed.

Figure I.5 is a schematic of an experimental arrangement to observe resonant two-photon processes.³ Fig.I.5(b) shows the normal absorption at IR and ultraviolet and also the

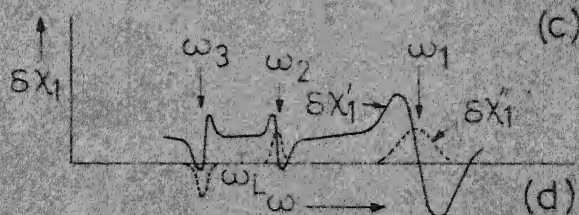
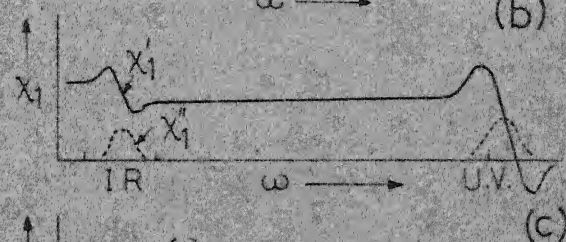
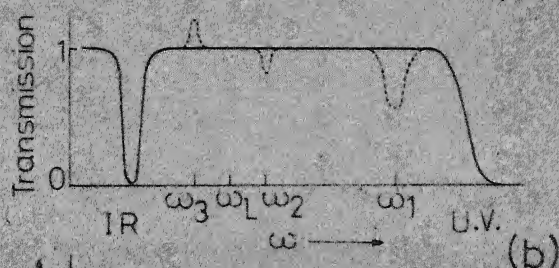
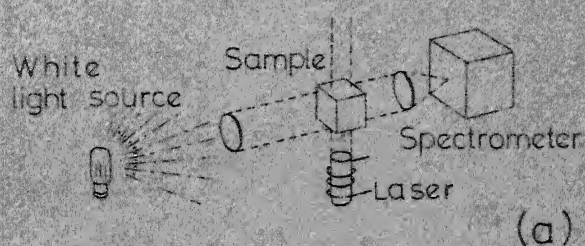


FIG. I. 5 SCHEMATIC ILLUSTRATING TWO PHOTON PROCESSES IN PRESENCE OF INTENSE LASER RADIATION OF FREQUENCY ω_L .

(a) EXPERIMENTAL SET UP

(b) ABSORPTION SPECTRUM

(c),(d) FREQUENCY DEPENDENCE OF $\chi_1(-\omega, \omega)$ AND $\delta\chi_1(-\omega, \omega)$ OR $\chi_3(-\omega, \omega, \omega_L, \omega_L)$

(Reproduced from ref. 3)

additional absorption at ω_1 and ω_2 and emission at ω_3 in the presence of the intense laser radiation of frequency ω_L .

Fig. I.5(c) shows the real and imaginary parts χ_1' and χ_1'' of the linear-susceptibility. The absorption in Fig. I.5(b) at IR and UV corresponds to the peaks in χ_1'' . The change in the linear-susceptibility $\delta\chi_1$ in the presence of the laser beam at ω_L is shown in Fig. I.5(d).

$$\delta\chi_{lm}^{(1)}(-\omega, \omega) = 6 \chi_{lmno}^3(-\omega, \omega, \omega_L, -\omega_L) E_n(\omega_L, z) E_o^*(\omega_L, z) \quad I.77$$

I.4.3C Two-photon absorption

In the case when all the three frequencies in the susceptibility are equal, retaining only the two-photon resonance term, we have

$$P_L^{(3)}(\omega_L, z) = 3\chi_{lmno}^3(-\omega_L, -\omega_L, \omega_L, \omega_L) E_m^*(\omega_L, z) E_n(\omega_L, z) E_o(\omega_L, z) \exp(ik_L z) \quad I.78$$

where

$$\begin{aligned} 3\chi_{lmno}^3(-\omega_L, -\omega_L, \omega_L, \omega_L) &= 3\chi_{lmno}^{NR}(-\omega_L, -\omega_L, \omega_L, \omega_L) \\ &+ \frac{1}{2} \chi_{lmno}^t(-\omega_L, -\omega_L, \omega_L, \omega_L) \frac{\Gamma_t}{\omega_t - 2\omega_L - j\Gamma_t} \end{aligned} \quad I.79$$

At resonance ie. $\omega_t = 2\omega_L$ this represents simultaneous absorption of two-photons of the laser radiation, the medium being excited to a state t of the same parity as ground state and separated

from it by $2\omega_L$. There need be no real level corresponding to ω_L as will be needed for single photon (linear) absorption at the laser frequency. At resonance ie. $\omega_t = 2\omega_L$, this term contributes to the linear susceptibility a purely (positive) imaginary term which is proportional to the square of the laser field amplitude and hence such a nonlinear absorption is characterized by a dependence of absorption intensity on the square of the laser intensity. The first observation of two-photon absorption was in $\text{CaF}_2:\text{Eu}^{2+}$ by Kaiser and Garrett⁶³ who observed blue-fluorescence from these crystals when illuminated by the red laser light. Two-photon absorption is also observed in CS_2 ⁶⁴ and the process is used for photo-ionization of Iodine.⁶⁵

I.4.3D Intensity-dependent changes in refractive index

When the incident laser frequency is far from any two-photon resonances then x_3 in eqn. I.79 is purely real and consequently contributes a real term proportional to $|E_L|^2$ to the linear susceptibility. This term gives rise to a change in the refractive index of the medium proportional to the square of the laser field amplitude.

The effect of $x_3(-\omega_L, \omega_L, \omega_L, \omega_L)$ on the wave itself can be described by the eqn.

$$\frac{dE(\omega_L, z)}{dz} = \frac{2\pi i k_L}{\epsilon_L} x_3 E^2(\omega_L, z) E^*(\omega_L, z) \quad \text{I.80}$$

writing $E(\omega_L, z) = |E(\omega_L, z)| \exp i\phi(\omega_L, z)$ and $x_3 = x'_3 + i x''_3$ we obtain from eqn. I.80

$$\frac{d|E(\omega_L, z)|}{dz} = - \frac{2\pi k_L}{\epsilon_L} x''_3 |E(\omega_L, z)|^3 \quad \text{I.81}$$

$$\frac{d\phi(\omega_L, z)}{dz} = \frac{2\pi k_L}{\epsilon_L} x'_3 |E(\omega_L, z)|^2 \quad \text{I.82}$$

eqn. I.81 integrates directly to give^{6,62}

$$\frac{1}{|E(\omega_L, z)|^2} = \frac{1}{|E(\omega_L, 0)|^2} + \frac{4\pi k_L}{\epsilon_L} x''_3 z \quad \text{I.83}$$

This equation describes the attenuation of the wave by two-photon absorption where x''_3 is given by eqn. I.79. When far from resonance $x''_3 \sim 0$ and $|E(\omega_L, z)|$ is constant. Eqn. I.82 can then be directly integrated and the nonlinear interaction can be expressed as an intensity-dependent change in the index of refraction given by $\delta n = \frac{2\pi}{n_L} x'_3 |E(\omega_L, z)|^2$ I.84 This is the familiar Kerr-effect.

I.4.4A Self-focussing and SRS

The intensity distribution across the laser beam is non-uniform and is in fact approximated by a gaussian distribution which is peaked about the direction of propagation. The intensity dependent refractive index produces a gradient across the laser beam, with the refractive index maxima along the

direction of propagation. The peripheral rays are refracted towards the beam centre resulting in a focussing action produced on the beam. This focussing results in a further increase in the gradient with the beam getting sharply focussed. This phenomenon is termed self-focussing.⁶⁶ The focussing process continues until limited by other limiting factors. One such factor is the natural spreading of the beam by diffraction.

The angular divergence due to diffraction of a beam of diameter D is $\theta \sim 1.22\lambda/n_0 D$. There is a large change in dielectric constant inside the beam. From the condition that the critical angle for total internal reflection at the beam boundary be greater than θ , so that spreading by diffraction will not occur, Chiao, Garmire and Townes⁶⁸ have predicted that a light beam may be trapped at any arbitrary diameter without spreading, if a threshold power P_{Cr} is exceeded.

$$P_{Cr} = \frac{\pi D^2}{4} \frac{n_0 E^2 C}{8\pi} \geq (1.22\lambda)^2 \frac{C}{64n_2} \quad \text{I.85}$$

From a solution of wave-equation in the geometric optics approximation, a self-focussing length could be defined within which the field intensity changes appreciably⁶⁹

$$z_f = \frac{n_0 a^2}{4} \left(\frac{C}{n_2} \right)^{\frac{1}{2}} / [P^{\frac{1}{2}} - P_{Cr}^{\frac{1}{2}}] \quad \text{I.86}$$

where P is the total power carried by the beam, a the beam radius.

The intensity dependent refractive index n_2 may be due to different mechanisms such as high-frequency Kerr-effect, electrostriction and electronic polarizability etc. Kerr effect due to molecular re-orientation in an applied field predominates in anisotropic liquids. The inequalities of molecular polarizability of anisotropic molecules along the molecular axis of symmetry α_{\parallel} and at right angle to it α_{\perp} , cause the molecules to re-orient themselves in an applied field with their axis of largest α along the electric-field, minimizing the interaction energy. The reduction in energy per molecule is $(\alpha_{\parallel} - \alpha_{\perp})E^2$, so that the resultant increase in dielectric constant is

$$\delta \epsilon = \frac{N}{KT} (\alpha_{\parallel} - \alpha_{\perp}) E^2 \propto \epsilon_2 E^2 \quad \text{I.87}$$

Where N is density of molecules, K the Boltzmann constant and T is the temperature.

The first experimental evidence of self-focussing was from studies of laser induced damage in glasses⁷⁰ where the damage appeared in the form of long, thin filaments along the lens axis. The occurrence and dynamics of self-focussing in liquids has been directly verified by studying the variation of beam diameter along the length of the liquid by Garmire, Chiao and Townes.⁷¹ Bright filaments at the end face have been photographed in Raman liquids⁷² by making use of the observed fact that the laser light in filaments are depolarized, so that background, untrapped, laser light could be eliminated

by placing the Raman liquid between crossed polarizers. The filaments were about 50μ in diameter.

Many of the anomalies in SRS have been interpreted in terms of self-focussing and the resulting filament formation in liquids. The intensity inside the small filaments are several orders greater than in the primary laser beam and hence even when the primary laser power is below the theoretical Raman threshold the intensities inside the filaments far exceed the Raman threshold by more than an order. Consequently the whole series of SRS ladder appears at a single threshold that is nearly two orders smaller than the theoretical value. Infact the threshold observed is actually the self-focussing threshold (P_{Cr}) of the liquid. The calculated values of P_{Cr} are one to two orders smaller than the Raman thresholds. ex: in CS_2 : $n_2 = 10^{-10}$ esu corresponding to a nonlinear susceptibility $\sim 2 \times 10^{-11}$ esu $\lambda \sim 10^{-6}m$ and thus one gets $P_{Cr} \sim 16$ kW and $l_{sf} \sim 10$ cm. This also explains the threshold on the length of Raman cell for the generation of SRS. Again this corresponds to the self-focussing length which should be less than the cell length, for self-focussing to occur, at which SRS also automatically appears. By writing eqn. I.86 in the form

$$P^{\frac{1}{2}} = P_{Cr}^{\frac{1}{2}} + \frac{A}{l} \quad \text{where} \quad A = \frac{n_o a^2}{4} \left(\frac{C}{n_2} \right)^{\frac{1}{2}} \quad \text{I.88}$$

and by plotting the square root of the observed threshold power for SRS for different cell length (l) against $1/l$ ⁷³, one gets a straight line with slope A and intercept $P_{Cr}^{1/2}$ which verifies eqns. I.86 and 88.

Interesting experiments⁷² in which a variable length of a self-focussing liquid (bromo-benzene) is placed before the Raman liquid (nitrobenzene) show that the threshold in the Raman liquid decreases considerably as the length of bromobenzene column is increased, even below its own threshold length for SRS. Stimulated Raman oscillation can be induced in liquids that remain below the threshold in the unfocussed laser beam by mixing them with a focussing liquid. Three orders of Raman lines of the 459 cm^{-1} in CCl_4 were observed with 75 cc CCl_4 , 15 cc nitrobenzene and 10 cc CS_2 .⁷² This mixture of the latter two liquids is adjusted to stay below the SRS threshold of both of them. These experiments conclusively prove that the experimental threshold for Raman laser action appears to be determined not so much by the Raman susceptibility but rather by the self-focussing capability of the liquid.

Chiao, Townes and Garmire⁷⁴ observed a new class of light filaments which were typically about 5μ in diameter, within which large scale depletion of laser light occurred, the energy being transferred to stimulated Raman frequency generation. They also observed bright filaments at Stokes frequency and dark spot corresponding to laser frequency, filament diameter

being 5μ . The dark spot is attributed to large scale depletion of laser light near the focus. Stimulated Stokes light was seen to be generated in these small size filaments in less than a few mm near the large scale self-focussing distance and increased by less than two orders in the next 50 cms. Hence gain as large as e^{24} per cm. is expected in these fine filaments to make SRS essentially a single pass effect as observed by many workers. These filaments last less than 1 ns. The anomalous high change in refractive index needed for the observed small scale light-trapping is attributed by these authors to the expansion of molecular dimensions under coherent molecular excitation. Such large refractive index changes cannot arise from any of the other earlier mentioned mechanisms at the calculated field strengths. The sudden discontinuity observed in the output characteristics of Raman amplifiers^{45,46} corresponds to the onset of self-focussing in the liquid.

I.4.4B Anti-Stokes rings

The generation and propagation of the SRS inside the small scale filaments modifies the cone-angles of anti-Stokes radiation from the values calculated for unbounded plane waves. The large changes of index of refraction and also waveguide effects inside the filaments modifies the phase velocities and hence the cone-angles of anti-Stokes emission from filamentary region.⁷⁴

It was observed that in liquids the direction of emission do not generally follow any simple theory⁷⁵ and the size and structure of these cones seemingly vary at random depending on the intensity distribution across the laser beam crosssection. E. Garmire⁵⁰⁻⁵² has proposed a new class of anti-Stokes cones which are termed as 'Class-II' radiation which are also discussed by Shimoda.⁷⁵ These anti-Stokes radiations appear as full rings of diameter somewhat larger than the cone-angles of the Class-I anti-Stokes obtained by volume phase matching (eqn. I.24 and 25). Most of the anti-Stokes rings obtained in liquids in the initial experiments proved to be Class-II radiation. The Class-I cone appear when the liquid cell is tilted in order to enhance Stokes radiation along the volume phase matching directions. Class-I radiation appears over part of a circular ring within the larger and fully circular Class-II rings. It is shown that these Class-II anti-Stokes radiation couples to forward Stokes radiation which involves a large tranverse mismatch of wave vectors. These are attributed to surface radiations essentially originating in small-scale trapped light filaments. In crystals such as calcite⁵³ the anti-Stokes emission angles and Stokes-absorption angles agree fairly well with the volume phase matching condition. These are essentially Class-I radiations. The experimental class II emission angles are also given in Table I.1.

U. T. T. FUR
CENTRAL LIBRARY
Acc. No. A 46003

I.4.4C Anomalous broadening

The anomalously broad widths of the SRS components observed by Stoicheff^{35,36} and others have been explained by Bloembergen¹⁴ as due to the modulation of the refractive index of the medium at the difference frequency between two laser frequency components ω_L, ω'_L with separation of the order of a few cm^{-1} . The laser radiation is observed to emit in more than one frequency whenever such broadening is noticed. When a wave at a new frequency ω_s traverses the material, it will be phase or frequency modulated at this difference frequency $\omega_L \sim \omega'_L$ resulting in the creation of side bands at $\omega'_s = \omega_s \pm (\omega_L \sim \omega'_L)$. This process can be described by the nonlinear polarizability.¹⁹

$$\chi^{(3)}(-\omega_s, \omega_s, \omega_L, -\omega'_L)$$

These side-bands experience gain through the stimulated Rayleigh scattering. Subsequent beating, in several passes of the laser beam through the liquid, leads to the creation of many side bands around the frequency ω_s , extending on either side from 50 to 100 cm^{-1} . Discrete components within this broadening are observed by Stoicheff.^{35,36} The complex phase shifts occurring inside the small-scale trapped filaments during the time of the multi-mode laser pulse are considered by Shimoda⁷⁴ and the resultant changes in the anti-Stokes cone angles and broadening of the SRS components are calculated.

I.4.4D Verification of SRS theory

The foregoing description of the effect of self-focussing and other nonlinearities on the SRS characteristics in liquids makes one to look for systems where self-focussing is absent in order to verify the gain characteristics of a Raman laser. Not surprisingly such verification has come from studies of SRS in gases such as hydrogen, in which self-focussing is absent.⁷⁶ Studies by Dennis and Tannenwald⁷⁷ at 90° to the laser radiation (using resonant feed back) also yield results comparable to the SRS theory. In this case the effects of self-focussing is averaged out. The majority of the studies of Raman laser action to this date is closely associated with the phenomenon of self-focussing, and other induced molecular scattering, thus rendering the observed phenomenon more complex than the simple SRS theory.

I.4.5 Coupled mode analysis of SRS

The nonlinear interaction in a medium among several participating waves can be studied by application of eqn. I.71 to each of the waves and solve the resultant equations, coupled through the nonlinear polarizations. The method of coupled mode analysis was introduced by Armstrong, Bloembergen, Ducuing and Pershan,⁵⁶ who treated in detail second harmonic generation and 3-wave interaction through second order polarization. The same method is extensively used to describe SRS^{46,81-86} and will be briefly outlined in the following Chapters.

I.4.5A Raman type Susceptibilities[†]

Several authors^{8,78-80} have given complete quantum mechanical derivation, using density matrix formalism, for the nonlinear susceptibilities describing stimulated Raman processes. The Stokes-susceptibility χ_s is given by⁸

$$P^{NL}(\omega_s) = \chi_s(-\omega_s, \omega_L, -\omega_L, \omega_s) E_L^2 E_s \quad I.89$$

$$\chi_s = - \frac{Ne^4 n^3 \eta^2}{(\omega_L - \omega_s - \omega_{g'g^0} - i\Gamma_{g'g^0})} \times \left[\frac{\chi_{ng} \chi_{gn}}{\omega_L - \omega_{n^0g^0}} - \frac{\chi_{ng} \chi_{gn}}{\omega_L - \omega_{n'g^0}} - \frac{\chi_{ng} \chi_{gn}}{\omega_s + \omega_{n^0g^0}} + \frac{\chi_{ng} \chi_{gn}}{\omega_s + \omega_{n'g^0}} \right] \quad I.90$$

g, n refer to electronic and $0, 1$ to vibrational states. These and the primary Stokes and anti-Stokes emission processes are shown in Fig. I.6. At resonance $\omega_L - \omega_s - \omega_{g'g^0} = 0$ and χ_s is negative pure imaginary, which corresponds to positive gain at ω_s (see Appendix) proportional to $|E_L|^2$. For the laser frequency we can write

$$P^{NL}(\omega_L) = \chi_s^* E_L |E_s|^2 \quad I.91$$

and hence there is absorption at ω_L proportional to $|E_s|^2$. On similar lines one can define a susceptibility χ_a^* for the primary anti-Stokes process by replacing ω_L by ω_a and ω_s by ω_L in eqn. I.90.

[†]Equation in Chapter I.4.5A, C and D follow the notations in references 8, 81 and 82.

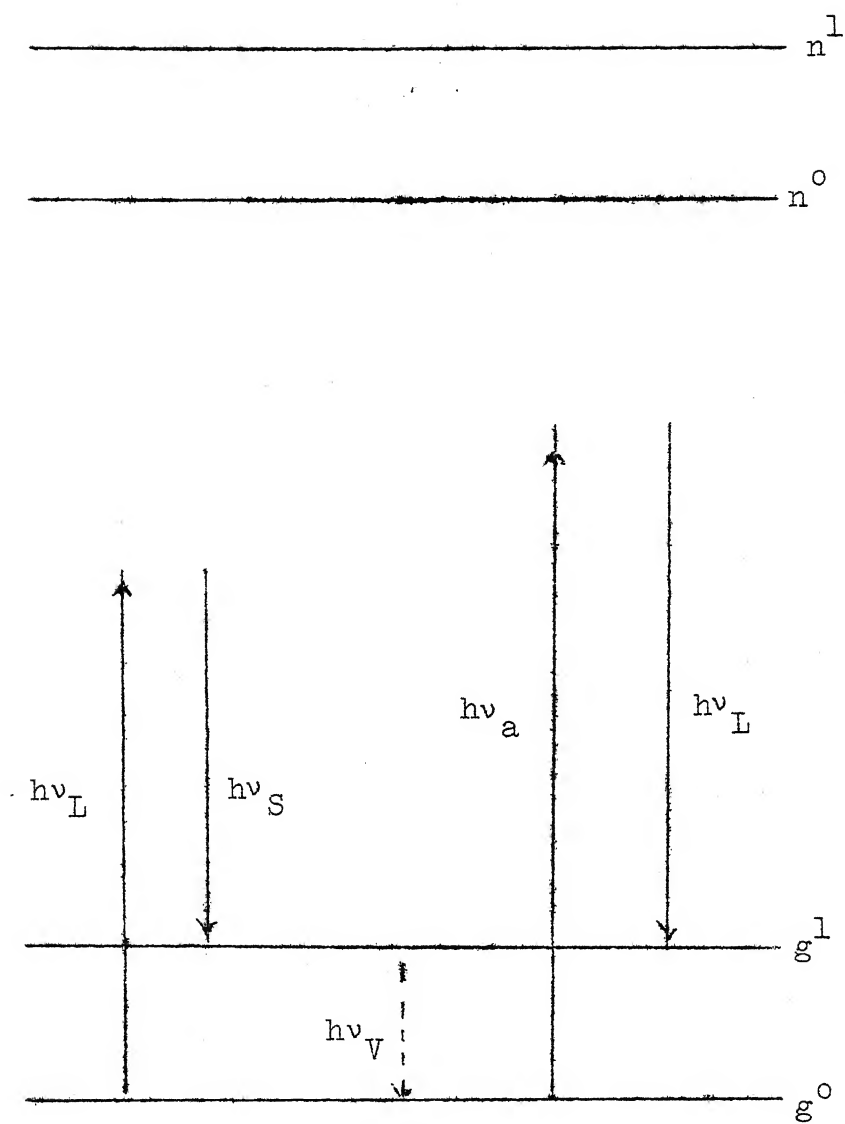


Fig. I.6. Schematic for the Raman type transitions in the quantum treatment of SRS (Refer eqn. I.90).

The nonlinear polarization describing anti-Stokes emission in the presence of E_L and E_S is given by

$$P^{NL}(\omega_a) = \chi(\omega_a = 2\omega_L - \omega_S) E_L^2 E_S^* \quad \text{I.92}$$

Nonlinear polarization due to Raman type resonance process can be found for each of frequencies ω_L, ω_S and ω_a in the simultaneous presence of fields E_L, E_S and E_a . By explicit calculation it can be shown that the susceptibility in eqn. I.92 may be expressed as $(\chi_S^* \chi_a)^{\frac{1}{2}}$. In the limit of negligible dispersion $(\chi_S^* \chi_a)^{\frac{1}{2}} = \chi_S^*$.

By writing χ_{NR} for the nonresonant contribution to the nonlinear susceptibilities we can write the detailed polarization at the three frequencies in the presence of all three waves, by explicit calculation similar to the one leading to eqn. I.90.⁸

$$P^{NL}(\omega_S) = (\chi_S + \chi_{NR}) |E_L|^2 E_S + [(\chi_S \chi_a^*)^{\frac{1}{2}} + \chi_{NR}] E_L^2 E_a^* \quad \text{I.93}$$

$$P^{NL}(\omega_a) = (\chi_a + \chi_{NR}) |E_L|^2 E_a + [(\chi_S^* \chi_a)^{\frac{1}{2}} + \chi_{NR}] E_L^2 E_S^* \quad \text{I.94}$$

$$P^{NL}(\omega_L) = (\chi_S^* + \chi_{NR}) |E_S|^2 E_L + (\chi_a^* + \chi_{NR}) |E_a|^2 E_L + [(\chi_S \chi_a^*)^{\frac{1}{2}} + (\chi_S^* \chi_a)^{\frac{1}{2}} + 2\chi_{NR}] E_L^* E_S E_a \quad \text{I.95}$$

The complex symmetry relationship can be written as:

$$(\chi_S \chi_a^*)^{\frac{1}{2}} = \chi(\omega_S = 2\omega_L - \omega_a) = \chi^*(\omega_a = 2\omega_L - \omega_S) \quad \text{I.96}$$

This can be readily seen from the sign of the damping term $i \Gamma_{n'n}$ in the resonant denominators, for example:

$$\chi(-\omega_s, \omega_L, \omega_L, -\omega_a) \rightarrow \frac{\Gamma_{n'n}}{\omega_{n'n} + (\omega_L - \omega_a) + i \Gamma_{n'n}} \quad \text{I.97}$$

$$\chi(-\omega_a, \omega_L, \omega_L, -\omega_s) \rightarrow \frac{\Gamma_{n'n}}{\omega_{n'n} - (\omega_L - \omega_s) - i \Gamma_{n'n}} \quad \text{I.98}$$

The real part of the terms in $(\chi_s \chi_a^*)^{\frac{1}{2}}$ corresponds to a scattering process in which two quanta at ω_L scatter into a quanta at each of ω_s and ω_a . The relative phases of E_L , E_s and E_a determines as to which transition between the two levels is enhanced or decreased by the interference between the two transitions in Fig. I.6. The phase information is completely lost in the quantum mechanical treatment in terms of the number of quanta in Chapter I.3.2. The coupled wave analysis is the only correct description of SRS.

I.4.5B Harmonic Oscillator model

The classical harmonic oscillator model can be used to derive the nonlinear polarization P^{NL} at the Stokes frequency and to study the amplification of Stokes wave E_s using eqn. I.71.

The polarization is $P = N\alpha E$ and using eqn. I.14 we obtain the nonlinear polarization in terms of the vibrational coordinate x_v as:

$$P_{NL} = N\alpha_1 xE \text{ where } \alpha_1 = (\partial\alpha/\partial x)_0 \quad I.99$$

Defining $x(z,t) = \frac{1}{2}[x_v(z)\exp(-i\omega_v t) + c.c.]$

$$E(z,t) = \frac{1}{2}[E_s \exp i(k_s z - \omega_s t) + E_2 \exp i(k_L z - \omega_L t)] + c.c. \quad I.100$$

$$P^{NL}(z,t) = \frac{1}{2} [P^{NL}(\omega_s) \exp(-i\omega_s t) + P^{NL}(\omega_L) \exp(-i\omega_L t) + c.c.] \quad I.100$$

We get

$$P^{NL}(\omega_s) = \frac{1}{2} N\alpha_1 E_L x_v^* \exp(ik_L z) \quad I.101$$

The vibrational co-ordinate can be solved from the simple harmonic eqn. I.13 and assuming resonance $\omega_L - \omega_s = \omega_v$, we get

$$x_v(z) = i \frac{\alpha_1 E_L E_s^*}{4m\gamma\omega_v} \exp i(k_L - k_s)z = x_v \exp i(k_L - k_s)z \quad I.102$$

Using eqn. I.101 and 102 in eqn. I.71, in the parametric approximation that assumes E_L as constant, we obtain the solution

$$E_s(z) = E_s(0) \exp[\frac{1}{2}(g - \ell_s)z] \quad I.103$$

where $\ell_s = \sigma/Cn_s$ and the gain per cm. is given by

$$g = \frac{\pi\omega_s}{4Cn_s} \frac{N\alpha_1^2}{m\gamma\omega_v} |E_L|^2 \quad I.104$$

On similar lines the polarization at anti-Stokes frequency

ω_a is:

$$P^{NL}(\omega_a) = \frac{1}{2} N \alpha_L E_L x_v \exp(ik_L z) \quad \text{I.105}$$

again using eqn. I.102 and eqn. I.71, we get

$$\frac{dE_a}{dz} = -\frac{\ell_a}{2} + \frac{\pi N \omega_a \alpha_L^2}{8 C n_a m \gamma \omega_v} E_L^2 E_S^* \exp i[(2k_L - k_S - k_a)z - \pi] \quad \text{I.106}$$

spatial build up at anti-Stokes frequency ω_a will accompany that at ω_s with $2k_L - k_S - k_a = 0$ and a phase difference of π .

I.4.5C Coupling between vibrational and light waves in a Raman media

Instead of the quantum mechanical picture of the Stokes process, one can consider, in place of the localized vibration R, an optical phonon wave at the vibrational frequency

$$Q = A_v \exp(ik_v z - i\omega_v t) \quad \text{I.107}$$

where $Q = R(2\rho\omega_v^2)^2$ is the normal co-ordinate of the vibrational wave, ρ is the mass density.

The primary Stokes process can be looked upon as a parametric process in which the constant laser wave $E_L \exp(i k_L z - \omega_L t)$ couples the Stokes wave $E_S \exp(i k_S z - \omega_S t)$ and the optical phonon wave Q. Bloembergen and Shen^{81,8} have analysed such a vibrational coupling. The phonon wave is much more strongly

damped than the optical wave, which is the reason it is not explicitly considered in most of the other analysis. The Stokes wave is considered on the same lines as in I.4.5B but the wave equation is different for the phonon wave. The amplitude equation can be written as:⁸¹

$$\frac{dE_S}{dz} = N\left(\frac{\partial\alpha}{\partial Q}\right)\left(\frac{2\pi i\omega_S^2}{C^2 k_S}\right) E_L A_V^* \quad \text{I.108a}$$

$$\frac{dA_V^*}{dz} = -\left(\frac{k_V}{\omega_V}\right) \Gamma_V A_V^* + N\left(\frac{\partial\alpha}{\partial Q}\right)\left(\frac{-ik_V}{2}\right) E_L^* E_S \quad \text{I.108b}$$

The damping term is included phenomenologically in eqn. I.108b. The solution leads to a mode with partly Stokes character with gain constant

$$K_S = \left(\frac{2\pi\omega_S^2}{k_S C^2}\right) \left[\frac{N^2\left(\frac{\partial\alpha}{\partial R}\right)^2}{2\rho\omega_V\Gamma_V} \right] |E_L|^2 = -\left(\frac{2\pi\omega_S^2}{k_S C^2}\right) \chi_S'' |E_L|^2 \quad \text{I.109}$$

where

$$\chi_S'' = -\frac{N^2\left(\frac{\partial\alpha}{\partial R}\right)^2}{2\rho\omega_V\Gamma_V} \quad \text{I.110}$$

χ_S'' is the imaginary Stokes susceptibility introduced here and it can also be obtained from eqn. I.90 in which both electronic and vibrational levels are quantized. Eqn. I.90 can be shown equivalent to eqn. I.110⁸. From eqn. 101 we obtain

$$\chi'' = -\frac{1}{4} \frac{N\left(\frac{\partial\alpha}{\partial R}\right)^2}{m\gamma\omega_V} \quad \text{I.111}$$

Eqn. I.110 and 111 are identical. The numerical factor $1/4$ in eqn. I.111 arises due to the definition of fields as in eqn. I.100. The susceptibility $\chi_3^r(\omega_s)$ in eqn. I.74 and 75 can also be shown to agree with eqn. I.110, by noting that the matrix element $\langle g | \alpha_{1m}(\omega_1, \omega_2) | s \rangle$ is the polarizability matrix element α_{01}^{62} which is related to $\partial\alpha/\partial R$ by

$$\left(\frac{\partial\alpha}{\partial R}\right)^2 = \frac{2\omega_v}{\hbar} \alpha_{01}^2 \quad \text{I.112}$$

It is evident from the foregoing that the several methods of analysis outlined give the same result and are identical.

I.4.5D Coupling between Stokes and anti-Stokes waves

In the analysis in Chapter I.4.5C the anti-Stokes wave is assumed to be absent. To study the anti-Stokes wave generation also, we have to solve the four coupled equations, ie. the three optical waves at ω_L, ω_s and ω_a and the phonon wave at ω_v . The problem can be made more simple by assuming the laser intensity as constant and neglecting the phonon wave as it is heavily damped. We will be left with only the two coupled equations at the Stokes and anti-Stokes waves only, which can be written down using eqn. I.71, 93 and 94. The detailed analysis is carried out by Bloembergen and Shen.^{8,81,82} They show that the solution of the coupled equations finally lead to an exponential gain constant

$$K = -\alpha \pm \left[\left(\frac{2\pi\omega_s}{C^2 k_s} \right) \chi_s |E_L|^2 \Delta k - \frac{1}{4} \Delta k^2 \right]^{\frac{1}{2}} \quad \text{I.113}$$

where α is absorption coefficient and $\Delta k = 2k_L - k_s - k_a$ is the linear phase mismatch. At exact phase matching i.e. $\Delta k = 0$, eqn. I.113 shows that there is no gain either at ω_s or ω_a . This apparently surprising result, in view of the earlier theoretical analysis by Garmire et.al.^{47,48} (see Chapter I.3.4), is nevertheless a well known result in the theory of parametric interaction where there is no gain at either of the sidebands if the other side band is not suppressed.

For sufficiently large Δk , one of the roots correspond to a purely Stokes wave with positive gain which is identical to that given by eqn. I.109 and the other root correspond to a purely anti-Stokes wave which is always attenuated as already observed in the earlier treatment of the primary Raman process. For any given mismatch $\Delta k \neq 0$, the Stokes wave in that direction has always an admixture of anti-Stokes character, the ratio of the anti-Stokes to Stokes amplitude is given by

$$\frac{|E_a|^2}{|E_s|^2} = \left(\frac{2\pi\omega_s^2}{C^2 k_s} \right) |\chi_s + \chi_{NR}|^2 |E_L|^4 / \Delta k^2 \quad \text{I.114}$$

In the forward direction, $\Delta k \sim 10^2 \text{ cm}^{-1}$ and the partial anti-Stokes character $|E_a/E_s|^2$ is 0.01% for a power gain of 2 cm^{-1} in nitrobenzene. This is however observable because of the high intensity of Stokes wave. The real part of the susceptibilities

introduce an offset $\Delta\omega$ of the waves from their resonance frequencies. These are dealt in detail in Ref. 8 and 82.

The anti-Stokes gain is maximum for values of Δk slightly offset from the phase matched direction $\Delta k=0$. The optimum gain occurs for $\Delta k \sim 2g_s$ where g_s is the Stokes gain given by eqn. I.109. The dip in the Stokes radiation corresponding to $\Delta k=0$ as predicted by eqn. I.113 has actually been observed.^{51,53} The dark anti-Stokes ring at $\Delta k=0$ is however not observed due to geometrical and other experimental limitations such as photographic sensitivity etc. Within experimental error one can still consider $\Delta k=0$ as providing the anti-Stokes angles. In gases the matching angles are essentially in the forward direction as the angle of optimum gain corresponding to $\Delta k \sim 2g_s$ is very small (10^{-2} rad or 0.57°).

The actual experimental conditions are more complex than the simple two wave theory considered above. The laser intensity is strictly not constant but is depleted during the interaction and the existence of several higher order Raman waves necessitates a solution of many coupled wave equations which is mathematically intractable. Further the multimode and non-uniform nature of the laser emission makes the even simple picture of the two waves considered, so far, more complex.⁸² A particular problem which includes several higher order Stokes waves has been solved by machine calculations⁸² which however

shows that over a particular distance z along the medium, only two waves are present. One of them essentially constant except in the overlapping region where one Stokes wave decreases and the newly generated higher order wave increases. The earlier analysis that treats laser as constant should be viewed from this aspect. Saturation mechanism limits the growth of higher order Stokes waves. Such a saturation occurs when a Stokes wave reaches the threshold for generation of the next higher order wave, when the latter takes over and grows rapidly and so on. Such nonlinear limiting processes find interesting applications.

The problem of parametric generation of higher order Raman radiations can only be carried out in steps without considering all higher order waves simultaneously, in view of the foregoing complexities and findings from machine calculation. One such problem will be encountered and solved in the next chapter dealing with our experimental work.

The coupled wave formalism can also be used to describe coupling of light waves with other modes such as spin waves, plasma waves etc. The coupled mode analysis is extensively used in the theory of travelling wave tubes⁸⁷ and parametric interaction.⁸⁸ The extension to nonlinear optics has led to the generalization of many of the laws of optics to nonlinear optical situations.⁵⁶

References

- 1 S.-P.S. Porto and D.L. Wood: J. Opt. Soc. Am., 52, 251 (1962)
- 2 S.A. Akhmanov and R.V. Khokhlov: Sov. Phys -Uspekhi, 394 (1968-69).
- 3 R.W. Minck, R.W. Terhune and C.C. Wang: App. Opt., 5, 1595 (1966).
- 4 R.W. Terhune: Int. Sci. and Tech., p. 38, (1964).
- 5 P.A. Franken and J.F. Ward: Rev. Mod. Phy., 35, 23 (1963).
- 6 R.W. Terhune and P.D. Maker: Advances in Lasers II, A.K. Levine, Ed. New York: Marcel Dekker (1968).
- 7 L.N. Ovander: Sov. Phy -Uspekhi, 8, 337 (1965).
- 8 N. Bloembergen: Nonlinear Optics, (Benjamin, New York 1965).
- 9 P.S. Pershan: In progress in Optics Vol. 1.5 (New York: Interscience., Amsterdam: North Holland 1966).
- 9a Ref. 19, p. 1018.
- 10 R.Y. Chiao, C.H. Townes and B.P. Stoicheff, Phy. Rev. Let., 12, 592 (1964).
- 11 E.E. Hagenlocker, R.W. Minck and W.G. Rado: Phy. Rev., 154, 226 (1967).
- 12 R.G. Brewer: Phy. Rev., 140, A 800 (1965).
- 13 Many of the papers on Stimulated Raman Scattering also deal with Stimulated Brillouin Scattering.
- 14 N. Bloembergen and P. Lallemand: Phy. Let., 16, 81 (1966).
- 15 C.W. Cho, N.C. Foltz, D.H. Rank and T.A. Wiggins: Phy. Rev. Let., 18, 107 (1967).
- 16 Y.R. Shen: Phy. Let., 20, 378 (1966).
- 17 K.A. Brueckner and S. Jorna: Phy. Let., 17, 78 (1966).
- 18 S.A. Akhmanov, P. Suchorukov and R.V. Khocklov: Sov. Phys -JETP, 23, 1025 (1966); Ibid, 24, 198 (1967).

- 19 N. Bloembergen: Am. J. Phys., 35, 989 (1967).
- 20 V.A. Zubov, M.M. Suschinskii and I.K. Shuvalov: Sov. Phy-USpekhi, 7, 419 (1964-65).
- 21 A.M. Bonch-Bruевич and V.A. Khodevoi: Sov. Phy-USpekhi, 8, 1 (1965-66).
- 22 G. Placzek: *Handbuch der Radiologie* (Academische Verlagsgesellschaft, Leipzig 1934), Vol. VI, p. 206-374.
 F. Kohlrausch: *Der Smekal-Raman Effect*, *Ergänzungs-band* (Springer-Verlag, Berlin, 1938).
 S. Bhagavantam: *Scattering of Light and the Raman Effect*, (Chemical Publishing Co., New York, 1942).
 B.P. Stoicheff: *Methods in Experimental Physics*, (Academic Press, Inc., New York, 1962) Vol. 3, p. 11.
 San. Ichire Mizushima., *Handbuch der Physik*: Ed. S. Flugge 1958, Vol. 26, p. 171.
- 23 E.J. Woodbury and W.K. Ng: Proc. IRE, 50, 2367 (1962).
- 24 R.W. Hellwarth: *Advances in Quantum Electronics*, J.R. Singer, (Columbia University Press, New York, 1961).
- 25 F.J. McClung and R.W. Hellwarth: Proc. IEEE, 51, 46 (1963).
- 26 E.J. Woodbury: *Proceedings of the Third International Conference on Quantum Electronics*, P. Grivet and N. Bloembergen Eds (Dunod, Paris, 1964), p. 1577.
- 27 G. Eckardt, R.W. Hellwarth, F. McClung, S.E. Schwartz, E. Weiner and E.J. Woodbury: Phys. Rev. Let., 9, 455 (1962)
- 28 R.W. Hellwarth: Phy. Rev., 130, 1850 (1963).
- 29 R.W. Hellwarth: App. Opt., 2, 847 (1963).
- 30 M. Geller, D.P. Bortfeld and W.R. Sooy: App. Phys. Let., 3, 36 (1963).
- 31 G. Eckardt, D.P. Bortfeld and M. Geller: App. Phys. Let., 3, 137 (1963).
- 32 R.W. Minck, R.W. Terhune and W.G. Rado: App. Phys. Let., 3, 181 (1963).
- 33 A. Javan: Bull. Am. Phy. Soc., 3, 213 (1958).

- 34 H.J. Zeiger and P.E. Tannenwald: Proceedings of the Third International Conference on Quantum Electronics, P. Grivet and N. Bloembergen Eds (Donod, Paris, 1964), p. 1589.
- 35 B.P. Stoicheff: Proceedings of the International School of Physics, Enrico Fermi, Course (Academic Press, New York, 1964) p. 306.
- 36 B.P. Stoicheff: Phy. Let., 7, 186 (1963).
- 37 R.W. Terhune: Bull. Am. Phy. Soc., 8, 359 (1963).
- 38 W.J. Jones and B.P. Stoicheff: Phy. Let., 13, 657 (1964).
- 39 A.K. MacQuillan and B.P. Stoicheff: Physics of Quantum Electronics, P.L. Kelley, B. Lax and P.E. Tannenwald, Eds, (Mc-Graw Hill Book Co., 1966) p. 192.
- 40 D. Weiner, S.E. Schwarz and F.J. McClung: J. App. Phy., 36, 2395 (1965).
- 41 F.J. McClung and D. Weiner: J. Opt. Soc. Am., 54, 641 (1964)
53, 1446 (1963).
- 42 N. Bloembergen and Y.R. Shen., Phy. Rev. Let., 13, 720 (1964).
- 43 F.J. McClung, W.G. Wagner and D. Weiner., Phy. Rev. Let., 15, 96 (1965).
- 44 F.J. McClung, W.G. Wagner and D. Weiner, Ref. 39, p. 155.
- 45 Georges Bret and Guy Mayer, Ref. 39., p. 180.
- 46 N. Bloembergen and P. Lallemand: Ref. 39, p. 137.
- 47 E. Garmire, F. Pandarese and C.H. Townes: Phy. Rev. Let., 11, 160 (1963).
- 48 R.Y. Chiao, E. Garmire and C.H. Townes: Ref. 35, p. 326.
- 49 R. Loudon: Proc. Phy. Soc. (Lond), A 82, 393 (1963).
Proc. Roy. Soc. (Lond), A275, 218 (1963).
- 50 E. Garmire, Phys. Let., 17, 251 (1965).
- 51 E. Garmire: Ref. 39, p. 167.

- 52 E. Garmire: Thesis, M.I.T. Cambridge, U.S.A (1965).
- 53 R. Chiao and B.P. Stoicheff: Phys. Rev. Let., 12, 290 (1964).
- 54 H. Takuma and D.A. Jennings: App. Phys. Let., 4, 185 (1964).
- 55 Paul N. Butcher: Nonlinear Optical Phenomenon, Bulletin
200, Engg. Expt. Station, Ohio State University, 1965.
- 56 J.A. Armstrong, N. Bloembergen, J. Ducuing and P.S. Pershan:
Phy. Rev. 127, 1918 (1962).
- 57 C.G.B. Garrett and F.N.H. Robinson: IEEE. J. QE. 2, 328 (1966)
- 58 A. Yariv: Quantum Electronics, (John Wiley and Sons Inc.,
New York, 1967).
- 59 W.G. Cady: Piezo electricity, (New York: Me-Graw-Hill, 1946)
p. 177-199.
- 60 J.F. Nye: The Physical Properties of Crystals (Clarendon
Press, Oxford, England, 1957).
- 61 R.R. Briss: Proc. Phy. Soc. (Lond), 79, 946 (1962).
- 62 P.D. Maker and R.W. Terhune., Phy. Rev. 137, A 801 (1965).
- 63 W. Kaiser and C.G.B. Garrett., Phy. Rev. Let., 7, 229 (1961).
- 64 J.A. Giordmaine and J.A. Howe: Phy. Rev. Let., 11, 207(1963).
- 65 J.L. Hall, E.J. Robinson and L.M. Branscomb: Phy. Rev.
Let., 14, 1013 (1965).
- 66 G.A. Askaryan: Sov. Phy-JETP, 15, 1088 (1962).
- 67 V.I. Talanov: Sov. Phy-Radio Phy., 7, 254 (1964).
- 68 R.Y. Chiao, E. Garmire and C.H. Townes: Phy. Rev. Let.,
13, 479 (1964).
- 69 P.L. Kelley: Phy. Rev. Let., 15, 1005 (1965).
- 70 E. Garmire; R.Y. Chiao and C.H. Townes: Phy. Rev. Let.,
16, 347 (1966).
- 71 M. Hercher: J. Opt. Soc. Am., 54, 563 A (1964).
- 72 P. Lallemand and N. Bloembergen: Phy. Rev. Let., 15,
1010 (1965).., Bull. Am. Phy. Soc., 10, 1129 (1965).

- 73 C.C. Wang: Phy. Rev. Let., 16, 344 (1966).
- 74 K. Shimoda: Jap. Jour. App. Phy. 5, 615 (1966).
- 75 K. Shimoda: Jap. Jour. App. Phy. 5, 86 (1966).
- 76 N. Bloembergen, G. Brot, P. Lallemant, A. Pine and
P. Simova: IEEE. J. QE-3(5), 197 (1967).
- 77 T.H. Dennis and P.E. Tannenwald: Appl. Phy. Let., 5, 58 (1964).
- 78 N. Bloembergen and Y.R. Shen., Phy. Rev. 133, A 37 (1964).
- 79 A. Javan: Ref. 35, p. 284
- 80 V.M. Fain and E.Q. Yaschin. Sov. Phy - JETP, 19, 474 (1964).
- 81 N. Bloembergen and Y.R. Shen: Phy. Rev. Let., 12, 504 (1964).
- 82 Y.R. Shen and N. Bloembergen: Phys. Rev. 137 A, 1787 (1965).
- 83 C. Tang and T. Deutsch: Phy. Rev. 138, 1 (1965).
- 84 H. Haus, P. Kelley and H. Zeiger: Phy. Rev. 138, 960 (1965).
- 85 V.T. Platonenko and R.V. Khokhlov: Sov. Phy - JETP. 19,
1435, 378 (1964).
- 86 V.T. Platonenko and R.V. Khokhlov: Optics and Spectroscopy,
18, 211 (1965).
- 87 J.R. Pierce: Travelling-wave Tubes, Van Nostrand,
New York 1950.
- 88 W.H. Louisell: Coupled Mode and Parametric Electronics.
(John-Wiley and Sons. Inc., N.Y., 1960).

CHAPTER II

THERMOSPECTRUM

OF SRS IN LIQUIDS

II.1 Introduction

The early part of the decade since the discovery of SRS saw a literature explosion dealing with various theoretical and experimental aspects of the phenomenon. The anomalies were noted and attempts made to satisfactorily explain them in the light of existing theoretical and experimental knowledge. However, it needed the discovery of another very interesting phenomenon of self-focussing of intense beam of light in matter, to satisfactorily explain many of the observed anomalies of SRS, especially in liquids. The available experimental results indicated a close interplay between self-focussing and SRS in liquids. These early developements are briefly reviewed in Chapter I. Some aspects of SRS such as the anomalous broadenings, forward-backward asymmetry of the SRS indicatrix and also the exact mechanism of self-focussing are still subjects of intensive investigations. 1-2

The effect of temperature on SRS was first studied by a group of Russian workers.⁴ They studied the SRS in CS_2 in the temperature range of + 20 to -90°C and found a large increase in the intensity of the various SRS components as the temperature was lowered towards -90°C . The second Stokes intensity increased by over two orders of magnitude, whereas the first Stokes and anti-Stokes intensities reached a saturation at different low temperatures. The temperature dependence of the ordinary Raman crosssection was found insufficient to explain the large increase observed in SRS. The authors attribute the additional factor to the change in the self-focussing properties of the liquid with temperature. The Kerr-constant of CS_2 increases by 80% over that at room temperature when the temperature drops by 100°C . The change in the mode of self-focussing affects the coefficient of energy transformation from the laser to the SRS components. One can distinguish a second mode at low temperatures with a higher conversion factor. The incident laser energy is considerably depleted after a certain temperature (below -50°C) and the energy is distributed among the various SR components favouring the higher order components with decreasing temperature. They also observed a large asymmetry in the forward-backward scattering with an increasing preference for the 'forward' direction. We also undertook a similar work and our preliminary, though inconclusive, results showed no such marked changes of SRS in acetone as the temperature

was lowered towards its melting point, indicating the absence of such anomalously large changes in SRS intensities in a non-self-focussing liquid.

Biscar, Braunstein and Gratch (BBG)¹²⁻¹⁷ have observed cyclical temperature dependence of the SRS intensity in benzene and have called the resulting periodic intensity variations with temperature as the Thermospectrum. The exact mechanism for these temperature behaviour is not known. These authors attribute the observed thermospectrum to a precise molecular mechanism, such as a molecular orbital electronic resonance.

We also observed similar thermospectrum in benzene and proposed a model of four wave interactions among the various SR components which might give rise to such a periodic behaviour with temperature.⁵ Subsequent calculations by us agreed favourably with the results obtained in benzene, toluene and cyclohexane.

Heumann and Trinks (HT)¹⁹⁻²⁰ have observed similar thermospectra in benzene, toluene, CS₂ and nitrobenzene. They attribute the periodic temperature dependence of the SRS intensities to a similar periodic change in the number of filaments or foci with temperature. Piekara²¹⁻²³ has proposed the mechanism of resonant enhancement of elastic lattice vibrations as responsible for the observed thermal periodicity both of the number of filaments and of the intensity of SRS.

The following sections of this chapter describes the theory on which our results are interpreted, the results observed by us and other workers and a discussion of our results in the light of these existing results.

II.2 Wave Interactions in a Nonlinear Media

The nonlinear susceptibilities and the coupled wave equations in a nonlinear media introduced in Chapter I.4, form a very powerful tool in the theory of SRS. Many nonlinear phenomenon observed with intense laser radiation such as harmonic generation, wave mixing, parametric amplification, SRS etc. can be conveniently described through the nonlinear interactions among the various waves present in the nonlinear medium and which are coupled via the nonlinear susceptibilities of higher orders.

The second Stokes wave E_{-2} at the frequency $(\omega_0 - 2\Delta)$ in the SRS process can be thought of as arising due to a nonlinear mixing through the third order susceptibility χ_3^{NL} , of the laser radiation E_0 at ω_0 , the first Stokes wave E_{-1} at $(\omega_0 - \Delta)$, and the first anti-Stokes wave E_{+1} at $(\omega_0 + \Delta)$, where Δ is the Raman shift. The polarization at the frequency $(\omega_0 - 2\Delta)$ will be given by:

$$P^{NL}(\omega_0 - 2\Delta, z) = \chi_3^{NL} [-(\omega_0 - 2\Delta), \omega_0, \omega_0 - \Delta, -(\omega_0 + \Delta)]$$

$$\times E_0(\omega_0) E_{-1}(\omega_0 - \Delta) E_{+1}^*(\omega_0 + \Delta) \exp i(k_0 + k_{-1} - k_{+1})z \quad \text{II.1}$$

In writing the above equation, for the sake of convenience in writing, we have omitted the tensorial nature of x_3 and consequently the co-ordinate indices on the field components.

This polarization will give rise to a wave at the frequency $(\omega_0 - 2\Delta)$ which will be obtained by using $P^{NL}(\omega_0 - 2\Delta, z)$ as the source term in the Maxwell's equation of the form of eqn.I.71.

$$\frac{dE_{-2}}{dz} = \frac{2\pi i(\omega_0 - 2\Delta)}{Cn_{-2}} x_3^{NL} E_0 E_{-1} E_{+1}^* \exp(i\Delta kz) \quad \text{II.2}$$

One can write similar equations for the waves E_{-1} , E_{+1} and E_0 as follows:

$$\frac{dE_{-1}}{dz} = \frac{2\pi i(\omega_0 - \Delta)}{Cn_{-1}} x_3^{NL} E_{-2} E_0^* E_{+1} \exp(-i\Delta kz) \quad \text{II.3}$$

$$\frac{dE_{+1}}{dz} = \frac{2\pi i(\omega_0 + \Delta)}{Cn_{+1}} x_3^{NL} E_0 E_{-1} E_{-2}^* \exp(i\Delta kz) \quad \text{II.4}$$

$$\frac{dE_0}{dz} = \frac{2\pi i\omega_0}{Cn_0} x_3^{NL} E_{-2} E_{+1} E_{-1}^* \exp(-i\Delta kz) \quad \text{II.5}$$

where $\Delta k = k_0 + k_{-1} - k_{+1} - k_{-2}$ is the wave-vector mismatch. As was shown in Chapter I.4.2, the overall permutation relation leads to a single susceptibility x_3 which describe the above four wave interaction. For a general solution of the problem the four coupled equations II.2 to II.5 should be solved simultaneously, which becomes quite cumbersome. As a first approximation, we can make the parametric approximation that the

waves E_{-1} , E_{+1} and E_0 which are initially present are not considerably changed during the interaction and hence can be taken to be constant. This is valid, in any case, when E_{-2} is small. Eqn. II.2 only remains to be solved. The solution can be written as:

$$E_{-2} = \frac{2\pi i(\omega_0 - 2\Delta)}{Cn_{-2}} \chi_3^{NL} E_0 E_{-1} E_{+1}^* \frac{[\exp(i\Delta kz) - 1]}{i\Delta k} \quad \text{II.6.}$$

We can write:

$$\begin{aligned} \exp(i\Delta kz) - 1 &= \exp\left(\frac{i\Delta kz}{2}\right) \left[\exp\left(\frac{i\Delta kz}{2}\right) - \exp\left(-\frac{i\Delta kz}{2}\right) \right] \\ &= \exp\left(\frac{i\Delta kz}{2}\right) 2i \sin\left(\frac{\Delta kz}{2}\right) \end{aligned}$$

Hence eqn. II.6 reduces to

$$E_{-2} = \frac{2\pi i(\omega_0 - 2\Delta)}{Cn_{-2}} \chi_3^{NL} E_0 E_{-1} E_{+1}^* \exp\left(\frac{i\Delta kz}{2}\right) \frac{\sin\left(\frac{\Delta k}{2} z\right)}{\frac{\Delta k}{2}} \quad \text{II.7}$$

In order to obtain an expression for the intensity of the radiation at $(\omega_0 - 2\Delta)$ which is usually obtained experimentally, we multiply II.7 by its complex-conjugate and making use of the expression for the intensity of a wave

$$S(\omega, z) = \frac{n(\omega)c}{8\pi} |E(\omega, z)|^2$$

where $n(\omega)$ is the refractive index of the medium at frequency ω , we finally obtain for the intensity of the wave at $(\omega_0 - 2\Delta)$

$$\frac{s(\omega_0 - 2\Delta, z)}{n_{-2}} = \left[\frac{2\pi k_{-2}}{\epsilon_{-2}} x_3 |E_{-1}| |E_{+1}| \right]^2 \frac{s(\omega_0, 0)}{n_0} \left[\frac{\sin(\frac{\Delta k}{2} z)}{\frac{\Delta k}{2}} \right]^2 \quad \text{II.8}$$

where $(\omega_0 - 2\Delta)/c$ is expressed as k_{-2}/n_{-2} to conform to similar expressions found in literature. The intensity of the exciting laser radiation is taken to be that at $z=0$ as it is assumed constant. So also the values of $|E_{-1}|$ and $|E_{+1}|$, though not explicitly mentioned. Eqn. II.8 can be written in a more familiar form as:

$$s(\omega_0 - 2\Delta, z) = \frac{n_{-2}}{n_0} \frac{s(\omega_0, 0)}{l_r^2} \left[\frac{\sin(\frac{\Delta k z}{2})}{\frac{\Delta k}{2}} \right]^2 \quad \text{II.9}$$

where $\frac{1}{l_r^2} = \left[\frac{2\pi k_{-2}}{\epsilon_{-2}} x_3^{NL} |E_{-1}| |E_{+1}| \right]^2$

Equation II.9 with II.10 occur extensively in literature.⁶

In particular the second harmonic intensity generated through the second order susceptibility x_2^{NL} can be written as:

$$s(2\omega, z) = \frac{n_{2\omega}}{n_\omega} \frac{s(\omega, 0)}{l_{SHG}^2} \left[\frac{\sin(\frac{\Delta k}{2} z)}{\frac{\Delta k}{2}} \right]^2 \quad \text{II.10}$$

where $\frac{1}{l_{SHG}^2} = \left[\frac{2\pi k_{2\omega}}{\epsilon_{2\omega}} x_2^{NL} |E(\omega, 0)| \right]^2 \quad \text{II.11}$

and $\Delta k = 2k_\omega - k_{2\omega} = \frac{2\omega}{c} (n_\omega - n_{2\omega})$

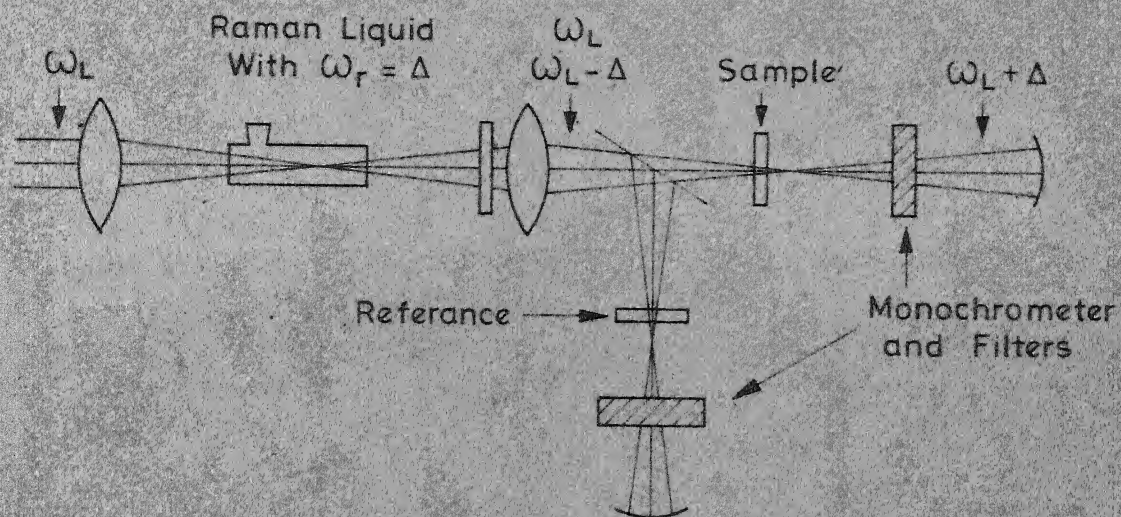
when $\Delta k = 0$ i.e. when the momentum matching is satisfied ($n_{\omega} - n_{2\omega}$), $s(2\omega, z)$ grows in intensity quadratically with z and becomes of the order of the fundamental after a distance $z = \ell_{\text{SHG}}$. Hence ℓ_{SHG} is termed the interaction length. When $\Delta k \neq 0$, according to eqn. II.10, the second harmonic intensity oscillates between zero and $(n_{2\omega}/n_{\omega})^2 \frac{4s(\omega, 0)}{\ell_{\text{SHG}}^2 \Delta k^2}$ with a period $2\pi/\Delta k$ as the distance z is changed. This period of oscillation is referred to as the 'coherence length' ($2\ell_{\text{coh}}$). This oscillatory behaviour of the second harmonic intensity generated in a KDP crystal was experimentally demonstrated by Terhune and co-workers^{6,7} by rotating the KDP platelet about an axis normal to the laser direction thus changing the thickness z of the crystal medium in which SHG is taking place.

Maker and Terhune⁶ have considered the generation of the anti-Stokes component at $(\omega_0 + \Delta)$ through the mixing of the laser (ω_0) and Stokes ($\omega_0 - \Delta$) frequencies. The intensity at $(\omega_0 + \Delta)$ can be written as:

$$s(\omega_0 + \Delta, L) = \frac{n_{+1}}{n_0} \frac{s(\omega_0, 0)}{\ell_{+1}^2} \left[\frac{\sin\left(\frac{\Delta k L}{2}\right)}{\frac{\Delta k}{2}} \right]^2 \quad \text{II.12}$$

$$\frac{1}{\ell_{+1}^2} = \left[\frac{2\pi k_{+1}}{\epsilon_{+1}} x_3^r |E(\omega_0, 0)| |E(\omega_0 - \Delta, 0)| \right]^2 \quad \text{II.13}$$

where L is the length of the liquid cell in which the mixing takes place. Their experimental set up is shown in Fig. II.1.



G. II.1 EXPERIMENTAL SET UP OF MAKER AND TERHUNE TO STUDY GENERATION OF $\omega_0 + \Delta$ THROUGH THE MIXING OF ω_0 AND $\omega_0 - \Delta$ (Reproduced from ref 6)

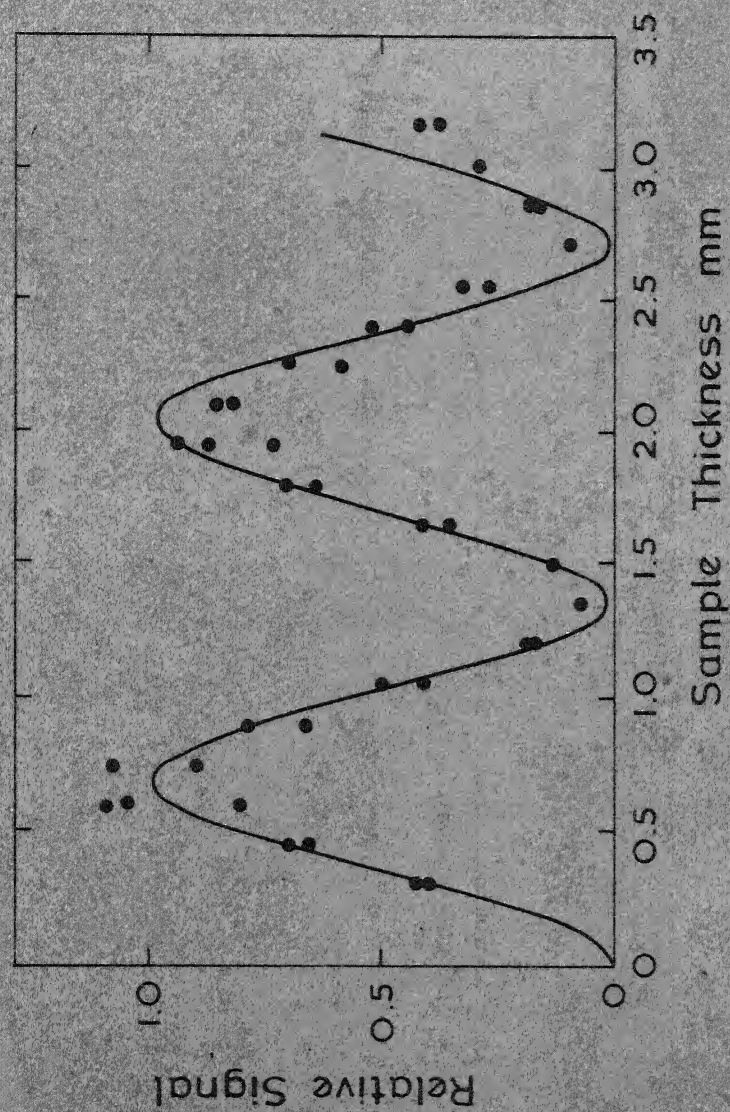


FIG. II 2 THE LENGTH DEPENDENCE OF THE SIGNAL AT $\omega_0 + \Delta$

CREATED IN BENZENE DUE TO PRESENCE OF ω_0 AND $\omega_0 - \Delta$

(Reproduced from ref 6)

The Stokes frequency is generated in a separate Raman oscillator, a long cell filled with benzene and after filtering out all unwanted radiations using corning filters (F) and aperture stop, only the frequencies ω_0 and $\omega_0 - \Delta$ were focussed into the sample cell filled with benzene. The intensity at $(\omega_0 + \Delta)$ in the beam coming out of the sample is monitored through a monochromator and detector. The sample thickness is varied by rotating the sample cell and the resulting variation of the intensity at $(\omega_0 + \Delta)$ as a function of the sample thickness is shown in Fig.II.2. The period of oscillation i.e. the change in the sample thickness corresponding to the successive peaks will give $2l_{coh}$.

By changing the Raman generating liquid in the experimental arrangement of Fig.II.1, it is possible to change the difference frequency Δ to be different from that of the sample (benzene) and by using different generating liquids with Δ assuming values close to that of the sample, the resonant behaviour and line shape of χ_3^R for the sample liquid could be obtained. The line shapes obtained are nearly lorentzian with widths comparable to the Raman widths for the sample.⁶

As the dispersion changes with temperature, it is possible to vary Δk by a change of temperature of the Raman liquid and in this way one should be able to demonstrate the oscillatory behaviour in eqn.II.9, 10 and 12 through a change in the temperature of the Raman liquid. This would naturally result in a thermal spectrum such as reported by BBG, HT and ourself. The thermal period would be the temperature change that changes $\frac{\Delta k}{2}L$ by π . This

thermal period could be estimated from a knowledge of refractive index data for the liquid sample. In what follows we will describe our experimental details for obtaining the thermospectrum of SRS in liquids and compare our results with the calculated values based on the above theory and in the light of recent reported results.

II.3 Experimental

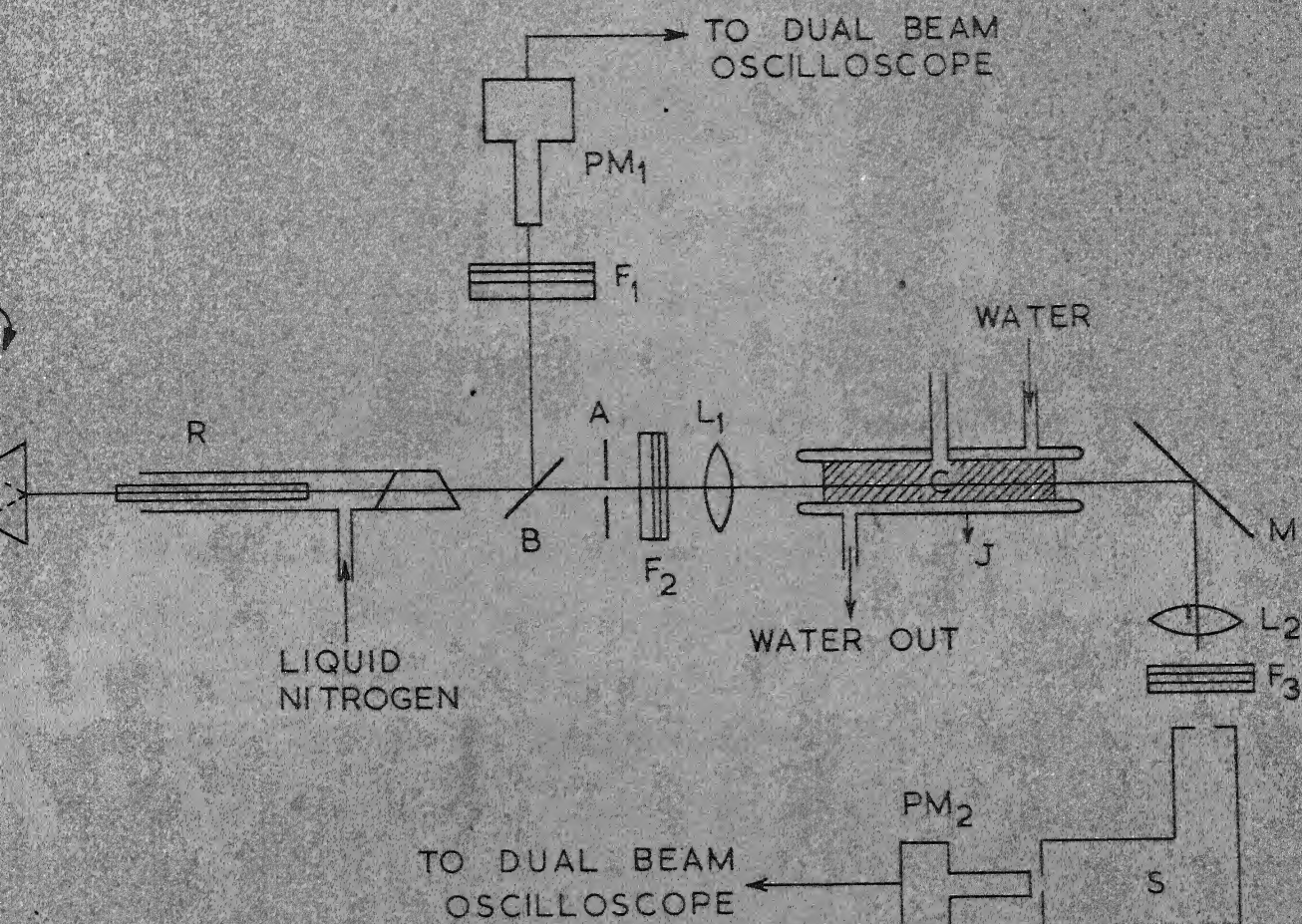
The experiments were carried out with a ruby laser system supplied by Laer-Seigler, Michigan, USA. The ruby rods are 1/4" dia and 3" long with the C-axis oriented at 0°, 60° and 90°. The ruby rod is housed in a cylindrical cavity with a helical xenon flash lamp capable of handling 4000J energy input, surrounding the ruby rod. The ruby rod is insulated thermally from the rest of the pump cavity by means of a double-walled glass dewar surrounding it completely from end to end of the cylinder housing. The ruby rod is cooled by passing cool nitrogen vapours by boiling liquid nitrogen in a separate dewar, the flow rate being controlled at the power console of the laser system. The laser was operated in the Q-switched mode using rotating prism mounted on a synchronous motor of speed 20000rpm. The flash lamp is triggered by means of a signal provided by the rotating prism by reflecting light from a lamp onto a photocell. The photocell output is fed to the trigger input through a gate and delay circuit to obtain proper synchronization and optimum Q-switched output. The laser could be triggered manually by resetting the trigger gate.

The experimental set up is shown in Fig. II.3. The laser cavity is formed between the right angled Q-switching prism and one end of the laser rod. Part of the output is deflected by means of a beam splitter (BS) and detected by means of an RCA 7102 photomultiplier (PM_1) whose output is displayed on a CRO. This serves as the input monitor. A corning glass filter is used to filter most of the background from xenon-flash lamp. The laser output is focussed into a cell containing the liquid under investigation, by means of a lens of about 5-8 cms focal length. The beam emerging from the cell is again collected by another lens onto the slit of a 3-prism carl-zeiss glass spectrograph/monochromator. A second photomultiplier (PM_2) at the exit of the monochromator is used to detect the intensity of different Raman shifted lines and displayed on another oscilloscope. The output pulse heights are read off the CRO. Corning glass filters are used to attenuate the light input falling on to the photomultiplier to keep it below the saturation level and operate as far as possible on the linear portion of the characteristics. Tektronix 545 and 555 (dual beam) oscilloscopes are used.

Most of the experiments are done with a cell length of 30 cms. The liquid cell is surrounded by a glass jacket through which water from a thermostat is circulated. The temperature regulation is obtained by the mercury column of the regulating thermometer making contact with a metal plunger which can be positioned at any temperature by means of a rotating magnetic

head at the top of the thermometer. This contact makes or breaks the heater circuit of the water bath. Cold water from outside is passed through a copper coil immersed in the water bath so as to maintain a positive control on the regulation. The temperature can be set at intervals of about 0.2°C by giving $\frac{1}{2}$ rotation to the magnetic head of the regulating thermometer. The unit has a regulation better than 0.05°C . The temperature uniformity along the cell length was checked by thermocouples monitoring the temperatures at both ends and centre of the cell. The temperatures were equal within experimental errors. Sometimes a gradient of about 0.1°C was observed between the ends. This was minimized by keeping the water inlet from thermostat to the water jacket at the centre and outlets back to the thermostat at either ends of the cell.

Each run was taken starting from low temperature (about 19°C) and increasing the temperature in steps of 0.2°C . Care being taken not to turn the head in the opposite direction at any time to prevent backlash. When the temperature stabilized after each setting the laser is fired. Pulse height and the temperature at the cell noted. A couple of pulses were fired at any setting and an average reading taken. The input monitor helps in keeping the input level constant throughout a run and to discard readings corresponding to unequal input levels. The laser is fired every 2-3 minutes to obtain repeatable conditions. The output intensities corresponding to the same input level are plotted against



\square = 90° PRISM

\square = RUBY

\square = BEAM SPLITTER

F_1, F_2 & F_3 = CORNING GLASS
FILTERS

A = APERTURE

L_1, L_2 = LENSES

C = CELL

J = WATER JACKET

M = MIRROR

S = MONOCHROMATOR

PM_1, PM_2 = PHOTOMULTIPLIERS

FIG.II.3. OUR EXPERIMENTAL SET-UP

temperature as read on the thermometer or thermocouple at the centre of the cell.

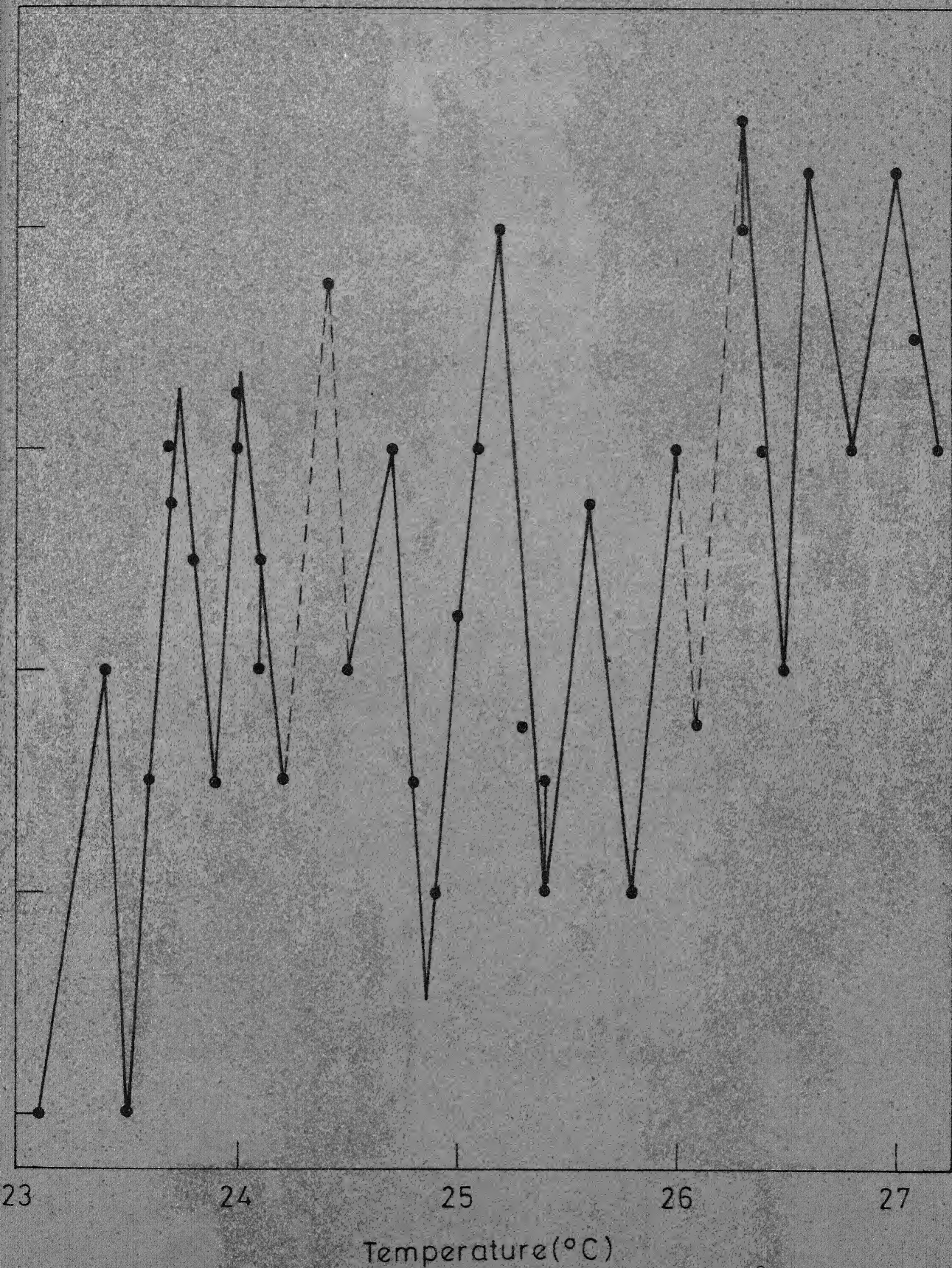
II.4 Results

Initially the SRS from benzene, toluene and cyclohexane are photographed on Kodak 1-N and 103-F plates. In benzene 2 to 3 orders Stokes and 2 orders anti-Stokes are seen corresponding to the C-C symmetric stretching vibration at 992 cm^{-1} . One Stokes component corresponding to the C-H stretching vibration at 3064 cm^{-1} is also seen. Often this was seen stronger than the 3rd order Stokes line corresponding to the 992 cm^{-1} mode, sometimes 3064 cm^{-1} Stokes was strongly present even when the 992 cm^{-1} third order Stokes component was absent. In toluene two orders of Stokes and first anti-Stokes were strong and the third Stokes and second anti-Stokes were somewhat weaker. In cyclohexane, one Stokes and two orders of anti-Stokes lines corresponding to the 2852 cm^{-1} vibration could be seen. The second Stokes line was beyond the sensitivity of the plates and the range of the spectrograph. Often the 801 cm^{-1} mode in cyclohexane could be seen upto two orders, strongly on Stokes side and weaker on anti-Stokes side. Often the Stokes and anti-Stokes lines corresponding to the 2852 cm^{-1} mode, showed satellite lines on either side corresponding to a shift of 801 cm^{-1} .

In benzene the experimentally obtained thermospectrum of the second Stokes line at 8050\AA corresponding to the 992 cm^{-1} gives an average period of $0.35\text{--}0.4^\circ\text{C}$ in a cell length of 30 cms. Earlier experiments with a cell length of 20 cms had given a period between successive maxima of 0.6°C . A typical thermospectrum of the 8050\AA line of benzene in a cell length of 30 cms. is shown in Fig. II.4. The thermospectrum in benzene was repeated using a shorter cell of length 12 cms. The spectrum of the 8050\AA showed a period of about 1.1°C . This spectrum is shown in Fig. II.5.

In toluene the second Stokes line at 8069\AA corresponding to the symmetric stretching vibration at 1004 cm^{-1} is studied. This line gives a thermal period of 0.6°C in a cell length of 30 cm. A typical thermospectrum is shown in Fig. II.6. A few runs on the first Stokes line (7465\AA) of the 1004 cm^{-1} in the same cell length showed more or less same thermal period as for the 8069\AA line.

The first Stokes at 8659\AA of the 2852 cm^{-1} vibration in cyclohexane showed an average thermal period of $0.5\text{--}0.55^\circ\text{C}$, in a cell length of 30 cms. This is shown in Fig. II.7. Some runs in cyclohexane with same cell length indicated a smaller period of about $0.3\text{--}0.4^\circ\text{C}$. In these runs the laser was observed to be operating with somewhat increased output. Attempts to obtain the thermospectrum in cyclohexane with a cell length of 12 cms were not successful as it was not possible to consistently observe SRS with this length in cyclohexane.



II.4. EXPERIMENTAL THERMOSPECTRUM OF 8050 Å LINE IN BENZENE (L = 30 cms)

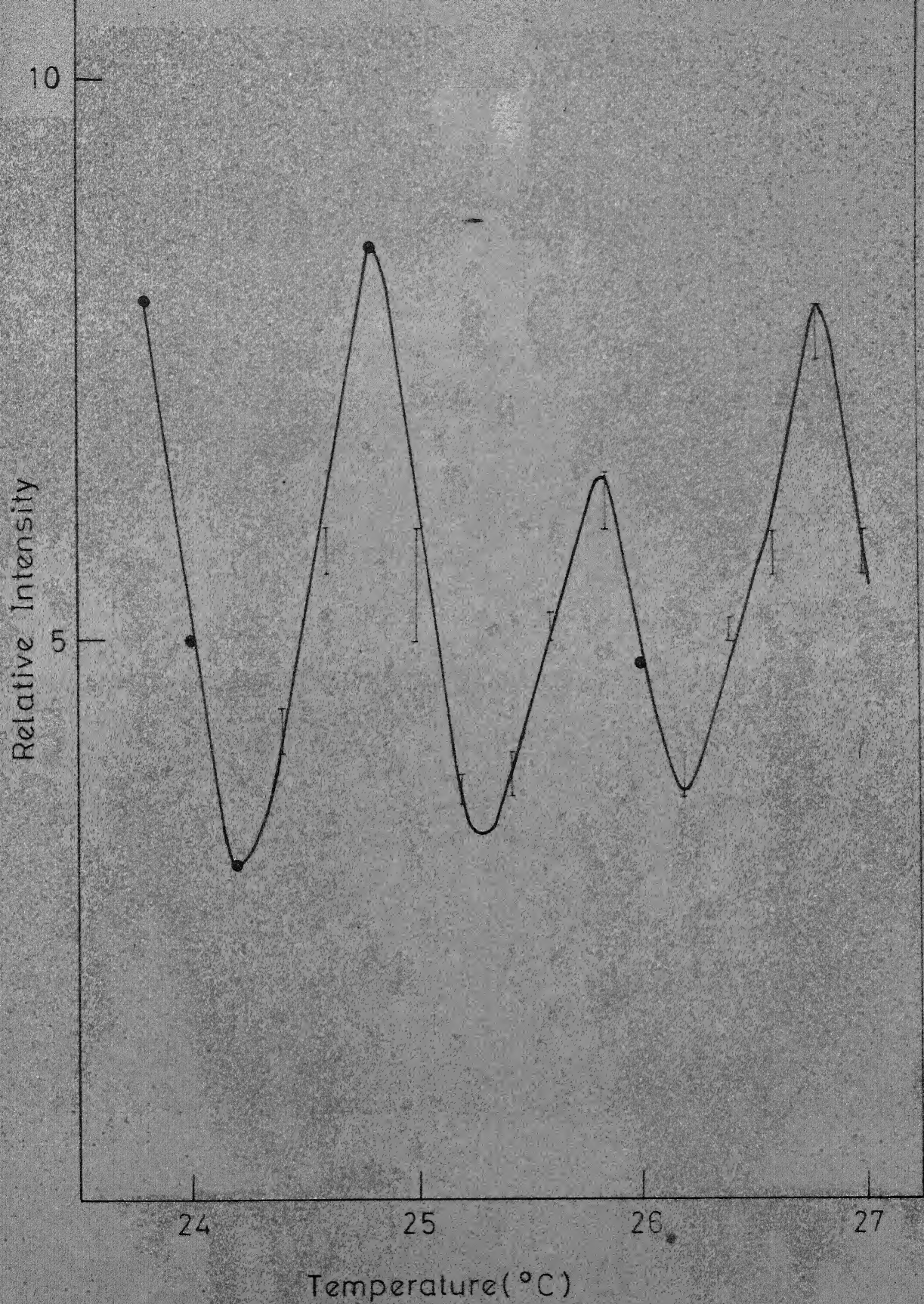
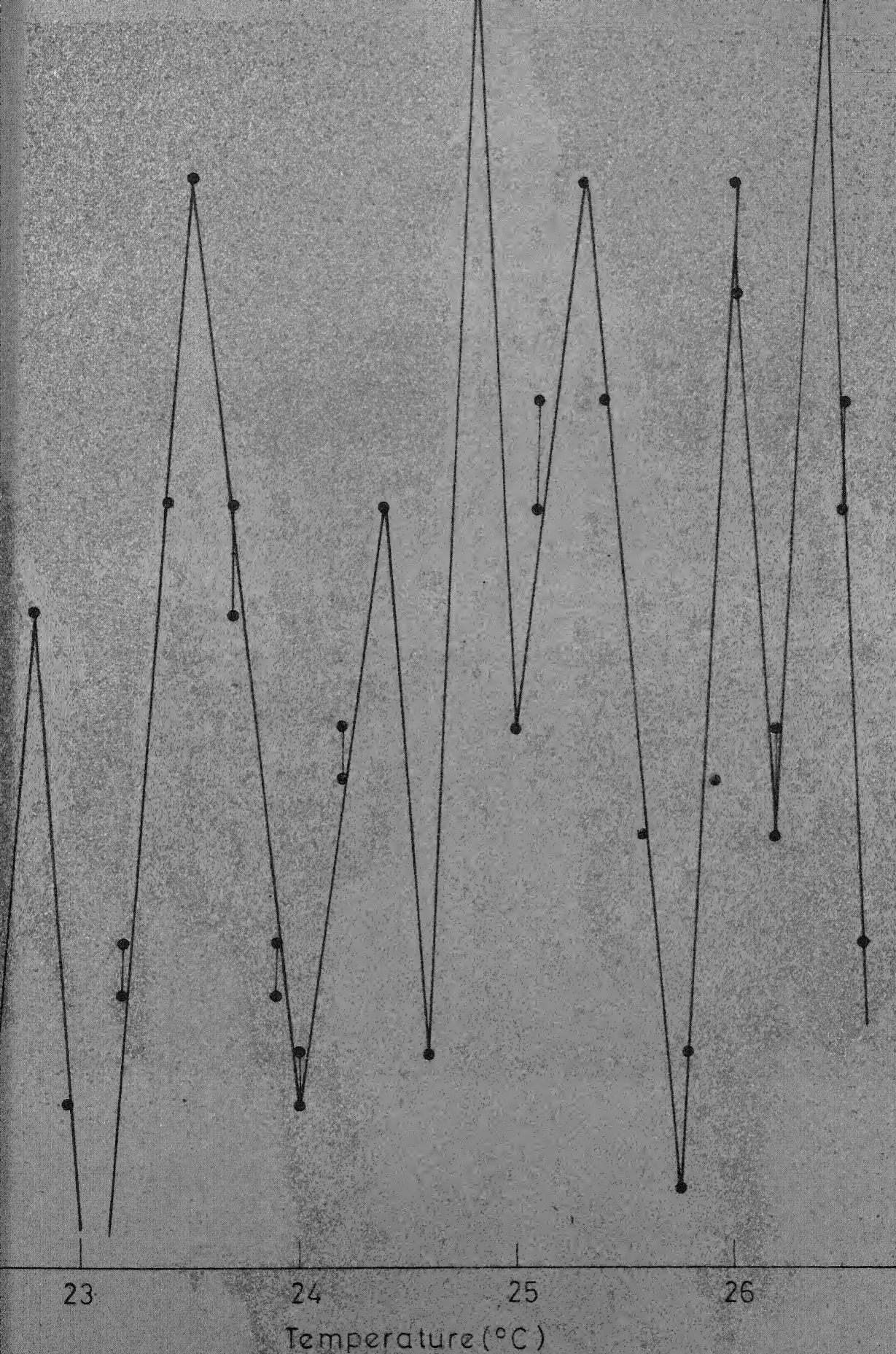


FIG. II. 5. EXPERIMENTAL THERMOSPETRUM OF THE 2nd STOKES LINE AT 8050 Å IN BENZENE IN A CELL LENGTH OF 12 CM.



16 EXPERIMENTAL THERMOSPECTRUM OF THE 2nd STOKES LINE

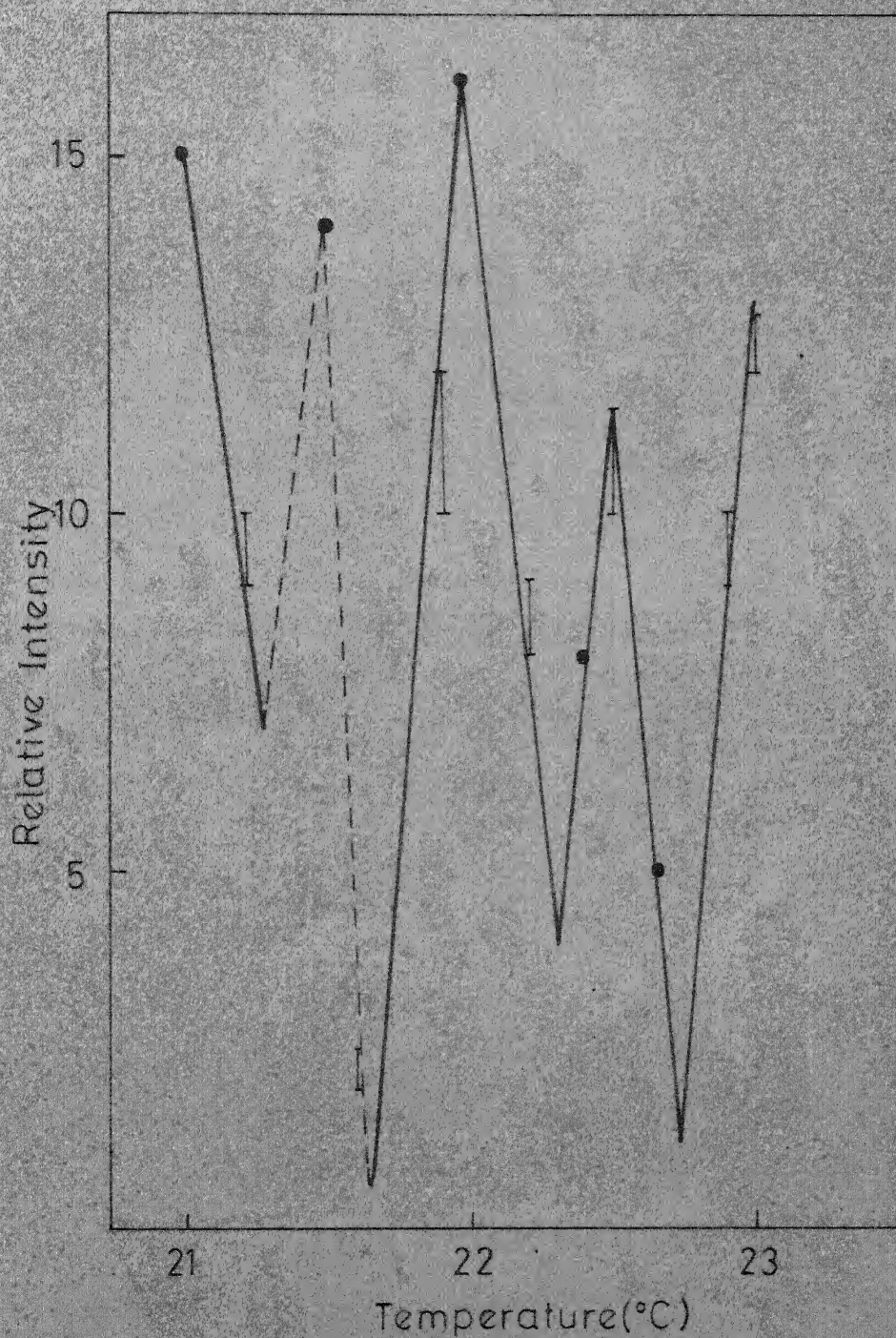


FIG. II. 7. EXPERIMENTAL THERMOSPECTRUM OF THE 1ST STOKES LINE AT 8659 Å IN CYCLOHEXANE IN A CELL LENGTH OF 30 cm.

The intensity variation or the modulation depth obtained by us is about one order of magnitude as against 2 to 3 orders obtained by BBG and HT.

II.5 Calculations

The temperature periodicity for any particular line can be calculated starting from the wave-vector mismatch Δk for the generation of the line. Further the refractive indices of the medium at the frequencies of the Raman waves participating in the process should be known, as also the temperature coefficient of each one of them. Usually such data are not directly available.

The refractive index at any wavelength is given by the modified Hartmann formula

$$n_{\lambda} = n_{\infty} + \frac{c}{(\lambda - \lambda^*)^{1.6}} \quad \text{II.14}$$

where n_{∞} , c and λ^* are constants, both λ and λ^* are in microns. The constants can be obtained by an interpolation method knowing the refractive indices at three well separated wavelengths. The refractive index at any other wavelength is obtained from eqn. II.14 by using these constants. A similar procedure at another temperature close-by could be carried out provided atleast three refractive indices at this temperature

52

are available. Having obtained the refractive indices at the various Raman shifted frequencies at two different temperatures, a linear temperature variation is assumed between the two temperatures and thus the temperature coefficient i.e. change of refractive indices per 1°C , obtained for each of these wavelengths. We have mostly used data at 20 and 25°C . The refractive indices data are obtained from reports of American Petroleum Institute Research Project, Carnegie Tech.⁸ and similar sources.⁹⁻¹¹ A computer programme is written for the entire calculation starting from the refractive indices at any three wavelengths to the final thermal period for any given cell length for different processes and hence different Δk . These are detailed in Appendix 1. The calculated values of the product of thermal period (P) and the cell length (L), for the liquids for which data were available are given in Table II.1. The contribution to the change in $\Delta kL/2$ because of the thermal expansion of the glass cell is three orders of magnitude less than that due to the change in Δk and hence can be neglected.

II.6 Results of other workers

II.6.1 Biscar, Braunstein and Gratch (BBG)

These workers first observed cyclic temperature dependence in benzene¹³ of the second Stokes line at 8050\AA corresponding to the 992 cm^{-1} phonon and of the 1.07μ line which is a new

Table II.1

Values of the product (PL) of the thermal period (P) and cell length (L) calculated by us, for the three processes mentioned.

Process	Benzene (992 cm ⁻¹)	Toluene (1004 cm ⁻¹)	CS ₂ (656 cm ⁻¹)	Cyclohexane (2852 cm ⁻¹)
1. Generation of 2nd Stokes 4-wave interaction with $\Delta k = k_0 + k_{-1} - k_{+1} - k_{-2}$	40	57	46	9.4
2. Generation of 2nd Stokes modulation process with $\Delta k = 2k_{-1} - k_0 - k_{-2}$	83.5	120	85	18
3. Generation of 1st anti- Stokes modulation process with $\Delta k = 2k_0 - k_{-1} - k_{+1}$	79	107	101.5	19

multiphonon stimulated Raman line involving two phonons of 992 cm^{-1} and one phonon of 3064 cm^{-1} of benzene, observed for the first time by them.¹² In all their work they have used the unfocussed, single mode laser beams with a 4 mm aperture before the cell. The 8050\AA line shows a maximum around 25°C and minima around 21°C and 29°C giving a period of about 8°C . The 1.07μ line shows two peaks near 20°C separated by about 2.7°C and one around 30°C . The cell length used for these runs was 67 cms.¹³ They have also observed stimulated infrared emission at 5μ corresponding to the $2 \times 992\text{ cm}^{-1}$ phonon,¹⁴ which also shows a cyclic temperature dependence which is more or less similar to that of 8050\AA line¹³ in a cell length of 69 cm and 80 cm both of which show similar results. Subsequently they observed a fine structure period of 2.2°C for the 8050\AA line in a cell length of 38 cms,¹⁵ with an input intensity of 60 MW/cm^2 , and soon afterwards found the same period (2.2°C) but for every other peak¹⁶ i.e. a period of 1.1°C between successive peaks. The authors refer to this as a doubled spectrum with a period 2.2°C . The laser intensity used for this spectrum is 80 MW/cm^2 . The first Stokes line of the 992 cm^{-1} phonon in benzene at 7456\AA also has been investigated¹⁷ and shows a doubled spectrum of period 2°C in a cell length of 25 cm at 90 MW/cm^2 . No temperature variation of this line is observed in a cell length of 38 cms because of saturation of the first Stokes intensity in such a long cell.

The observed periods of 2.7°C for the 1.07μ , 2.2°C for the 8050\AA and 2.0°C for the 7456\AA indicates a linear dependence of the thermal period with wavelength. They have observed an increase in the thermal period as the temperature is decreased below 20°C . This temperature dependence of the period yields the following linear relation.¹⁷

$$\frac{P(T)-P_0}{P_0} = b - aT \quad \text{II.15}$$

where $b=2.18$ and $a=0.093$ per $^{\circ}\text{C}$. This indicates that the same physical mechanism is responsible for the linear temperature variation of the thermal period of both the lines. The authors attribute this to nonlinear expansion of carbon ring and the molecular π -orbital.

The intensity variations of the 8050 and 7456\AA lines are more than two orders where as those of the 1.07μ and 5μ lines are within one order of magnitude.

The authors conclude that the thermospectra observed are associated with a precise molecular mechanism, possibly a new type of molecular orbital electronic resonance. They favour a localized interaction whereby the vibrational mode generated in each molecule interacts with electrons in the benzene bonds and modulates the density of the π -electron streamers. The C-H vibrations (3064 cm^{-1}) seem to be less efficient than C-C vibration ($2 \times 992\text{ cm}^{-1}$) in this process, as evidenced by the

higher generation threshold for the 1.07μ line involving both 3064 and $2 \times 992 \text{ cm}^{-1}$ phonons.

II.6.2 Heumann, Trinks and others^{19,20}

These authors have obtained thermospectrum of SRS in toluene, CS_2 and nitrobenzene¹⁹ using a Q-switched ruby laser of 4 mm diameter and 30 MW/cm^2 . The cell length used was 20 cms . In all the three liquids the second Stokes line of the fundamental stretching vibrations 1004 , 656 and 1344 cm^{-1} in toluene, CS_2 and nitrobenzene respectively, are investigated. The largest thermal period obtained in toluene is 1.2°C and the spectra is very similar to that of 8050\AA of benzene. The period in CS_2 is about 1°C . The thermospectrum in CS_2 is obtained at a much lower laser power to avoid saturation. The period in nitrobenzene is about $0.5\text{--}0.6^\circ\text{C}$. The variation in intensity is within two orders of magnitude and in the case of nitrobenzene it is about an order of magnitude.

They have also observed a periodic variation in the number of filaments in the beam passing through benzene.²⁰ The filaments were counted by fixing a film to the exit window of the cell. The position of maxima and minima and the periodicity of the filament number agree with the thermospectrum of the first Stokes of benzene at 7456\AA corresponding to the 992 cm^{-1} obtained in the same cell of length 25 cm under similar conditions. Further they

did not observe any variation of the 7456\AA line under conditions when no self-focussing occurs in the liquid such as when using cell lengths below the self-focussing length in benzene (4 cm). They used cell lengths slightly more than 2 cm in order to obtain sufficient intensity of SRS. Hence they conclude that the thermo-spectrum is caused by the temperature dependence of the self-focussing characteristics of the medium.

II.6.3 Piekara's theory

As existing molecular models of light trapping effects are not sufficient to completely explain details of the phenomenon experimentally observed, Piekara proposed^{22,23} an alternative mechanism of filament formation which involves the resonant enhancement of elastic lattice vibrations. This framework is based on the rigidity of liquids ie. the existence of a molecular lattice capable of elastic vibrations, which give the possibility of resonance with electromagnetic waves and this resonance frequency is in the range of hypersonic waves 10^9 - 10^{13} cps. Unlike in dielectric resonance, in self-trapping resonance occurs when the lattice vibrations are in resonance with the modulation frequency of the incident light wave. The self-modulation frequency of the laser pulse, ie. the repetition rate of short light pulses within the envelope of the laser pulse, is given by the inverse of the double pass transit time of the laser cavity of length L

$$\Delta v = c/2L$$

II.16

These pulses will be in resonance with an axial mode of thermal lattice vibration in the liquid of frequency^{21,22}

$$f_h = \frac{1}{2} k \Delta v, \quad k = 1, 2 \dots$$

II.17

the most efficient enhancement occurs for $k=1$. The spacing between two resonances will be $\lambda_h/2$ where

$$\lambda_h = \frac{4v_h L}{kc}$$

II.18

where v_h is the hypersound velocity in the medium. This resonance leads to an enhancement of lattice vibrations owing to a polarizability increase of displaced molecules. These light filaments are produced in time intervals of about 10^{-9} secs.²²

For $L=15$ cm and $v_h \sim 10^5$ cm/sec, we find $\lambda_h/2=1\mu$. A glass cell of length $\ell=10$ cm increases in length by this amount for temperature change of 1°C . Hence there exists a correspondence of the observed thermal period to the calculated space period for the first resonance.

The energy exchange between the light pulse to lattice vibration will be destroyed and restored periodically owing to finite light pulse velocity v_p . The energy transfer will be destroyed at a distance ℓ_1 from the entrance, where the lattice vibrations and light modulations are out of phase. Such a vibration arise when the light pulse transit time through the liquid cell is $1/4 f_h$. This time delay corresponds to a path length of

$$\lambda_1 = \frac{v_P}{kC} L$$

II.19

For cell length of λ_1 the observed periodicity of filament formation vanishes. It appears again for a cell length of $2\lambda_1$ and so on. In the absence of dispersion $\lambda_1 = L/n$ where n is refractive index of liquid. Thus λ_1 is of the order of tens of cms.

Thus light filament formation appears to be a phenomenon of double periodicity (i) a spatial periodicity of resonance of period $\lambda_h/2$ which gives a short distance periodicity and (ii) a long distance periodicity of spatial period $\Lambda = 2\lambda_1$. Some experiments are suggested as proof of the proposed resonant mechanism:

- 1 Change of length λ of the cell from λ to $\lambda + \frac{1}{2} \lambda_h$ or changing the resonator length by ΔL given by

$$\frac{\Delta L}{L} = - \frac{\lambda_h/2}{\lambda}$$

This can be done by means of an inclined glass plate inside the resonator. This is called mechanical tuning of the self-trapping system displaying filament formation. This determines v_h .

- 2 Changing the thermal period or the space period $\frac{1}{2} \lambda_h$ by a large change in resonator length L according to eqn. II.18. The difference in the thermal periods obtained by Biscar et.al and Heumann et.al is ascribed to the dependance of λ_h on L .

- 3 Demonstration of the disappearance of the periodicity with a cell length $\ell = \ell_1$. Such a length ℓ_1 will directly determine v_p .

The author concludes that the double space periodicity of filament formation leads to the periodic variation of intensity of Stimulated Brillouin and Raman Scattering. Only thermal periodicity of this phenomenon has been observed so far, which may be understood in terms of thermal expansion as described above. To further prove the validity of their proposed mechanism they suggest experiments which are detailed above.

II.7 Discussion

II.7A Our results

The higher order stimulated Raman components are generated by more than one process. One can distinguish the following processes²⁴:

- 1 The direct SR generation; the previous SR component acting as the exciting radiation. This process is similar to the generation of first Stokes wave from the laser frequency ω_0 by the primary SRS process with a threshold on exciting radiation.
- 2 Modulation of the previous SR component by the coherently driven molecular vibrations due to the presence of the strong laser and first Stokes radiations.

- 3 Nonlinear mixing(four-wave interaction) of the laser and existing SR components.

Some or all of them may be simultaneously possible to different extents depending upon experimental conditions. In particular the second Stokes wave E_{-2} at the frequency $(\omega_0 - 2\Delta)$ can be generated by the following processes:

- 1 The direct SR generation with the first Stokes wave acting as the pumping radiation,²⁴ the generated power being proportional to $E_{-1}^2 E_{-2}^2$. This process has a threshold condition on E_{-1} and is very similar to the process of direct SR generation of the first Stokes wave. The wave vector matching is identically satisfied for this process. The second Stokes is emitted diffusely with a maximum along the forward direction.
- 2 Modulation of the first Stokes wave E_{-1} at $(\omega_0 - \Delta)$ by the coherently driven molecular oscillation at the difference frequency of the laser E_0 at ω_0 and the first Stokes wave. This process also recreates the laser frequency. The generated power is proportional to $E_0(E_{-1})^2 E_{-2}$ and the process requires the momentum-matching condition $\Delta k = 0$ where $\Delta k = 2k_{-1} - k_0 - k_{-2}$ II.20
- 3 A four-wave interaction in which the three waves E_{-1} , E_{+1} and E_0 at $(\omega_0 - \Delta)$, $(\omega_0 + \Delta)$ and ω_0 respectively interact giving rise to the fourth wave E_{-2} at frequency $(\omega_0 - 2\Delta)$.

Such a process generates a power proportional to $E_0 E_{-1} E_1^* E_{-2}$ and takes place with wave-vector mismatch given by:²⁵

$$\Delta k = k_0 + k_{-1} - k_{+1} - k_{-2} \quad \text{II.21}$$

The process 1 with a threshold condition and no wave-vector matching is the dominant process when the Raman medium is within the laser resonator as in the early SRS experiments. The other two processes cannot take place with the medium inside the laser resonator since the wave-vector matching is not possible if both E_0 and E_{-1} are in the forward direction (for process two) and as for (process three) no anti-Stokes wave E_{+1} exists in such a configuration. Hence these two will dominate when the Raman medium is outside the laser resonator, not only because of the lack of a threshold but due to the possibility of exact momentum matching. We are considering both of them in our calculation of the thermal period for the second Stokes wave.

It should be noted that all the three processes are described by a nonlinear susceptibility χ_3^r with a resonant denominator at the difference frequency resulting in a purely negative imaginary susceptibility and hence positive exponential gain for these processes. One can in general consider another process for E_{-2} under process 3 which also is resonant at one of the difference frequencies and may give positive gain. This involves the first Stokes, first and second anti-Stokes waves E_{-1} , E_{+1} and E_{+2} respectively, generating power proportional

to $E_{-1}E_{+1}E_{+2}^*E_{-2}$ with a wave vector mismatch

$$\Delta k = k_{-1} + k_{+1} - k_{+2} - k_{-2} \quad \text{II.22}$$

as $E_{+2} < E_{+1} < E_{-1} < E_0$ this process, in general, can be neglected.

For the first anti-Stokes wave E_{+1} the direct Raman generation leads to an attenuation and the only process to be considered is by the modulation of the laser beam ω_0 for which Δk is given by:

$$\Delta k = 2k_0 - k_{-1} - k_{+1} \quad \text{II.23}$$

The first Stokes wave is generated by the

$$k_{-1} = k_0 - q \quad \text{II.24}$$

where q is the wave-vector of the phonon at the vibrational frequency Δ (or ω_v in general notation) and is given by $q = \omega_v / v_s$ where v_s is the velocity of hypersound in the medium. The generation of the first Stokes by the modulation of the laser beam ω_0 occurs without a threshold and with no wave-vector mismatch.

The second-Stokes wave by the processes (2) and (3) i.e. modulation and mixing are emitted at directions off axis from the laser direction and are collected by a second lens on to the spectrograph slit in our experiments.

The periods are calculated for both the processes as given in Table II.1. We see that the period for the four-wave mixing process is much smaller than for the modulation process.

Assuming both the processes to be present the resultant thermo-spectrum will reflect the smaller of the two periods as can be easily verified. According to Shen and Bloembergen²⁵ the mixing process is the stronger process experimentally, both on account of the momentum matching condition and the dependance on $(E_{-1})^2$ of the modulation process. Hence we compare our result as well as other with the period of the mixing process for the second Stokes wave.

From eqn. II.9, 10 and 12 it is clear that the cyclic intensity changes of SRS components arise from the dependence of the intensity I of the SRS wave on the wave vector mismatch Δk and L the length of Raman medium according to the relation:

$$I \propto \sin^2\left(\frac{\Delta k L}{2}\right) \quad \text{II.25}$$

The period of the cyclic intensity variation corresponds to a change in the argument by π ie.

$$\delta\left(\frac{\Delta k L}{2}\right) = \pi \quad \text{II.26}$$

Length period:

When Δk is fixed by the process and at constant temperature the SRS intensity periodically changes with a change in the length of the Raman medium with a period of $2\pi/\Delta k$. As already mentioned in Chapter II.2 such a periodic variation with length L has been demonstrated⁶ for the generation of anti-Stokes frequencies

$(\omega_0 + \Delta)$ from ω_0 and $(\omega_0 - \Delta)$ in the Raman media. Their experimental curve is reproduced in Fig. II.2. The period as observed from the figure is about 1.36 mm. The refractive index data obtained by us as detailed in Chapter II.5 and appendix 1 are used to calculate Δk for this process (see Appendix 1) and thus the length period $\delta l = \frac{2\pi}{\Delta k}$. The calculated period is 1.368 mm for the data at 20° and 1.41 mm for 25°. The value for 20°C agrees very well with the experimental value of Maker and Terhune.⁶

Thermal Period:

For a fixed length L , a variation in Δk through a change of temperature would result in a similar periodic intensity variation. The temperature change that changes $\frac{1}{2} \Delta k L$ by an amount π will be called the 'Thermal Period'. One can see that a smaller temperature change will give the required increment for a larger L . Thus halving the cell length L will double the thermal period. The calculations list the value of the product (PL) of the thermal period (P) and the cell length (L) for each of the processes.

The calculated values of PL for the second Stokes component by the four-wave mixing process through eqn. II.21 are 40 and 57 respectively for the 8050Å line of benzene and 8069Å line of toluene. The thermal period in benzene is hence $P = 1.3^\circ\text{C}$ for a cell length of 30 cm and $P = 3.3^\circ\text{C}$ for a shorter cell length

of 12 cm. Similarly $P=1.9^{\circ}\text{C}$ for a cell length of 30 cm. in toluene. The experimental and theoretical values are given in Table II.2.

The experimentally observed thermal periods are about 0.4°C for 30 cm of the 8050\AA line in benzene and 0.6°C for 30 cm of the 8069\AA line in toluene.

The experimental periods are close to $1/3$ the calculated periods. The experimental spectrum can be thought of as the superposition of three thermospectra, with the calculated thermal period, displaced w.r.t. to each other by more or less equal amount. Such a superposition can be shown to give rise to a spectrum with a period, between successive peaks, $1/3$ of the period of the individual spectrum. The existence of more than one thermospectrum in the same liquid can be attributed to the existence of light filaments with different peak-intensities during the passage of the laser beam through the liquid. Each filament or a group of filaments gives rise to a thermospectrum with the thermal period typical of the particular liquid. The thermospectrum generated in different filaments may be shifted along the temperature scale due to possible differences in the instantaneous temperature in these high intensity filaments. The existence of a number of such light filaments when a laser beam passes through certain self-focussing liquids is a well established fact. Intense generation of higher order Stokes and anti-Stokes SR components are found to be strongly occurring in such small scale

Table II.2

Our theoretical and experimental thermal periods

Experimental

		Observed Period (°C) in Cell Lengths of	
		30 cm	12 cm
Second Stokes:			
Benzene	8050Å	.4	1-1.1
Toluene	8069Å	0.6	-
First Stokes:			
Cyclohexane	8659Å	0.55	
Toluene		0.6	
Cyclohexane (25 cms)		(0.35-0.4)	

Theoretical

		Observed Period (°C)			
		Period x length PL	30 cm $P = \frac{PL}{30}$	12 cm $P = \frac{PL}{12}$	
Second Stokes:					
Benzene	8050Å	40	1.3	0.43	3.3
Toluene	8069Å	57	1.9	0.63	
First Stokes:					
Cyclohexane	8659Å	19.2	0.64		
(Length 25 cm)		9.3	.37		

high intensity filaments.²⁷ With this interpretation our experimental results agree well with the calculated period. Our attempts to obtain SRS and hence the thermospectrum in conditions when no filamentary formation occurred in benzene and toluene were unsuccessful and could not be pursued due to equipment failure during the course of these experiments.

On the other hand we have investigated the thermal periodicity in Cyclohexane which is usually referred to as one of the non-self focussing liquids.²⁸ The first Stokes line at 8659\AA corresponding to 2852 cm^{-1} of cyclohexane shows a thermal period of about 0.55°C in a cell length of 30 cms. (The second Stokes line of 2852 cm^{-1} phonon in cyclohexane was out of range of our spectrograph/monochromator). As mentioned earlier in this section the first Stokes wave generation, in general, occurs with no momentum mismatch. The primary generation process occurs with a Δk given by eqn. II.24 as

$$\Delta k = k_0 - k_1 - q \quad \text{II.27}$$

which gives an unrealistically small period. On the otherhand the first Stokes wave which strongly participates in the generation of the second Stokes and first anti-Stokes SR components as described in the foregoing sections is likely to reflect the intensity variations of the latter waves ie. the first Stokes wave shows periodical depletions due to the generation of the other waves. Though in the parametric approximation used in deriving eqn. II.9 the other three participating waves were

assumed constant, in reality one has to solve the set of four simultaneous equations which complicates the mathematics. The intensity variation of the various waves would still be characterized by the Δk for the process, some waves exhibiting gain and others attenuation. Only a simultaneous monitoring of one or more of the participating waves could reveal the phase change in the intensity variations. Suffice it to say that the first Stokes wave would reflect the thermospectrum corresponding to any one of the processes in which it participates and in the event of more than one processes being present the smaller thermal period will be reflected.

At the power levels used to obtain the thermal period of 0.55°C we did not generally observe the second anti-Stokes line in cyclohexane and hence possibly second Stokes also, though it was out of the range of the spectrograph and hence not directly verified. We expect the first Stokes intensity to reflect the modulation process leading to the generation of the first anti-Stokes wave with the mismatch given by eqn. II.23. The calculated value of PL for cyclohexane for this process being 19 (Table II.1), the theoretical estimated thermal period for a cell length of 30 cm is 0.63°C which compares well with the experimentally observed value of 0.55°C . In a few earlier runs with somewhat higher powers and a cell length of 25 cm, we have observed a lower periodicity for the same first Stokes line 8659\AA in cyclohexane, of about $0.35\text{--}4^{\circ}\text{C}$ though the data were not

very reproducible. Possibly under these conditions the first Stokes wave may essentially be reflecting the smaller period corresponding to the second Stokes generation by the four wave mixing process for which the calculated thermal period would be $9.3/25=0.37^{\circ}\text{C}$. Thus in cyclohexane we are observing a single thermospectrum with the theoretical period unlike the triple-superposed spectra as in the case of self-focussing liquids benzene and toluene. This fact lends credence to the consideration of our experimental thermospectra in benzene and toluene as a superposition of three thermospectra generated in light filaments in these liquids.

The observed period of 1.1°C for the 8050\AA of benzene in a shorter cell length of 12 cms. can be considered as a superposition of three spectra each with the calculated period of 3.3°C . This proves the inverse dependence for the thermal period on cell length which is indicated by eqn. II.26. Attempts to obtain thermospectrum of the 8659\AA line in cyclohexane in a cell length of 10-12 cm. was not successful as we could not obtain consistent generation of SRS in these small lengths in cyclohexane, in keeping with its non-self-focussing nature with rather long self-focussing lengths (12 cm.) as against 2-4 cm. for CS_2 and benzene.

The non-uniformity apparent in the observed thermospectra can be attributed to several factors:

- 1 The superposed spectra may not be symmetrically shifted w.r.t. each other, giving rise to non-uniform period between different successive peaks.
- 2 Small temperature inhomogeneities in the liquid.
- 3 The liquid temperature occasionally changed by large amounts due to accidental wrong setting of thermostat or due to lack of positive control in the thermostat.
- 4 Backlash in the temperature setting.
- 5 Slight changes in the pulse to pulse laser power output which is otherwise maintained constant.

Only one order of magnitude variation between maxima and minima observed in our spectra can be attributed to the following causes:

- 1 A superposition of three spectra as envisaged by us will lead to considerable reduction in the variation of the resulting thermospectra as can be easily verified.
- 2 In the long lengths used, the intensities may be somewhat saturating resulting in a reduced modulation.

The minima in the experimental thermospectra do not go to zero as expected from eqn. II.9, since the thermospectra are usually superposed over a constant level of the particular Raman frequency component generated in a straight forward process with no phase-mismatch, such as process (1) enumerated earlier.

II.7B Comments on the results of other workers

The observed periods of other workers along with our calculated periods are shown in Table II.3.

HT¹⁹ have obtained thermospectrum of the second Stokes lines in toluene, CS₂ and nitrobenzene in a cell length of 20 cms. The experimental periods were 1.2°C, 1.0°C and 0.5-0.6°C respectively. Our calculated periods for this length are 2.9°C, 2.4°C for toluene and CS₂. Again the experimental values are close to 1/3 the theoretical values ie. 0.97°C and 0.8°C. The reported periods are quoted to be the maximum values and further, particularly in toluene, the experimental period is between 15 and 20°C where as our calculation are particularly valid between 20 and 25°C. According to the experimental observation of BBG,¹⁷ the thermal periods will be smaller towards the higher temperatures ie. between 20-25°C. Taking these into consideration the experimental values 1.2°C and 1.0°C of HT and our theoretical 1/3 values 0.97°C and 0.8°C in toluene and CS₂ are in reasonable agreement. These workers have actually counted the number of light filaments and hence the occurrence of self-focussing is assumed. The first Stokes line 7456Å in benzene exhibited²⁰ a period of 1.25°C (as apparent from published curves) in a length of 25 cms. As in the case of cyclohexane, if we consider the first anti-Stokes wave generation whose periodicity is reflected by the first Stokes wave, the period turn out to be $80/25 = 3.2^\circ\text{C}$ and its 1/3 value being 1.1°C is reasonably close to the observed 1.25°C. The theoretical period for nitrobenzene could not be calculated due to lack of refractive index data.

Table II.3

Observed thermal periods of other workers and the periods calculated from our PL values

	Raman shift (cm ⁻¹)	2nd Stokes		1st Stokes	
		Observed period in a cell length L	Calculated	Observed period in a cell length L	Calculated
			$\frac{(PL)_1}{L}$ P/3		$\frac{(PL)_3}{L}$ P/3
<u>Heumann et al.</u>					
L = 20 cm					
CS ₂	656	1.0	2.4	0.8	
Toluene	1004	1.2	2.9	0.97	
Nitrobenzene	1374	0.5-0.6			
L = 25 cm				1.25	1.1
Benzene	992				3.2
<u>Biscar et al.</u>					
L = 38 cm					
Benzene	992	1.1	1.05		
L = 20 cm				1.0	4.0
Benzene	992		2.0		1.3

117

The intensity variations obtained by HT are within two-orders unlike three orders in the case of BBG. This could possibly be due to the superposition in the case of the former similar to ours except that Heumann et.al. use larger laser intensity than ourselves.

As for the periodicity in the number of light filaments being responsible for the observed thermospectrum of the SRS components, we note that we have obtained thermospectrum in cyclohexane which is one of the non-self-focussing liquids.

The thermal period of 1.1°C between successive peaks for the 8050\AA line in benzene in a cell length of 38 cm, obtained by BBG¹⁶ compares well with our theoretical value $40/38 = 1.08^{\circ}\text{C}$. Thus it would seem that the thermospectrum observed by them is a single spectrum with the calculated period of 1.08°C (1.1°C) between successive peaks, instead of a doubled-spectrum with a period of 2.2°C . The observation of a single spectrum in their case, unlike the triple spectra envisaged in our work and those of HT is in agreement with their claim¹⁸ of avoiding filament formation using aperture limited, single mode, unfocussed laser beam.

The observed doubled-spectrum of period 2°C for the first Stokes (7456\AA) line in benzene in a length of 20 cm. does not correspond to any of the calculated values from either of the processes of second Stokes generation and first anti-Stokes

generation by modulation. In either case this period must be larger than that for the 8050\AA in a cell length of 38 cm., from our foregoing analysis of experimental and calculated results.

The similarity in the large period spectrum (period 7°C) of the 5μ infrared radiation and the 8050\AA second Stokes lines¹⁴ is similar to our argument of the first Stokes intensity variation reflecting those of either second Stokes or first anti-Stokes in the generation of which it (first Stokes) is involved. It is not clear whether the 5μ radiation also shows a fine spectrum as found for 8050\AA .

The thermal periods for the 1.07μ and 5μ reported by BBG^{13,14} could not be theoretically calculated from possible generating processes as all of them involve the participation explicitly of optical-phonons whose data were not readily available.

The only other theory proposed for an analytical description of the mechanisms of the thermospectrum is the resonant enhancement of elastic lattice vibration proposed by Piekara^{21,22} as an alternative mechanism of filament formation in liquids. This is described in II.6.3.

The only direct corroboration of his theory is by HT²⁰ who have experimentally shown a 1:1 correspondance between the periodic variation in the number of filaments and the periodic intensity variation of the 7456\AA line in benzene, leading to the conclusion that the former is the cause of the latter.

It would be interesting to investigate the possibility that the periodic variation in the number of filaments observed is infact due to the periodic variation in the intensity of the first Stokes wave investigated by them. Since the Raman waves are strongly generated in the filaments with large conversion factors, any strong variation in intensity of these waves will be reflected in the number of filaments viewed in the light of their frequency. By photographing filaments in the light of different frequencies of the Raman waves a better understanding might be obtained.

Otherwise we observe several discrepancies between this theory and existing experimental results. From eqn. II.18 it is clear that the space period $\frac{1}{2}\lambda_h$ is directly proportional to the hypersound velocity v_h of the medium. Consequently, all else held constant, the thermal period is expected to be directly proportional to v_h . Table II.4 gives the experimentally obtained periods in toluene, CS_2 and nitrobenzene by HT.²⁰ Also shown alongside each liquid is the hypersound velocity in the liquid.²⁹ The benzene value of 25 cm. is converted to that corresponding to 20 cm. Though the trend in the first three liquids in both v_h and P are same, the ratios of the periods do not agree with the corresponding ratios of v_{20} . This could partly be attributed to different authors quoting different values for the velocities. But the important factor is that nitrobenzene which has the maximum value of v_h has the smallest thermal period thus contradicting eqn. II.18 and hence Pickara's theory.

Table II.4

Experimental thermal periods and hypersonic velocities for four liquids

Liquid	Hypersonic velocity m/sec	Thermal period in °C
CS ₂	1256	1.0
Toluene	1355	1.2
Benzene	1473	1.55
Nitrobenzene	1541	0.5-0.6

The thermal periods are taken from Ref. 19 and 20. The hypersonic velocities are from Ref. 29.

Assuming, in benzene, a value for $v_h = 1.5 \times 10^5$ cm/sec., and taking our laser cavity length $L = 40$ cms, we obtain from eqn. II.18

$$\frac{1}{2} \lambda_h = 40 \times 10^5$$

assuming temperature coefficient of glass to be $\alpha = 10^{-5}$ cm/oc and a cell length of 30 cm., the thermal period is obtained from:

$$\alpha \delta T = \frac{1}{2} \lambda_h \therefore \delta T = 1.33^\circ \text{C}$$

our experimental value of the thermal period in benzene is 0.4°C between successive peaks, Pickara's theory is not amenable to the proposition of the possibility of existence of, say, a superposition of triple spectra such as the one proposed in comparing our theoretical period and experimental spectra.

BBG¹⁸ have the value $L = 50$ cm and $\ell = 38$ cm., hence $\delta T = 1.25^\circ \text{C}$ for $\ell = 38$ cm, 2.5°C for $\ell = 20$ cm. whereas the experimental values are, for successive peaks, 1.1°C for $\ell = 38$ cm (8050\AA). and 1°C for $\ell = 20$ cm (7456\AA). The theory does not distinguish different periods for different SRS in the same liquid and same length and hence the data of 8050 and 7456\AA lines in benzene can be used to verify the theory. The period for the 20 cm. length happensto be less than for 38 cm. unlike that expected by Pickara's theory. Thus it is seen that the existing experimental results do not corroborate Pickara's theory. The verification of the experiments suggested by him to verify his theory is yet awaited.

II.8 Conclusions

In this chapter, thermospectrum of SRS in liquids observed by us and other workers is explained on the basis of nonlinear interactions among the SR waves giving rise to a $\sin \frac{2\Delta kL}{2}$ dependence of the intensity of the SR lines on the product of the length L and wave vector mismatch Δk characteristic of the particular process giving rise to the SR line under investigation. The thermal periods are calculated using available refractive index data for the liquid as shown in Appendix 1. Our experimentally observed thermal period in benzene and toluene are exactly $1/3$ the calculated values and we attribute this to the existence of three overlapping thermospectra with the calculated period but shifted w.r.t. each other in temperature. Different thermospectrum can originate in a different group of high intensity light filaments in which the instantaneous temperature may be slightly different resulting in a shifted spectrum. This possibility is somewhat corroborated by the observation of a single spectrum with the experimental period close to the calculated value in cyclohexane which is taken to be a non-self-focussing liquid. A similar agreement is found between the periodicity observed by HT in toluene, benzene, CS_2 with our calculated values on the same assumption of the superposition of a triple spectra. Our observed period in a shorter length agrees with the larger period expected with a shorter length according to the theory. The observed period

of BBG in benzene at 8050A agrees with our value if we assume that they observe a single spectra with our calculated period. This is in agreement with their claim that filamentary formation is avoided in their experiments by the use of single mode, unfocussed laser beam with a small aperture before the cell. The proposal of HT and that of Piekara that periodic variation in the numbers of filaments is responsible for the observed thermospectrum does not appear very likely because of our observation of thermospectrum in cyclohexane. The resonant enhancement of lattice vibration proposed by Piekara as the mechanism for the observed thermospectrum does not agree quantitatively with observed data. The observed thermal period of ours is much smaller than is expected from this theory. The smaller period obtained by BBG for a much shorter length also contradicts this theory. Lastly the smallest thermal period is observed for nitrobenzene which has the largest hypersound velocity among the liquids investigated, again contrary to the linear proportionality of the thermal period with hypersound velocity in liquids according to Piekara's theory. Thus an analysis of the existing results of the thermospectra of SRS in liquids shows a reasonably good agreement with the analytical theory proposed in this thesis. The existing results cannot be very well interpreted in terms of the only other theory proposed by Piekara et.al.

References

1. V. N. Lugovoi, Sov. Phy - Uspekhi, 16, 658 (1973).
2. V.V. Korobkin: JETP Lett., 16, 419 (1972).
3. S.A. Akhmanov, et al., Sov. Phy - JETP, 35, 279 (1972).
4. A. I. Sokolovskaya, A. D. Kudryatseva, T. P. Zhbanova and N. M. Sushinskii: Sov. Phy - JETP, 26(2), 286 (1968).
5. D. Madhavan and D. Ramachandra Rao: Presented at the symposium on solid state and nuclear physics, Department of Atomic Energy, India, held at Roorkee, India (Dec. 1969).
6. R. W. Terhune and P. D. Maker: Advances in Lasers II, A. K. Levine, Ed., (Marcel Dekker, New York, 19).
R. G. Brewer: Phy. Rev., 140, A800 (1965).
7. P. D. Maker, R. W. Terhune, M. Nisenhoff and C. H. Savage: Phy. Rev. Lett., 8, 21 (1962).
8. Reports of the American Petroleum Institute Research Project, Carnegie Institute of Technology, Vol. I and II.
9. A. F. Forziati: J. Res. Nat. Bur. Stds., 44, 373 (1950).
A. F. Forziati and D. Rosini: J. Res. Nat. Bur. Stds., 43, 473 (1949).
10. J. Timmermans: Physico Chemical Constants of Pure Organic Compounds, I Set 2 (Elsevier Publishing Co. Ltd., N.Y., 1950).
11. Landolt-Börnstein: Chemical Properties of Compounds. (Springer, Berlin, 1950).
12. J. P. Biscar, R. Braunstein and S. Gratch: Phy. Lett., 25(A), 427 (1967).
13. J. P. Biscar, R. Braunstein and S. Gratch: Phy. Rev. Lett. 19, 890 (1967).
14. J. P. Biscar, R. Braunstein and S. Gratch: Phy. Rev. Lett., 21, 195 (1968).
15. J. P. Biscar, R. Braunstein and S. Gratch: Phys. Lett., 27A, 636 (1968).
16. J. P. Biscar, R. Braunstein and S. Gratch: Chem. Phy. Lett., 2, 435 (1968).

17. J. P. Biscar: Private communication (Internal Tech. Report).
18. J.P. Biscar, R. Braunstein and S. Gratch: Phys. Lett., 31A, 43 (1970).
19. E. Heumann and R. Trinks: Z. Chem., 10Jg, 274, Heft 7 (1970).
20. E. Heumann, D. Schubert, R. Trinks and B. Wilhelmi: Phys. Lett., 32A, 62 (1970).
21. A.H. Piekara: Phy. Rev. Lett., 25, 1336 (1970).
22. A.H. Piekara: Phy. Stat. Solidi, 42, 43 (1970).
23. A.H. Piekara: Jap. J. App. Phy., 10, 226 (1971).
24. R.Y. Chiao, E. Garmire and C.H. Townes: Proceedings of the International School of Physics, Enrico Fermi, Course XXXI (Academic Press, New York, 1964) p 326.
25. Y.R. Shen and N. Bloembergen: Phy. Rev. 137A, 1787 (1965).
26. M. Hercher, J. Opt. Soc. Am., 54, 563A (1964).
P. Lallemand and N. Bloembergen, Phy. Rev. Lett., 15, 1010 (1965).
27. R. Y. Chiao, C. H. Townes and E. Garmire, IEEE J. QE-2, 467 (1966).
28. N. Bloembergen and P. Lallemand. IEEE J. QE-2, 246 (1966).
29. I.L. Fabilinskii: Sov. Phy. Uspekhi, 5, 667 (1963).
R.Y. Chiao and B.P. Stoicheff: J. Opt. Soc. Am., 54, 1286 (1964).
H.Z. Cummins and R. W. Gammon: J. Chem. Phy., 44, 2785 (1966).
I.L. Fabilinskii and V.S. Sturnov, App. Opt., 6, 1793 (1967).
Physical Optics: Proc.(Trudy) of the P.N. Lebedev, Phy. Institute, Moscow, Vol. 30 (Ed. D.V. Skobeltsyn).

PART 2

CHAPTERS III AND IV

STIMULATED RAMAN SCATTERING

IN

H_2O AND D_2O

spectra of molecules are very sensitive to local environment in condensed phase and in hydrogen - bonded systems this sensitivity is accentuated, and hence infrared and Raman spectral data in water can be suitably interpreted to provide an appropriate model for water structure and vice-versa. In what follows we will briefly mention some water models and deal, at some lengths, with the Raman spectra of water.

It is more than 40 years since X-ray investigations²⁻⁵ have revealed the structure of ice and ever since various attempts have been made to provide a better insight into a suitable model for the structure of liquid water that will satisfactorily explain the anomalous properties of water. With the increasing availability of sensitive detectors and improved signal processing techniques in the last decade or so and more recently with the discovery of lasers, the infrared and Raman spectrum of water are studied extensively, not only to interpret the spectra better, but in doing so to develop a suitable water structure model. It is only recently that a consensus on the structure of water is emerging based on the cumulative data from spectroscopic (IR and Raman) and thermodynamic studies of water.

III.2 Models of Water Structure

It is well known that water exists as a highly associated liquid due to strong intermolecular interactions and it has been generally accepted that hydrogen bonding between individual

water molecules is mainly responsible for this interaction and is also the source for most of the anomalous properties exhibited by water.

The structure of ice (in the temperature range 0 to -80°C) is well established²⁻⁵ with each oxygen atom tetrahedrally bound to four neighbouring Hydrogen atoms in a Tridymite - like structure similar to SiO_2 where oxygen atoms take the place of the silicon lattice. The O-O distance in ice is 2.76\AA . Along each of the four O-O axis, one hydrogen atom is placed. Two of the hydrogen are chemically bonded to the oxygen just as in the ordinary water molecule with an O-H distance of 0.99\AA and the remaining two hydrogen atoms, belonging to two neighbouring water molecule, are bonded to the central oxygen by hydrogen bonding at a O..H distance of 1.77\AA . The unequal distances of the hydrogen atoms along the O . . . O axis is established by neutron diffraction studies.⁶⁻⁷ This unequal placement of the protons gives a C_{2v} structure to the five-molecular water model as suggested by Walrafen.²⁵ The five molecular tetrahedral structure of water molecules is shown in Figure III.1.

The nearest approach of water molecules of 2.76\AA in ice gives the radius of a water molecule as 1.38\AA . A close packing of molecules of this radius gives a density quite different (larger) from the density of water. Hence some mutual rearrangement of molecules in liquid water is to be envisaged with a somewhat loose structure. The earliest hypothesis,

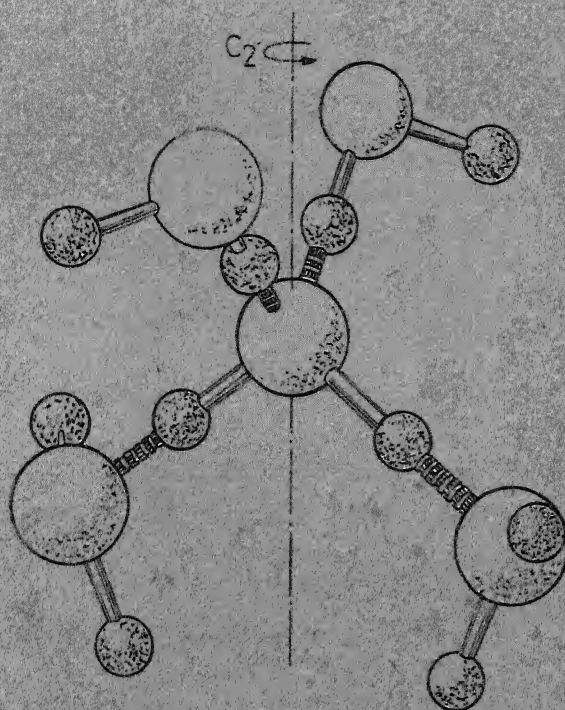


FIG.III.1. Five-molecule hydrogen-bonded structure of C_2 symmetry. Small spheres, H atoms; large spheres, O atoms. Disks refer to hydrogen bonds.

(Reproduced From Ref. 25)

which is also generally accepted, is by Bernal and Fowler¹ according to whom, liquid water has a broken-down ice structure with a considerable amount of coordination still persisting through hydrogen bonding. 50-80% of water molecules are hydrogen bonded at room temperature.

In the vapour phase water molecules are close packed as in any normal liquid. In the broken-down ice structure water molecules retain the tetrahedral co-ordination but with a somewhat weaker hydrogen bonding, resulting in a quartz-like structure which incidentally has a 17% smaller molar volume compared to the Tridymite structure of ice. As the temperature is increased more number of hydrogen bonds are broken and the structure tends towards a more and more close packing. This and similar picture explains the decrease in volume on melting of ice in the temperature region 0-4°C. As the temperature increases the increase in mean distance between neighbouring molecules due to thermal agitation more than compensates for the geometrical contraction in the increasing tendency towards a closely packed structure.

Radial distribution curves for the intermolecular 0..0 distances for liquid water, in the temperature range 1.5-83°C, give,⁸ for the average nearest neighbour distance a value of 2.9-3.05Å and for the average number of nearest neighbours (area below the peak in the distribution curve) a value 4.4-4.9. In ice these numbers are 2.76Å and 4 respectively. The observed

co-ordination numbers and bond distances in liquid water are accounted for by postulating the existence of a mixture of hydrogen bonded tetra-co-ordinated molecules with a non-hydrogen-bonded species which tend to be closely packed resulting in a higher number of nearest neighbours. X-ray diffraction confirms the radial distribution curve.

Early works on water structures are presented in a review by H.M. Chadwell⁹. More recently Nemethy and Scheraga¹² have briefly reviewed the existing theories on water models.

Two models should be mentioned here as representative of recent trend of thinking. The first is the one propounded by Frank and Wen¹⁰ and used by Nemethy and Scheraga¹² for detailed thermodynamic calculations yielding satisfactory values for density, entropy, enthalpy, free energy, relaxation times in various processes and structural changes in solution. Partially co-valent nature of the hydrogen bond is made use of and a resonant scheme proposed for hydrogen bond, which leads to the postulate that hydrogen bonding is a co-operative phenomenon ie. bonds are made and broken, not singly, but several at a time, thus producing short-lived clusters of highly hydrogen bonded region surrounded by non-hydrogen-bonded molecules. The local energy fluctuations cause the clusters to form and dissolve in a continuous process thus giving rise to the name 'Flickering Clusters'. The formation of small aggregates such as dimers etc. are ruled out as being unfavourable

due to the ensuring charge separation. The molecules participate in different number of hydrogen bonds in the clusters, especially those at the surface. The hydrogen bonded ice-like clusters of H_2O molecules and the non - hydrogen bonded monomers are in equilibrium, the equilibrium favouring either one of the two species at different temperatures and pressures. As temperature is increased the molar concentration of clusters increase slightly, the cluster size decreasing; this process is countered by a shift in equilibrium towards an increase in the mole fraction of non-hydrogen bonded molecules.

The second model is proposed by Pauling¹³ and qualitatively treated by Frank and Quist.¹⁴ The basis for this model is the well known structure of solid gas hydrates (such as $Cl_2 \cdot n H_2O$, $CH_4 \cdot 6 H_2O$. . .) in which the water molecules form a hydrogen bonded, closed, bulky network which enclose one or more cavities of size 5.2-6.9Å, which are occupied by the non-polar molecules (Cl_2 , CH_4 . . etc.). Liquid water could be looked upon having a similar structure in which the voids or interstitials are occupied by unbonded water molecules. This structure is referred to as 'Clathrate Crystal' and as applied to liquid water will account for the maximum density, unusually low partial molal entropies, high heat capacity etc. The 'Pauling model' may be looked upon as one class to which 'flickering clusters' belong.

The models proposed for water structure can be broadly clasified into two classes:

Mixture model: which describe liquid water as an equilibrium of a mixture of molecular species with different degrees of association (or hydrogen bonds) per molecule. There might be a finite number of distinct local regions with more or less well defined structural species. The liquid properties are calculated as the concentration weighted average of the contribution of each species. The vibrational spectrum of water should reflect individual components corresponding to the molecular vibration as modified in the local environment.

Continuum model: In the limit of a large number of distinct regions, the mixture model will pass over to a continuum model, which describes water as still a complete hydrogen bonded network, with a distribution of hydrogen bond strengths and geometries. The average hydrogen bond strengths will be less than in ice due to the irregular distortion and elongation, both of which increase with temperature.

Recent studies are increasingly in favour of a two-species model such as due to Walrafen³² and others which will be described subsequently.

III. 3 Water-solute models

Different solutes have different effects on the structure of water in its immediate neighbourhood. Solute ions promote the formation of strongly hydrated units, the degree of hydration (n) should be possible to be evaluated simply by measurement of specific gravity¹. All strongly polarizing ions H^+ , Li^+ , Na^+ and all divalent, trivalent positive ions, as well as $(OH)^-$ and F^- are hydrated, while $(NH_4)^+$, Rb^+ , Cs^+ and most negative ions are not. The lower viscosity of certain solutions compared to pure water, results from a relatively loose structure due to unhydrated ions.²³ There is a structure breaking effect of ions as against increasing co-ordination around some solute ions. A 'Structure breaking entropy' is associated with each solute ions to enable a gradation of their net structure altering effect on a convenient scale.²⁸ These are, to quote typical values: Li^+ (-1), K^+ (+ 12.0), Cs^+ (+ 15.7), F^- (- 3.5), Cl^- (+ 10.2), Br^- (+ 13.9) and I^- (+ 17.9). In this scale kations, smaller or more highly charged than K^+ , F^- , H^+ and $(OH)^-$ are net structure formers. K^+ is slightly structure breaking on balance and this tendency increases through Rb^+ , Cs^+ etc. The other halide ions are net structure breakers increasing in tendency with increasing size (from Cl^- to I^-). $(NO_3)^-$ and $(ClO_4)^-$ are strongly structure breaking.¹⁰

A few of the structural models of water have also been especially suitable as water solute models. The 'flickering cluster model',¹⁰⁻¹⁵ is especially useful in understanding the increase in ice-likeness of the structure due to non-polar solutes. The ^{non-}polar solutes surrounding the clusters just as unbound water are only weakly able to transmit the disruptive forces i.e. torques and displacements from the surrounding to the clusters and consequently increase the half-life of clusters. This will be reflected as an increase in the dielectric relaxation time of the solution which can be easily measured and used as a scale of the increased ice-likeness of the water-solute structure.^{10,11} The nature of water solvent surrounding weakly interacting or Non-polar solutes can be likened to the co-ordination polyhedra observed in solid gas-hydrates, the solute-ions occupying the interstitial voids formed at low-energy expenditure within the 3-dimensionally hydrogen-bonded water structure.¹⁶

Frank and Wen¹⁰ picture a model of ionic solution involving three concentric zones of water molecules about each solute ion. In the innermost zone (A), next to solute ion, the water molecules are closely bound to the ion. The outer most region (C) consists of the normal unbound water molecules polarized by the ionic field, which is nevertheless weak at this distance. In the middle region the water molecules are less ordered (less ice-like) under the competing forces due

to the normal structure orienting influence of adjacent water molecules and the orienting influence of the spherically symmetric ionic field. The strength of this ionic field determines the equilibrium between ice-like and non-ice-like water molecules, giving rise to the concept of the 'structure-breaking entropy'. In general water molecules adjacent to a solute ion are subjected to greater orientational constraints such as reduced hydrogen bond bending and reduced librational freedom.

III.4 IR AND RAMAN SPECTRUM OF WATER

III.4.A Assignments and Temperature effects

The early Raman work on water is reviewed by Hibben¹⁷ and a few others.^{9,18} Water vapour exhibits three fundamental bands^{19,17} at 1595 cm^{-1} (ν_2^π or δ_π), 3652 cm^{-1} (ν_1^π or ν_π) and 3756 cm^{-1} (ν_3^a or ν_σ) corresponding to the bending, symmetrical stretching, and the asymmetrical stretchings respectively, of the H_2O molecule corresponding to C_{2v} symmetry.²⁰ The band at 3652 cm^{-1} is observed strongly in Raman. It is also observed very weakly in IR (indicating that H_2O is non-linear) and 1595 and 3756 bands are strongly observed in IR. The Raman spectra of liquid water corresponding to the valence band is reported to show three bands in the region $3400\text{--}3600\text{ cm}^{-1}$.¹⁷ The interpretation and assignments

of these bands has been the most controvertial problem in the history of Raman spectra. These bands have been attributed to water molecules having different co-ordination by a few authors.²¹⁻²³ Others assign the higher of the two bands to the OH stretching modes (ν_1 and ν_3) and the lower frequency to the overtone ($2\nu_2$) of the bending vibration (ν_2) in Fermi resonance with the symmetric stretching vibration (ν_1). Normally the overtone is very weak.

In addition to these intramolecular valence and bending frequencies the IR and Raman spectrum of liquid water also exhibits low frequency bands in the region 0-1600 cm^{-1} which are not present in the vapour phase. The observed bands in liquid water are at 60, 175, 500, 780 and 2170 cm^{-1} . These are observed both in Raman and IR except the 60 cm^{-1} which is observed only in Raman spectra. Due to their large depolarization factors and weak intensities these low frequency components have been studied extensively and assigned properly only after the availability of ultraviolet light sources, sensitive detection and recording facilities. These intermolecular bands correspond to the hindered Translation or Hydrogen bond bending and stretching (60, 175 cm^{-1} , ν_{h_1} , ν_{h_2}) and hindered rotation or Hydrogen bond libration modes (500, 780 cm^{-1} , ν_{l_1} , ν_{l_2}) of the water molecules in a tetrahedral environment.²⁵ Corresponding frequencies for D_2O are: 60, 175, 350, 500 cm^{-1} .

The band at 2170 cm^{-1} in water is due to the combination of hydrogen bond libration (ν_{l_1}, ν_{l_2}) and bending modes of the valence band (ν_2). Early investigations are reviewed by Hibben¹⁷ and more recent works are reported by Fox and Martin²⁷, Weston²⁸ and Walrafen.²⁴⁻²⁶ Early workers¹⁷ have even attributed these low frequencies to the valence band (3400 cm^{-1}) shifts corresponding to other exciting frequencies of the Hg source used and hence claim wrongly assigned excitation frequencies. The 450 cm^{-1} band in H_2O and 350 cm^{-1} in D_2O are IR forbidden. All the frequencies in D_2O are in ratio $1/\sqrt{2}$ to those in H_2O , except the hindered translation which has a ratio $(20/18)^{-\frac{1}{2}}$. For the rest of the chapter we will confine to the discussion of the valence band. A typical spontaneous Raman spectrum recording is shown in Fig. III.2.

Hydrogen bonding decreases the frequencies of the valence stretching modes and increases (to a much lesser extent) the frequency of the bending vibration. This is clearly evident from the decrease of nearly 200 cm^{-1} from 3650 cm^{-1} in vapour to 3450 cm^{-1} in liquid water to 3250 cm^{-1} in ice at 0°C of the symmetric stretching frequency. A systematic change in the valence band is noted with change in temperature of liquid water. The maxima of the band as a whole shifts towards higher frequency (towards vapour phase $3600\text{--}3650\text{ cm}^{-1}$) with increasing temperature. A trend in the opposite direction is evident in going from water to ice.¹⁷ The intensity of the

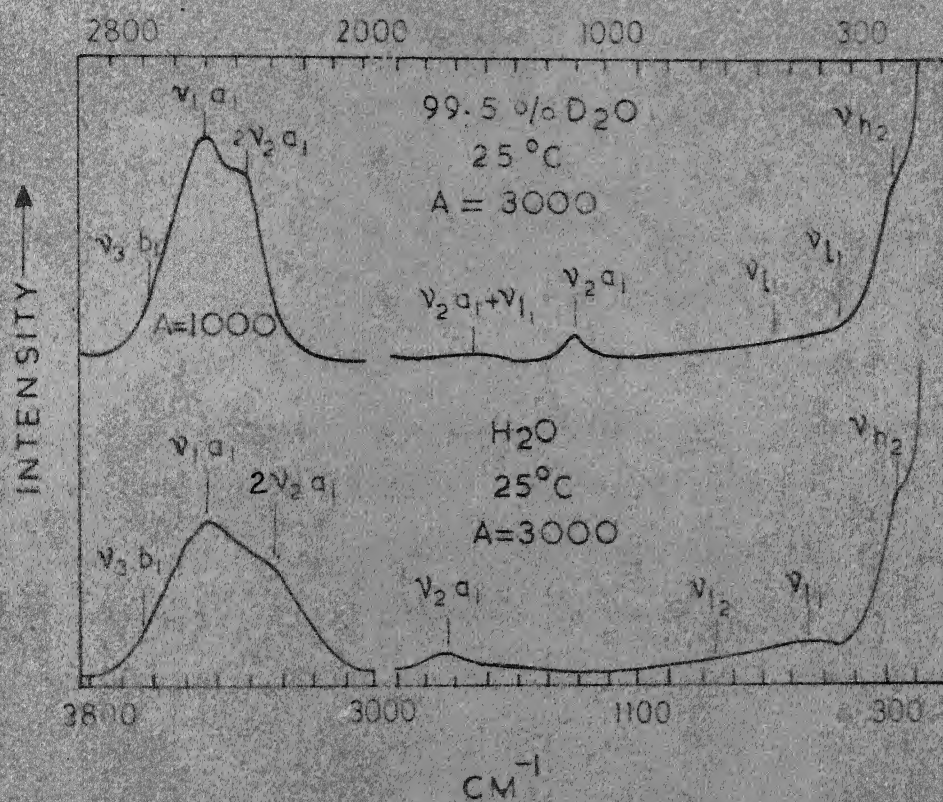


FIG. III 2. PHOTOELECTRIC RAMAN SPECTRA OF H_2O & D_2O . (Reproduced from ref 25)

3450 maxima decreases with increasing temperature.^{17,26,28,29}

The bending frequency decreases slightly and the intensity of the bending mode generally increases with increasing temperature.

In general, the effect of electrolytes in aqueous solutions on the water bands are similar to an increase in temperature.^{38,39,28,24}

From these observations, one interpretation of the OH stretching band in water is that it is composed of many individual frequencies, each due to a particular configuration of associated molecules, the high frequencies arising from the least associated or even unbonded water molecules. The fact that the intensity of the low frequency components decrease and that of high frequency components increase with increasing temperature, is interpreted as the result of decrease in the concentration of highly associated molecules and increase in the concentration of least associated molecules as a result of breakage of hydrogen bonds. This is the so called 'Mixture model' mentioned earlier. The Protagonists of the continuum model²⁹⁻³¹ contend that the observed single, broad valence band reflects continuous distribution of hydrogen bond energies and geometries in the liquid, which would gradually shift towards higher frequencies as the temperature increased and the average strength of hydrogen bond decreased. The mixture model assign the observed bands to molecular species with different co-ordination (0 to 4) or to Polymers.²¹⁻²³ Many of these conclusions are based on

experimentally obtained results which probably suffer from lack of resolution, sensitivity etc. and some which could be reinterpreted to support the alternate model.³² The present trend seems to be a two-species model which envisages an equilibrium between Hydrogen Bonded (HB) tetrahedrally co-ordinated water molecules as in ice and non hydrogen bonded (NHB) vapour like molecules (monomers), the equilibrium gradually shifted by change of temperature or addition of solutes etc. Though there has been several earlier proposals¹¹⁻¹³ Walrafen in a series of recent papers^{24-26,32-36} has ably supported this model.

The existence of a well defined structural region or a species with a particular co-ordination should be reflected in the presence of a distinguishable peak in each one of the valence bands corresponding to the crystal frequency of the species modified by its presence in the disordered water environment.

Interpretation of the broad bands in water or D_2O , especially in assigning any distinguishable peaks, is rendered difficult by the complexity of the water bands and their complex temperature dependence for the following reasons:

- (i) Frequencies of the fundamental O-H stretching modes ν_1 and ν_3 and the first overtone $2\nu_2$ of the bending vibrations lie close to one another. A still more confusing picture prevails for the higher overtones and combination bands²⁹ which almost form clusters of frequencies.

- (ii) Fermi resonance, such as between $2 \nu_2$ and ν_1 , produce intensity borrowing and frequency shift, both of which further varies in a complex manner with temperature due to the variation in the fundamental frequencies.
- (iii) Intermolecular interaction between like vibrations of neighbouring molecules leads to a general broadening and distortion of all band shapes.
- (iv) Because of asymmetry of the local field of force in the liquid, the effective symmetry of water molecule is lowered from C_{2v} to C_s . Therefore ν_1 and ν_3 lose their symmetric and anti-symmetric nature and both can participate in Fermi resonance with $2 \nu_2$.

Many of the complexities could be overcome by studying dilute solution of HDO in H_2O or D_2O which provides a far simpler spectra free from the above complexities and enabling better analysis and interpretation for the reasons:

- (i) The three fundamentals and many of the overtones are widely separated, so that Fermi resonance does not occur.
- (ii) Intermolecular coupling is absent. For example, in dilute HDO in H_2O the OD vibrational frequencies are quite different from the OH frequency of the surrounding water molecules. This results in considerably narrow bands of simple shape for the OD valence contours.

- (iii) Due to reduced absorbance in dilute HDO, larger cell thickness could be used for recording IR spectra unlike in H_2O where very thin samples have to be used, often unsuccessfully.

Falk and Ford²⁹ have investigated the IR spectra of dilute HDO and the observed fundamental stretching bands of HDO are $\nu_1(\text{HDO}) = 2500 \text{ cm}^{-1}$ (uncoupled OD stretching in HDO) $\nu_3(\text{HDO}) = 3400 \text{ cm}^{-1}$ (uncoupled OH stretching in HDO) and bending vibration $\nu_2(\text{HDO}) = 1450 \text{ cm}^{-1}$, which is in between the bending frequencies 1210 cm^{-1} and 1650 cm^{-1} of D_2O and H_2O respectively. The 2500 cm^{-1} and 3400 cm^{-1} bands are simple gaussian profiles with single maximum, no shoulders corresponding to different species of water molecules at any temperature, especially no high frequency shoulders at $3550\text{--}3750 \text{ cm}^{-1}$ for the O-H or $\nu_3(\text{HDO})$ band and $2600\text{--}2700 \text{ cm}^{-1}$ for OD or $\nu_1(\text{HDO})$ where absorption from any non-hydrogen bonded species would occur. The intensities of these stretching bands increased and the peak shifted to high frequencies with increased temperature. The opposite was observed for the bending mode. Hence these authors claim that their result supports the continuum model and is incompatible with the existence of discrete molecular species differing in the extent of hydrogen bonding. Horning, White and Reding³¹ claim support to the continuum model through their investigations of the IR spectrum of crystalline H_2O , D_2O and HDO. They also observe single peaked symmetrical gaussian

contours for the uncoupled O-H and O-D stretching vibrations at 3310 cm^{-1} (width: 100 cm^{-1}) and 2400 cm^{-1} (width: 75 cm^{-1}) respectively. The intermolecular couplings existing in the pure compounds (H_2O or D_2O) lead to a splitting of the respective uncoupled intramolecular components of the same order as the $\nu_1 \sim \nu_3$ separation. The resulting spectra would consist of two overlapping bands, symmetrical about the uncoupled frequencies and separation equal to their widths, giving rise to a symmetrical smooth gaussian band in the spectrum of the pure compounds. Thus the 3250 cm^{-1} and 3350 cm^{-1} bands in pure ice and the 2445 cm^{-1} and 2500 cm^{-1} bands (or a broad symmetric band around 2514 cm^{-1}) in D_2O - ice must be associated with O-H and O-D vibrations respectively. From their appearance and non appearance in the IR and Raman spectrum they are assigned to ν_3 and ν_1 respectively in each pure liquid. The other frequencies 3148 cm^{-1} in H_2O and 2347 cm^{-1} in D_2O - ice in their spectra are attributed to $2\nu_2$. Table III.1 lists the frequencies of the three fundamental intramolecular frequencies in H_2O , D_2O and HDO in the vapour, liquid and ice phase for each as reported by different authors. One can observe both close agreements and widely differing values.

Recently Walrafen^{33,34} has obtained Raman spectra of HDO in H_2O and D_2O in the temperature range of $19-97^\circ\text{C}$. Raman spectrum of 6.2 M solution of D_2O in H_2O at 25°C give an O-D stretching contour peaked at $2575 \pm 5\text{ cm}^{-1}$ with a pronounced

Table III.1

Vapour, liquid and ice phase frequencies of the valence Raman bands in H_2O , D_2O and HDO .

Shifts in cm^{-1}					
	ν_2	$2\nu_2$	ν_1	ν_3	Ref.
<u>H_2O</u>					
Vapour	1595		3652	3756	20
	1595		3600	3757	17
Liquid		3220	3420	3630	17, 21, 22
Ice	1620	3148	3350	3250	31
<u>D_2O</u>					
Vapour	1178		2666	2790	20
Liquid	1235	2360	2515	2662	17
	1207	2390	2509		
Ice	1212	2330-2347	2500	2445	31
<u>HDO</u>					
in CCl_4			2690 2719	3670 3705	29
Vapour	1402		2719	3365	20
Liquid	1450		2500 2540	3400 3450	29
Ice 0°C	1470		2440	3300	29
-170°C			2421	3277	
			2440	3310	31

high frequency shoulder at $2660 \pm 20 \text{ cm}^{-1}$ with increasing temperature the intensity of the low frequency component decreases while that of the high frequency component at 2660 cm^{-1} somewhat increases. The contour maxima gradually shifts from 2507 cm^{-1} to 2550 cm^{-1} (± 5) between 25 to 62°C , while the shoulder changes to a smaller extent. They observe an isosbestic point at $2570 \pm 5 \text{ cm}^{-1}$. From computer fitting (average least square fits), the broad experimental contours are resolved into two gaussian bands at 2525 cm^{-1} (width $160 \pm 10 \text{ cm}^{-1}$) and 2645 cm^{-1} (width $110 \pm 10 \text{ cm}^{-1}$). In a similar work with 0.56 M (1 mole %) of H_2O in D_2O the Raman spectrum of uncoupled O-H band yields two components at 3435 cm^{-1} and 3628 cm^{-1} with an isobestic point around 3470 cm^{-1} . The observed asymmetry of the OH and OD stretching bands alone suggests the incorrectness of the uniformist or continuum model of water structure. Further the presence of an isosbestic point require the existence of components of opposite temperature dependence. Thus these results, in addition to his earlier works,²⁴⁻²⁶ give full support to the two-species model of water structure in which Hydrogen bonded (HB) tetrahedrally co-ordinated water molecules are in equilibrium with non-hydrogen bonded (NHB) monomers. The low and high frequency components are attributed to HB and NHB species respectively.

Worley and Klatz³⁷ have obtained IR absorbance of HDO in D₂O at various temperatures for the overtone region and report an isosbestic point at 6812 cm⁻¹. Hartmann³⁸ reports an isosbestic frequency near 3473 cm⁻¹ in the OH stretching region.

It is expected that in pure H₂O or D₂O the HB and NHB components of the OH and OD stretching modes will further split into two components due to intermolecular couplings, as suggested by Hornig, White and Reding.³¹ Detailed work by Walrafen^{32,35,36} on the Raman spectrum of water at various temperatures has clearly shown the existence of four components in the valence stretching band of the water molecule, with an isosbestic point at 3460 cm⁻¹. The high frequency NHB component corresponding to OD-stretching in HDO (around 2620 cm⁻¹) appears to be weak in IR. Similarly the low frequency HB coupling component (2380-2413 cm⁻¹) appears to be more intense in IR than in Raman spectra.³⁵ The four components are obtained by least square computer fitting of gaussian profiles to the experimentally obtained broad Raman (or IR absorbance) bands. These are shown in Table III.2. The spontaneous Raman contour of the valence band obtained by Walrafen along with the four gaussian into which it is decomposed by Analog method is shown in fig. III.3. The components below the isosbestic points decrease in intensity with increasing temperature with the peak position and width remaining constant. These refer to the

Table III.2

Valence band components of spontaneous Raman contour in H_2O and D_2O obtained by G. E. Walrafen

Spectra	Low frequency		NHB coupling		Refer- ences
	HB coupling component (cm^{-1})	HB peak (cm^{-1})	NHB component (cm^{-1})	NHB peak (cm^{-1})	
a. 6.2M (11 mole) D_2O in H_2O i.e. OD stretching in HDO	IR Width Intensity Raman Av. least square fit	2413 (190) 23% 2420(ν_3) 2525(160) 2520(ν_1)	2520 (140) 66% 2645(110) 2650	2620 (117) 11% 2650	33
b. Pure D_2O (Ar ⁺ laser Raman)		2380	2500	2660	35
c. 0.56M H_2O in D_2O i.e. OH stretching in HDO .			3435 (260)	3628 (90)	33
d. Pure H_2O	Raman Intensity depolariza- tion IR	3234 44.6% 0.24 3240 (310) 41.5	3420 37% 0.46 3522 12.3% 0.36 3540 (150) 7.0	3624 5.6% 0.26 3620 (140) 8.0	32
e. Pure H_2O : Hg-excited Ar ⁺ -laser 5M NaClO_4 in H_2O	Raman Raman Raman	3250 3225 3280	3425 3415 3460	3625 3640 3605	35

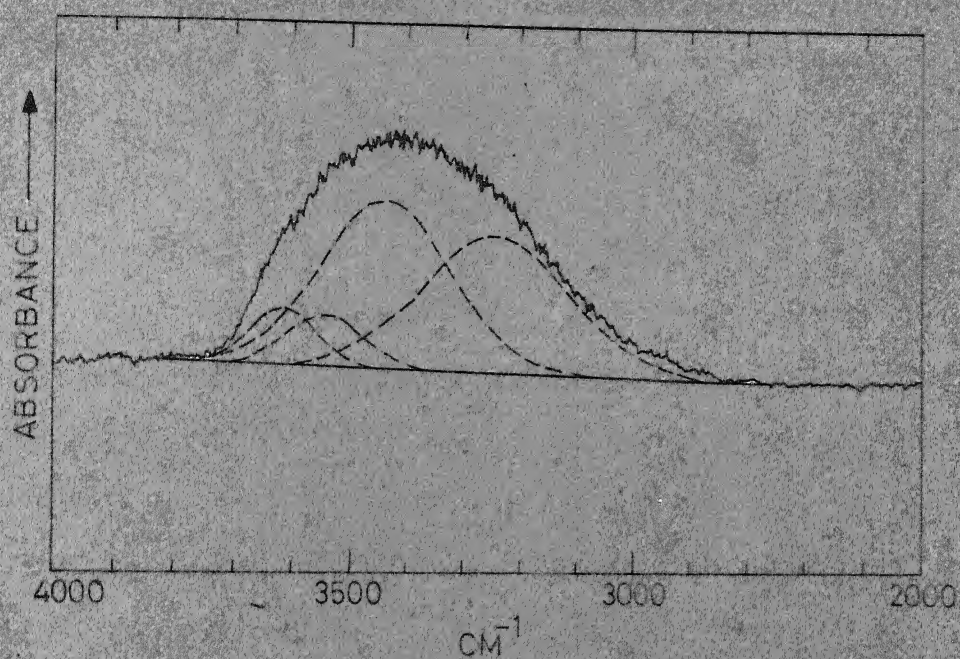


FIG.III.3 Infrared absorbance spectrum of the intramolecular valence contour of water at 40°C. The four Gaussian components comprising the contour are shown by dashed lines.

(Reproduced From Ref.32)

Hydrogen-bonded lattice water molecules. The components above the isosbestic frequency increase in intensity with increasing temperature with more or less temperature independent peak position and widths. These refer to the non-hydrogen bonded monomers. The net result is a shift of the contour maxima to high frequency with increase in temperature.

IR and Raman spectra of water at or near the critical point (374°C) show well resolved bands at 3535 , 3622 cm^{-1} corresponding to the NHB-monomeric water.³⁷ Saumagne³⁹ observed 3545 cm^{-1} ($\nu_1 a_1$) and 3650 cm^{-1} ($\nu_3 b_1$) in the IR absorbance spectra of water at the critical point. The low frequency tails extend upto 3300 cm^{-1} . These components are also observed at as low a temperature as 10°C , thus NHB water exists at these low temperatures, consistent with the breakdown of a considerable percentage of hydrogen bonds in a transition from ice to water as generally accepted after the theory of Bernal and Fowler.¹

It should be noted that the NHB-monomers, though free from hydrogen bonding are subject to strong short range forces such as Vander Waal's forces etc. and to that extent differs from the free water molecule in low pressure steam (or that of water molecules in dilute solution of water in CCl_4). The vapour component is altered by KBM shift of $\sim 70\text{ cm}^{-1}$ or by stark effect of the spherically symmetric environment. etc. and finally contributes a frequency in the 3600 cm^{-1} region to the IR and Raman spectrum of liquid water.³⁰

The small intensity dependence and frequency shifts with increasing temperature of the bending mode ν_2 could be explained³² by the overlapping of the more or less equal bending frequencies of both the NHB and HB water molecules and their opposite behaviour with change in temperature.

Walrafen^{32,33} suggests that it might be possible to reconcile the data of Falk and Ford, Wall and Hornig etc. to conform to the two-species model. The uncoupled fundamental vibrational band of HDO in the spectra of Falk and Ford²⁹ may contain unresolved components from the NHB species also which are not observed probably due to insufficient sensitivity. Further, with increasing temperature the maxima of the band shifts to 3470 cm^{-1} at 130°C , a frequency beyond the isosbestic point obtained by Walrafen. This could be due to an increase in intensity of the unresolved NHB component at this high temperature. Wall and Hornig³⁰ do observe slight asymmetry. They used a 30 cm^{-1} slit-width which might obscure the asymmetry, whereas Walrafen³³ used a slit-width of 10 cm^{-1} ; when using a 30 cm^{-1} slit-width, Walrafen claims to have obtained bands very similar to Wall and Hornig's.

Linewidths:

The uncoupled widths of the O-H, O-D stretching bands³⁰ though considerably narrower than in pure compounds are still broader than the few cm^{-1} widths found in the vapour phase (i.e NHB liquid) or in the intramolecularly coupled water bands

in dilute solutions of H_2O in CCl_4 . At the same time fairly narrow widths of a few cm^{-1} are reported for the strong bonds in crystal hydrates. The uncoupled widths in HDO-ice are found to be fairly narrow, which indicates that the uncoupled band widths reflects the structural disorder in liquid water. The widths are associated with coupling of the motion of molecules in the disordered structure.³¹ The distribution of intermolecular O..O distances in water is responsible for the band widths²⁹ and infact this distribution can be obtained from the observed Raman frequency contours and confirmed by X-ray results.³⁰

III.4B: Effect of Electrolytes

Busing and Hornig,⁴⁰ Schultz and Hornig⁴¹ and Weston²⁸ have investigated the effects of dissolved KBr, HCl, KOH and other halogen compounds such as LiI, KI, CsI, LiCl, CsF, KF etc., on the Raman spectrum of water. Walrafen²⁴ has also studied these effects especially on the Intermolecular bands below 1640 cm^{-1} in water. The accumulated facts can be summarized as follows: The O..O stretching mode at 175 cm^{-1} decreases in intensity, the librational bands 450 cm^{-1} and 780 cm^{-1} are shifted down in frequency and increased in intensity, the 3225 cm^{-1} band decreases and the 3450 cm^{-1} increases considerably in intensity. The effect is greatest for iodide and increases in proportion to ionic size $\text{I}^- > \text{Br}^- > \text{Cl}^- > \text{F}^-$. Similarly for the cations $\text{Li}^+ > \text{Na}^+ > \text{K}^+$. The effect of cations are much less. The bending mode at 1640 cm^{-1} increases much more than the 3450 cm^{-1} band

for KBr and Hcl but very little for KOH.⁴⁰ The intensity changes are considerable for LiI and in this LiI, KI and CsI are indistinguishable. The intensity changes are much smaller with LiCl and CsCl. With KF and CsF the changes are minor and slightly in the opposite direction.⁴¹

The stretching frequency ν_1 shifts to higher frequency with added electrolyte except KF.²⁸ The fluorides cause considerable broadening and the frequencies of the ν_1 component (3450 cm^{-1}) show a slight downward shift.⁴¹ KI produces a slight downward shift in the bending frequency. From the majority of the results it can be generally concluded that dissolved salts (especially halogen compounds) affect the Raman spectrum similar to increasing temperature i.e. brings about breakdown of the associated structure of water. For ex. the Raman spectra of a solution of NaClO_4 in H_2O with varying NaClO_4 concentration at fixed temperature shows a concentration isosbestic point at 3480 cm^{-1} . The effect of 1M solution of NaClO_4 in H_2O is equivalent to a temperature rise of 34°C .³⁵ The intensity decrease of the 3225 cm^{-1} band ($2 \nu_2$) can be ascribed to change in the degree of Fermi-resonance between $2 \nu_2$ and ν_1 due to increase in the frequency of ν_1 on addition of electrolytes.

Raman scattering intensity increases with decreased bond polarity. The larger halide ions form a longer $\text{O-H}\cdots\text{X}^-$ bonds and hence weaker and less polarized bonds resulting in an intensity increase with increasing anion size from Cl^{-1} to I^- . At the

other end of halogens F^- , the bonds $O-H...F^-$ would be stronger and highly polarized resulting in decreased Raman intensity.⁴¹ Kations have less polarizability than anions and hence affect the Raman intensities much less in keeping with observed results. Small ions like F^- and K^+ go into water interstitials, whereas the other ions being larger must necessarily introduce some distortion. Thus not only is $O-H...I^-$ bond less polar but a number of hydrogen bonds are broken or loosened in the vicinity of the ions contributing further to the total effect.

Direct ion-dipole interaction (present even in gas phase) causes a decrease in vibrational frequency of water molecule in the electrostatic field of a kation, determined by the polarizing power of the ion (charge/radius), whereas the orientational constraints under this dipolar effect will decrease the hydrogen bonding between water molecules and increase the stretching frequency. Both the competing effects influence the molecules even outside the first sphere of co-ordination of the ion.²⁸ Purely electrostatic effect decreases with increasing ionic-radius ie. frequency shift downward from gas phase value is greatest for fluoride ion.

The structure breaking effect of ions has already been discussed in Ch.III.3 and observed results corroborate the structure breaking entropy scale-envisaged and conversely this scale helps in interpreting the effect of different ions on the Raman spectrum in particular and structure of water in general.

References

1. J. D. Bernal and R.H. Fowler: J. Chem. Phys., 1, 515 (1935).
2. D.M. Dennison: Phy. Rev., 17, 20 (1921).
3. W.H. Bragg: Proc. Phy. Soc., 34, 98 (1921).
4. W.H. Barnes: Proc. Roy. Soc. 125, A570 (1919).
5. H. D. Megaw: Nature (Lond), 134, 900 (1934).
6. E.O. Wollen, W.L. Davidson and H.G. Schull: Phys. Rev., 75, 1348 (1949).
7. S.W. Peterson and A.A. Levy: Phy. Rev., 92, 1082 (1953).
8. J. Morgan and B.E. Warren: J. Chem. Phys., 6, 666 (1938).
9. H.M. Chadwell: Chem. Revs., 4, 375 (1927).
10. H.S. Frank and Wen_Yang Wen: Disc Faraday Soc., 24, 133 (1957).
11. H.S. Frank: Proc. Roy. Soc., A247, 481 (1958).
12. G. Nemethy and H. A. Scheraga: J. Chem. Phys., 36, 3382 (1962).
13. L. Pauling: 'Hydrogen Bonding', Ed. D. Hadzi (Pergamon Press, London, 1959) p 1. 'The Nature of Chemical Bond' (Cornell Univ. Press, Ithaca, N.Y., 1960), 3rd Ed., p 472.
14. H.S. Frank and Arvin S. Quist: J. Chem. Phys., 34, 604 (1961).
15. G. Nemethy and H.A. Scheraga: J. Chem. Phys., 36, 3400 (1962).
16. D.N. Glew: J. Phy. Chem., 66, 605 (1962).
17. J. H. Hibben: The Raman Effect and its Chemical Application, (Reinhold Publication Corp., New York, 1939), p 319-335.
18. P. K. Narayanaswamy: Proc. Ind. Acad. Sci., 27A, 311 (1948).
19. W. A. Senior and W.K. Thompson: Nature, 205, 170 (1965).
20. G. Herzberg: Molecular Spectra and Molecular Structure, Part II (D. Van Nostrand Co., Inc., N.Y. 1945).
21. I. R. Rao: Ind. J. Phys., 3, 123 (1928); Phil. Mag., 17, 1113 (1934).
22. P. C. Cross, J. Burham and P.A. Leighton: J. Am. Chem. Soc., 59, 1134 (1937).

23. G.R. Chopin and K. Buijs: J. Chem. Phy., 39, 2035, 2042 (1963).
24. G.E. Walrafen: J. Chem. Phy., 36, 1035 (1962).
25. G. E. Walrafen: J. Chem. Phy., 40, 3249 (1964).
26. G. E. Walrafen: J. Chem. Phy., 44, 1546 (1966).
27. J.J. Fox and A. E. Martin: Proc. Phy. Soc. (Lond), A174, 234 (1940).
28. R. E. Weston Jr.: Spectrochim Acta., 18, 1257 (1962).
29. M. Falk and T.A. Ford: Can. J. Chem., 44, 1699 (1966).
30. T.T. Wall and D.F. Hornig: J. Chem. Phy., 43, 2079 (1965).
31. D.F. Hornig, H.F. White and F.P. Reding: Spectrochim Acta, 12, 338 (1958).
32. G.E. Walrafen: J. Chem. Phy. 47, 114 (1967).
33. G.E. Walrafen: J. Chem. Phy., 48, 244 (1968).
34. G. E. Walrafen: J. Chem. Phy., 50, 560 (1969).
35. G. E. Walrafen: in 'Water: A Comprehensive Treatise' Vol. I, Ed. Felix Franks (Plenum Press, New York, 1972).
36. G. E. Walrafen: in 'Hydrogen-Bonded Solvent Systems', Eds. A. K. Covington and P. Jones (Taylor and Francis Ltd., London, 1968).
37. J.D. Worley and I.M. Klotz: J. Chem. Phy., 45, 2868 (1966).
38. K.A. Hartman Jr.: J. Phy.Chem., 70, 270 (1966).
39. Saumagne: Doctoral Dessertation, Univ. of Bordeaux (1961).
40. W.R. Busing and D.F. Hornig: J. Phy. Chem., 65, 284 (1961).
41. J.W. Schultz and D.F. Hornig: J. Phy. Chem. 65, 2131 (1961).

CHAPTER IV
STIMULATED RAMAN SCATTERING
IN H_2O AND D_2O

IV.1 Introduction:

Previous investigations of SRS were restricted to non-associated liquids whose Raman line-widths were only a few cm^{-1} . Associated liquids such as water and D_2O have Raman line-widths of the order of 200 cm^{-1} and hence are interesting for SRS studies. Early attempts following the discovery of SRS, failed to obtain SRS in water. Liquid water exhibits very broad spontaneous Raman bands. Individual water molecules are subject to a range of intermolecular environment resulting in a distribution of vibrational frequencies. The observed broad bands are often resolvable into distinguishable components (refer Chapter III).

A large number of spontaneous Raman spectral investigations report three frequencies in the intramolecular (valence) region $3200\text{--}3600 \text{ cm}^{-1}$ in H_2O at about 3220 , 3450 and 3600 cm^{-1} and these are attributed to the overtone $2 \nu_2$ of the bending mode (ν_2), the fundamental symmetric and antisymmetric valence stretching components ν_1 and ν_3 respectively. Walrafen² has

proposed a model in which Hydrogen bonded (tetrahedrally Coordinated) and Non-hydrogen bonded water molecules exist in equilibrium and contribute distinguishable frequency components to the vibrational-spectrum weighted by their respective concentrations. The valence band of either H_2O or D_2O could be separated into Hydrogen bonded (HB) and Non-hydrogen bonded (NHB) components in the decoupled HDO system; each of them can further be resolved into the components arising out of intermolecular coupling in the pure liquids and denoted by ν_1 and ν_3 depending upon their intensities in IR and Raman spectra and also depolarization. The peak positions, line-width and intensities of these are obtained by Walrafen by a computer fitting of their observed IR and Raman valence contours in term of gaussian profiles and are given in Table III.2 of Chapter III.

Stimulated Raman scattering studies in H_2O and D_2O , apart from their interest because of the broad Raman bands, could provide confirmation or other additional information on these bands. The O-H (or O-D) stretchings are stimulated only at high incident powers due to the large component line-widths and low-scattering crosssections. Hence the threshold powers for SRS in H_2O and D_2O are one to two orders higher than for most of the other liquids. Colles, Walrafen and Wecht³ (CWW) have reported SRS studies in H_2O and D_2O at different temperatures, as well as in aqueous solutions, using picosecond pulses at the second harmonic frequency 0.53μ of a mode-locked Nd^{3+} -glass laser.

Rahn, Maier and Kaiser⁴ (RMK) and Ved Prakash, Dheer and Jaseja⁵ (VDJ) have reported SRS in H_2O only using Q-switched ruby laser of 0.5 and 30 nsec pulses respectively. These studies differ somewhat in the relative intensities and frequencies of the observed SRS components. In view of these contradictory reported results, SRS studies in H_2O and D_2O are reinvestigated by us using a Q-switched ruby laser pulses of about 50 nsec duration. Our results help to bring the earlier observed results by different workers³⁻⁵ in conformity with a single consistent picture such as the existence of HB and NHB components which show characteristic trends with temperature. Further, we believe our work indicates the lack of a significant difference in the results obtained using picosecond and nano-second laser light pulses.

Though spontaneous Raman data of H_2O and D_2O are available in the literature, we have also obtained the spontaneous Raman contours for comparison with earlier Raman profiles and our own SRS profiles.

IV. 2. EXPERIMENTAL:

The SRS spectra of H_2O and D_2O were taken at room temperature by us using a giant pulse ruby laser Q-switched by means of a rotating prism. The laser is a Raytheon LES-system with a $6\frac{3}{4}$ inch long and $\frac{3}{8}$ inch dia. ruby rod in an elliptical cavity pumped by EG and G FX-47 B-6.5 linear flash lamp. The

laser cavity, flash lamp and ruby are water cooled by recirculating cool distilled water through the laser head. The ruby rod is having a brewster cut at one end and plane-parallel at the other end, with no anti-reflection coating at the plane end. The plane-parallel end acts as one end of the fabry-perot laser cavity the other end reflector being the 90° Q-switching prism. The experimental set up is similar to that shown in Fig. II.3 except for the water jacket, PM_2 etc. A beam splitter deflects a fraction of the output beam on to a photomultiplier RCA 7102 whose output is displayed on a Tektronix 545 or 555 oscilloscope to monitor the laser output. The Q-switching part of the laser system such as the prism, delay-circuit etc. are completely fabricated in our laboratory. The laser beam is typically about 4-5 mm in diameter and about 50 ns in duration. The beam is focussed into the liquid cell by means of a lens of 5 cms focal length. The H_2O or D_2O is kept in a cylindrical glass cell about 20 cms in length with optical flats at either end. The radiation emerging from the cell is collected and condensed on to the slit of the spectrograph. Corning CS-2.60 and 2.58 filters are used to remove most of the light from the xenon lamp. But the xenon light output in the region between 7000 to 8000\AA cannot be avoided due to lack of suitable filters.

Two spectrographs are used to photograph the SRS spectrum. One is a Carl-Zeiss 3-prism spectrograph with a dispersion of about $300 \text{\AA}/\text{mm}$ in the 8000\AA region. The other is a $3/4$ meter Jarrell-ash grating spectrograph with a dispersion of $40 \text{\AA}/\text{mm}$

in first order. The threshold of the laser was around 750 Joules (1150 volts). The SRS in H_2O and D_2O could be obtained only at input exceeding 1200 Joules (1450 volts). Operation at this high power level resulted in the ruby rod getting severely damaged over a small length at one end rendering it quite unusable for subsequent experiments.

Kodak 1-N plates were used to photograph the spectrum. Four to five pulses were used to expose each spectrum. Corning glass filter CS 7.59 is used in front of the spectrograph slit to attenuate the laser light considerably and pass only the Stokes shifted Raman component. This precaution was necessary to safeguard the spectrograph slit from getting damaged by the focussed ruby laser radiation. The Raman cell is removed sufficiently far from the laser in order to minimize the Xenon lamp background which was found to extend over a wide range in the exposed spectra. We were not very successful in completely eliminating the background.

We could also record the spontaneous Raman spectra of H_2O and D_2O at room temperature and higher temperatures, using a recording spectrophotometer. A spectra-physics argon-ion laser was used as the exciting source. The 3/4 meter Jarrell-ash spectrograph mentioned earlier is used as a monochromator with the grating rotated at constant speed. The camera is replaced by a slit behind which a photomultiplier ITT FW 130 is placed and the photomultiplier output is fed to a pico-ammeter which

feeds a varian-chart recorder. This spectrophotometer⁶ has been assembled for recording laser excited fluorescence from Rare-earth impurities in various host lattices. The Raman spectra were recorded with the crystal replaced by a cell containing H_2O and D_2O and with suitably placed windows to observe the spectrum at 90° to the direction of exciting radiation. Spectra were taken both at room temperature and at high temperatures ($60-70^\circ C$).

IV.3 Earlier Reported results

IV.3 A. Colles, Walrafen and Wecht (CWW)³

H_2O :

The SRS spectrain H_2O and D_2O obtained by these authors is reproduced here in Fig. IV.1. The SRS spectrum of water at $5^\circ C$ shows one intense component at 3400 cm^{-1} with a broad low-intensity tail around 3250 cm^{-1} . These naturally correspond to the HB class and no evidence for the NHB components between $3500-3650\text{ cm}^{-1}$ is visible in the SRS spectrum at this temperature. The spectra at $85^\circ C$ shows a shift of the maxima to higher frequency.

The spectra of H_2O diluted with 40% by volume of D_2O shows the stimulation of the HB class only, whereas a 50% dilution with D_2O shows both the NHB components with very little trace of the HB components.

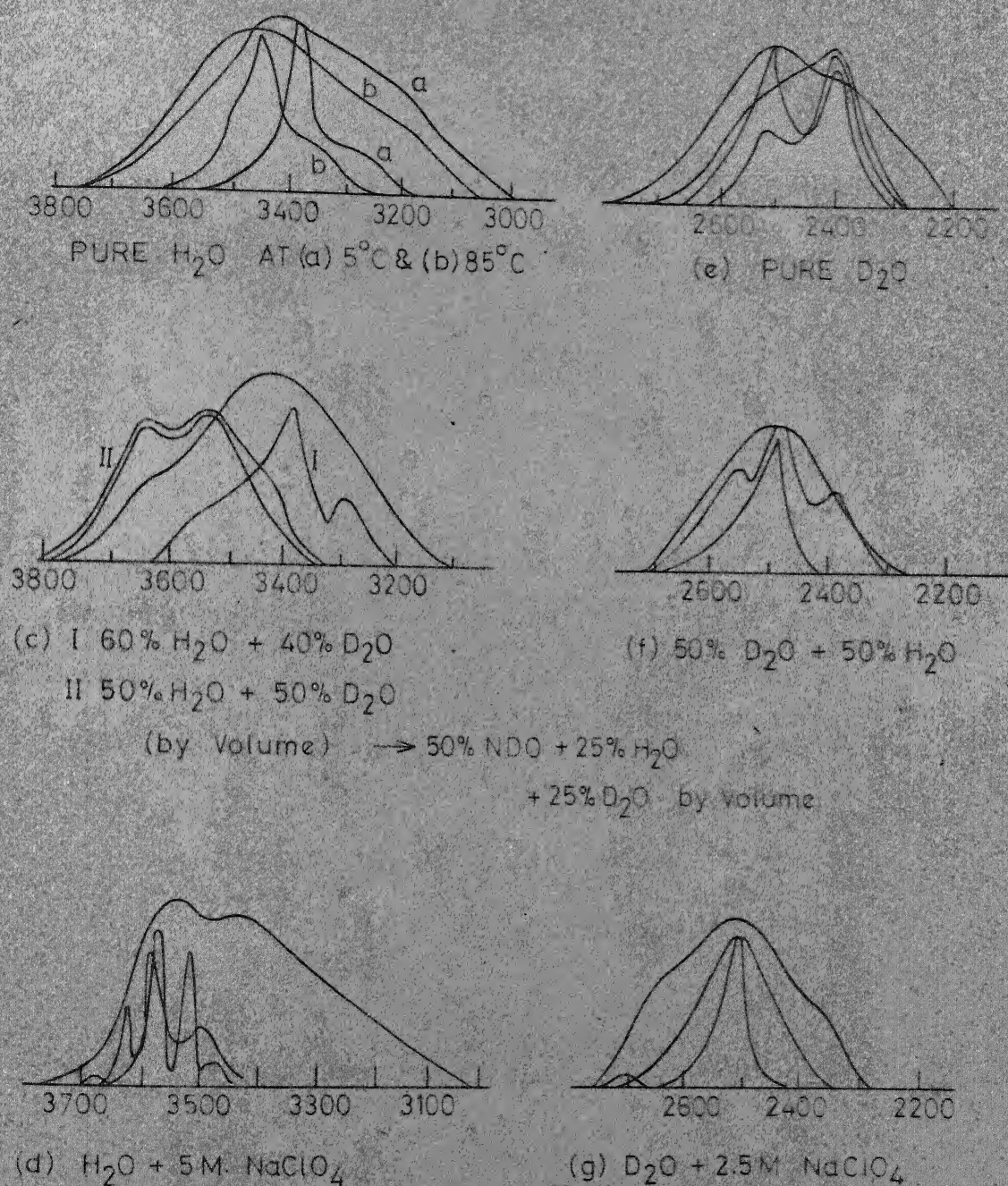


FIG. IV.1. SRS AND SPONTANEOUS RAMAN CONTOURS IN H_2O , D_2O AND HDO (From ref 3) ABCISSA IS RAMAN SHIFTS IN cm^{-1}

The spectra of 5M-solution of NaClO_4 in H_2O clearly shows the NHB components with some modulation apparent from the figure.

D_2O :

In pure D_2O , two intense components are observed belonging to the HB class. The spectra of the OD stretching band in 50% HDO shows an intense component from the HB class near 2500 cm^{-1} with components at higher and lower frequencies corresponding to a NHB and HB components.

Spectra of 2.5 M solution of NaClO_4 in D_2O shows a single HB component at 2500 cm^{-1} stimulated with a weak component from the NHB class.

These spectra according to the authors indicate that:

(1) The SRS spectra obtained in D_2O under different conditions seem to correspond more nearly to the spontaneous contour.

Whereas in H_2O the spontaneous contours fail to predict the observed SRS components.

(2) In H_2O there seems to be an exclusive stimulation of either HB or NHB class only, whereas in D_2O both HB and NHB components are observed together.

The authors observe relatively smaller SRS widths compared to that observed by other workers. They attribute this to the occurrence of self-focussing in water. The pico-second pulses

used by them (CWW) may reduce the possibility of self-focussing in their experiments. However, they observe, the possibility of much faster refractive index changes (than through molecular-reorientation) with time constants of 0.2 psec due to jump-diffusion process in molecular reorientation does not completely rule out the occurrence of self-focussing in water with psec light pulses.

In their SRS spectra of 5 M solution of NaClO_4 in H_2O , they obtain closely spaced lines about the NHB SRS components, similar to the modulation lines such as discussed by Lallemand and Bloembergen.⁸

B. Rahn, Maier and Kaiser (RMK)⁴

These authors report the observation of SRS in water and also what they term as stimulated librational scattering (SLS) in which the intermolecular vibrational mode in water, at 500 cm^{-1} is stimulated at thresholds higher than for SRS of the valence band. Their SRS is obtained by using a mode-locked ruby laser of pulse width 0.5 nsec in a cell of length 40 cm. The SRS threshold is approximately 3 GW/cm^2 . The emission were photographed with the help of a 3-prism spectrograph.

Their SRS spectrum show two frequencies 3260 and 3420 cm^{-1} of more or less equal intensities, close to the reported values of 3247 and 3435 cm^{-1} of Walrafen.² They have calculated the gain of the SRS from the spontaneous scattering crosssection

$d\sigma/d\Omega = 8 \times 10^{-31} \text{ cm}^2$ and linewidth $\Delta\nu = 176 \text{ cm}^{-1}$ for the 3435 cm^{-1} component and the calculated theoretical gain $g_R = 7 \times 10^{-5} \text{ cm}^{-1}/\text{MW}$ compares well with that estimated $g \sim 10^{-4} \text{ cm}^{-1}/\text{MW}$ from the blackening of spectrum, sensitivity of photographic plate and with the assumption that the Stokes wave grows from spontaneously emitted noise level 10^{-2} W/cm^2 .

C. Ved Prakash, Dheer and Jaseja (VDJ)⁵

These authors report the investigation of SRS in water at different temperatures in the range $6-70^\circ\text{C}$, using a Q-switched ruby laser with 30 nsec pulse width. They observed frequency shifts corresponding to 3650 cm^{-1} and 3450 cm^{-1} , the former appearing throughout the investigated temperature range and the latter appearing below 16°C and increasing in intensity as the temperature is lowered. The two components 3650 and 3450 cm^{-1} are attributed to the H_2O and $(\text{H}_2\text{O})_2$ species respectively. Though the 3200 cm^{-1} component corresponding to $(\text{H}_2\text{O})_3$ is present in the spontaneous spectrum¹⁵ at low temperature, the absence of this component in SRS is attributed to breakage of hydrogen bond by the high electric field intensities of the laser. The same bond breakage is said to be responsible for the constant intensity of the 3650 cm^{-1} component, corresponding to free monomers, throughout the investigated temperature region.

IV. 4. Our Results:

The spontaneous Raman contours of H_2O obtained by us is shown in Fig. IV.2a for two temperatures 20 and 65°C. The Raman bands obtained in D_2O at 28 and 65°C are shown in Fig. IV. 2b. Fig. IV.2a shows the spectra at the two different temperatures superposed for comparison.

Our SRS spectra in H_2O and D_2O , at room temperature, taken on the 3-prism spectrograph are shown in Fig. IV.3. The water spectrum in Fig. IV.3a shows two bands around 3200 and 3380 cm^{-1} and D_2O spectrum in Fig. IV.3b shows two components around 2400 and 2500 cm^{-1} . The 3380 cm^{-1} component in water is stronger than the 3200 cm^{-1} band and in some of the water spectrum only 3380 cm^{-1} was present. In D_2O , both the 2400 and 2500 cm^{-1} seem to be equally intense and were always observed together.

The spectra obtained on the grating spectra are shown in Fig. IV.4. Densitometric traces are obtained of these spectra and these are shown in Fig. IV.5 superposed on the corresponding traces of Walrafen (Fig. IV 1a and 1e) for comparison. The H_2O spectra show a peak at about 3380 cm^{-1} with a pronounced but less intense shoulder at 3220 cm^{-1} , with no evidence of any high-frequency shoulders. The D_2O spectra show two peaks of more or less equal intensity around 2410 and 2500 cm^{-1} . In addition there is a distinct but weak shoulder at 2660 cm^{-1} .

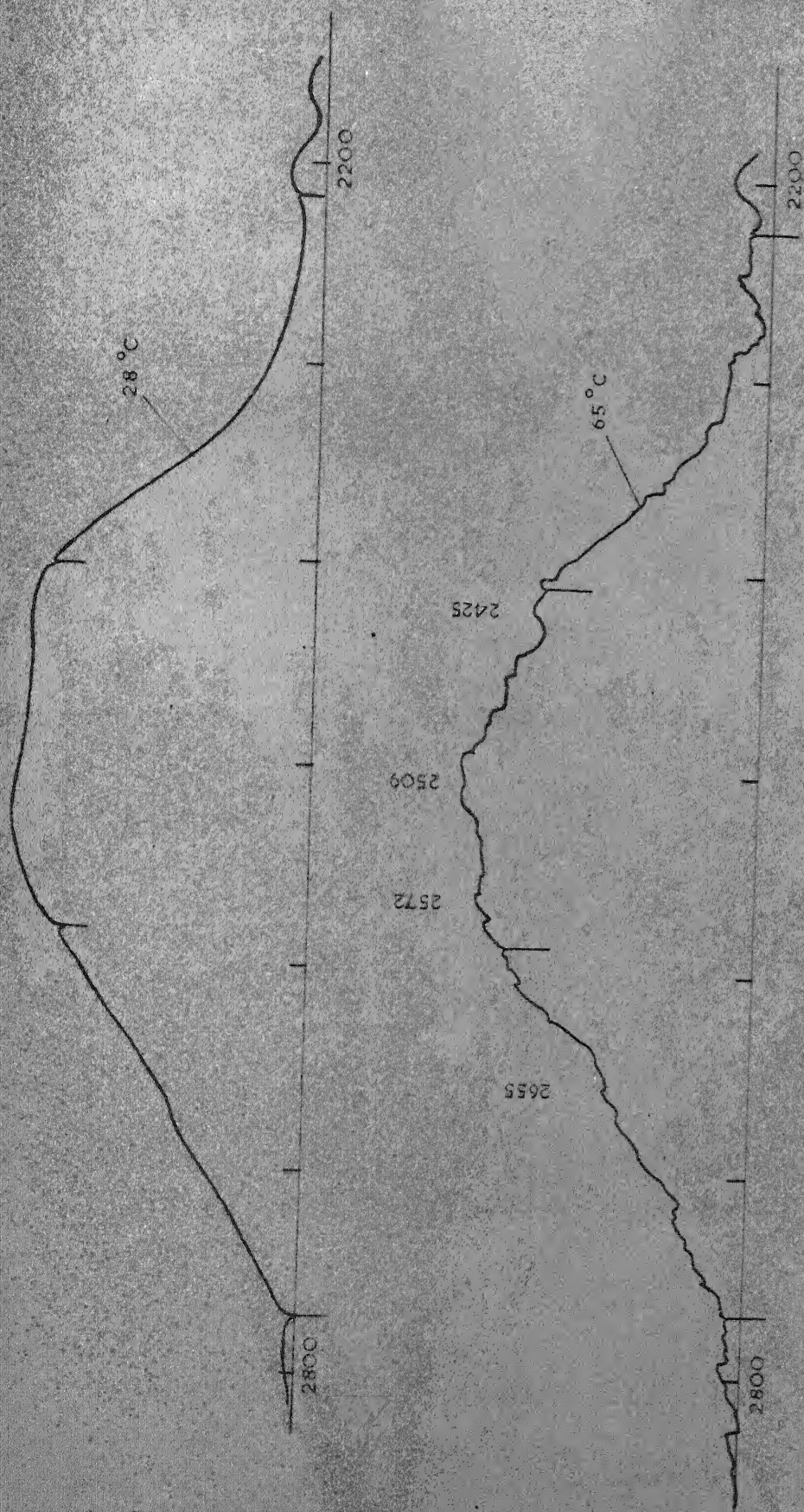


FIG. IV.2b EXPERIMENTAL SPONTANEOUS RAMAN PROFILE OF THE VALENCE BAND IN D_2O

(SCALE GIVES SHIFTS IN cm^{-1})



FIG. IV.2c SUPERPOSITION OF TWO SPONTANEOUS RAMAN PROFILES OF THE VALENCE BAND OF (a) H_2O AND (b) D_2O AT TWO TEMPERATURES
(SCALE GIVES SHIFTS IN cm^{-1})

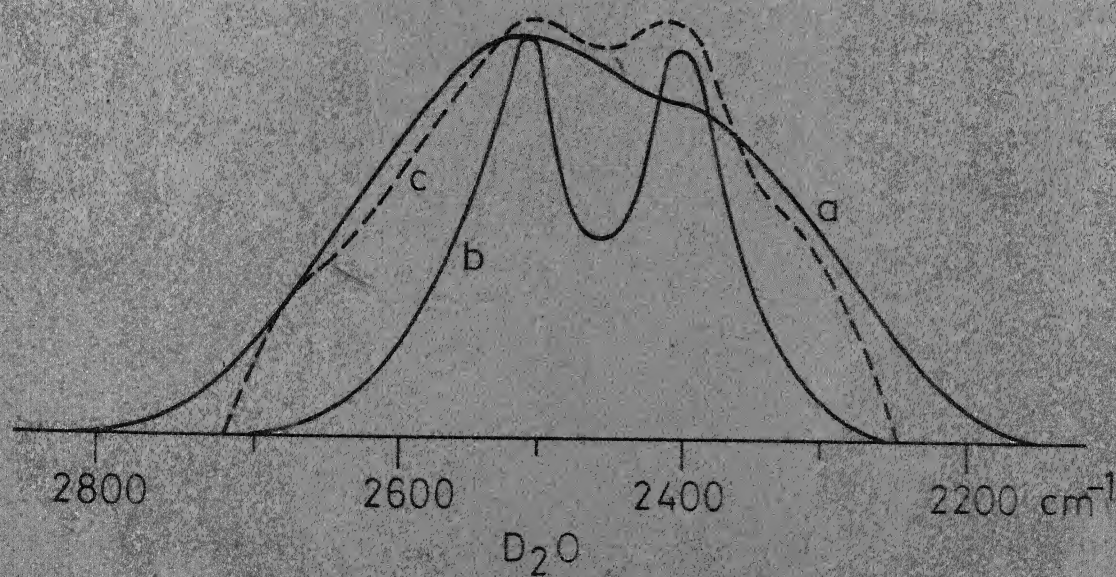
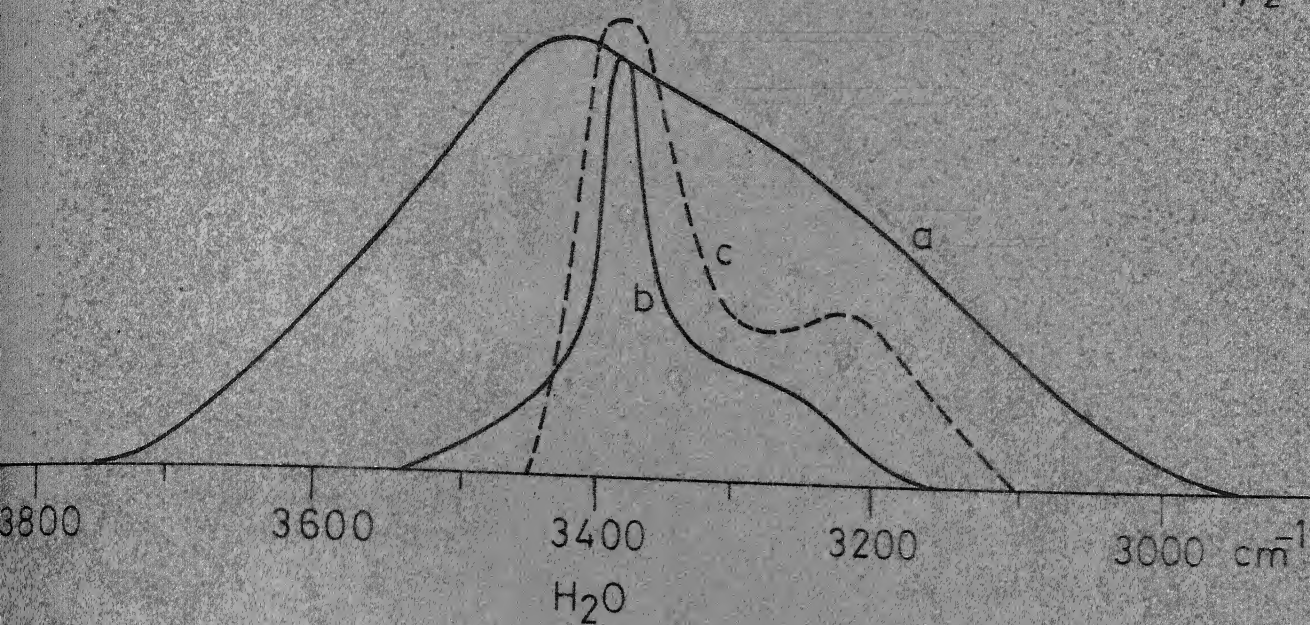


FIG. IV.5 Experimental Raman Contours

- a. Spontaneous
 - b. SRS
 - c. SRS (Our Spectra)
- } Walrafen (Ref. 3)

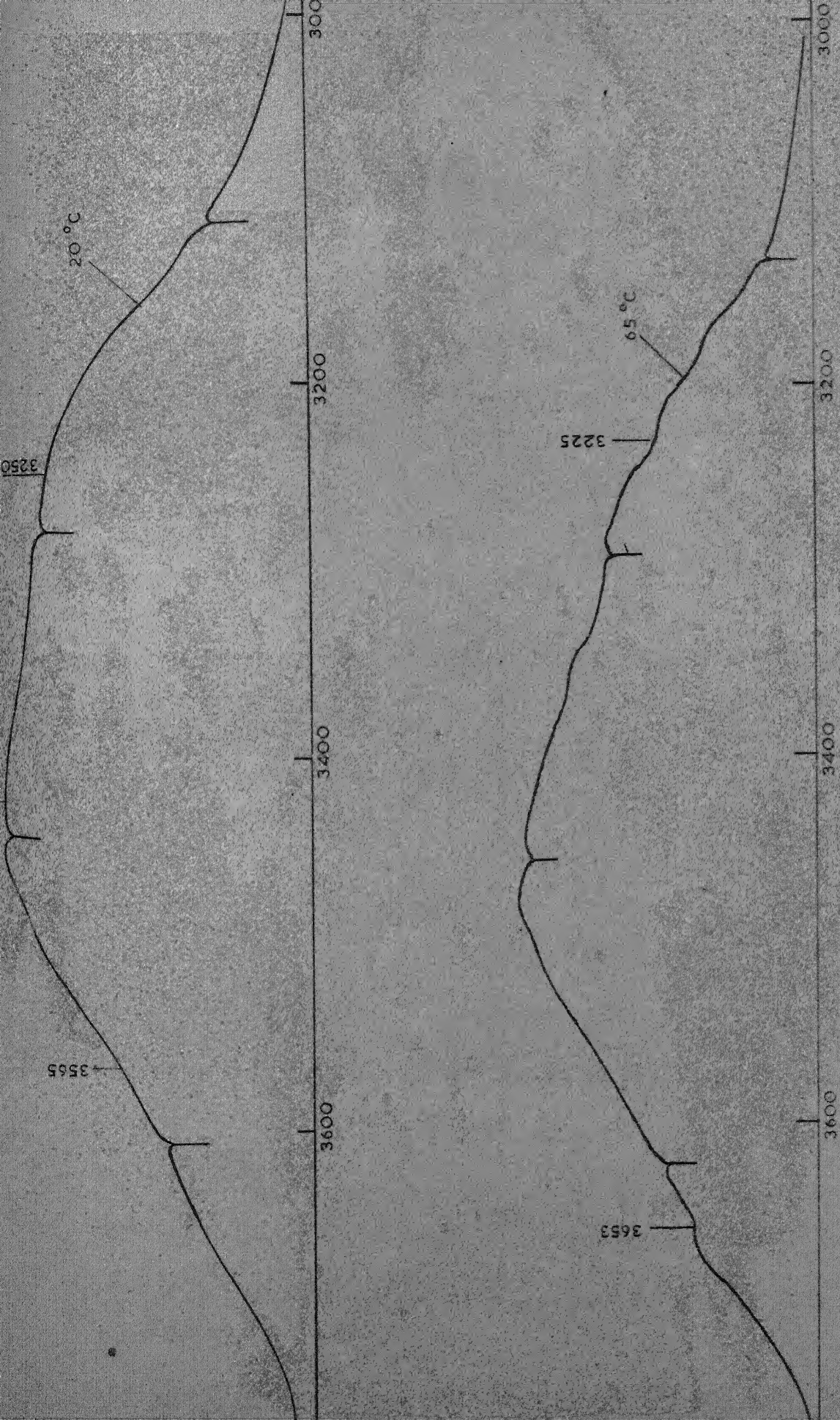


FIG. IV.2a EXPERIMENTAL SPONTANEOUS RAMAN PROFILES OF THE VALENCE BAND IN H_2O
(SCALE GIVES SHIFTS IN cm^{-1})

Some of our spectra of D_2O show very sharp lines at 7640\AA and 8115\AA which correspond to shifts from the exciting wavelength of 1315 and 2080 cm^{-1} . In the prism spectra these lines are observed when no SRS is recorded, but in the grating spectra (Fig. IV.4b) these are present even in the presence of the SRS components. The grating spectra of H_2O (Fig. IV.4a) also show two lines at 8096 and 8719\AA corresponding to shifts of 2050 and 2935 cm^{-1} .

One or two spectra of D_2O show a few equally spaced lines towards the exciting wave length of the low-frequency component 2400 cm^{-1} , one can distinguish 2-3 components which are separated by about 100 cm^{-1} . Our quoted shifts can be taken accurate to $\pm 10\text{ cm}^{-1}$.

IV.5. Discussion

The spontaneous Raman profiles obtained by us (Fig. IV.2a and IVb) agree fairly well with that of Walrafen and others. The approximate positions of peaks and evidence of shoulders (indicated in the figure) correspond fairly well with the components obtained by Walrafen (Table III.2). At higher temperatures the intensity decrease of the HB class (below 3450 cm^{-1}) and intensity increase of the NHB class (above 3500 cm^{-1}) are clearly visible and in some cases shoulders at the expected component positions become evident. Due to considerable noise in the system at the time of these recordings, the pico-ammeter

had to be operated at reduced sensitivity and the recordings were taken at a somewhat increased slit width of 100μ , otherwise the resolution of the spectra could have been better. Attempts at superposing the contours obtained at different temperatures (Fig. IV.2c) failed to yield a consistent isosbestic point such as reported by Walrafen.¹ This is possibly due to the extreme reproducibility of the optics, especially with laser sources, needed for such a superposition.⁷

Our experimentally observed SRS bands 3220 and 3380 cm^{-1} in H_2O , 2400 and 2500 cm^{-1} in D_2O , agree closely with that reported by Walrafen¹ and the band profiles follow closely that of CWW. These frequencies belong to the HB class of molecules. In our spectra taken at room temperature (20°C) there is no evidence for the NHB components around 3600 cm^{-1} in H_2O but the weak shoulder around 2660 cm^{-1} visible in the densitometric profile of the grating spectra of D_2O (Fig. IV.4b) indicates the existence of the NHB component and it agrees in position with the shift predicted and verified by Walrafen.²

In contrary to the above results, VDJ⁵ report that in their experiments with H_2O , the 3650 cm^{-1} band was strongly present throughout the temperature range of their study $6-70^\circ\text{C}$ and the component at 3450 cm^{-1} starts appearing below 16°C and increase in intensity as temperature is lowered from 16 to 6°C . If we interpret their results on the basis of the two-species model of Walrafen, the presence of intense component at 3650 cm^{-1} ,

would seem to indicate that even at very low temperatures, as low as 6°C considerable percentage of water molecules are unbonded and their percentage of NHB species hardly changes as temperature is increased to as high as 70°C , whereas the proportion of tetrahedrally bonded HB class of molecules increases sufficiently, for the appearance of the corresponding component in the SRS, only below 16°C . It is very unlikely that the NHB monomers would exist in any great proportion exceeding the proportion of HB molecules at low temperatures. A close inspection of their spectra in comparison with our own prism spectra of H_2O indicates clearly that they have actually observed the components at 3400 and 3200 cm^{-1} instead of the reported 3600 and 3400 cm^{-1} . As the 3-prism-spectrograph-camera combination used by these workers in their experiment is identical to the 3-prism spectrograph used by us, an enlargement of our spectra to match the size of their published spectra⁵ enabled us to point out this error in the measurement and assignment of their spectra and further to identify their observed SRS components as 3400 and 3200 cm^{-1} identical to our own results. Thus their results also conform to ours and those of CWW³ in the position of the observed SRS components in H_2O and hence their results could also be interpreted in terms of the two-species model.

CWW conclude that in water there is an exclusive stimulation of either HB or NHB components alone, where as in D_2O , there is evidence that both HB and NHB are stimulated simultaneously. But their Fig. 1c show weak shoulders on the high

frequency side in spectrum I and on the low frequency tail in spectrum II. In either case it is evidence for the simultaneous stimulation of both HB and NHB class, though depending upon individual cases, one or the other maybe weak enough not to be clearly distinguishable.

The structure breaking effect of dissolved salts in aqueous solution on the water structure (discussed in Chapter III.3 and III.4C) is clearly apparent from the spontaneous and stimulated Raman contours of CWW^3 (Fig. 1d and 1g). The SRS of 5 M solution of $NaClO_4$ in H_2O shows exclusive stimulation of the NHB components. Similar SRS spectra of 2.5 M $NaClO_4$ in D_2O show a NHB component along with a strong HB component. The NHB component appears to be relatively weaker probably due to the decreased concentration of the salt in D_2O , resulting in a decreased structure breaking and consequently a smaller proportion of NHB molecules. A more concentrated solution (say 5 M- $NaClO_4$ in D_2O) might lead to a stronger stimulation of NHB component at the cost of or exclusion of HB component. In a similar way, a decreased concentration of $NaClO_4$ in H_2O (say 1-2 M) might lead to additional stimulation of HB component also, thus negating the concept of exclusive HB or NHB stimulation. Either spectra conclusively prove the structure breaking nature of the ClO_4 ions (Ref. Chapter III.3). The increase in the proportion of NHB molecules due to the resultant bond breakings lead to a considerable increase in the intensity and even to exclusive stimulation of the NHB components even at room temperatures or lower.

The overall width of the SRS bands obtained by us are comparable to those obtained by CWW³ using mode-locked pico-second pulses (see Fig. IV.5). This indicates that the broad SRS bands in water cannot be attributed to self-focussing at all or else if self-focussing is responsible for the broad bands, then self-focussing in water occurs as easily with pico-second light pulses as with nano-second light pulses, indicating that refractive-index changes in water occur faster than a few pico-seconds, for, it is known⁸⁹ that self-focussing is reduced if the molecular re-orientation time of the liquid is greater than the pulse duration. This would give credence to the so called jump diffusion process occurring in water² and to the recently established fact that refractive index changes in liquids resulting from molecular rocking motion can occur with time-constants of the order of 0.2 pico-seconds. Early works on SRS classify water as a non-self-focussing liquid.¹¹ Recently M Paillette¹² has conclusively shown that the nonlinear index of refraction n_2 of water is small and the threshold for self-focussing is high ($> 10^{12}$ w/cm²) and the frequency broadening due to self-phase modulation is negligible ($\Delta\nu \sim 6$ cm⁻¹ at 10^{11} w/cm²).

It looks to us only natural to attribute the broad bands of SRS in water to the same cause that gives rise to the broad spontaneous bands. Because of the asymmetry of the local field of force about a water molecule in the liquid, the effective symmetry of water molecules is lowered from C_{2v} to C_s . The

short lived C_s distortions are sensitively reflected by the intra molecular valence bands and leads to the polarized nature and roughly equal intensities of the intramolecular valence components (ν_1 and ν_3) in both HB and NHB class of water molecules.^{1,13} C_s perturbation provides an explanation for the large band width observed in the spontaneous intramolecular Raman spectra. Thus the polarized nature of all the four valence components, the equal intensities of components within each class and the changing intensities of the bands with the concentration of either species of molecules (with temperature, or electrolyte addition), may well lead to simultaneous stimulation of two or more of the components in the SRS. In spite of the reduction in the width of each components due to stimulated emission, overlapping components will still lead to a broad band in SRS, with perhaps, more clearly distinguishable peaks than in the spontaneous profile. As seen in Fig. IV.5 our D_2O spectra show shoulders at 2660 cm^{-1} corresponding to the NHB class and at 2335 cm^{-1} which could be attributed to the overtone of the bending vibration enhanced by Fermi resonance as discussed in Chapter II. The stimulation of these extra components result in our SRS contour in D_2O being broader than that of CWW³ whereas in H_2O our SRS contour width compares well with theirs.

In some spectra of D_2O the SRS spectrum shows a few equally spaced lines on the lower wavelength side of the Raman band at 2400 cm^{-1} . These look very similar to the beating observed by

CWW (Fig. 1d, Ref. 3) in the SRS of 5 M solution of NaClO_4 in H_2O , except for the fact that whereas their modulation lines were within the spontaneous Raman contour, in our case they lie outside the spontaneous Raman contour. Also, their separation between the modulation components is reported to be 60 cm^{-1} which also corresponds to the Raman active intermolecular hydrogen-bond bending-vibrations, but our lines are separated by about 100 cm^{-1} . Broadening and the existence of discrete side bands about the stimulated Raman components are explained in the literature as due to modulation of refractive index at the difference frequency between two frequency components in the incident laser beams.⁸ The spacing between the lines (100 cm^{-1}) **in our spectra agrees very closely with the difference between** the two HB valence components excited in D_2O . These are at 2400 and 2500 cm^{-1} with a difference in frequency of 100 cm^{-1} . Thus the modulation observed seems to be due to the close proximity of the stimulated intramolecular valence components. A similar correspondence has been recently pointed out by Walrafen.¹⁴ In his case, the two NHB components at 3550 and 3605 cm^{-1} in the spontaneous Raman band of 5 M solution of NaClO_4 in H_2O differ by 55 cm^{-1} which agrees very closely to the beating frequency observed in the SRS of the same solution by CWW (see Fig. IV.1d). He also proposes a similar reasoning to the modulation observed in their case.

The sharp lines corresponding to shifts of 1315 and 2080 cm^{-1} in D_2O and 2050 and 2935 cm^{-1} in H_2O , observed by us in some of our spectra (Fig. IV.3) could not be properly explained.

IV.6. CONCLUSION:

The SRS in H_2O and D_2O obtained by us are in conformity with the HB and WHB components obtained by Walrafen¹ for the spontaneous Raman bands of H_2O and D_2O based on their two-species model of water structure. They also agree well with their³ SRS spectra of H_2O and D_2O . However, our results lead us to disagree with their conclusion that self-focussing in water is responsible for the observed broad bands in SRS of H_2O and D_2O . Our observations are strengthened by the values for the nonlinear refractive index, self-focussing threshold etc. for water obtained by Paillette.¹² An alternative reason is suggested, based on the observed polarization and intensities of the components in the IR and spontaneous Raman spectra of these two liquids, according to which more than one component can be stimulated simultaneously resulting in a broader profile. Our spectra has also led to clarifying an error in the assignment of the observed bands of VDJ ⁵ so that their results also conform to the model proposed by Walrafen.

Thus the few preliminary works on SRS of H_2O , D_2O and mixtures by a few workers has already provided interesting results.

The stimulation of HB or NHB components and also the existence of a pair of components in each of them, provides conclusive support for the mixture model of water as against the continuum model. The particular two-species model proposed by Walrafen² is amply substantiated by the observed SRS results.

References

1. G. E. Walrafen: J. Chem. Phys., 47, 114 (1967).
2. G.E. Walrafen: J. Chem. Phys., 48, 244 (1968).
3. M.J. Colles, G.E. Walrafen and K.W. Wecht: Chem. Phys. Lett., 4, 621 (1970).
4. C. Rahn, M. Maier and W. Kaiser: Opt. Commn., 1, 109 (1969).
5. Ved Prakash, M. K. Dheer and T.S. Jaseja: Phys. Lett., 29A, 220 (1969).
6. D. Ramachandra Rao, U. V. Kumar, Bansi Lal and P. Venkateswarlu: Symposium on Applied Optics, Indian Institute of Science, Bangalore, India (Nov. 1974).
7. G.E. Walrafen: in 'Water: A Comprehensive Treatise' Ed. Felix Franks (Plenum Press, N.Y., 1972).
8. P. Lallemand and N. Bloembergen: Phys. Rev. Lett. 15, 1010 (1965).
9. S.L. Shapiro and J.A. Giordmaine: Phys. Rev. Lett., 19, 1093 (1967).
10. S. Polioni, C.A. Sacchi and Svelto: Phys. Rev. Lett. 23, 690 (1969).
11. N. Bloembergen and P. Lallemand: IEEE J. QE-2, 248 (1966).
12. M. Paillette: Ann. Phys. (Paris), 4, 674 (1974).
13. G. E. Walrafen: J. Chem. Phys. 44, 1546 (1966).
14. G. E. Walrafen: 'Advances in Molecular Relaxation Processes! Vol. 3, Ed. W. J. Orville-Thomas (Elsevier, Amsterdam, 1972); and also Ref. 7.
15. J. H. Hibben: 'The Raman Effect and its Chemical Application', (Reinhold Publication Corp., N.Y., 1939).

PART III

CHAPTERS V AND VI

SPECTROSCOPIC INVESTIGATIONS OF LASER
GENERATED PLASMA FROM SOLID SURFACES

CHAPTER V

LASER PRODUCED PLASMAS AND THEIR DIAGNOSTICS

V.1 Introduction

Exceedingly high optical field strengths are obtained by focusing the intense radiation from solid state lasers. Power outputs of 10-100 MW from giant pulse ruby or Nd-glass lasers, when focused to an area of 10^{-4} cm², will yield electric field strengths of the order of 10^6 - 10^7 V/cm, and are found to cause breakdown of matter (gaseous or solid) at the focal point. A dense and high temperature plasma is then produced which emits intense visible and ultraviolet (uv) radiations. The first report of laser produced gas breakdown is by Maker et al.,¹ and of laser produced plasma (LPP) at the surface of a solid target is by Linlor.² LPP has now become a potential laboratory source of high density, high temperature plasma. The potentialities of the LPP for

generating high enough temperatures for fusion reactions to occur was recognised very early that the first report of LPP from solid target by Linlor² also mentions the possible applications of such plasmas for controlled fusion experiments. Basov and Krokhin³ and Dawson⁴ have presented theoretical analysis for the feasibility of producing plasmas with densities of 10^{21} cm^{-3} and temperature of the order of several keV. These early predictions were followed by the development of very high power laser systems for fusion experiments. Production of neutrons from LPP have already been reported, first by Basov et al.⁵ and later by Floux et al.⁶

However, the disadvantages with LPP's are their smallness and extremely-short life. Further they expand and cool subsequent to their formation. The smallness, short duration and inhomogeneity of these plasma make investigations of such plasmas extremely difficult necessitating good space and time resolutions for their diagnostics. In spite of these, better than order of magnitude values are obtained experimentally for the plasma parameters, such as electron/ion densities, temperatures, expansion velocities and emission parameters etc. An interesting variety of experimental techniques are used for the diagnosis of LPP such as:

Probe measurements,⁷⁻⁹ electrostatic analysers and Mass spectrometers^{10,11} for detecting and measuring the velocities, kinetic energies and total numbers of ions,

electrons and neutral particles emitted by the plasma.

Framing and streak photography^{12,13} for time resolved study of the expansion of the luminous plasma. Shadow and Schlieren photography^{14,15} to map the dense regions of the plasma.

Conventional and holographic interferometry¹⁵⁻¹⁹ for measurement of refractive index gradients and hence distribution of electron densities.

Spectroscopic techniques²⁰⁻²⁴ of studying the plasma emission is a versatile method yielding several plasma parameters such as electron/ion densities, temperatures, velocities etc. X-ray absorber techniques²⁵⁻²⁷ are especially employed for measuring the peak electron temperatures.

Apart from their interest per-se, LPP's can be used for various special purposes such as:

As sources of energetic electrons²⁸ and ions²⁹ for use in particle accelerators etc.

As the only available source of spectra of highly ionized species^{30,31} through which some lines in the solar spectrum have been recently identified.

As pulsed source of X-rays³² and neutrons.³³

For simulation of conditions in hot stars etc. and for studying atomic processes at high densities and temperatures.

The radiation pressures in these plasmas being of the order of 10^6 - 10^8 atm., thermodynamic properties of target materials such as evaporation, etc. at high pressures could be evaluated without actually subjecting the material to high pressure.

It is but natural that such LPP's should be extensively studied. DeMichelis³⁵ has presented a bibliographical review of laser induced gas breakdown and the resulting plasma formation and expansion. Mulser et al.³⁴ have reviewed the LPP from solid targets, especially solid deuterium.

The early part of this chapter presents some aspects of LPP and its diagnosis. The latter part deals with spectroscopic diagnostic techniques of plasmas which will be used in analysing our experimental results in Chapter VI.

V.2 LASER PRODUCED BREAKDOWN IN GASES

V.2.1 Ionization Mechanism

It is experimentally observed³⁶ that the plasma formed at the focus in a gaseous medium absorbs an anomalously large fraction of the incident laser energy, several orders larger than needed to ionize all the particles in the focal volume. It is of interest to identify the mechanisms of energy absorption and ionization leading to the plasma formation. Direct photo-ionization and emission of electrons is ruled out

as the ruby laser photon energy (1.78 eV) is small in comparison to the ionization energies (10 eV) of rare gases.

At high laser flux densities (q), multiphoton absorption of laser energy is a possible mechanism of ionization of gas atoms, the absorption probability is $w_n \propto q^n \propto E^{2n}$ which indicates a sharp threshold on the laser intensity (or field strength). Gold and Bebb³⁷ have made quantum mechanical calculation of the multi-photon absorption cross-sections involving, quasi-resonant-intermediate transitions at multiples of laser frequency. At an initial atomic density of 10^{20} cm^{-3} the breakdown threshold is defined as the photon flux required to produce 10^{13} electrons in the focal volume within the duration of the laser pulse (10 ns). The theoretical estimate of threshold laser intensity is found to be two-orders greater than the experimental value. The discrepancy is attributed to causes such as the reduction in the ionization potential in the strong EM field, stark shifts of intermediate states³⁸ and multi-mode character of laser radiation resulting in large effective flux in small areas within the focal volume³⁶.

The second possible mechanism for the ionization and the subsequent heating of the resultant plasma is the cascade ionization process,³⁹⁻⁴³ in which free electrons present in the focal volume absorb light photons by collision with neutral

atoms. This process is referred to as 'Inverse Bremsstrahlung', being the reverse of the process of emission of radiation by electrons accelerated in the field of ions. Electrons acquire energy, exceeding the ionization potential, during repeated collisions. They transfer this energy to an atom by collision, thus ionizing the atom and producing one more electron and so on the cascade process proceeds, with the electron number increasing exponentially with a characteristic cascade time τ according to

$$N = N_0 \exp(t/\tau) = N_0 2^k \quad \text{V.1}$$

The critical number of electrons N_{cr} and the number of binary generations k_{cr} , needed for breakdown within the laser pulse duration Δt are given by

$$k_{cr} = 1.45 \ln \frac{N_{cr}}{N_0} = \frac{\Delta t/\tau}{\ln 2} \quad \text{V.2}$$

with $N_{cr} = 10^{13}$, $\Delta t = 30$ ns ($N_0 = 1$) we get $k_{cr} = 43$ and $\tau = 1$ ns. τ being inversely dependent on laser intensity q , eqn. V.2 indicates a sharp threshold condition.

Classical microwave theory of energy absorption by electrons can be extended to optical frequencies. During collisions the oscillation energy (10^{-2} w) possessed by the electrons in an EM field is continuously transferred to translational energy. In the quantum picture an electron acquires energy $h\nu$ once in many collisions. The two can be

considered same if photon energy $h\nu$ is much less than ionization potential I_0 . The classical theory gives a breakdown threshold laser intensity³⁵

$$I_{th} = \frac{\pi m_e c k_{er} v^2 I_0}{e^2 \sigma_{tr} v_e n_a \Delta t} \quad V.3$$

where m_e , e , v_e are mass charge and velocity of electron, n_a is atomic density and σ_{tr} is a transport cross-section. The classical theory also predicts a threshold minimum at high pressures.

Diffusion of electrons out of the focal volume is a serious source of loss which results in an increase in threshold. Diffusion loss within laser pulse duration Δt is lower, higher the gas density (pressure) and larger the focal dimension (i.e. a longer focal length of focussing lens).

Experimentally, at moderate pressures (10^3 - 10^5 mm of Hg), the breakdown threshold is found to show a monotonic decrease with increasing pressure⁴⁴⁻⁴⁷ thus favouring the cascade theory and is incompatible with multiphoton ionization which predicts a weak pressure dependence ($p^{-1/2n}$) of breakdown threshold. The threshold minima at high pressure is observed at a pressure somewhat lower than the minimum predicted by classical theory.

Frequency dependence of breakdown threshold laser intensity:

Experiments^{48,49} using four frequencies at the fundamental

and second harmonics of ruby and Nd-glass lasers indicate a threshold maximum, in the threshold laser intensity vs frequency characteristics. The cascade theory predicts a threshold proportional to square of the frequency⁵⁰ and the multiphoton theory predicts an inverse dependence. Other experiments^{44,51} favour the cascade process.

Effect of electron diffusion on threshold intensity have been verified,^{44,52,53} using longer focal length lens, adding impurity gas⁵⁴ and applying an axial magnetic field⁵⁵ to reduce diffusion loss.

The cascade process has been shown to be favoured by the experimental results, the multiphoton ionization providing the initial electrons to trigger the cascade⁵⁶ since natural causes are unable to provide it.⁵⁷ At very low pressures (10^{-2} - 10^{-5} torr) when electron mean-free path exceeds the focal dimensions, inverse bremsstrahlung is inhibited and multiphoton absorption process predominates.⁵⁸ It is possible to separate the multi-photon process from the cascade process by shortening the light pulse duration, the multi-photon process dominating below a critical pulse duration.⁵⁹

Mennicke,⁶⁰ in experiments on LPP with solid H_2 , O_2 , and N_2 , suggests that SRS may possibly be the source of the first electron that trigger the cascade process. In the very early portion of the laser pulse intense SRS is observed.

from the targets, in the forward scattering. Anti-Stokes lines up to 5.4 eV (7th order in hydrogen: 2300 \AA) and perhaps higher orders are seen and may cause direct photoionization.

V.2.2 Dynamics of Plasma Expansion

The plasma, resulting from the breakdown and ionization, strongly absorb, the laser light by free-free electron transitions in the field of ions (inverse bremsstrahlung). The laser light is absorbed in an extremely thin layer of the order of the mean free-path of laser photons $\ell_v \sim 1/k_v$ where k_v is the free-free absorption coefficient⁶¹ and heats the plasma. $\ell_v \sim 10^{-2} - 10^{-3}$ cm for ruby laser photons at $T = 10^5 - 10^6$ oK.

Experimentally it is found that the luminous plasma, initially formed at the focus, expands rapidly in the direction of the lens. Three different mechanisms are proposed for this expansion:

1. Radiation supported detonation wave : The gas heated in the thin layer expands, due to radiation pressure, very rapidly with velocities of a few Mach numbers and sets up a shock wave travelling in all directions. The gas behind the shock front is heated and ionized and becomes highly absorbing. The wave-front towards the lens absorbs the laser energy behind the shock front and the zone of intense absorption moves along the incident light channel

towards the lens. This hydrodynamic mechanism is similar to the 'Detonation wave' in reacting gases where the reaction energy is replaced by the energy absorbed per unit mass (specific energy) from the laser beam.

2. Breakdown wave : Regions of the gas in the light cone towards the lens, of increasing cross-section, reach the breakdown threshold later during the pulse duration at a higher laser intensity. Thus the region of breakdown moves along the light channel towards the lens.
3. Luminous mechanism : The thermal radiation from the initial high temperature plasma heats and ionizes the gas surrounding it. The surrounding gas in the direction of the lens- absorb the laser radiation and is heated to a high temperature in a thin layer δ_v . Thus the absorbing high temperature boundary moves towards the lens.

Each mechanism being characterized by a unique velocity of the absorption wave, can be verified by experimental measurement of velocity of luminous front.

Ramsden and Savic⁶² first proposed the radiation supported detonation wave model for the hydrodynamic expansion of the plasma, and analysed it on the basis of detonation theory in reacting gases.⁶³ Taking into consideration the variation of focal radius along the axis of light cone w.r.t x (measured from focus), he deduced the following

relationship between x and t for constant laser power.

$$x \propto t^N, \quad N = 3/5$$

V.4

A typical theoretical velocity for a laser power of 20 MW is about 10^7 cm/sec which compares well with their own experimental value.

After the end of the laser pulse the shock wave is treated like a Taylor's spherical blast wave,⁶⁴ which yields a relation: $x \propto t^{2/5}$.

From an experimental log-log plot of x vs t , from streak photographs of LPP in air, Ramsden and Savic⁶² obtains a slope of 0.65 during laser pulse and 0.38 after the end of laser pulse. Daiber and Thompson⁶⁵ from similar studies obtain an exponent that varies from 0.6 to 0.9 during laser pulse. They consider the gaussian pulse shape of laser intensity variation and show that the slope N depends on the point (t_0) in the laser pulse w.r.t. the peak (t_m) at which the breakdown occurs. $N = 0.6$ corresponding to $t_m - t_0 = 0$. The exponent after laser pulse also deviates from blast wave theory due to deviation from spherical symmetry of the plasma.

The breakdown wave has been treated by Raizer⁶¹ for a triangular laser pulse of peak power W and pulse width Δt and the velocity of the luminous front is found to be

$$v \propto \frac{(W/\Delta t)^{1/2}}{\tan \alpha}$$

V.5

where α is the half-angle of the light cone. The breakdown wave velocity is higher for short, powerful laser pulses focussed with long focal length lenses. An analysis of the third mechanism, though involved, yields a velocity and dependence on laser power similar to the detonation wave.⁶¹

Ambartsumyan et al.⁶⁶ and Alcock et al.⁶⁷ interpret their framing photograph results in terms of the 'Breakdown wave'. Korobkin et al.⁶⁸ observe discontinuous structure and intermittent expansion of the spark and explain their results in terms of the third model. Study of air spark with a train of pico-sec pulses,⁶⁹ yields a series of successive breakdowns from the first breakdown towards the lens. Successive breakdowns occur when the spherical shock front from previous spark meets the next laser pulse. The distance between sparks and the pulse interval yielding the shock velocity (8×10^6 cm/sec for a total energy of 1J in 10 pulses). Basov et al.⁷⁰ using a LGW laser focussed by a long focal length lens ($f = 2.5$ mt), obtain several hundred discrete sparks over 2 mts, the discharge front moving towards and away from lens at velocities 1.2×10^9 cm/sec and 3.8×10^9 cm/sec respectively.

Indirect evidence for the plasma expansion is obtained from the doppler shift of laser light scattered at 90° from plasma.⁶² A shift of 3\AA , towards blue is observed, yielding a velocity of 10^7 cm/sec for the moving plasma front. Mandel Shtam et al.⁷¹ observed scattering in the direction of the

lens and obtains a shift twice that for 90° scattering, proving conclusively that it is doppler shift due to the moving front. From studying the amount of shift vs laser power (W), they obtain close to $W^{1/3}$ dependence for the velocity that is predicted by the detonation theory.

V.3 LPP from Solid Targets

When a radiation of flux density q and duration τ falls on the surface of a strongly absorbing medium (like metals), the surface is heated up and a thermal wave penetrates into the matter to a depth $l_t \propto (K_e t)^{1/2}$ where K_e is the thermal conductivity. If the specific energy of the medium spanned by the thermal wave ($\varepsilon = q\tau/\rho_0 l_t$ where ρ_0 is density of the medium), exceeds the binding energy Ω , fast evaporation occurs without a phase transformation and the substance expands under the influence of the pressure gradient.⁷² For the condition

$$q > q_1 \propto \frac{\Omega \rho_0 K_e^{1/2}}{t^{1/2}}; \tau \gg t_1 \propto \frac{\Omega^2 \rho_0^2 K_e}{q^2} \quad V.6$$

strong evaporation occurs during the laser pulse.⁷³ If $q < q_1$ (or $\tau < t_1$) evaporation is small and it is necessary to consider the thermal equilibrium of the phase transition.⁷⁴ For $q > q_1$ ($\varepsilon \gg \Omega$), the velocity of substance motion will be equal to the sound velocity $C = \sqrt{\varepsilon} \propto \sqrt{T}$. The time t_0 in which the expansion wave catches up with the thermal wave is given by

$$Ct_0 \sim \ell_t \therefore t_0 \sim K_e \left(\frac{\rho_0}{q}\right)^{2/3}$$

V.7

for $t_0 \ll \tau$, the problem is a gas-dynamic one in which the thermal conductivity in the condensed medium can be neglected.

At high intensities, the same primary ionization mechanism described earlier in Chapter V.2.1, ionize and heat the material and within a few nsecs the target surface is covered⁷⁵ by a highly ionized layer of thickness $\ell_v = 1/k_v$ where k_v is the free-free absorption coefficient. For strongly absorbing materials such as metals k_v is as high as 10^4 - 10^5 cm⁻¹. Very high surface temperatures can be reached with material boiling inhibited by the large radiation pressures of the order of 10^2 - 10^4 atmos. It is shown⁷⁶ that the free-free absorption has a 'take-off' temperature, depending on the ionization potential, above which rapid heating will take place. As the plasma reaches very high temperatures the absorption coefficient decreases. Further electron density increases to such an extent that the plasma frequency $\nu_p = \left(\frac{e^2 n_e}{\pi m_e}\right)^{1/2} = 8.9 \times 10^3 \sqrt{n_e}$ exceeds the laser frequency which is then reflected from the plasma. Critical density for the ruby laser ($\nu = 4.35 \times 10^{14}$ sec⁻¹) is $n_{ec} = 2.4 \times 10^{21}$ cm⁻³. During the subsequent expansion of the plasma the temperature and electron density decrease and the plasma once again becomes transparent to the laser radiation. The incident radiation is able to reach the target and produce another layer

of material plasma which is then heated to a high temperature. Thus the plasma at the target surface is maintained at a high temperature by this self-regulating mechanism.

The plasma pressure at the interface (F) between the cool, dense undisturbed target material and the hot plasma initiates a shock or compression wave (s) into the solid matter.³⁴ This compensates the momentum of the plasma outstreaming into vacuum. The boundary F gradually travels into the target as more and more material is evaporated and converted into hot plasma. This is referred to as a 'deflagration wave' by Floux²⁷ in their model. With this and similar models, the plasma production and hydrodynamic expansion are analysed by various authors^{14,73,77,78} using momentum, energy and mass conservations at the different boundaries, to obtain the dependence of mass of material evaporated, temperature, velocity and density on the laser flux (q), wavelength (λ) and time (t). In the plane-geometry one obtains

$$T \propto q^{1/2} \lambda^{1/2} t^{1/4}, \quad \bar{v} \propto q^{1/4} \lambda^{1/4} t^{1/8}, \quad m \propto q^{1/2} \lambda^{-1/2} t^{3/2}$$

V.8

With laser powers of 10^9 watts, temperatures up to 500 eV and velocity of the boundary close to $2-3 \times 10^6$ cm/sec are measured in solid targets. Lower temperatures (80-150 eV) and greater velocities $1-4 \times 10^7$ cm/sec are observed in gases, the two cases being distinguished by processes of deflagration and detonation respectively.²⁷

LPP with sub-nsec pulses:

One can distinguish two-regimes of operation in the plasma formation w.r.t laser pulse duration. When the laser pulse is short so that during the heating process the plasma has very little time to move, then heat conduction is the mechanism of energy transfer till such time when the heated matter expands hydrodynamically. On the other hand, if the laser pulse duration is long, the expansion process occurs during the initial process itself and heat conduction is neglected. From considerations similar to eqn. V.7, the time instant (t_0) and the extent of the thermal wave (l_0) at which the thermal conduction ceases and gas-dynamic expansion takes over, can be evaluated.^{78,27}

Very high temperatures and densities are possible with sub-nsec pulses. Reflection of laser light from plasma becomes an important factor. The first observation of neutron emission from LPP used p-sec light pulses.⁵ Other experiments^{79,80} have also used p-sec pulses. The heat diffusion equation is solved⁸¹ and effect of heat conduction on mass and temperature of plasma also experimentally verified.⁷⁹ Systems for laser-fusion experiments use sub-nsec pulses to reach high temperatures before the plasma has time to cool by expansion.

LPP with sub-nsec pulses:

One can distinguish two-regimes of operation in the plasma formation w.r.t laser pulse duration. When the laser pulse is short so that during the heating process the plasma has very little time to move, then heat conduction is the mechanism of energy transfer till such time when the heated matter expands hydrodynamically. On the other hand, if the laser pulse duration is long, the expansion process occurs during the initial process itself and heat conduction is neglected. From considerations similar to eqn. V.7, the time instant (t_0) and the extent of the thermal wave (x_0) at which the thermal conduction ceases and gas-dynamic expansion takes over, can be evaluated.^{78,27}

Very high temperatures and densities are possible with sub-nsec pulses. Reflection of laser light from plasma becomes an important factor. The first observation of neutron emission from LPP used p-sec light pulses.⁵ Other experiments^{79,80} have also used p-sec pulses. The heat diffusion equation is solved⁸¹ and effect of heat conduction on mass and temperature of plasma also experimentally verified.⁷⁹ Systems for laser-fusion experiments use sub-nsec pulses to reach high temperatures before the plasma has time to cool by expansion.

V.4 Plasma Diagnostics

V.4.1 Probe measurement

Probe measurements are extensively used, especially in the early studies of LPP, to detect the emission of electrons and ions from such plasmas.⁷⁻⁹

In a typically simple set up⁹ a collector with a hole for the beam and at negative potential detects ions and from the time of flight to the collector the velocity of the ion is measured. For given kinetic energy of ions, a plot of the time of flight against mass number of target material gives a straight line indicating constant kinetic energy of ions. Energies up to 1000 eV are detected with 5-6 MW focussed to 10^{-3} cm^2 of target area.

Later works^{82,83} give evidence of a fast and slow ion peaks. A negative peak coinciding with laser pulse is attributed to photo-emission from collector by the uv emission from the plasma. Gregg and Thomas⁸⁴ have measured ion energies from the time of flight measurement when ions cross a slit at 40 cm behind which an IP28 photo-multiplier detects the ion emission. Average ion energies of 2000 eV were detected at laser intensity of 10^{11} W/cm^2 . Very early in the study of LPP - from solid targets, laser induced thermionic emission of electrons from various metal targets (W, Ta) as well as germanium etc. have been investigated.⁸⁵⁻⁸⁸

From retarded potential and time-of-flight studies, Dentröder and Jantz⁸ have obtained energy distribution of different ions. The large velocities of ions are attributed to acceleration by precursor electrons which leave the plasma early in its formation and form a space charge at the periphery.

Basov et al.^{14,15} have detected the presence of this negative space charge at the plasma boundary followed by the positive plasma in their probe measurement. The neutral boundary, clearly indicated in the probe signals is used for time of flight and velocity measurements.

V.4.2 Measurement of Electron Density and Temperature

The first measurement of electron density in LPP was by Ramsden and Savic⁶² who measured the absolute intensity of scattered laser radiation from an air spark. For scattering by electrons, the fraction scattered is given by⁸⁹

$$8 \times 10^{-26} n_e \ell \Omega$$

where n_e is electron-density in cm^{-3} and ℓ is the length of beam scattered in the direction of observer into a solid angle Ω . With $\ell = 0.01 \text{ cm}$ and $\Omega = 1/46$ they have obtained a density of $5 \times 10^{19} \text{ cm}^{-3}$ corresponding to a fraction 10^{-9} in air and $5 \times 10^{17} \text{ cm}^{-3}$ corresponding to a fraction 10^{-11} in Helium at a laser flux 10^{11} W/cm^2 . The Helium value agrees with that obtained from stark widths of HeI lines.

Interferometric methods : The density could be evaluated from fringe shifts obtained when the plasma is included in one arm of a Mach-Zender-type interferometer. A separate He-Ne laser could be used to illuminate the interferometer. The fringe shift δ in a disturbed region of thickness l is given by³⁴

$$\delta \lambda = (\mu_m - 1) \lambda - 4.46 \times 10^{-14} \lambda^2 n_e l \quad \text{V.8}$$

where the first term is contribution due to neutral atoms. This term is independent of wavelength. Interferometric measurements using two wave-lengths⁹⁰ enable the separation of the contribution of neutral atoms in eqn. V.8, from electronic and ionic fringeshifts. Due to lack of resolution because of large density gradients in the early stages of plasma and the minimum fringe shift measurable when density decreases due to plasma expansion, interferometric methods are applicable only over a limited time of plasma existence. Incorporating scanning and photographic techniques time resolution at different distances from target can be obtained. Basov et al.^{14,15} show three different versions of the Mach-Zender interferometer adopted for plasma studies. The same ruby laser radiation is used for interferometer illumination.

Holographic interferometry is also well suited for these short lived plasma studies. One such arrangement is shown by Witkowski⁹¹ in which part of the main laser is

deflected to the holographic set up. Such an arrangement possess inherent synchronization. Incorporating delay in the path of the deflected beam, holographic interferograms can be obtained at different instants. Integrating the fringe shift throughout the interferogram the total number of electrons in the ejected plasma can be found out ($\sim 4 \times 10^{16} \text{ cm}^{-3}$).

Schlieren photography is especially useful where sharp density gradients are present, such as in the shock fronts and hence is used to determine the width of compression shock in the shock wave.^{14,15}

Electron/ion currents can also be used to evaluate the plasma densities. Basov et al.⁹² obtain a current of 20 A corresponding to electrons with energies above 100 eV and obtain the electron density in the space-charge near the neutral boundary from:

$$\eta_e = \frac{i}{2\pi R^2 \langle v_e \rangle} ; \langle v_e \rangle = \left(\frac{2 \omega_e}{m_e} \right)^{1/2} \quad \text{V.9}$$

where R is plasma radius and ω_e is electron energy. They obtain η_e is $5 \times 10^{11} \text{ cm}^{-3}$ (for $R = 0.25 \text{ cm}$). Since $i_e = i_{\text{ion}}$ and $\langle v_i \rangle = \langle v_{\text{ion}} \rangle (m_e/m_i)^{1/2}$, one gets $n_i \sim n_e (m_i/m_e)^{1/2} = 6 \times 10^{13} \text{ cm}^{-3}$. The electron density varies from 10^{21} cm^{-3} at $R=0$ to $5 \times 10^{11} \text{ cm}^{-3}$ at $R = 0.25 \text{ cm}$ indicating presence of large field gradients.

Surface temperatures are estimated by use of Langmuir-Saha formula using current-density vs collector voltage plots.^{87,88}

The ion temperature can be estimated from lateral expansion velocity of the plasma. For air, in the range of $5 \times 10^5 - 10^6$ °K the ion temperature can be obtained from

$$T_i = 1.25 \times 10^{-2} (v_e)^{8/7} \text{ °K} \quad \text{V.10}$$

Korobkin et al.⁶⁸ have obtained a temperature of $T_i \sim 6 \times 10^5$ °K for an air-spark.

A majority of the techniques for plasma temperature measurement, including the widely used X-ray absorber technique, are based on spectroscopic methods. For this reason and also because we are restricting our LPP diagnosis to spectroscopic method, the next few sections of this chapter present, in brief, some aspects of plasma spectroscopy and spectroscopic methods of measuring plasma temperature and densities.

V.5 Plasma Spectroscopy

V.5.1 Introduction

Spectroscopy is a powerful tool for the diagnosis of plasmas. The spectroscopic technique possess the added advantage that the plasma conditions are not interfered with during measurement of plasma parameters. The theoretical foundations necessary for the evaluation of plasma parameters from experimentally obtained spectra or other relevant data, form a field in itself called 'plasma spectroscopy'. It has gained prominence initially through its use in Astrophysics for the recording and interpretation of Stellar spectra. Laboratory plasmas have been playing the dual role of simulating conditions existing in stellar sources for an understanding of processes occurring in astral bodies and also as sources of known characteristics for the verification of theoretical models and predictions for atomic processes. With the use of plasmas for controlled thermonuclear energy production these plasmas have become a source of study and diagnosis in themselves. The increasing need for a better understanding and greater utility of LPP have made stringent demands on the techniques of plasma diagnostics. With the inherent stigmatic imaging capabilities of spectrographs, and scanning techniques the spectroscopic technique is amenable to the time and space resolution needed for a proper study of laser produced plasmas. Access to vacuum ultraviolet and X-ray spectrum region makes

spectroscopic measurements the only suitable diagnostic tool of highly ionized, dense, hot plasmas.

The subject of plasma spectroscopy is presented in the standard work of Griem.⁹³ A review of plasma spectroscopy by Cooper presents the final results of Griem and similar other contributions to the field in a concise manner.⁹⁴ A few important works which are often encountered in regard to extensive calculations of rate coefficients etc. are those of Bates and Damgaard⁹⁵ for line-strength calculations by Coulomb-approximation method, Bates, Kingston and McWhirter⁹⁶ for detailed collision-radiative model calculations, McWhirter and Hearn⁹⁷ for calculations of instantaneous excited state population densities, Karzas and Latter⁹⁸ for Gaunt-factor calculations. Standard works on plasma diagnostics^{99,100} and plasma physics^{101,102} deal with various spectroscopic methods for plasma diagnostics and also list various atomic processes of importance in a plasma.

In the following sections, we briefly mention the different spectroscopic methods of measurement of plasma parameters with reference to the relevant theoretical background necessary for the particular method.

Plasma spectroscopy is essentially concerned with the study of electro-magnetic radiations emitted by ionized media. The rates and cross-sections of the different excitations and de-excitations, with or without emission of radiation are

calculated by both classical and quantum mechanical methods. The latter involves a solution of the Schroedinger equation for different systems and calculation of transition probability, matrix elements etc. Exact solution exists only for hydrogen which is the simplest system with a single electron. Even here the large number of discrete energy levels close to the ionization limit makes the calculations of such quantities as partition function, continuum-radiation etc. which involve accounting for all the levels, quite difficult and approximations are to be resorted to. Many electron systems are extremely complicated and are dealt with only in individual cases. The hydrogen calculations are extended with suitable corrections to hydrogenic ions such as He^+ , Li^{2+} etc. Various atomic parameters such as oscillator strengths, excitation cross-sections etc. are not available for all transitions nor are very reliable experimental values available for all. Because of the approximation and uncertainties involved, the evaluated quantities will of necessity be in considerable error. Nevertheless by selection of suitable methods and use of reasonably good values for the atomic parameters it has been possible to obtain plasma temperatures and densities with errors of 5-10% or better.

Whereas, in the conventional spectroscopy, one deals with atoms and ions at low density, in plasma we have to consider the atoms to be subjected to the effect of neighbouring charged particles through the long-range coulomb

interactions between electrons and ions. The effect of neighbouring charged particles, especially in dense plasmas, affects the radiation from such plasmas in many ways such as shifts and broadening of lines (via Stark effect), lowering of ionization energy of an atom in plasma, cause continuum (free-free) radiation, shielding effects are to be considered, due to which electron-ion interactions within a distance roughly equal to the Debye-radius only are to be considered. Owing to correlations between the electrons and ions, no electromagnetic radiation is propagated below the plasma frequency and in the immediate vicinity of this frequency the spectrum of continuous emission is considerably modified by the collective effects.¹⁰³ With a wide range of temperatures and densities as also inhomogeneous and transient nature of plasmas, thermodynamic equilibrium conditions are to be investigated. The foregoing indicates the complexities of situations dealt in plasma spectroscopy.

V.5.2 Local Thermodynamic Equilibrium (LTE)

The physical processes which occur in the reversible process of ionization from an (hydrogen-like) ionic species of charge $(Z-1)$ to the next ionic state with charge Z has several pair-wise reversible processes such as^{94,100}

- (1) Radiative transitions between discrete levels of ion $(Z-1)$,
- (2) photo-ionization and radiative-recombination,

(3) excitation and de-excitation between levels p and q by electron collisions and (4) ionization and three-body recombination by electron collisions.

In complete thermodynamic equilibrium with both kinetic (or collisional) and radiative equilibrium at the same temperature T , the pairs of inverse processes in (1)-(4) occur in detailed balance: The distribution among bound levels is governed by Maxwell-Boltzman statistics (eqn. V.12) and the distribution between ionization stages by the Saha equation (Eqn. V.14). It is useful to obtain the population density of any level in terms of the ground state population of same ion or of the next higher ionization stage.

If the mean free path for electron-electron collisions is far smaller than the extent of plasma and the time between collisions (collisional relaxation time) is short compared to other characteristic times in plasma, such as plasma heating and containment, then free electrons will have a Maxwellian velocity distribution characterized by a temperature T_e which can be called 'electron temperature'. The electron-electron relaxation time is¹⁰⁴

$$t_{ee} = \frac{0.266 T_e^{3/2}}{n_e \ln \Lambda} \quad \text{V.11}$$

where T_e is in $^{\circ}\text{K}$. n_e in cm^{-3} and $\ln \Lambda$ a constant usually of the order of 10. This is usually small compared to plasma heating and confinement times. Similarly if the mean free

path for absorption of radiation is less than the dimension of plasma, there will be radiation equilibrium and a corresponding radiation temperature.

Astrophysical plasmas are optically thick i.e. radiation from such plasmas of large dimension is reabsorbed in the plasma before reaching the earth's atmosphere. In the interior of such plasmas complete thermodynamic equilibrium is said to exist. In laboratory plasmas, however, though the electrons are still described by a Maxwellian distribution at temperature T_e , the plasmas are optically thin i.e. the plasma is transparent to its own radiation and the radiation field is no longer in equilibrium, the two radiative processes (1) and (2) are no longer balanced. In high density plasmas, collisional effects completely dominate radiative ones and the collisional processes (3) and (4) still hold. The equilibrium temperature is that of the species with dominating reaction rates i.e. that of electrons (T_e). Thermodynamic arguments, independent of a detailed knowledge of rate coefficients, can still be applied. Such an equilibrium with a diluted radiation field is called 'Local thermodynamic equilibrium' (LTE). The radiation from a plasma in LTE is no longer black-body radiation at temperature T_e .

The population densities among different energy levels are given by the Boltzmann formula. In particular the population densities $n(p)$ of level p of species S_z is given by

$$\frac{n_z(p)}{n_z} = \frac{g_z(p)}{U_z(T_e)} \exp \left[\frac{-E_z(p)}{kT_e} \right] \quad V.12$$

where $g_z(p)$ is the statistical weight and $E_z(p)$ the energy measured from its ground state of state p , $U_z(T_e)$ is the partition function of the species S_z given by

$$U_z(T_e) = \sum_p g_z(p) \exp \left[\frac{-E_z(p)}{kT_e} \right] \quad V.13$$

The densities of the successive ionic species n_{z-1} and n_z are related through the Saha equation

$$\frac{n_z n_e}{n_{z-1}} = 2 \left(\frac{2\pi m k T_e}{h^2} \right)^{3/2} \frac{U_z(T_e)}{U_{z-1}(T_e)} \exp \left[\frac{-E_{z-1}(\infty)}{kT_e} \right] \quad V.14$$

where n_e is the electron density, m mass of electron and $E_{z-1}(\infty)$ is the ionization potential of the species S_{z-1} .

For the validity of LTE the collisional rate process in any level dominate the radiative decay and recombination (since absorption is anyway absent). As collisional cross-sections increase and radiative decay rates decrease with higher quantum numbers, the radiative decay rates for the lower levels are high and validity of LTE for these levels may need a very dense plasma. Griem¹⁰⁵ has given the validity criterion for partial LTE in which a level p is in equilibrium with higher levels and the next higher ionization stage, if the electron density satisfies

$$n_e \geq 7 \times 10^{18} \frac{z^7}{p^{17/2}} \left(\frac{kT_e}{z^2 E_H} \right)^{1/2} \text{ cm}^{-3} \quad V.15$$

where E_H is the ionization potential of hydrogen. The validity criterion for complete LTE is obtained from the condition that the radiative population rate of ground state is small compared to collisional population rate, both of which are considered for the resonance transition $1 \rightarrow 2$. The criterion on electron density is¹⁰⁵

$$n_e \geq 9 \times 10^{17} z^7 \left(\frac{kT_e}{z^2 E_H} \right)^{1/2} \left(\frac{E_{z-1}(2)}{z^2 E_H} \right)^3 \text{ cm}^{-3} \quad \text{V.16}$$

$E_{z-1}(2)$ is the excitation energy of the upper level of the resonance transition. All the above derivations are for a hydrogen-like ions for which $z^2 E_H = E_{z-1}(\infty)$. Further the above conditions were derived for a homogeneous and time-independent plasma. Since eqn. V.16 is not very sensitive to oscillator strengths, this can also be used for other low z species.

Applying eqn. V.15 to hydrogen we get $n_e = 1.7 \times 10^{14} \text{ cm}^{-3}$ at $T = 1 \text{ eV}$ for $p=3$ and for ionized helium at $T=4 \text{ eV}$, $n_e = 2.2 \times 10^{16} \text{ cm}^{-3}$ and for doubly-ionized lithium at $T = 9 \text{ eV}$, $n_e = 3.6 \times 10^{17} \text{ cm}^{-3}$. The electron densities needed for complete LTE according to eqn. V.16 are quite high, for example, $n_e = 1.2 \times 10^{17}$ for hydrogen at $kT = 1 \text{ eV}$ and $n_e = 1.5 \times 10^{19}$ for ionized helium at $kT = 4 \text{ eV}$. If the resonance line is self-absorbed, the radiative population rate of ground state from first excited state is effectively decreased and the electron densities can be an order smaller for complete LTE.

For transient plasmas the validity of LTE needs a further condition that the equilibration time (inverse of collisional-excitation rate from ground or upper states for complete or partial LTE respectively) should be short compared to characteristic times of plasma. Griem¹⁰⁵ shows that complete LTE in transient plasma is often not indicated, whereas partial LTE deviations are not very serious.

Corona Equilibrium

When the electron densities are small, LTE is no longer achieved and an alternative equilibrium model is considered. The radiative decay rates predominate over collisional decay rates. This is the situation occurring in the solar corona¹⁰⁶ and hence the name 'Corona model'.

In the simple 'Corona Model' collisional excitation and ionization are balanced by radiative decay and radiative recombination respectively. In this model practically no collisional excitation or de-excitation of atoms in excited level occurs. The ionization-recombination balance gives

$$n_{x-1,1} n_e S_{z-1,1} = n_{z,1} n_e \alpha_{z,1} \quad V.17$$

where subscript 1 refers to ground state and $S_{z-1,1}$ and $\alpha_{z,1}$ are the ionization coefficient and radiative-recombination coefficient respectively. The ratio of the population of the two ionization stages are obtained from eqn. V.17 as

$$\frac{n_z}{n_{z-1}} = \frac{S_{z-1,1}}{\alpha_{z,1}} \quad \text{V.18}$$

An approximate expression for the above ratio is given by McWhirter⁹⁹ for hydrogenic ions

$$\frac{n_z}{n_{z-1}} = 1.3 \times 10^8 \left[\frac{kT_e}{X_{z-1}} \right]^{3/4} \frac{1}{X_{z-1}^2} \exp \left[-\frac{X_{z-1}}{kT_e} \right] \quad \text{V.19}$$

where X_{z-1} is the ionization potential of ions of charge $z-1$ (species S_{z-1}) in eV. The accuracy of this formula is estimated to be $\pm 50\%$.

Collisional-Radiative Model

This model is intermediate to LTE and Corona model and considers both radiative and collisional de-excitation. The final equilibrium relation is similar to eqn. V.18

$$n_z/n_{z-1} = S^{\text{CR}}/\alpha^{\text{CR}} \quad \text{V.20}$$

where S^{CR} and α^{CR} are the collisional-radiative ionization and recombination coefficients. Griem¹⁰⁷ obtains expressions for these by a simple model and extensive calculations through rate equations are done by Bates, Kingston and McWhirter.⁹⁶

In the absence of any such equilibrium, the detailed rate equations for each level are to be solved for individual systems. With improved data on rate coefficient available and by use of computers, such a solution is now possible. Many such attempts with references are listed by Cooper.⁹⁴

V.5.3 Radiations from Plasma

The radiation emitted from a plasma containing hydrogenic ions S_{Z-1} contain line radiation corresponding to transition between discrete levels of the ion S_{Z-1} . When sufficient ionization has occurred there is also the radiation emitted when a free electron combines with the ion S_Z to give the species S_{Z-1} in one of its bound states q and the balance of energy emitted as radiation. This is called 'Free-bound' or recombination radiation. Free electrons in the field of ions also radiate. This corresponds to transition between free states of electrons. This is called 'free-free' radiation or 'Bremsstrahlung'. Since one or both the levels of each transition corresponds to a free electron state, both free-bound and free-free radiation spectrum are continuous. This is the source of the 'continuum' spectrum of a plasma. In the case of a non-hydrogenic atom or ion with more than one electron, there exist several ionization stages, each contributing to the continuum, thus making the resulting spectrum quite complex. Formulae derived are for hydrogenic ions with the so-called 'Gaunt factors'⁹⁸ included to account for deviations from semi-classical cross-sections for hydrogen-like ions and deviation of hydrogen-like cross-section for high z atoms.

Line Radiation

The radiative transitions between bound levels q (lower)

and p (upper) are characterized by spontaneous emission coefficient A_{pq} and the induced emission coefficients $B(p,q)$ and $B(q,p)$ which are related by

$$g(p) B(p,q) = g(q) B(q,p) \quad V.21$$

$$\text{and } A(p,q) = \left(\frac{2h\nu^3}{c^2}\right) B(p,q) \quad V.22$$

where $h\nu = E(p) - E(q)$. At equilibrium the population densities of the levels are related through the Boltzmann distribution:

$$\frac{n(p)}{n(q)} = \frac{g(p)}{g(q)} \exp\left(-\frac{h\nu}{kT}\right) \quad V.23$$

The total rate of emission of energy between states $|p\rangle$ and $|q\rangle$, in the electric dipole approximation is obtained by Quantum mechanics as

$$4/3 \frac{(2\pi\nu)^4}{c^3} |\langle p | ex | q \rangle|^2 \quad V.24$$

The absorption cross-section $\sigma_{qp}(\nu)$ (the probability per unit time of an absorption of photon taking place with an incident photon crossing per unit area per unit time per unit frequency range) is

$$\sigma_{qp}(\nu) = \frac{8\pi^3}{3hc} |\langle p | ex | q \rangle|^2 \quad V.25$$

The spontaneous emission coefficient is given by

$$g(p) A(p,q) = \frac{64\pi^4 \nu^3}{3hc^3} \sum_{p,q} |\langle p | ex | q \rangle|^2 \quad V.26$$

where $\sum_{p,q}$ is over all sub-levels of upper and lower levels.

The spontaneous transition probability is often written in terms of the absorption oscillator strength f_{qp}

$$g(q) f_{qp} = q(p) A(p,q) \frac{mc^3}{8\pi^2 e^2 \nu^2} \quad V.27$$

The power radiated per unit volume per unit solid angle per unit frequency interval is

$$\varepsilon(\nu) = \frac{h\nu}{4\pi} A(p,q) n(p) \phi(\nu) \quad V.28$$

where $\phi(\nu)$ is the line-profile which is normalized such that

$\int \phi(\nu) d\nu = 1$. The total power radiated in line per unit solid angle is

$$\varepsilon_L = \frac{h\nu}{4\pi} A(p,q) n(p) \quad V.29$$

In the optically thin plasma of thickness D , the total emitted intensity is

$$I_L = \int I_\nu d\nu = \frac{h\nu}{4\pi} A(p,q) n(p) D \quad V.30$$

Using eqn. V.12 the population density $n(p)$ of level p can be expressed in terms of the population density of ground level and hence in terms of the total number of particles in the stage Z . Eqn. V.30 becomes

$$I_L = \frac{h\nu}{4\pi} A(p,q) g_Z(p) \frac{n_Z}{U_Z(T_e)} \exp \left[-\frac{E_Z(p)}{kT_e} \right] D \quad V.31$$

Continuum Radiation¹⁰⁸ : Free-bound radiation

The total photo-ionization cross-section per unit frequency range is obtained from eqn. V.25 where the upper state of the transitions are free states

$$\sigma_{qv}(\nu) = \frac{8\pi^3 \nu}{3hc g_{z-1}(q)} \sum_{p'q'} | \langle p' | ex | q' \rangle |^2 \quad V.32$$

The calculations of these cross-sections from solutions of Schroedinger equation are given by different authors through different approximations.¹⁰⁹

The semi-classical photo-ionization cross-section of hydrogen-like systems is given by,¹¹⁰

$$\sigma_{qv}^{cl}(\nu) = \frac{64\pi^4 m e^{10}}{3\sqrt{34} ch^6} \frac{z^4}{\nu^3 q^5} \quad V.33$$

The cross-section from eqn. V.32 differs from this only slightly. The exact cross-section is obtained by multiplying eqn. V.33 by a Gaunt factor g_{fb} .

The total power radiated in frequency interval $d\nu$ for recombination to level q is

$$P_q^R(\nu) d\nu = h\nu n_e n_z f(\nu) \nu \sigma_{vq} d \quad V.34$$

where σ_{vq} is the recombination coefficient to level q and is related to the photo-ionization cross-section σ_{qv} , through the detailed balancing by the relation¹¹⁰

$$\sigma_{\nu q} = \frac{v_h^2}{m^2 c^2 v^2} \frac{q_z(1)}{g_{z-1}(q)} \quad \text{V.35}$$

$f(v)$ is the Maxwellian velocity distribution of electrons at temperature T_e .

$$f(v) dv = 4\pi \left(\frac{m}{2\pi kT_e} \right)^{3/2} \exp \left(-\frac{1}{2} \frac{mv^2}{kT_e} \right) v^2 dv \quad \text{V.36}$$

The relationship between the frequency of emission to level q and velocity is given by

$$h\nu = \frac{1}{2} mv^2 + E_{z-1}(\infty) - E_{z-1}(q) \quad \text{V.37}$$

The complete spectral distribution of free-bound emission is obtained by summing over all bound levels of ion $(z-1)$. At any frequency ν , the lowest q contributing to the summation is given by

$$h\nu = \frac{1}{2} mv^2 + \frac{Z^2 E_H}{q^2} \geq \frac{Z^2 E_H}{q^2}$$

$$\text{nence } q_{\min} > \left(\frac{Z^2 E_H}{h\nu} \right)^{1/2} \quad \text{V.38}$$

where E_H is the ionization potential of hydrogen and $Z^2 E_H / q^2$ is the binding energy of the level q of the hydrogenic ion. From eqn. V.33 to V.38 we get

$$P^R(\nu) dv = \frac{n_e n_z g_{fb} K Z^4}{(kT_e)^{3/2}} \exp \left(-\frac{h\nu}{kT_e} \right) \times \sum_{q \geq \left(\frac{Z^2 E_H}{h\nu} \right)^{1/2}}^{\infty} \exp \left(\frac{Z^2 E_H}{q^2 kT_e} \right) \frac{dv}{q^3} \quad \text{V.39}$$

where $K = \frac{64\pi^{1/2} e^4 h}{3^{3/2} m^2 c^3} (E_H)^{3/2}$

At large values of q , the levels merge into a continuum beyond $q = q^*$. q^* corresponds to the so-called Inglis-Teller limit obtained from the advance of the series limit due to large line-width of lines close to the series limit (see Ch. V.5.4b). If ΔE_{z-1} is the advance of the series limit, then

$$q^* \sim \left(\frac{Z^2 E_H}{\Delta E_{z-1}} \right)^{1/2} \quad \text{V.40}$$

for $q > q^*$

$$\sum_{q=q^*+1}^{\infty} \frac{1}{q^3} \exp \left(-\frac{Z^2 E_H}{q^2 k T_e} \right) \rightarrow -\frac{1}{2} \int_{q^*+1}^{\infty} \exp \left(-\frac{Z^2 E_H}{q^2 k T_e} \right) d\left(\frac{1}{q^2}\right) \quad \text{V.41}$$

Equation V.39 with only eqn. V.41 replacing the summation gives the recombination into the merged levels.

Free-free Radiation

The free-free radiation power emitted by the ion can be obtained from eqn. V.39 and V.41 by suitably extending the limits of integration to include all free-free transitions. This corresponds to negative binding energy (for electrons) i.e. the limits are from ∞ to -0 on q or 0 to $-\infty$ on $1/q^2$. Hence the Bremsstrahlung power into frequency interval $d\nu$ at ν is given by

$$P^B(\nu) d\nu = n_e n_Z g_{ff} \frac{Z^2 K}{2E_H} (kT_e)^{-1/2} \exp\left(-\frac{h\nu}{kT_e}\right) d\nu \quad V.42$$

where g_{ff} is the free-free Gaunt factor. At high frequencies the Bremsstrahlung power drops steeply as $\exp(-h\nu/kT)$ and at longer wavelengths it varies as $1/\lambda^2$. The Bremsstrahlung power as a function of wavelength is maximum at a frequency given by

$$h\nu = 2kT_e \quad \text{i.e. at } \lambda = \frac{6.2}{kT_e(\text{keV})} (\text{\AA})$$

Since Bremsstrahlung and recombination radiation always exist together, the recombination into the merged levels is included into the Bremsstrahlung integral and the total power radiated per volume by both free-free and free-bound transitions in a plasma of fully-stripped ions of charge Z is given by

$$\begin{aligned} P^{B+R}(\nu) d\nu = & \frac{32\pi^{1/2} e^4 h Z}{3^{3/2} m^2 c^3} \left\{ g_{ff} \exp\left[\frac{Z^2 E_H}{kT_e (q^*+1)^2}\right] \right. \\ & + \frac{2Z^2 E_H}{kT_e} \sum_{q_{\min}}^{q^*} \frac{g_{fb}}{q^3} \exp\left[\frac{Z^2 E_H}{q^2 kT_e}\right] \left. \right\} \\ & \times n_e n_Z \left(\frac{Z^2 E_H}{kT_e}\right)^{1/2} \exp\left(-\frac{h\nu}{kT_e}\right) d\nu \quad V.43 \end{aligned}$$

At low-frequencies ($q > q^*$), $P^{B+R}(\nu)$ has a flat-response between 0 and ν^* . At high frequencies it falls off as $\exp(-h\nu/kT_e)$. In between these frequency limits, it has a step-like structure with discontinuities corresponding to series limits ($1 \leq q \leq q^*$).

V.5.4 Plasma Effects

a. Lowering of ionization potential

Though plasma is implicitly assumed to be neutral, still charges of one sign tend to have, on an average, an excess of charges of opposite sign in their neighbourhood. This is due to the coulomb interaction whose ordering effect is not completely countered by thermal agitation. Because of this polarization an atom needs less energy for ionization in plasma than when it is isolated. This is due to the effect of surrounding field. This decrease of ionization potential depends on charge of the ion, plasma density and temperature. Different expressions are obtained for $\Delta E_{Z-1}(\infty)$ by different workers. Experimental verification has not been possible because of the inaccuracies inherent in spectroscopic methods to be able to observe such small effects. The various formulae for $\Delta E_{Z-1}(\infty)$ are:

1. Griem,¹¹¹ Ecker and Kroll¹¹²

$$\Delta E_{Z-1}(\infty) = \frac{Ze^2}{\rho_D} \quad \text{V.44}$$

where ρ_D is the Debye-radius, given by

$$\rho_D = \frac{1}{e} \left[\frac{kT}{n_e + \sum_Z Z^2 n_Z} \right]^{1/2} \quad \text{V.45}$$

This is valid for densities where Debye theory^{is} still valid i.e. $n_e + \sum n_Z \geq (8\pi\rho_D^3)^{-1}$. This criterion is valid in most laboratory plasmas.

This cannot be experimentally measured because it is overshadowed by a larger shift due to another effect.

The lines near the series limit are hydrogenic as they correspond to levels of large principal quantum number. The stark broadening of levels increases with the principal quantum number. As the lines come more and more closer nearer the series limit, when the line width due to stark effect equals line separation, the lines of the series merge together to give the impression of a continuum and an effective shift of series limit to higher wave-lengths. Inglis and Teller have first investigated the line merging.¹¹⁶ This condition gives:

$$\frac{3}{2} \frac{a_0 q_m^2 e F}{z} = \frac{e^2 z^2}{2 a_0 q_m^3} \quad \text{V.48}$$

a_0 is the Bohr-radius and F the normal field strength for which Inglis-Teller inverts $F = 3.7 e n_{ch}^{2/3}$. On substituting in eqn. V.48, one gets the well known Inglis-Teller relation between charged particle density n_{ch} and the maximum principal quantum number q_m for the highest observable series member.

$$\log n_{ch} = 23.26 - 7.5 \log q_m \quad \text{V.49}$$

In the plasma $n_{ch} = (n_e + n_i)$ if T_e obeys the inequality,

$$T_e < \frac{3\pi^3 e^2}{64 a_0 k q_m} = \frac{4.6 \times 10^5}{q_m} \text{ } ^\circ K \quad \text{V.50}$$

Otherwise $n_{ch} = n_i$.

Vidal has improved the above approximation by giving the shift due to line merging as

$$\Delta \nu_m = -Z^2 E_H / q_m^2 \quad V.51$$

for $Z=1$ and considering eqn. V.49, an approximation for $\Delta \nu_m$ is given by

$$\Delta \nu_m \sim -2 \times 10^9 n_{ch}^{4/15} (\text{sec}^{-1}) \quad V.52$$

The shift $\Delta \nu_m > \Delta \nu_g$ and we have

$$\frac{\Delta \nu_g}{\Delta \nu_m} \sim 2.5 \times 10^{-3} n_{ch}^{7/30} T_e^{-1/2} \quad V.53$$

V.5.5 Line broadening

The theory of line broadening has been pursued in plasma spectroscopy due to the fact that line profiles of radiation from a plasma will reflect the conditions in the plasma in the neighbourhood of the emitting atom or ion. The line radiation will act as a non-interfering probe for the diagnostics of the plasma.

Also the radiation-transfer equations in the case of an optically-thick plasma need a detailed knowledge of actual absorption and emission line profiles.

The fast moving electrons will cause broadening through collisions. The pressure broadening was first discussed by

Lorentz for an oscillator which is submitted to sudden changes due to inelastic collisions with disturbing particles. The linewidth will then be proportional to the frequency of collisions and hence to the density^{of} disturbing particles. In plasmas this will be the electron density. When the broadening is determined by Doppler broadening, the width is determined by the temperature of ions emitting the line. The field due to neighbouring ions will produce a stark shift of the levels. In plasma of moderate temperatures and high density, Doppler broadening is negligible and the stark and collisional effects are together referred to as pressure broadening. The perturbing effects on the radiator are more for charged particles such as electrons and ions.

The broadening due to charged particles can be classified into two extreme approximations:

Impact approximation :

One can consider the radiating atom to be perturbed due to collisions from charged particles lasting for time periods defined by $\tau_c \sim \rho / \bar{v}$ where ρ is the impact parameter and \bar{v} the mean velocity of the perturber. The time τ_c of collision is taken to be small compared to the time between collisions, i.e. broadening is due to impacts which are well separated in time. The collisions are supposed to be weak and not disturb the state of the emitting particle, i.e. strong

collisions causing excitations and de-excitations are assumed to occur very rarely and only weak collisions are considered and hence can be treated by perturbation methods. This impact theory is discussed by Lindholm¹¹⁷ using a quasi-classical_{model}. Broadening due to electrons in plasma are usually treated by this impact theory. For long range coulomb interactions, collision can never be separated in time, however, it can be considered so if average interaction is weak.

Quasi-static approximation :

The relatively heavy positive ions are taken to be moving slowly and the ions perturbation on the emitter is considered constant over the duration of interest (of the order of the inverse of linewidth) and hence ions can be considered stationary. Their effect on the field is evaluated and averaged over the statistical distribution of ions. This is the treatment given by Hotsmark.¹¹⁸

The pressure broadening (both impact and quasi-static approximations) calculations are done in the 'classical-path' approximation in which both the perturbing electrons and ions are considered to be classical particles moving along fixed trajectories that are independent of the state of the emitting system. When the emitters are neutral atoms the trajectory is a straight line and when it is an ion, a hyperbola. This approximation neglects any back reaction on the perturbers

which can cause a change in their trajectory. This means that any exchange of energy due to inelastic collisions must be considerably less than the energy of the perturber ($\sim kT_e$). This is almost always the case for lines in the optical range. For the validity of classical path approximation, the extent of the wave-packet, which represents the electron, should be negligible, i.e. the de-Broglie wavelength of perturbing electron is considerably smaller than the impact parameter contributing significantly to broadening i.e. $\hbar/m\bar{v} \ll \rho_{\min}$.

The condition of validity of the impact approximation is that $\tau_c \ll w$ (half-width in angular frequency) which is equivalent to the earlier requirement for the duration of collision to be short compared to the average interval between collisions.

The modern treatment of pressure broadening are well presented by Baranger¹¹⁹ and Griem⁹³ who have contributed significantly for the development of this theory. The classical path approximation is still valid. Impact approximation is carried out quantum mechanically. The stark split levels due to the static-ionic field are considered and the broadening evaluated in the impact approximation, resulting in a dispersion or Lorentz profile with line-width (w) and shift (d) due to electron impacts. This line profile is averaged over the statistical distribution of the ions by using a field strength distribution function $W(F)$. $W(F)$ may be calculated initially by

neglecting interactions between ions. At high densities the ion-ion interaction has to be considered. The field-strength distribution function are given by Mozer and Baranger.¹²⁰ These interactions are limited to distances within the Debye-radius ρ_D because of the shielding effects.

The frequency shift of a line due to a perturber at a distance r is given by

$$\Delta\omega = C_\mu / r^\mu \quad \text{V.54}$$

where C_μ is a constant, $\mu = 2$ for linear stark effect and $\mu=4$ for quadratic stark effects.

Griem and co-workers have carried out detailed calculations of line-profile for different hydrogen lines and also singly-ionized helium lines. For hydrogenic lines, the levels are overlapping i.e. degenerate in orbital quantum number and hence a linear stark effect results. For isolated lines such as strong lines of neutral helium, different ℓ are well separated, it is found that quadratic stark effect is operative.

The initial calculations of Griem on hydrogen and neutral helium lines have been experimentally verified by various workers. These have been listed by Cooper in his review.⁹⁴ Because of the condition $\Delta\omega \tau_c \ll 1$ impact approximation is particularly valid near the line centre. Quasi-static approximation is to be used for the line-wings.

The electron-impact theory gives a Lorentzian line profile with a shift d and w about an unshifted centre frequency ω_0 . The line profile is given by

$$I(\omega) \sim \frac{1}{\pi w} \frac{1}{1 + [(\omega - \omega_0 - d)/w]^2} \quad \text{V.55}$$

The final profiles are given in terms of the following parameters:

(i) The reduced frequency

$$x = (\omega - \omega_0 - d)/w \quad \text{V.56}$$

(ii) The quasi-static ion broadening parameter

$$\alpha = \frac{4\pi n_e}{3} \left[\frac{2\pi C_4}{w} \right]^{3/4} \quad \text{V.57}$$

where n_e is the electron-density and C_4 is the constant C_μ of eqn. V.54 with $\mu=4$ corresponding to quadratic stark effect operative in isolated lines.

(iii) The ion-ion correlation and Debye-shielding by electrons accounted for in the ion field-strength distribution function expressed by the parameter

$$R = \frac{\rho_m}{\rho_D} = \frac{\text{mean distance between ions}}{\text{Debye radius}}$$

$$R = \left(\frac{3}{4\pi n_e} \right)^{1/3} \frac{1}{\rho_D} \quad \text{V.58}$$

$$(iv) \quad \sigma = \frac{w}{v} \left(\frac{3}{4\pi n_e} \right)^{1/3}$$

$$= 8 \times 10^{-2} w \lambda^{-2} \left(\frac{T_e}{M} \right)^{-1/2} n_e^{2/3} \quad \text{V.59}$$

where \bar{v} is perturber thermal velocity, M the molecular weight of the perturbers.

The quasi-static character of ions prevails for $\sigma \gg 1$. In the limit, $\sigma \rightarrow \infty$ for a static ion fields the final line profile is given as

$$j_R(x, \alpha) = \frac{1}{\pi} \int_0^{\infty} \frac{W(\beta, R) d\beta}{1 + (x - \alpha^{4/3} \beta^2)^2} \quad \text{V.60}$$

where $\beta = F/F_0$, F is the field at the emitter due to an ion at a distance r ($F = Ze/r^2$), $W(\beta, R)$ is the normalized field distribution corresponding to a shielding parameter R , F_0 the value of F corresponding to $r = \rho_m$.

The final expressions for the half-half width and shift of the line are given by

$$w_{\text{total}} = [1 + 1.75\alpha (1 - 0.75R)]w \quad \text{V.61}$$

$$d_{\text{total}} = [d/w \mp 2.0\alpha (1 - 0.75R)]w \quad \text{V.62}$$

In eqn. V.62, the + or - sign is taken according to whether the quasi-static effects shifts the line to the red or blue, respectively (i.e. depends on the sign of C_4). Eqn. V.61 and V.62 are for neutral emitters. For singly-ionized emitters, the term $0.75R$ should be replaced by about $1.2R$. These equations are reasonably accurate for $\alpha \leq 0.5$ and $R \leq 0.8$. For higher values of α the complete profiles $j_R(x, \alpha)$ are tabulated by Griem.¹²¹ He has also given Tables listing the

values of w , d/w , α at different temperatures for a value of $n_e = 10^{16} \text{ cm}^{-3}$ for neutral and singly-ionized lines of various elements. w is linearly dependent on n_e and α depends on $n_e^{1/4}$, d/w is independent of n_e and so the values of w and α corresponding to $n_e = 10^{16} \text{ cm}^{-3}$ tabulated by Griem can be converted to any other value of n_e by multiplying w by $(n_e/10^{16})$ and α by $(n_e/10^{16})^{1/4}$.

For multiply-ionized emitters correction factors which are some fractional powers of Z are to be used. The corrections to the complete profile are usually smaller.⁹³ Since the theory depends only on the velocity distribution of free electrons being Maxwellian and not on velocities of ions or their population densities, L.T.E is not a necessary requirement for the validity of the line broadening theory.

V.6 Spectroscopic Methods of Measuring Plasma Parameters

Having presented the basic theoretical material with relevant formulae, we can enumerate the various methods adopted for the measurement of plasma parameters such as electron/ion temperatures, densities etc. References are made where available to some existing experimental results on laser produced plasma studies. Standard books on plasma diagnostics,^{99,100} list a variety of measurement methods. Griem⁹³ presents the conditions under which different methods are especially applicable. An article by Robinson and Denn lists some spectroscopic diagnostic methods.¹²¹

V.6.1 Temperature Measurement

V.6.1.1 Line intensity ratio

The intensity ratio of two lines 1 and 2 of the same ionization species is given by (use eqn. V.31)

$$\frac{I_1}{I_2} = \frac{g_1 A_1 \nu_1}{g_2 A_2 \nu_2} \exp \left[- \frac{(E_1 - E_2)}{kT} \right] \quad \text{V.63}$$

where g, E are the statistical weight and excitation energies of the upper level of the line, A is the spontaneous transition probability and ν the frequency of the line. Instead of the spontaneous transition probability, the absorption line-strength f can be used for the line thus

$$\frac{I_1}{I_2} = \frac{g_1 f_1 \lambda_2^3}{g_2 f_2 \lambda_1^3} \exp \left[- \frac{(E_1 - E_2)}{kT} \right] \quad \text{V.63A}$$

By measuring the line intensity ratio and using values of g_1, A_1, E from standard tables¹²² for the lines, excitation temperature T can be obtained.

It is necessary that LTE should exist down to the lower of the two levels E_1 and E_2 . Otherwise it will be difficult to eliminate the population density of the two levels as is done in eqn. V.31 from eqn. V.30. Griem⁹³ gives alternative methods in which either or both levels do not satisfy condition for LTE (eqn. V.15). The error in the calculated temperature due to errors in measured intensity

ratio is given by

$$\frac{\Delta T}{T} = \frac{kT}{E_1 - E_2} \frac{\Delta(I_1/I_2)}{I_1/I_2} \quad \text{V.64}$$

The oscillator strengths are not always known to good accuracy, with possible uncertainties of factor of 2-3. Intensity ratios are measurable to better than 10% accuracy. These errors will reflect in a smaller error in evaluated temperature, if the excitation energies of (eqn. V.54) the two lines differ considerably (eqn. V.64). For hydrogen, the maximum value of $E_1 - E_2$ is 1 eV for $\lambda > 2000 \text{ \AA}$. Uncertainty of 10% in line intensities would lead to an uncertainty in temperature of 40% at 2000 \AA .

It is possible to increase the difference in excitation energies by choosing lines from successive ionization of the same species. Using eqn. V.31 and the Saha equation V.14 we have

$$\frac{I'}{I} = 2 \frac{A' g' \lambda}{A g \lambda'} \left(\frac{2\pi m k T}{h^3} \right)^{3/2} \frac{T^{3/2}}{n_e} \exp \left[\frac{-(E' - E + E_\infty - \Delta E_\infty)}{kT} \right] \quad \text{V.65}$$

where the prime indicates the higher ionization species. E_∞ is the ionization energy of the lower stage and ΔE_∞ is the reduction in the ionization energy referred to in Chapter VI.2.3a.

This method is better than the earlier one using lines of same ionization species, but it needs the knowledge

of electron density for a determination of temperature, If electron density is available (say by linewidth method - see Chapter VI.6.2.2). Further eqn. V.65 is valid if LTE is valid for the higher ionization stage. More than $n_e = 10^{18} \text{ cm}^{-3}$ is needed in the case of neutral and singly ionized helium for an accuracy about 10% in line-intensity ratio from given temperature. Even at 75000°K where neutral helium lines are still visible, at electron densities of 10^{18} cm^{-3} , 20% error in intensity ratio and electron density would cause only 2% error in the temperature. At lower densities the error is more due to uncertainty of LTE.

When several lines of the same species are available, it easily follows from eqn. V.31, that a plot of $\log \frac{I\lambda}{gA}$ against E for each line will give a straight line whose slope will yield the temperature. If E is in cm^{-1} the slope will be $-0.625/T$ and if E is in eV the slope will be $-5040/T$, T being in $^\circ\text{K}$. Only relative line intensities are to be measured. This plot is referred to as 'Boltzmann plot'. It is generally found¹²³ that higher temperatures are obtained for Boltzmann plots using lines from higher ionization stages.

When densities are not high enough for complete LTE to be satisfied, if partial LTE holds upper level densities can be expressed in terms of the densities of the ground state of next higher ionization stage $n_z(1)$ and electron density n_e through the Saha equation in the form

$$\frac{n_e n_z(1)}{n_{z-1}(p)} = 2 \left(\frac{2\pi m k T}{h^2} \right)^{3/2} \frac{g_z(1)}{g_{z-1}(p)} \exp \left(\frac{-E'_p}{kT} \right) \quad \text{V.66}$$

where E'_p is the binding energy of the upper level p
 $[E'_p = E_{z-1}(\infty) - E_{z-1}(p)]$. The densities of the successive ionization stages n_z/n_{z-1} is expressed using the Coronal equilibrium relation eqns. V.18 and V.19. Griem¹²⁴ gives several examples of a judicious use of both LTE and Coronal equilibrium relations to obtain line intensity ratio from successive stages.

V.6.1.2 Line to continuum intensity ratio

The relative intensity ratio of a line to that of the underlying continuum in a bandwidth $\Delta\lambda$ centered around the line centre can be used for temperature determination. It has the advantage that it is independent of electron density, but it is useful only for pure gases and especially well suited for hydrogen and helium for which the continuum formula are more accurately known.

Expressing the upper state density $n_{z-1}(p)$ in eqn. V.30 in terms of $n_z(1)$ (for a hydrogenic system $n_z(1) = n_z$), using Saha equation V.66 and using eqn. V.43 for the total continuum power radiated we get,¹²⁵ using $\Delta\lambda = \lambda^2 \Delta\nu / c$ for $Z=1$:

$$\frac{I_1}{I(\Delta\lambda)} = \frac{3^{3/2} \pi^3 \left(\frac{h^3 c}{8 \pi^3 m_e^4} \right)^2 f_{qp} g_{z-1}(q) \exp \left[\frac{E_{z-1}(\infty) - E_{z-1}(q)}{kT_e} \right]}{2 \lambda \Delta \lambda g_z(1) \left[\frac{g_{ff}}{2} \left(\frac{kT_e}{E_H} \right) \exp \left[-\frac{E_H}{(q^*+1)^2 kT_e} \right] + \sum_q^q \left(\frac{g_{fb}}{q} \right) \exp \left(-\frac{E_H}{q^2 kT_e} \right) \right]}$$

V.67

$\Delta E_{z-1}(\infty)$ cancels out. For each line suitable values of q and q^* are to be substituted in the summation in the continuum expression. For most HeI lines and Balmer lines of hydrogen $q=3$ and $q^*=6$. The temperatures with better than 10% accuracy can be obtained for 10-20% errors in intensity ratio. In hydrogen this is valid up to 100,000°K.

In HeI the range of application (with above accuracy) is applicable in the range 15,000 to 30,000°K, in which the continuum is mostly due to HeII. Above this temperature HeII/HeI line-intensity ratio method is preferable, since the continuum is no longer that of HeII only but also HeIII. When most of the helium atoms are completely ionized in which case the continuum is solely due to doubly ionized helium atoms, line to continuum ratio for HeII (4686 or 3209 Å) and continuum underlying these lines can be used for temperature determination. Eqn. V.67 is applicable to the relevant lines, with $Z=2$ and E_H replaced by $4E_H$. $q=5$ and 4 for the continuum around the above two HeII lines respectively. The minimum value of density required is determined by the validity of LTE used for either of the line in question (10^{16} and 10^{15} cm^{-3} respectively) and temperatures in the range 75000 to 500,000°K can be measured to good accuracy.

Measurement of continuum under the line is important. The total line intensity should be obtained after subtracting continuum contribution, especially when a monochromator and photometric measurements are used. Account should be taken of line intensity in the wings that is cut by the slit.

A typical example of these methods in LPP measurements is that of Brearman et al. on a laser spark in helium,¹²⁶, with temperatures at different stages of the spark from 50 to 3 eV measured by the above line to continuum and line ratios. For multi-electronic system line to continuum intensity ratio necessitates the isolation of continuum due to different ions at the line frequency. Further the use of Gaunt factors and other constants makes the continuum formula approximate.

V.6.1.3 Relative continuum intensity ratio

For photon energies such that $h\nu \gg kT$, the continuum falls off according to $\exp(-h\nu/kT)$ and in principle the slope of the continuum vs frequency on a log-log scale will yield the temperature. This method can also be applied in between the series limits. Presence of impurities and line radiation may render the measurement subject to considerable errors and difficulties. The method will yield more accurate temperatures at shorter wave lengths, where photon energy differences considerably exceed thermal energy.

The X-ray absorber technique generally employed^{25,127} is essentially a continuum intensity ratio method in which the wavelength dependence of continuum falling on the detector is obtained by means of different thickness of absorbing foils.

At a series limit the ratio of continuum intensity on either side of the series limit is found to be a steep function of temperature. To avoid confusion because of smooth transition of line to continuum near the series limit, frequencies can be chosen well removed on either side from series limit, provided the wave-length dependence is accounted. For example, for the Balmer limit in hydrogen at 3646 Å the continuum ratio $\lambda(3000)/\lambda(4500)$ can be considered.¹²¹

In the IR region the continuum is mainly Bremsstrahlung and the free-free emission coefficient is represented by the expression¹²⁸

$$\epsilon_{sp}(\nu) = \frac{C \tau^2 G n_e n_i}{(kT_e)^{1/2}} \exp(-h\nu/kT_e) \quad V.68$$

where $C = 6.36 \times 10^{-47}$ cgs units, τ denotes effective charge number of the ions, G is the Gaunt factor. Continuum slope measurements yield T_e .

The optical thickness of the free-free continuum in the IR region increases with increasing wave length and the emission is essentially Black-body emission. The Bremsstrahlung intensity approaches the Planck's function as wavelength

increases. By absolute intensity measurement of the optically thick portion in the IR and equating it to Planck's function one can evaluate T_e .¹²⁸ Some typical measurements in the IR are done by Harding et al.¹²⁹ and Kimmith et al.¹³⁰ This method has the advantage that it does not need the knowledge of any atomic parameters.

However there is an abrupt decrease of intensity at the plasma frequency ν_p , and only if the continuum is optically thick above this frequency, the above method is applicable. This depends on electron density. At low densities the free-free continuum approaches the Planck function at frequencies lower than ν_p .

One can list a few more methods of temperature measurements such as Line Reversal Method,¹³¹ measuring absolute intensity at the centre of strong lines where emission is essentially Black body radiation, From appearance times of different ionization lines through a detailed selection of rate equation,¹³² measurement of line-width when doppler broadening predominates,¹³³

V.6.2 Density Measurements

V.6.2.1 Absolute intensity measurements

Electron densities are mostly obtained through absolute intensity measurement which needs calibration

through the use of standard radiation sources such as tungsten ribbon lamp etc.

Absolute line intensity measurement will yield directly the population density of the upper level of the transition, as seen from eqn. V.29. Through the use of suitable equilibrium relations this can be related to the ground state density (hence total density) of the same or next ionization species and further, use of charge neutrality principle, the electron density can be obtained. A knowledge of electron temperature will be needed in the LTE relations.

Absolute continuum intensities also yields electron densities, especially the measurement of the free-free radiation in the IR and microwave region, depending on the density values. Eqn. V.68 can be used along with the value of T_e obtained by measuring the optically thick portion of the free-free radiation.

The sudden decrease of intensity at the plasma frequency, could be used to find ν_p and hence n_e from the relation

$$\nu_p = (e^2 n_e / \pi m_e)^{1/2} \quad \text{V.69}$$

V.6.2.2 From stark widths of lines

The broadening by stark effect is determined by the number of the perturbers at the site of the emitting atom or ion.

In hydrogen and hydrogenic ions in which linear stark effect is applicable, the quasi-static broadening predominates and the linewidth is proportional to $n_e^{2/3}$. If $\Delta\lambda_s$ is the total width of the line, n_e can be obtained from,

$$n_e = C(n_e, T_e) \Delta\lambda_s^{3/2} \quad \text{V.70}$$

$C(n_e, T_e)$ is a constant, weakly dependent on n_e . The above is fairly accurate for hydrogenic system and best for H_β for which error is less than 5%. The constant $C(n_e, T_e)$ is tabulated by Griem⁹³ for hydrogenic lines. The temperature dependence is very slight.

For isolated lines in which quadratic stark effect is operative, the impact broadening predominates and the linewidth is proportional to n_e . The line-width is given by eqn. V.51, and can be used for determination of n_e using the tables of Griem on the impact width w , quasi-static broadening parameter α and shielding parameter R . As the line-broadening theory does not involve population densities of level, the validity of LTE is not required.

The stark broadening dominates at low temperatures and can be distinguished from doppler broadening by its Lorentzian profile. Doppler broadening dominates at high temperatures and for highly ionized atoms. The profile is gaussian. Burgess et al.²² have obtained electron density from the widths of OVI and KIX lines in a LPP.

When the line-width is determined by Doppler width (for highly ionized, high temperature plasma), ion temperature (T_i) can be directly obtained from line-widths.

V.6.2.3 Advance of series limit

The advance of the series limit, which is a consequence of stark broadening, can be used for determining n_e . It is necessary to find out the principal quantum number q_m of the last member of the series before they merge with the series. If the ratio of line intensities to the background between lines is measured and plotted with the principal quantum number, the line merging is given by the plot crossing the axis. Eqn. V.49 can be used to obtain n_e . Though the method is based only on an estimation, it gives fairly reliable results, the discontinuity or the series limit may be difficult to find. At low temperatures n_{ch} should be replaced by $(n_e + n_i)$ in eqn. V.49, whereas for high temperatures it is n_e only.

Refractive index measurement gives by far the most accurate values of n_e as both the theory and measurement are well developed. In spectroscopic methods both the absolute intensity measurements and stark widths are widely employed for the determination of electron density.

Spectroscopic methods can also be used in determining the outstreaming or expansion velocities of LPP by measuring the doppler shift in the radiation scattered by the moving plasma boundary.¹³⁴

References

1. P. D. Maker, R. W. Terhune and C. M. Savage: Proceedings of the Third International Conference on Quantum Electronics, P. Grivet and N. Bloembergen, Eds. (Dunod, Paris, 1964), p 1559.
2. W. I. Lonlor: Bull. Am. Phy. Soc., 7, 440 (1962).
3. N. G. Basov and O. N. Krokhin: Sov. Phys - JETP, 19, 123 (1964).
4. J. N. Dawson: J. Phy. Fluids, 7, 981 (1964).
5. N. G. Basov, P. G. Kruikov, S. D. Zakharov, Yu. V. Senatskii and S. V. Tehekalin: IEEE J. QE - 4, 864 (1968).
6. F. Floux, D. Cognard, J. L. Bobin, F. Delobbeau and C. Fauquignon: C. R. Acad. Sci (Paris), 269B, 697 (1969).
7. R. E. Honig: App. Phy. Lett., 2, 138 (1963); 3, 8 (1963).
8. W. Demtröder and W. Jantz: Plasma Phys., 12, 691 (1970).
9. W. I. Linlor: Laser Interaction and Related Plasma Phenomenon, Vol. I (Plenum Press, N.Y., 1971).
10. P. Langer, G. Tonon, F. Floux and A. Ducauze: IEEE J. QE-2, 499 (1966).
11. R. E. Honig: Ref. 9, p. 85.
12. J. L. Bobin, F. Delobbeau, G. DeGiovanni, C. Fauquignon and F. Floux: Nucl. Furion., 9, 115 (1969).
13. C. Fauquignon and F. Floux: Phy. of Fluids, 13, 386 (1970).
14. N. G. Basov, V. A. Gribkov, O. N. Krokhin and G. V. Sklizkov: Sov. Phy - JETP, 27, 575 (1968); IEEE J. QE-4, 988 (1968).
15. G. V. Sklizkov: Ref. 9, p. 235.
16. C. David, P. Avizonis and K. D. Pyatt: IEEE J. QE-2, 493 (1966).
17. N. G. Basov, O. N. Krokhin and G. V. Sklizkov: App. Opt., 6, 1814 (1967).

18. E. Fabre and H. Lamaine: *Phy. Lett.*, 29A, 497 (1969).
19. R. Sigel: *Z. Naturf.*, 25a, 488 (1970).
20. E. Archbold, D. W. Harper and T. P. Hughes: *Brit. J. App. Phys.*, 15, 1321 (1964).
21. N. G. Basov, V. A. Boiko, Yu. P. Voinov, E. Ya. Koronov, S. L. Mandel'shtam and G. V. Sklizkov: *JETP Lett.*, 5, 141 (1967); 6, 291 (1967).
22. D. D. Burgess, B. C. Fawcett and J. Peacock: *Proc. Phys. Soc.*, 92, 805 (1967).
23. B. C. Boland, F. E. Irons and R. W. McWhirter: *J. Phys. B, Ser. 2*, 1, 1180 (1968).
24. W. Seka, J. L. Schwob and C. Breton: *J. App. Phys.*, 42, 315 (1971).
25. T. S. Stratton: *Plasma diagnostics Techniques*, eds. R. H. Huddleston and S. L. Leonard (Academic Press, New York, 1965) p 362.
26. H. Puell, H. J. Neusser and W. Kaiser: *Z. Naturf.*, 25a, 1815 (1970).
27. F. Floux: *Ref. 9*, p 447.
28. G. Siller, K. Buchl and H. Hora: *Ref. 9*, Vol. 2 (1972), p 253.
29. G. F. Tonon: *IEEE Trans. Nucl. Sci.*, ns-19(2), 172 (1972).
30. B. C. Fawcett, A. H. Gabriel, F. E. Irons, N. J. Peacock and P. A. H. Saunders, *Proc. Phy. Soc.*, 88, 1051 (1966).
31. N. J. Peacock and B. C. Fawcett, *Proc. Phy. Soc.*, 91, 973 (1967).
32. S. W. Mead, R. E. Kidder, J. E. Swain, F. Rainer and J. Petruzzzi: *App. Opt.*, 11, 345 (1972).
33. Yu. V. Afanasayav, E. M. Belenov, O. N. Krokhin and I. A. Polenktov: *JETP Lett.*, 13, 182 (1971).
34. P. Mulser, R. Sigel and S. Witkowski: *Phys. Reports*, 6C(3), 189 (1973).
35. Claudio DeMichelis: *IEEE Q.E-5*, 188 (1969).
36. R. G. Meyerand and A. F. Haught: *Phy. Rev. Lett.*, 13, 7 (1964).

37. A. Gold and H. B. Bebb: *Phy. Rev. Lett.*, 14, 60 (1965).
H. B. Bebb and A. Gold: *Phy. Rev.*, 143, 1 (1966).
38. G. S. Voronov: *Sov. Phys. - JETP*, 24, 1009 (1967).
39. G. A. Askranyan and M. S. Rabinovich: *Sov. Phys. - JETP*, 21, 190 (1965).
40. V. A. Barynin and R. V. Khokhlov: *Sov. Phys. - JETP*, 23, 314 (1966).
41. Y. B. Zeldovich and Yu. P. Raizer: *Sov. Phys. - JETP*, 20, 772 (1965).
42. M. Young and M. Hercher: *J. App. Phys.*, 38, 4393 (1967).
43. J. K. Wright: *Proc. Phy. Soc.*, 84, 41 (1964).
44. A. F. Haught, R. G. Meyerand Jr. and D. C. Smith: *Physics of Quantum Electronics*, Eds. P. L. Kelley, B. Lax and P. Tannenwald (McGraw-Hill, N.Y. 1966), p 509.
R. G. Meyerand Jr. and A. F. Haught: *Phy. Rev. Lett.*, 11, 401 (1963).
45. R. W. Minck and W. G. Rado: Ref. 44, p 527; *J. App. Phys.*, 35, 252 (1964).
46. D. A. Gill and A. A. Dougal: *Phy. Rev. Lett.*, 15, 845 (1965).
47. E. K. Damon and R. G. Tomlinson: *App. Opt.*, 2, 546 (1963).
48. M. C. Barthelémy, M. Leblanc and M. T. Bousault, C. R. Acad. Sci (Paris), 266B, 1234 (1968).
49. H. T. Buscher, R. G. Tomlinson and E. K. Damon: *Phy. Rev. Lett.*, 15, 847 (1965).
50. S. A. Akhmanov, S. V. Bobashev and E. P. Andreev, *JETP Lett.*, 21, 26 (1965).
51. R. G. Tomlinson, E. K. Damon and H. T. Buscher: Ref. 44, p 520.
52. V. E. Mitsuk and V. A. Chernikov: *JETP Lett.*, 6, 124 (1967).
53. V. E. Mitsuk, V. I. Savoskin and V. A. Chernikov: *JETP Lett.*, 4, 88 (1966).
54. D. S. Smith and A. F. Haught: *Phy. Rev. Lett.*, 16, 1085 (1966).

55. L.E. Vardzigulova, S.D. Kaitmazov and A.M. Prokhorov
JETP Lett., 6, 253 (1967)
56. R. G. Tomlinson: Phy.Rev. Lett., 14, 489 (1965).
57. B. A. Tozer: Phy. Rev., 137A, 1665 (1965).
58. G. S. Voronov, G. A. Delone and W. B. Delone: JETP Lett.,
3, 313 (1966); Sov. Phys. - JETP, 24, 1122 (1967).
59. F. V. Bunkin and A. M. Prokhorov: Sov. Phy. - JETP,
25, 1072 (1967).
60. H. Mennicke: Phys. Lett., 36A, 127 (1971); 37A, 381 (1971).
61. Yu. P. Raizer: Sov. Phy - JETP, 21, 1009 (1965).
62. S. A. Ramsden and P. Savic: Nature, 203, 1217 (1964).
63. Ya. Zeldovich: Theory of Detonation (Academic Press, 1960).
64. G. I. Taylor: Proc. Phy. Soc., 201A, 159 (1949).
65. J. W. Daiber and H. M. Thompson: Phy. Fluids, 10, 1162
(1967).
66. Ambartsumyan, N. G. Basov, V. A. Boiko, V. S. Zuel,
O. N. Krokhin, P. G. Kryukov, Yu. V. Senatskii and
Yu. Yu. Stoilov, Sov. Phy. JETP, 21, 1061 (1965).
67. A. J. Alcock, C. DeMichelis, K. Hamal and B. A. Tozer:
Phy. Rev. Lett., 20, 1095 (1968).
68. V. V. Korobkin, S. L. Mandel'shtam, R. P. Pashinin, A. V.
Prokhideev, A. M. Prokhorov, A. K. Sukhodrev and M. Ya.
Shchelev, S. Phy. JETP, 26, 79 (1968).
69. A. A. Medvedev and A. M. Prokhorov: Sov. Phy - Doklady,
13, 581 (1968).
70. N. G. Basov, V. A. Boiko, O. N. Krokhin and G. V. Sklizkov,
Sov. Phy - Doklady, 12, 248 (1967).
71. S. L. Mandel'shtam: Sov. Phy - JETP, 22, 91 (1966).
72. Yu. V. Afanasayev and O. N. Krokhin: Sov. Phy - JETP,
25, 639 (1967).
73. Yu. V. Afnasayev, O.N. Krokhin and G.V. Sklizkov,
IEEE J. Q.E-2(9), 483 (1966).

74. J. F. Ready: J. App. Phys., 36, 462 (1965).
75. T. V. Arifov, G. A. Askaryan and N. M. Taresova: JETP Lett., 8, 77 (1968).
76. E. Archbold, D. W. Harper and T. P. Hughes: Brit. J. App. Phys., 15, 1321 (1964).
77. A. Caruso and R. Gratton: Plasma Phys., 10, 867 (1968).
78. A. Caruso, Ref. 9, p. 289.
79. A. Caruso, A. De Angelis, G. Gatti, R. Gratton and S. Martellucci, Phys. Lett., 29A, 316 (1969).
80. G. W. Gobeli, J. C. Bushnell, P. S. Percy, and E. D. Jones; Phys. Rev., 188, 300 (1969).
81. A. Caruso and R. Gratton: Plasma Phys., 11, 839 (1969).
82. S. Namba, P. H. Kim and A. Mitsuyama: J. App. Phys., 37, 3330 (1966).
83. H. Schwarz: Ref. 9, p. 207.
84. D. W. Gregg and S. J. Thomas: J. App. Phys., 37, 4313 (1966).
85. F. Giori, L. A. Mackenzie and E. J. McKinney: App. Phys. Lett., 3, 25 (1963).
86. D. Lichtman and J. F. Ready: Phy. Rev. Lett., 10, 342 (1963).
87. R. E. Honig: App. Phys. Lett., 3, 8 (1963).
88. S. H. Khan, P. A. Richards, and D. Walsh, IEEE J. QE-1, 359 (1965).
89. A. W. Desilva and G. C. Goldenbaum: in Methods of experimental physics: Vol. 9A, Plasma Physics. Eds. H. R. Griem and R. H. Lovberg (Academic Press, N.Y. 1970) p 83.
90. A. J. Alcock and S. A. Ramsden: App. Phy. Lett., 8, 187 (1966).
91. S. Witkowski: Ref. 9, p. 223.
92. N. G. Basov, V. A. Beikov, O. N. Krokhin and G. V. Sklizkov: Sov. Phys - JETP, 24, 659 (1967).
93. H. R. Griem: Plasma Spectroscopy (McGraw-Hill, New York, 1964).

94. J. Cooper: in Reports on Progress in Phys, Vol. XXIX (1966), Part I, p 35-130.
95. D. R. Bates and A. Damgaard; Phil. Trans. Roy. Soc., 242A, 101 (1949).
96. D. R. Bates, A. E. Kingston and R. W. P. McWhirter: Proc. Roy. Soc., 267A, 297 (1962); 270A, 155 (1962).
97. R. W. P. McWhirter and A. G. Hearn: Proc. Phy. Soc., 82, 641 (1963).
98. W. J. Karzas and R. Latter: Astrophys. J. (Suppl), 6, 167 (1961).
99. R. H. Huddleston and S. L. Leonard: Eds. Plasma Diagnostic Techniques (Academic Press, New York, 1965).
100. W. Lochte-Holtgreven: ed. Plasma Diagnostics (North-Holland Publishing Co., Amsterdam, 1968).
101. Venugopalan: ed. Reactions under Plasma Kinetics, Vol.1,2 (Wiley Interscience, 1971).
102. R. C. Elton, Ref. 89, p 115.
103. J. Dawson and C. Oberman: Phys. Fluids, 5, 517 (1962).
104. L. Spitzer: Physics of Fully Ionized Gases (Wiley Interscience, 1962).
105. H. R. Griem, Ref. 93, p 145-154.
106. G. Elwert: Z. Naturf., 7a, 432 (1952).
107. H. R. Griem, Ref. 93, p 159-165.
108. H. R. Griem, Ref. 93, p 114-116.
J. Cooper, Ref. 94, p 83-87.
109. H. R. Griem, Ref. 93, p 107-112.
110. J. Cooper, Ref. 94, p 84. J. Richter, Ref. 100, p 33.
111. H. R. Griem, Ref. 93, p 137-140.
J. Cooper, Ref. 94, p 45-46. J. Richter, Ref. 100, p 16-17.
112. G. Ecker and W. Kröll: Phys. Fluids, 6, 62 (1963).
113. A. Unsöld, Z. Astrophys., 24, 355 (1948).
114. H. W. Drawin and P. Felenbok: Data for Plasmas in Local Thermal Equilibrium (Gauthier-Villars, Paris, 1965).

115. H. R. Griem, Ref. 93, p. 140-142. J. Cooper, Ref. 94, p. 47.
116. D. R. Inglis and E. Teller: *Astrophys. J.*, 90, 439 (1939).
117. E. Lindholm: *Arkiv. Math. Astronom. Och. Physik*, 28B, nr3 (1941).
118. J. Holtsmark: *Ann. Physik*, 58, 577 (1919).
119. M. Baranger: in *Atomic and Molecular Processes*, Ed. D. R. Bates (Academic Press, New York, 1962) Chap. 13.
120. B. Mozer and M. Baranger: *Phy. Rev.*, 118, 626 (1960).
121. D. Robinson and P. D. Denn: *App. Opt.*, 6, 983 (1967).
122. W. L. Wiese, M. W. Smith and B. M. Miles, National Bureau of Standards (NSRDS-NBS 22), October 1969.
123. J. R. McNally Jr: *Optical Spectrometric Measurements of High Temperatures*, Ed. Philip J. Diekerman (University of Chicago, 1961) p. 82.
N. K. Sukhodrev and S. L. Mandelshtam, *Sov. Phy - Optics and Spectroscopy*, 6, 473 (1959).
124. H. R. Griem, Ref. 93, p. 270-279.
125. J. Cooper, Ref. 94, p. 101.
126. W. F. Brearman, C. R. Stumpfel and H. j. Kunze: *J. App. Phy.*, 40, 2549 (1969).
127. F. C. Jahoda, E. M. Little, W. E. Quinn, G. A. Sawyer, and T. F. Stratton, *Phy. Rev.*, 119, 843 (1960).
128. H. Zwickler, Ref. 100, p. 221; Equation (22) and Fig. 3. p. 223.
129. G. N. Harding, N. F. Kimmitt, J. H. Ludlow, P. Parteau, A. C. Priai, and V. Roberts: *Proc. Phy. Soc. (Lond.)* 77, 1069 (1971).
G. N. Harding and V. Roberts: *Nucl. Fusion Suppl.*, 3, 883 (1962).
130. N. F. Kimmitt and G. B. F. Niblett: *Proc. Phy. Soc. (Lond)*, 82, 938 (1963).
131. H. R. Griem, Ref. 93, p. 289. W. Lochte-Holtgreven, Ref. 100, p. 197.
132. H. R. Griem, Ref. 93, p. 291-293.
C. R. Stumpfel and J. L. Robitail: *J. App. Phy.*, 43, 902 (1972).

133. H. R. Griem, Ref. 93, p 293. W. Lochte-Holtgreven, Ref.100,
p.166.
134. S. A. Ramsden and P. Savic: Nature, 203, 1217 (1964).
S. L. Mandel'shtam, P. P. Pashinin, A. M. Prokhorov,
Yu. P. Raizer and N. K. Sukhodreëv, Sov. Phy - JETP,
22, 91 (1966).

CHAPTER VI

SPECTROSCOPIC INVESTIGATIONS OF LASER GENERATED PLASMA FROM SOLID TARGETS

VI.1.1 Introduction

In this chapter we present some of our results on the spectroscopic investigations of laser generated plasma from solid targets of CaF_2 , SrF_2 , aluminium and carbon. The spectra of the emission from the plasma formed at the target surface are photographed both when the target is exposed to air and when it is in vacuum. These spectra are analysed to obtain plasma temperatures and densities in both cases of target in air or vacuum. Through such an analysis of the spectra, possible effects of the atmosphere on the plasma formation at the target surface are also inferred.

Most of the earlier studies of LPP at solid targets¹⁻¹¹ have been performed with the target in vacuum of the order of

10^{-4} - 10^{-5} torr. However, a few investigations^{12,13} are reported with the target in a gaseous atmosphere at ambient pressures of 0.1-10 torr. These, study the detonation wave formation in the gas in the presence of the target. One investigation¹⁵ studies the effect of different ambient pressures on the crater formation. We have made a comparative study of the spectra of the target plasma emission, with the target in air or in vacuum.

In a parallel investigation, using the same set up, we were investigating possible two-photon absorption and blue-fluorescence from rare-earth ions, such as Nd^{3+} in different host lattices such as CaF_2 , SrF_2 etc., when irradiated with ruby laser and different stimulated Raman radiations generated in several organic liquids. Hence the choice of CaF_2 , SrF_2 crystals for LPP studies also. As these crystal targets could not withstand more than a couple of laser pulses without getting damaged, we chose aluminium as one of the target, especially when many pulses are to be incident on the same target spot.

Plasma spectra have been photographed both with target in air and in vacuum of the order of 1-10 μ . The spectra are then analysed for evaluation of plasma parameters. The spectra clearly indicate that in vacuum the plasma exhibits a higher degree of ionization, with the vacuum spectra yielding a higher temperature. This is interpreted as due to the screening action of the plasma that is formed in front of the target due to air breakdown and formation of an atmospheric

plasma when target is in air, whereas in vacuum the entire laser radiation is able to reach the target surface and heat the material plasma to a higher degree of ionization and temperature.

Time profiles of the different ionic lines were studied photometrically for an aluminium target, with the same target area exposed to successive laser pulses. The observed results indicate a steepening and an advance of the peaks of the time profiles of all the ionic lines after a number of pulses. This is attributed to the formation of a deep crater on the surface and the consequent plasma heating in the laterally confined area of the crater. This results in a greater velocity of the ejected particles and plasma heating in a denser plasma. A similar effect on ion emission through probe measurement were mentioned by Linlor.²⁶

VI.1.2 Earlier Spectroscopic Investigations of LPP

Early spectroscopic investigations of LPP were by time-integrated spectra. For studying the early stages of plasma formation and heating, space as well as time resolution are found absolutely necessary.

Mandel'shtam et al.¹ have investigated a laser spark in air through time integrated spectrum in the visible and have obtained electron densities of $2.3 \times 10^{18} \text{ cm}^{-3}$ from the stark widths of nitrogen lines N II 3995 and 5045 Å. Temperature of $3-6 \times 10^4 \text{ }^\circ\text{K}$ are estimated from line intensity

ratio of N II 5197 Å multiplet and 5045 Å lines, with 30 MW, 40-50 nsec laser pulses. These values of n_e and T_e , according to them, refer to an already developed stage of the air-spark. The same authors² investigating the early stages of the spark with a 2J, 40 nsec pulse obtain a temperature of 60 eV for the maximum temperature from X-ray absorber technique near the 10 Å region. Evthushenko et al.³ studied the laser spark in helium (with hydrogen impurities) at pressures 1-10 atm., through time-integrated spectra as well as time-swept profiles of the H_α and He I 5876 Å. The electron densities obtained from stark widths of the He I lines, He II 4686, H_α and H_β lines in the time-integrated spectra varied by two-orders between $5 \times 10^{16} - 6 \times 10^{18} \text{ cm}^{-3}$. The maximum value obtained from He II line agreeing closely from the density determined at the early stages by means of the time-swept profiles. The authors attribute these values as possibly belonging to different stages of the spark. Time resolved spectra of LPP in helium are studied by Brearman, Stumpfel and Kunze⁴ using laser powers of 200-550 MW, focussed by lens of focal length 65 mm. Electron densities are obtained from stark widths of lines using approximately determined temperature values. The temperature are obtained by the ratio of He II 4686 Å to underlying continuum, in the first 200 nsec obtaining temperatures between 50-10 eV in that time spread. Between 200 nsec - 1 μsec, they use the He II to He I line ratio (especially useful in the

temperature range of 3-7 eV) and the Coronal model. The values of n_e and T_e for this region being $5 \times 10^{17} \text{ cm}^{-3}$, 5.4 eV at 200 nsec and $1.2 \times 10^{17} \text{ cm}^{-3}$, 4.3 eV at 1 μsec respectively. For times between 1 μsec and 20 μsec the temperature is estimated by the He I 5876 Å line to underlying continuum ratio. The three methods span a range of temperature from about 50 eV to 1 eV and density from 10^{19} to 10^{16} cm^{-3} . Decay coefficients were obtained for the He II \rightarrow He III recombination from the relation

$$\frac{dn^Z}{dt} = -\gamma n^Z n_e, \quad \gamma = \frac{d}{dt} \left(\frac{1}{n_e} \right) \text{ since } n_Z = \text{He}_{\text{III}} = \frac{n_e}{2}$$

The experimental value of γ obtained from an n_e vs time plot is compared to the theoretically calculated collisional-radiative recombination coefficient α . Burnett and Smy⁵ have evaluated the temperature of an aluminium LPP produced by using 2J, 20 ns laser pulses. They photometrically measure the transmission through the plasma of a He-Ne gas laser beam and use the absorption coefficient due to inverse Bremsstrahlung. The photometric method provides an automatic time-evolution and the plasma temperature is estimated to drop from 7eV^{at} the end of laser pulse to 2 eV after 100 ns. Scott and Strasheim⁶ have investigated LPP in aluminium using normal mode, semi-Q-switched and Q-switched lasers for possible analytical spectroscopy works. They find that in the giant-pulse excitation the line-emissions from the plasma can be separated from the background continuum. They have reported

asymmetrically reversed self-reversal lines with both the absorption minima and emission line maximum red shifted w.r.t the unshifted line. Valero et al.⁷ have also reported on the extremely unsymmetrical self-reversal of lines of highly ionized species in the vacuum ultra violet (VUV) spectra of LPP of iron and aluminium. Burgess, Fawcett and Peacock⁸ have obtained VUV spectra, using a grazing incidence spectrograph, of LPP from a partly oxidized potassium targets using laser powers of 500 MW. They have extended the line-width calculations of Griem, to the OVI and KIX lines to obtain electron-densities from line-widths. The electron temperatures were estimated from the frequency interval in which the continuum intensity dropped by $1/e$. The temperatures estimated thus from CV continuum are $113 (+20)$ eV within 0.5 mm from target surface and $15 (+3)$ eV at a distance of 1.0 mm from the target surface. From the steady-state ionization balance alone they determine temperatures of 130 eV for ions of ionization potential $E_{\infty} = 500$ eV, the balance described by a Corona model (and $N_z = N_{z+1}$). For lower ionization stages using LTE and Saha's equation a temperature of 23 eV is obtained for OVI with $E_{\infty} = 130$ eV. Dhez et al.,⁹ using a grazing incidence spectrograph and spectra taken at different distances from target surface have plotted the spatial variation of intensities from lines from Al IV-VI. Al IV line peak is spatially separate from the continuum whereas Al V and VI almost coincide with the continuum and show a second peak.

They also study the plasma zone in which these ions emit strongly. They attribute Al IV^{as} due to recombination of Al V and VI during plasma expansion and cooling. Time development of lines of different ionizations in a LPP is studied by Seka et al.¹⁰ and Boland et al.¹¹ From their studies on LPP in LiH particles using 1 MW, 3nsec Nd-glass laser pulses, Seka et al. observe that the periphery of the plasma expands more rapidly than the core; oxygen lines (O IV-VI) from oxide layer are seen confined to this periphery and are emitted ahead of the plasma. Most of the ions have recombined within 100-150 ns. Continuum distribution and also existence of Li³⁺ ions independently give a maximum temperature (at $t = 5$ ns) of 30-35 eV and density $5 \times 10^{20} \text{ cm}^{-3}$. Boland et al. have made a much more quantitative study through the time profiles of different ionization stages in a carbon plasma from a polyethylene target (laser output 5J, 17 ns, flux $3 \times 10^{11} \text{ W/cm}^2$). The maxima of successive lower ionizations occur later in time, the C V and VI almost coinciding and CI peak occurring almost 100-150 ns later. The peaks of each ionization occur later further away from the target. From these, expansion velocities and hence kinetic energies of different ions are obtained. They estimate that nearly 75% of laser energy goes into the expansion energy of the plasma. From time-resolved free-bound continuum distribution between 20-35 Å corresponding to CV and VI ions, they obtain $T_e = 90-12 \text{ eV}$ between 0-2 mm from target and about 3-4 eV at 5 mm from target. From their calculations

of recombination times they conclude that plasma is not recombining in the expansion regime of their study.

So far the studies have been of target in vacuum. Bobin et al.¹² and Emmony and Irwing¹³ studied LPP in beryllium and carbon targets, immersed in a gas at low pressures of 0.2-3 torr and 0.1-10 torr respectively. High speed streak and framing photography of the expanding plasma is used. Bobin et al. also obtain space resolved spectra. Both the study indicate the formation of a shock wave travelling ahead of the expanding plasma and lasting for a long time after the end of laser pulse. Initial Mach numbers of up to 200 has been recorded for the shock front. Unlike in the case of a pure gas, in the above cases the material plasma acts as a piston supplying energy to the shock wave long after the laser pulse has ended. Piepmeier and co-workers^{14,15} have studied plasma production from aluminium and copper targets in air. They indicate the formation of an expanding atmospheric plasma in front of the target. Material (atoms and ions) ejected from the target soon replace the atmospheric species farther and farther away from the target. They conclude that the formation of an atmospheric plasma screens the target from further laser radiation.

These studies illustrate the variety of methods adopted for laser plasma diagnosis and the range of values for different plasma parameters with different or sometimes the

same laser powers. Each result has to be viewed in the background of the particular experimental conditions and methods adopted.

VI.2 Experimental

Our experiments were carried out with the Raytheon-make ruby laser mentioned in Chapter IV. The ruby rod is $6\frac{3}{4}$ inch long and $\frac{3}{8}$ inch diameter and housed in an elliptic cavity. It is pumped by a linear xenon flash lamp. The ruby rod and cavity are water cooled. The laser is Q-switched using a rotating-prism mounted on a 400 c/s synchronous motor. The laser power output is estimated to be about 2-3 J of pulse duration 50 nsec. The laser output has not been directly measured. The pulse width has been measured as detailed in a later section on temporal measurements of plasma emission. The laser output is monitored by the photomultiplier PM_1 as shown in Fig. II.3. The beam is focussed onto the target by means of a plano-convex lens of focal length 65 mm of 1.5 inch diameter.

The target is mounted on a movable brass mount capable of axial movement. For studies with the target in vacuum, the target is mounted on the cold-finger of a double-walled evacuated dewar. The sample is mounted on a slot in the copper block so that no copper is backing the sample at the point where the laser beam is incident. The sample is fixed to the cold

finger or any support (in air) by means of a very small amount of quick-fix. The dewar has three quartz windows one in the direction of incident beam and two normal to it. In our work the dewar is continuously evacuated by means of a rotary pump capable of producing vacuum in the range of $1-10\mu$, sometimes also with a diffusion pump (reaching 10^{-4} torr), the dewar holding vacuum during the experiment.

The plasma spectra is recorded with a Carl-Zeiss Q-24 medium quartz spectrograph. The spectrograph has typical dispersion of 30 \AA/mm near 4000 \AA and 14 \AA/mm near 3000 \AA . The spectrograph axis is normal to the laser axis with the slit parallel to the target surface. The plasma at the target surface is imaged onto the slit by means of a quartz lens (L_2) of focal length 75 mm. For taking spectra with the spectrograph axis passing through different points in front of the target, the target along with the focussing lens is moved along the laser axis back and forth w.r.t the spectrograph axis.

Spectra are recorded on Kodak 103 a-0 plates which have flat sensitivity range from 2500 \AA to 5000 \AA except between 4700 \AA and 5000 \AA . Each spectra is exposed with 3-5 pulses, each of them invariably falling on the same area of the target surface. The spectrograph has a built-in wave length scale that can be superposed on the spectrum. Most of our spectra has such a scale superposed on them. Densitometric.

traces of the spectra are taken for us at the Spectroscopy Division of BARC Bombay.

The targets investigated were CaF_2 and SrF_2 (both either pure or doped with Nd^{3+} or Gd^{3+} . In most of the later spectra the pure samples are used), Aluminium (pure aluminium 99.99% rods of $1/8$ " were flattened into strips of 1-1.5 mm thickness) and carbon (2 mm thick disc cut from spectroscopic pure graphite electrodes).

VI.3 Results

VI.3.1 Physical Characteristics of the Plasma

When the laser radiation is focussed onto the target surface in air, a characteristic sound of considerable intensity is heard and a very intense blue flash is seen which seem to emanate from an area that is around 1 cm or more along the laser axis and somewhat less transverse to it. The luminous blob has more or less a spherical front with the lateral extent converging to a small area close to the target. When the target is in vacuum, hardly any sound is heard at all except very close to the dewar. The brightness of the plasma is considerably reduced and the plasma extent is also very small compared to that when in air.

When the target is in air, the crater formed for each pulse seen to be very small, whereas when the target is in

vacuum, the crater formed is of good size, and visible with a metallic shine from the crater material (in aluminium). When the laser is focussed on the same spot repeatedly, in the case of aluminium target, after many pulses a fine hole is drilled through the target. The number of pulses needed for the hole to be through is much less in vacuum (about 30-40) and considerably more in air.

VI.3.2 Spectra

The spectra obtained with the different targets are shown in Figure VI.1 to 6, with each spectra showing both the spectra in air and in vacuum for comparison.†

CaF₂

The spectra corresponding to CaF₂ are shown in Figs. VI.1 and 2. Fig. VI.1 is that of CaF₂:Nd³⁺ and shows the spectra when the plasma is not imaged onto the spectrograph slit but the slit is receiving emission from all parts of the plasma. The spectrograph is moved nearer for this purpose. In Fig. VI.2 the spectra of CaF₂:Gd³⁺ is shown with the plasma imaged onto the spectrograph slit by means of the quartz lens.

† For the sake of brevity, henceforth we will refer the plasma spectra obtained with the target in air as the 'air spectra' and the spectra obtained with the target in vacuum as the 'vacuum spectra'.

The alignment is such that the spectra of plasma close to the target surface (0-0.5 mm) is taken. Spatial resolution is obtained by imaging the plasma on to the slit.

In both the spectra (air and vacuum) one can distinguish lines corresponding to Ca I-III, F II and III, couple of lines of nitrogen or oxygen and lines of some impurity in the crystal. The lines are measured w.r.t copper standard superposed on the spectra (shown in Fig. VI.1 and not in VI.2), and identified using the standard wave lengths obtained from standard Tables.^{16,17}

Some of the characteristic features of these spectra are as follows:

1. The focussed spectra show a continuum extending from 2300 to 5000 Å (the sensitive range of the Kodak 103a-C plate used). In each spectra the continuum is restricted to the central portion of the spectra which corresponds to the laser axis. Lower ionization stages, especially CaI and II, extend to the full height of the spectra, whereas the higher ionization lines CaIII are predominantly confined to the continuum, extending slightly above it.

2. In this spectra (and also in several other focussed spectra, not shown), one can distinguish a second, somewhat weaker, continuum below the central continuum. This might correspond to the second pulse seen while monitoring the laser radiation.

3. The lines of CaI (4227 \AA) and CaII (3933, 3968, 3159, and 3179 \AA) are self-reversed in air. In most of the vacuum spectra self-reversal of the line was absent, while in some was present to much lesser extent, restricted to an area at the centre of the line coinciding with the continuum.

4. In the vacuum spectra, many of the CaI lines almost disappear or otherwise weak. CaIII lines become stronger and some of the lines are seen only in the vacuum spectra. F II lines also become stronger and some additional lines also appear. In most of the spectra F III lines are not always seen in the spectra in air but are seen strongly in vacuum.

5. The lines are, in general, broad, especially the CIII lines in vacuum which extend to the same height and a little above the continuum.

6. Nitrogen lines are virtually absent. In some of the spectra in air, particularly at distances slightly removed from the target surface, a broad line around 5005 \AA is conspicuously seen which is identified as NII. This is not present in the vacuum spectra. A few lines between $2500\text{--}2550 \text{ \AA}$ found in the air spectra can be assigned to some NII and OII lines. These lines are present in many of the air spectra of SrF_2 and Al also and absent in the corresponding vacuum spectra.

7. In the spectra, one can identify lines due to small traces of Sr in CaF_2 . The resonance lines of Sr (4077 \AA SrII, 4607 \AA SrI) are clearly seen in CaF_2 spectra.

CaIII lines were not available from the Tables mentioned in Refs. 16 and 17. They have been obtained from Zaidel et al.¹⁸ and Bowen¹⁹ and we have been able to identify all the lines listed in these references (Only a few in air spectra but nearly all of them in vacuum spectra). All the lines obtained in our spectra (Fig. VI.1 to 6) are listed in Appendix 3, along with their term assignment of the levels concerned and with the values of g and A needed for line intensity calculations. Along side each line, specified by its wavelength and identification, two columns specify whether the line is seen in air spectra or vacuum spectra or both and their intensity in each.

SrF₂

The plasma spectra of pure SrF_2 are shown in Fig. VI.3 and Fig. VI.4. In Fig. VI.3 the plasma is not imaged on the spectrograph slit and conditions are similar to Fig. VI.1. In Fig. VI.4 the plasma is imaged onto the spectraph slit. The inclined lines in the spectra, especially in Fig. VI.3, are due to a inclined slit by mistake. Subsequently, the slit was made vertical but still some small inclination remained in the opposite direction (Fig. VI.4).

The characteristic features of the spectra are similar to that of the CaF_2 spectra. Resonance lines SrI (4607 \AA) and SrII (4215 and 4077 \AA) are strongly seen and are self-reversed in air throughout the height of the spectra, whereas in vacuum spectra self-reversal of the line is confined to the same extent as the central continuum.

As in CaF_2 , SrI lines get weaker and almost vanish (Fig. IV.4) in the vacuum spectra. SrIII line identification were not available in any of the literature cited here nor in any other source. Hence we have not been able to identify SrIII lines. However, in similarity to the CaF_2 spectra, from their behaviour in air and vacuum, we have shown the SrIII lines in Fig. VI.3 and 4, most of which, we believe, are SrIII.

Some impurity lines have been identified as belonging to magnesium, such as 2852 \AA (MgI), 2802.5 and 2795.5 (MgII). The other Mg lines being much weaker are not seen. These three lines are seen in CaF_2 spectra also. Lines characteristic of CaII (3933 \AA and 3968 \AA) are clearly seen in SrF_2 spectrum, arising from Ca impurities in SrF_2 .

Aluminium

Fig. VI.5 shows the aluminium plasma spectra when plasma is not imaged on the slit and Fig. VI.6 when plasma close to target surface is imaged on the slit. The same

general characteristics as in Fig. VI.1-4 are also seen in these. Several of the aluminium lines are self-reversed, such as 3092 \AA , 3082 \AA , 2660 \AA , 2652 \AA , 2575 \AA , 2568 \AA , 2373 \AA and 2367 \AA all of AlI. The last two lines almost look as absorption lines in a continuum background. The same lines appear as sharp emission lines in vacuum spectra.

As in the earlier ones AlI lines are weaker in the vacuum spectra and AlII also show similar behaviour. In Fig. VI.5 some AlII lines are also absent (ex: 2669 \AA) in vacuum spectra.

Spectra at different distances from target surface

With CaF_2 as target (in air) spectra were taken with the spectrograph axis passing at different distances (x) from the target surface. For this purpose, the target and the lens are moved w.r.t the spectrograph axis and spectra taken with the target surface at $x=0$, 0.5, 1.0, 2, 4 and 6 mm from this axis. These are shown in Fig. VI.7. These sets of spectra indicate:

1. The continuum begins to appear at around $x=1 \text{ mm}$ in our spectra and is not seen beyond $x=2 \text{ mm}$.
2. The Ca lines are very weak between $x = 0$ and 1 mm and appear strongly for $x=1 \text{ mm}$ till $x = 5 \text{ mm}$. The resonance lines appear self-absorbed as early as $x=1 \text{ mm}$.

3. The broad line at 5005 \AA , identified to be W II line does not appear before $x = 1 \text{ mm}$ where Ca lines are already present. It appears from $x=2 \text{ mm}$ onwards and is not seen strongly beyond $x = 4 \text{ mm}$.

4. The F III lines near 3200 \AA appear strongly at $x=0$ and do not appear beyond $x=1 \text{ mm}$. Further they are confined to the lower half of the spectrum whereas the other lines appear fully.

It should be noted that what we refer to as $x=0$ may possibly be just within the surface of the transparent target (CaF_2) due to uncertainty in the alignment, the inaccuracy may be of the order of 0.5 mm , and correspondingly positions $x = 1, 2 \dots$ etc mm may have to be shifted closer to the target surface.

VI.5.3 Temperature and Density Evaluation from the Spectra

Densitometer traces of the spectra are obtained from which intensities of lines are obtained after taking due consideration of the non-uniform dispersion of the prism spectrograph. For Kodak 103a-0 plate we assume a flat sensitivity up to about 4600 \AA , after which the sensitivity starts decreasing for higher wavelengths.

Full-widths of the lines corresponding to half-intensity points are found for CaI, CaII, AlI and AlII lines. These are used to estimate the electron densities from the

pressure-broadening data-tables provided by Griem.²⁰ Such data-tables are not given for SrI and SrII lines.

Temperatures are calculated by the following three methods:

1. By the ratio of line-intensities from two successive ionization stages, assuming the existence of LTE.

2. From the line intensity ratio of two lines from the same ionization. The temperatures obtained for different pairs of lines from the same ionization show considerable scatter.

3. From the slope of the Boltzmann plot (see Chapter V.6.1.1) for each ionization stage. The resultant points are often widely scattered, which seems to be characteristic of the method.²¹ Both the last two methods give higher temperatures for each successive higher ionization stages. The average value of the temperatures from the two highest stages correspond more nearly to the actual temperature.²¹

A typical Boltzmann plot obtained for aluminium is shown in Fig. VI.8. This corresponds to the time and space-integrated spectra shown in Fig. VI.5. In what follows we will cite the temperatures obtained from the ratio of intensities of lines from successive ionization stages unless otherwise specified.

CaF₂

Oscillator strength data were not available for CaIII lines. Hence we were restricted to CaI/CaII line intensity ratio for the estimation of temperature. The densitometer trace of the spectrum considered is shown in Fig. VI.9. This is a focussed spectra similar to Fig. VI.2, but exposed with only two pulses each to avoid the spectra getting over dense. The trace corresponds to wavelengths above 3200 Å.

The intensity of the line is measured w.r.t the background level at the line and hence the base line for the traces is not shown.

In the focussed spectra the lines show intensity distribution with maximum at the centre of the spectrum and decreasing either way. As the lateral extent of the plasma is imaged onto the slit, the continuum coincides with the centre of the spectra. Densitometer traces are taken at different heights of the lines starting with the continuum. Estimation of temperature from these traces by any of the above mentioned methods will provide a distribution of temperature in the lateral extent of the plasma. Temperatures are estimated for the air spectrum along the continuum (Fig. VI.9) and slightly above it (Fig. VI.10). The respective temperatures and densities are about 12750°K and $8 \times 10^{18} \text{ cm}^{-3}$ along continuum and 12500°K and $5 \times 10^{18} \text{ cm}^{-3}$ above it. These are average values from different line ratios. The densities

intensity also we arrive at approximately the same temperature of 60000°K . The F II line widths give linewidths of 10^{19} cm^{-3} and more.

Fig. 13A and 13B are the densitometer traces of the spectra shown in Fig. VI.7 in which spectra at different distances from the target surface ($x = 0, 0.5, 1, 2, 4, 6 \text{ mm}$) are shown. Fig. 13A shows the traces between $4600-4220 \text{ \AA}$ for each of spectra corresponding to $x = 1, 2$ and 4 mm . Fig. 13B shows the traces for the same spectra in the wavelength region $4000-3100 \text{ \AA}$. These traces clearly show the considerable reduction in continuum between $x = 1$ and 2 mm and its virtual absence at $x = 4 \text{ mm}$. Temperatures are evaluated from the line intensity ratios of CaI/CaII from the traces of spectra corresponding to $x = 1, 2$ and 4 mm . Densities are obtained from line-widths of several lines of CaI and CaII. The temperature shows an increase between $x = 1$ and 2 mm and then decreases. The density shows a similar trend. The temperatures obtained from different line pairs and the densities from the width of the corresponding lines are tabulated in Table VI.2. Apart from slight differences from pair to pair the temperatures are $11000, 12500$ and 9000°K at $x = 1, 2$ and 4 mm respectively. Densities obtained from different lines, though different (by factor of 5 or more between CaI and CaII lines), show a similar trend as temperature. The intensities of the different lines of CaI

and CaII at the different distances from the target are also listed in Table VI.2. The intensities of lines of CaI increases from $x = 1$ to 4 mm, whereas the intensity of lines of CaII shows a maximum at $x = 2$ and has decreased considerably by $x = 4$ mm.

Aluminium

The temperature, from the spectra of aluminium plasma, is obtained both by the AlII/AlIII and also by AlI/AlII line intensity ratios. Since most of the AlI lines especially in air spectra are considerably self-reversed, these are not used in all the spectra.

Fig. VI.14 is a densitometer tracing of the vacuum spectra in Fig. VI.5. The air spectra is too dense for obtaining a useful trace. Fig. VI.15 and 16 are densitometer traces of the air and vacuum spectra respectively of the aluminium plasma spectra with plasma imaged onto the slit. In Fig. VI.15, the AlI lines from an Al arc spectra, are also shown for comparison. The temperature close to the target surface ($x = 0.5$ mm) when target is in air is evaluated from the AlII/AlIII line intensity ratios and an average temperature of 27500°K is obtained. The electron densities from the AlII line ($3900, 4663 \text{ \AA}$) is about $1 \times 10^{18} \text{ cm}^{-3}$. The 2816 \AA line of AlII gives a much higher value for the density ($7.5 \times 10^{18} \text{ cm}^{-3}$) and the ratio of the $2816 \text{ \AA}(\text{II})/3605 \text{ \AA}(\text{III})$ also gives a higher temperature value (37500°K).

The intensity ratio of the same ionization stage gives a value around 2.4 eV from AlIII lines, a widely varying range of values such as 0.7, 0.3, 2.4 eV from AlII lines. A similar analysis of the spectra with target in vacuum gives an average temperature of about 32000°K (2.3 eV) and a density of $5 \times 10^{17} \text{ cm}^{-3}$ from linewidths of AlII lines and $1-2.5 \times 10^{17} \text{ cm}^{-3}$ from AlI lines.

The spectra of the aluminium plasma with the target in vacuum and plasma not imaged onto the slit is also analysed for temperature and density measurement. The temperature estimated by the AlII/AlIII line intensity ratio is of the order of 28500°K, with the AlII 2816 Å line giving a much higher temperature of 37500°K. The density from AlII linewidths is about $2 \times 10^{18} \text{ cm}^{-3}$. AlI/AlII line intensity ratio yields a temperature of 20000-21000°K whereas the AlI linewidths yield a density value of $1 \times 10^{17} \text{ cm}^{-3}$. Intensity ratios of same ionization lines yield 2.4-2.5 eV from AlIII lines, around 0.45 eV from AlI lines.

The spectrum of a d.c. arc with aluminium electrodes are superposed on some of the aluminium plasma spectra not only to obtain the temperature and electron density in such an arc in comparison with that in the plasma, but also to observe any shifts of the plasma emission/absorption lines from the corresponding line from an ordinary arc standard. The arc spectrum shows predominantly AlI lines and AlII lines

if present are very weak. The temperature of the arc obtained from several spectra both by the line intensity ratio of AlI lines and a Boltzman plot of AlI lines yield a value between 6000-7000^oK. The densities were 4-5 times smaller than the corresponding values for the plasma spectra with target in air.

A similar arc spectrum is obtained for Ca by obtaining the same d.c arc with graphite electrodes with a small cavity scooped in the cathode, into which powder samples of calcium (CaF_2 or CaCl_2) or strontium (SrF_2) are introduced. The spectra was taken on Jarrell-ash grating spectrograph (3.4 metre, Ebert mounting) with 5 \AA /mm dispersion in first order. Only CaI lines with the 3933 and 3968 \AA lines of CaII were seen. The 4226 \AA (CaI) and 3933, 3968 \AA (CaII) lines were self-reversed with a very sharp absorption line. The Boltzmann plot for CaI line yields a temperature of about 4000^oK, whereas the CaI line ratios yield various values with a majority of them around 0.45-0.5 eV (5500^oK). The line widths are easily a factor of 4-5 narrower and some lines are even sharper. The spectra also shows CN bands. The line shifts are discussed later.

Carbon

Only one carbon plasma spectrum is analysed from its densitometer trace (not shown). The spectrum in air show CN bands which obscure the atomic lines. The vacuum spectra

is free from the CN bands and shows C I - III lines. The temperature is estimated to be 23000°K by the C II/C III line intensity ratio using the C II 2509-2512 \AA and C III 2297 \AA lines. This agrees with the temperature indicated by the plot of C III/C II intensity ratio vs temperature given by Griem²² (using combination of Saha equation and corona model). We have used the line oscillator strength values of Weiss et al.¹⁷ The temperature value corresponding to our C III/C II intensity ratio of 0.055 is to be used in their plot corresponding to our electron density of $5 \times 10^{18} \text{ cm}^{-3}$. The C II 2509-12 \AA and C II 2837 line intensity ratio yields a value of 1.50 eV and the C II 2509-12 \AA and C I 2478 \AA line intensity ratio yields a value of 1.75 eV for the temperature. The C II 2836 \AA line width leads to an electron density estimate of $6 \times 10^{18} \text{ cm}^{-3}$.

VI.4 Discussion

Atmospheric plasma

The results of our experiment presented in the previous section indicate considerable difference in the physical, as well as, spectral characteristics of the target plasma formed when the target is in air or in vacuum. The luminous plasma extends to a considerably bigger volume when target is in air than in vacuum. On the other hand, the depth of crater formed for each pulse is more when target is in vacuum.

Further considerably less number of pulses are needed to drill a through hole in the aluminium target in vacuum than in air.

From the spectra of the plasma with target in air and in vacuum, it is clear that there is a tendency towards higher ionization of the plasma with target in vacuum as compared to that in air. The lines of the lower ionization stages (CaI, II, AlI, II etc.) get weaker or completely disappear in the vacuum spectra, whereas the lines due to CaIII especially appear strongly in vacuum spectra. Existence of still higher ionization stages (CaIV, AlIV) could not be ascertained as the lines of these species fall in the vacuum ultraviolet region which is beyond the range of the spectrograph available in our laboratory. A test exposure with the target in helium atmosphere showed similar plasma characteristics as for air.

The change in the characteristics of the target plasma from air to vacuum seem to be equivalent to an increase in the intensity of the laser reaching the target surface. Hence in accounting for the observed plasma characteristics we should look for a mechanism that regulate the energy reaching the target. One such phenomenon that is now well understood is the breakdown of air in front of the target and the formation of an air spark (atmospheric plasma). However, the laser intensity used for

most of our study on target plasma studies did not consistently induce air breakdown at the focus of the lens in air alone (target removed). In the presence of the target, the few electrons needed to carry on the cascade ionization in air might be provided by thermal electrons from the target. Radiation intensity needed to sustain the spark formed by breakdown of air is two-orders smaller than the breakdown threshold intensity.²³ Thus it is possible for air-breakdown and formation of an atmospheric plasma in front of the target. The shock wave that is produced on the formation of the spark carries the ionization front towards the lens, absorbing laser radiation on its way. The laser energy is considerably absorbed by the atmospheric plasma and the absorbing shock front created. Hence very little energy reaches the target subsequent to the formation of air spark in front of it. On the other hand, when the target is in vacuum, most of the laser energy is able to reach the target throughout the duration of the pulse. The target plasma formed in vacuum is, hence, heated to a higher temperature and greater ionization. When the target is in air, the target particles initially evaporated and ionized at the target are further heated in the atmospheric plasma.

Thus the formation of an atmospheric plasma in front of the target in air seems to account for the differences in the target plasma characteristics observed by us with the

target in air and in vacuum. The decreased energy reaching the target in air, as compared to that in vacuum, being responsible for the smaller crater size etc. The shock wave created in air carries the luminous front away from the focus and is responsible for the larger luminous area seen in air.

The spectra in Fig. VI.7 taken at different distances from the surface of the target (CaF_2) in air, show that the continuum appears at $x = 1$ mm and is not seen beyond $x = 2$ mm. Temperature and density estimation from these spectra show that these parameters go through a maxima near $x = 2$ mm. The NII line at 5005 \AA is seen only in the spectra corresponding to $x = 2$ mm and in the next one. As mentioned earlier, due to possible uncertainty in our alignment, the point corresponding to $x = 0$ may possibly lie just within the surface of the target (by 0.5 mm or so). But, still the spectra could be recorded due to the transparency of the crystal. The above facts indicate that the atmospheric plasma is formed in front of the target at around $x = 1$ mm from the surface.

Piepmeyer and Osten¹⁵ have investigated the size of the crater and quantity of material evaporated from the surface of the target in air at different pressures and different laser intensities. At atmospheric pressure, with increasing laser intensities these remain constant, whereas, at reduced pressure (1 torr) both the crater size and material

evaporated increase with increasing laser intensity. Further at any laser power the continuum intensity at the target surface decreases while that at $x = 0.5$ mm increases with increasing pressure. From these, they conclude that an atmospheric plasma is formed in front of the target, giving rise to the observed results. Our results also indicate a similar phenomenon.

Estimation of maximum plasma temperature

From the previous analysis, we should naturally expect the temperature of the plasma near the target surface to be higher in vacuum than in air. This is not observed to be so in the Ca spectra we have analysed, whereas from the aluminium spectrum we get a temperature in air of 27500°K and 33500°K in vacuum from the $\text{AlIII}/\text{AlIII}$ line intensity ratio. Though neither temperature is indicative of the maximum plasma temperature, it is indicative of the trend of change from air to vacuum. In Ca spectra, we are restricted to the calculation of the temperature by the CaI/CaII ratio only, due to the non-availability of oscillator strength values for CaIII lines. Hence, we have been unable to detect the change in maximum plasma temperature between air and vacuum. These lowest ionization stages are useful only below 12000 - 13000°K for temperature evaluation and will indicate only a later cooler stage of the plasma and will not reflect sensitively

evaporated increase with increasing laser intensity. Further at any laser power the continuum intensity at the target surface decreases while that at $x = 0.5$ mm increases with increasing pressure. From these, they conclude that an atmospheric plasma is formed in front of the target, giving rise to the observed results. Our results also indicate a similar phenomenon.

Estimation of maximum plasma temperature

From the previous analysis, we should naturally expect the temperature of the plasma near the target surface to be higher in vacuum than in air. This is not observed to be so in the Ca spectra we have analysed, whereas from the aluminium spectrum we get a temperature in air of 27500°K and 33500°K in vacuum from the $\text{AlIII}/\text{AlIII}$ line intensity ratio. Though neither temperature is indicative of the maximum plasma temperature, it is indicative of the trend of change from air to vacuum. In Ca spectra, we are restricted to the calculation of the temperature by the CaI/CaII ratio only, due to the non-availability of oscillator strength values for CaIII lines. Hence, we have been unable to detect the change in maximum plasma temperature between air and vacuum. These lowest ionization stages are useful only below $12000\text{--}13000^{\circ}\text{K}$ for temperature evaluation and will indicate only a later cooler stage of the plasma and will not reflect sensitively

the maximum temperature we are interested in.

For high Z elements the degree of ionization of the plasma is a good indication of the temperature of the plasma. In a time-integrated spectra the highest ionization will give the maximum temperature.²⁵ In the calcium spectrum the existence of a CaIII lines indicate a temperature of at least 22500°K (corresponding to unity density ratio of CaIII to CaII ions i.e. $n_{\text{CaIII}}/n_{\text{CaII}} \sim 1$). The existence of FIII lines show a much higher temperature than CaIII (this follows from the ionization potentials 6.1, 11.8 eV of CaI and II as against 17.4, 34.9 eV for FI and II). $n_{\text{FIII}}/n_{\text{FII}} \sim 10$ indicates a temperature of $60,000^{\circ}\text{K}$. The FIII lines are strongly observed only very close to the target up to 1 mm and hardly exist beyond 1-2 mm from target (Fig. VI.7). This suggests that FIII lines are emitted during the early stages of the plasma development and accordingly should provide temperatures nearer to the maximum temperature than the other lines. Further FIII lines are very much stronger in vacuum (Fig.VI.2), and almost missing in some air spectra. Thus our investigation of the plasma radiations in the visible and ultra-violet region indicate temperatures of the order of $60,000^{\circ}\text{K}$. In the absence of information on the higher ionization stages (whose radiations lie in the vacuum ultra-violet region) this temperature sets the lower limit to the maximum temperature in the plasma.

The temperature value of 12500°K obtained by the CaI/CaII indicates a later stage of the plasma development during its cooling due to expansion. In a similar manner the different electron densities obtained from CaI and CaII lines (Table VI.1) again indicate that they represent different stages of the plasma development, the higher ionization lines representing an earlier stage. This fact is borne out by an order of difference between the electron densities obtained from CaI and CaII lines (and in some cases among some CaI lines themselves), the densities from CaII lines being greater. Electron densities of 10^{19} cm^{-3} obtained from FII lines indicate an earlier stage in the plasma. Similar results have been reported by Evthushenko et al.³ Mandel'shtam et al.^{1,2} obtained a temperature of $3-6 \times 10^4 ^{\circ}\text{K}$ by time integrated spectra in the visible and 60 eV by X-ray absorber studies (near 10 \AA) in a laser produced He-spark, the former value representing a later already developed stage of plasma and the latter value representing the maximum temperature in the earliest stages of the plasma.

Self-reversal and shift of lines

All of the Ca, Sr and Al spectra show considerable self-reversal of many of the neutral and singly ionized resonance lines. These self-reversals are also highly asymmetric with the emission maximum occurring on the higher

wavelength wing of the line. The self-reversals indicate the presence of cooler outer layers of plasma containing neutral atoms in their ground state. There is considerable evidence for this fact in literature on LPP. The line emissions are shifted in the plasma due to such high density effects as stark shift etc.⁷ Similarly the ground and lower states may experience shifts due to similar reasons. Thus both the absorption and line emission peak show shifts. In order to detect these shifts in an aluminium plasma we simultaneously superposed spectra from an aluminium arc. We could obtain good superposed densitometer traces for only one or two lines. Such a superposition is shown for the AlI 3961 Å line along with Fig. VI.15. The absorption and emission peaks both are shifted to the red w.r.t the corresponding arc line, the emission peak having a shift of about 2.2 Å. Using the stark shift data of Griem²⁰ the shift corresponds to an electron density of 10^{18} cm^{-3} (with the negative sign in the formula for shift eqn. V.62).

Validity of LTE

The use of the line ratio methods assume existence of LTE for the lower ionization levels, (upper level of the lines) to be in equilibrium with the next ionization stage. Using eqn. V.16 for the total LTE and replacing E_2^{Z-1} by $E_{z-1}^{(\infty)}$ we can calculate the minimum electron densities needed for complete

LTE to hold. For a temperature of 2 eV this yields values of 3×10^{16} and $3 \times 10^{17} \text{ cm}^{-3}$ for CaI and CaII stages respectively. AlI and AlII need 3×10^{16} and 10^{18} cm^{-3} for $T_e \sim 2.5 \text{ eV}$ and finally FII stage gives nearly 10^{19} cm^{-3} for $T_e \sim 5 \text{ eV}$. From the electron densities obtained from the lines of these stages, we can see that in our case the use of Saha's equation is justified.

Recombination

Fig. VI.13A and B show the densitometer traces of the spectra shown in Fig. VI.7. The densitometer traces are shown for $x = 1, 2$ and 4 mm . As mentioned earlier, the temperature and electron densities obtained from these traces show a maximum at $x = 2 \text{ mm}$. The intensities of Ca I lines are found to be increasing from $x = 1 \text{ mm}$ through 4 mm , whereas CaII line intensities show a maximum at $x = 2 \text{ mm}$ (Table VI.2). This trend in the intensities of CaI and CaII lines could be attributed to recombination of Ca ions between $x = 0$ and 2 mm giving rise to increasing number of neutral species.

The FIII lines seen in most of the spectra, especially in Fig. VI.7 are confined predominantly to the lower part of the spectrum unlike the other lines. This behaviour of FIII lines is not clearly understood.

VI.5 Time-domain Studies

VI.5.1 Introduction

Time-domain studies of the emission from LPP at solid target surface have been studied by several workers,^{6,9,10} notably Boland et al.¹¹ From these studies, the following features of the temporal characteristics of the plasma emission emerge. By monitoring the emission of lines of different ionization stages at different distances (x) from the surface of the target it is found¹¹ that except the highest ionization stages, the lines of other lower ions at any distance x occur later in time lower the ionization and also correspondingly last longer with decreasing ionization. The highest ionization stages are more or less unresolved from the continuum which lasts for a short time during the laser pulse. The appearance time (or peak time) for each species increases with increasing distance from the target surface, from which their velocity and kinetic energies could be evaluated. It is estimated that as much as 75% of the laser energy goes into the expansion energy of the plasma¹¹ and this agrees with measurements with probes and mass spectrometers, mentioned in Chapter V.

In all the studies of the plasma heating and expansion done so far, the laser pulse is focussed on a new target area for each pulse to obtain reproducible and comparable results. In what follows we present some results

of photometric studies of the plasma emission from a LPP from aluminium, when successive laser pulses are incident on the same spot of the target surface.

VI.5.2 Experimental

The experimental set up is same as described for the spectroscopic studies. For the photoelectric detection, a slit is placed at the plate holder end of the Q-24 spectrograph and positioned at different lines of the spectrum. An RCA 6199 (S-11 response) photo-multiplier (PM_2) or a photodiode as the case may be is placed behind the slit and well screened from all other radiation except that coming through the spectrograph. The PM_2 output is monitored on an oscilloscope which is externally triggered by the laser pulse monitored by means of a beam-splitter, by photo-multiplier PM_1 (RCA 7102) just at the output of the laser (see Fig. II.3).

For this study care was taken to improve the response-time of the PMT and associated electronics. The anode load was $50\ \Omega$ and connected to the oscilloscope with a RG-59U cable of characteristic impedance nearly $50\ \Omega$. The cable was connected to the oscilloscope input through a $50\ \Omega$ matching termination. The last four dynode stages of the photo-multiplier are by-passed by capacitances to improve its high frequency response.

A high frequency photo-diode (Hewlett-Packard 5082-4205 Pin Photodiode) is also used to monitor the laser output and plasma emission. The diode using a supply of 9 V d.c. from a dry battery pack is terminated with a $50\ \Omega$ load and connected to the CRO input as described above. The photo-diode could not detect the light intensity at the camera end of the spectrograph, behind the slit. Hence it is essentially used to monitor the laser pulse to determine the pulse width and to monitor the plasma emission at the spectrograph entrance. The response of the photo-diode with $50\ \Omega$ termination is found better than that of the photo-multiplier.

The laser pulse and the plasma emission were monitored on a Tektronix storage scope. But none of the available storage scopes could write and store at the maximum sweep speed of $0.01\ \mu\text{sec}/\text{cm}$ used for these studies. Attempts at photographing the trace from the CRO screen using a Tektronix C-12 camera and fast polaroid films (3000 ASA) were not successful as the films which had exceeded the expiry date failed to record the single sweep trace at this sweep speed ($.01\ \mu\text{sec}/\text{cm}$), even with multiple exposure. Hence, for these studies, we had to contend with visual observation of CRO signal. Hence no quantitative estimate is made and only qualitative analysis of the CRO signals observed is attempted. Though the signal traces shown are due to repeated

observation, because of the high sweep speed and fast rise-times of signals the initial portion of the signals and the instant of peak position are subject to errors.

VI.5.3 Results and Discussion

Laser pulse

The laser pulse is monitored by the photo-diode placed in front of the spectrograph slit, the beam deflected onto it by means of a beam splitter placed at the site of the target, none of the lenses being used. Laser intensity falling on the photo diode is considerably attenuated by using corning filters. Typical laser pulse signal obtained from the photo-diode is shown in Fig. VI.17(a). The laser output contains two pulses separated by about 500-600 nsecs. The main pulse is of the order of 50 nsec in width and the second is broader, whereas the main pulse is seen to be consistently of the same width, the second pulse varies both in its position on the time-scale relative to the first pulse and also in its width.

The laser pulse was also monitored at the end of the spectrograph by PM_2 with the beam deflected onto the spectrograph slit. Typical outputs from PM_2 are shown in Fig. VI.17(b) and (c). The main pulse so obtained is broader than with the photo-diode. Often a second broader pulse immediately follows the main one. Since only the first pulse is monitored

in detail, the position and structure of second pulse is left considerably uncertain and is not always shown. Quite often only the main pulse is seen, somewhat broader without the second pulse.

Plasma emission

Photo diode is used to monitor the plasma emission by focussing the plasma emission normal to laser axis on to the photo diode in front of the spectrograph entrance slit. The output with two corning 2.58 filters (transmits only above 6200 Å) before the diode is shown in Fig. VI.17(d). This may be predominantly the scattered laser radiation and part of the plasma continuum. With filter 4.96 (transmits between 3500-6000 Å) replacing the two 2.58 the signal is as shown in Fig. VI.17. This would consist predominantly the line emissions from the aluminium plasma and the continuum. It shows a delay between the start of the laser pulse and plasma emission. This can be attributed to the plasma formation and strong heating occurring only above certain laser power level. This delay would naturally depend on the laser pulse power. The rest of the results that follow are that of plasma line emission as monitored by PM₂ at the camera end of the spectrograph.

The emission of Al^{III} (4480-4529 Å) Al^I (3082 and 3092 Å) and the continuum around 4300 Å as monitored through PM₂ at different distances ($x = 0, 2$ and 5 mm) from target

surface are shown in Fig. VI.18 (target in air) and Fig. VI.19 (target in vacuum).

Target in air

The AlII and AlIII time-profiles were not well resolved (hence AlII not shown), whereas AlI is slightly separated from AlIII. The emission profiles often showed a twin pulse profile (shown as 2 in Fig. VI.18(a)) which is found to be due to a similar structure in the laser pulse as monitored by PM_1 (Fig. VI.17(b) - 2). In the subsequent figures these twin pulse traces are indicated by 2 and the normal single pulse by 1.

There is a considerable change in slope of the initial rising portion of the AlIII signals at $x=0$ and $x=1.5$ and 5 mm. The convex rising portion at $x = 0$ could be due to accompanying continuum which is absent already at $x = 1.5$ mm. The amplitude of AlIII signal is considerably less at $x = 5$ mm, in accordance with the presumption that this being one of the highest ions in the plasma is confined close to target surface. While observing the traces pulse after pulse, it was seen that the pulses used to peak earlier than before and after many pulses the AlIII pulse at $x = 5$ mm was seen to peak much earlier (shown by 3 in Fig. VI.18b) than the initial pulses (shown by 1 in same figure). The pulse was seen to have advanced at $x = 1.5$ mm also. At this

stage when the target surface was shifted to expose a fresh area to the laser radiation the pulse was now seen to peak later (shown by 3' in Fig. VI.18c) corresponding to the early pulses in the previous run (such as 1 in Fig. VI.18b).

The continuum around 4300 \AA is shown in Fig. VI.18d and it is seen that it is reduced considerably in intensity at $x = 2 \text{ mm}$. There was no detectable signal at $x = 5 \text{ mm}$. Thus the continuum emission seems to be restricted to a distance of 1-2 mm from surface.

All profiles are shown in Fig. VI.18e for $x = 0$ and 5 mm (shown by 1, and the distances indicated on the profile). It is seen that the peaks are somewhat delayed and separated w.r.t AlIII peaks. Further All profile corresponding to $x = 5 \text{ mm}$ peaks slightly later and also starts slightly later than the one for $x = 0 \text{ mm}$. This delay (of about 40 nsec) in the arrival time and peaks between the profiles for $x = 0$ and $x = 5 \text{ mm}$ leads to a rough estimation of the ion-velocities to be of the order of 10^7 cms/sec . This value seem to be somewhat high for our power levels and plasma temperature. This might indicate the velocity of the detonation wave. Similar to the AlIII lines, here also we observe that after many pulses the peak advances to a position indicated by 3 in Fig. VI.18c and the difference in peak position for $x = 0$ and 5 mm is hard to distinguish visually. In general, All pulses last longer and are equally strong both at $x = 0$ and

5 mm (see the amplitude scales in figure).

Target in vacuum: (shown in Fig. VI.19)

The general features are similar. As before the normal pulses are indicated by 1, the twin-pulse structure by 2 and the advanced peak profile after repeated pulses by 3. The AlI peak also advances and seems to be indistinguishable from the peak position of AlIII after repeated pulses. In vacuum the apparent advance of the peaks is felt after only a few pulses, fewer than needed when target is in air.

It is also observed that after repeated pulses a very deep crater with a somewhat tapered structure is seen on the target surface. After many pulses a through hole is drilled in the target (1.5 mm thick aluminium strip) at which time the signals get very weak and disappear. The number of pulses of the same intensity needed in vacuum are much fewer (about 30 or so) than that required in air. This is possibly due to the fact that all the laser energy is useful in vaporizing and producing material plasma in vacuum than when target is in air and screened by an atmospheric plasma.

The advance of the peaks of the time-profiles indicate a greater velocity of the ions and/or formation of the plasma much earlier in the laser pulse. It is quite possible that the plasma formed in the interior of the crater

where the beam is focussed, is subjected to increased pressure due to lateral confinement. The particles are ejected at a greater velocity due to the increased pressure. The plasma is heated to greater temperature in the confined region. As the crater develops, the laser radiation is focussed further into the surface where the laser intensity will be higher; the tapering hole indicates that the focus lies within the target surface. Both these facts might explain the advance in the peaks in the time-profile of the ion emissions. Similar effect of the crater formation was observed by Linlor²⁵ during studies of ion emissions by probe methods.

VI.6 Conclusions

LPP from the surfaces of solid targets such as CaF_2 , SrF_2 , Al and C are investigated spectroscopically for spectral studies and photometrically for time-domain studies. The effect of atmosphere on the material plasma formation is evaluated from spectra of the target plasma taken both when target is in air and in vacuum (1-10 μ). Spectra of CaF_2 clearly showed that CaIII lines appeared newly or increased in intensity in vacuum, a similar behaviour observed for FII lines, no FI lines being observed. FIII lines were mostly seen strongly in vacuum spectra only. From the presence of strong FIII lines a temperature of 60000°K is estimated for the maximum temperature of plasma close to target. Access

to VUV region of spectra not being available, this places a lower limit on the maximum temperature. The temperature in vacuum is found to be higher than in air from an analysis of Al-plasma spectra using AlIII/AlIII line intensity ratio. The observed changes both in the spectra and also in the physical nature of the plasma, when the target was in air or vacuum, is interpreted as due to the breakdown of air and formation of an atmospheric plasma in front of the target. The breakdown threshold is considerably reduced by the presence of the target which (by its initial evaporation) supplies the initial electrons needed for avalanche breakdown. The atmospheric plasma so formed will subsequently absorb the laser energy and effectively screen the target from the laser. No such screening will be effective in vacuum.

The temperatures evaluated at the top of the spectra (corresponding to the lateral extreme of plasma) are smaller than at the centre of the plasma. This is in keeping with the fact that this temperature is that of a plasma which has already cooled due to expansion. Further, in air, the temperature and densities are maximum around $x = 2$ mm in front of the target, indicating the presence of the atmospheric plasma. Asymmetric self-reversals and shifts of lines are observed and measured.

The time-domain studies of plasma emission profiles show the effect of successive laser pulses being focussed on

the same target area, unlike the previous studies in which a new target surface is provided for each laser pulse. The lines of AlI and AlIII from an aluminium plasma are monitored by photo-multiplier at the back of a slit at corresponding line positions at the spectrograph camera end. AlI lines showed slight temporal separation from AlIII lines. Its peak occur a little later at a distance of 5 mm from target surface as compared to close to target surface. After many pulses are incident on the same target spot, all the line profiles showed a considerable advance of the peaks of the time profiles. Simultaneously, a deep crater is being formed on target surface finally resulting in a through-hole formation. This advancement of the peaks is interpreted as being due to the increased ejection velocity of particles and plasma being heated to higher temperature due to the increased lateral confinement inside the crater.

Incidentally, this crater formation and drilling is faster in vacuum than in air due to the screening action of the atmospheric plasma formed in air. This aspect of the study is important from the point of view of laser machining and drilling. One method of circumventing and overcoming the atmospheric plasma effect, as most laser drilling are to be done in open atmosphere, is to operate the laser at lower outputs and provide the same energy over a longer

period of time, thus reducing the formation and heating of atmospheric and/or material plasma. Study of these aspects will lead to a better utilization and design of lasers for industrial purposes.

References

1. S. L. Mandel'shtam, P. P. Pashnin, A. M. Prokhorov, Yu. P. Raizer and N. K. Sukhodreev, Sov. Phy - JETP, 20, 1344 (1965).
2. S. L. Mandel'shtam, P. P. Pashnin, A. M. Prokhorov, Yu. P. Raizer and N. K. Sukhodreev, Sov. Phy - JETP, 22, 91 (1966).
3. T. P. Evthushenko, A. N. Zaidel, G. V. Ostrovskaya and T. Ya. Chelidze: Sov. Phy - Tech. Phy., 11, 1126 (1967).
4. W. F. Brearman, C. R. Stumpf and H. J. Kunze: J. App. Phys., 40, 2549 (1969).
5. N. H. Burnett and P. R. Smy: Can. J. Phys., 48, 1421 (1970).
6. R. H. Scott and A. Strasheim: Spectrochim Acta, 25B, 311 (1970).
7. F. P. J. Valero, D. Goorvitch, B. S. Frankel and B. Ragent, J. Opt. Soc. Am., 59, 1380 (1969).
8. D. D. Burgess, B. C. Fawcett and N. J. Peacock: Proc. Phy. Soc., 92, 805 (1967).
9. P. Dhez, P. Jaegle, S. Leach and M. Velghe: J. App. Phys., 40, 2545 (1969).
10. W. Seka, J. L. Schwob and C. Breton: J. App. Phys., 41, 3440 (1970).
11. B. C. Boland, F. E. Irons and R. W. P. McWhirter, J. Phys. B (Proc. Phy. Soc.), Ser. 2, 1, 1180 (1968).
12. J. L. Bobin, P. P. Langer and G. Tonon: J. App. Phys., 39, 4184 (1968).
13. D. C. Emmony and J. Irwing: J. Phys. D, 2, 1186 (1969).
14. E. H. Piepmeier and H. V. Malmstadt: Anal. Chem., 41, 700 (1969).
15. E. H. Piepmeier and D. E. Osten: App. Spectros., 25, 642 (1970).
16. A. N. Zaidel, W. K. Prokofev and S. M. Raiskii, Tables of Spectral Lines (Veb Verlag Technik, Berlin, 1961).

17. W. L. Weise, M. W. Smith and B. M. Miles: Atomic Transition Probabilities, Vol. I-III (Nat. Bur. of Stds: NSRDS-NBS 22).
18. A. N. Zaidel', V. K. Prokofev, S. M. Raiskii, V. A. Slavnyi and E. Ya. Shreider: Tables of Spectral Lines (Plenum Press, N.Y., London, 1970).
19. I. S. Bowen, *Phy. Rev.*, 31, 497 (1928).
20. H. R. Greim, *Plasma Spectroscopy* (McGraw-Hill, New York, 1964) Table 4-5 and 4-6.
21. J. R. McNally Jr: in *Optical Spectrometric Measurements of High Temperatures*, Ed. P. J. Dickerman (Univ. of Chicago Press, 1961), p 81-83.
22. H. R. Greim, Ref. 20, p 275, Fig. 13-2.
23. Yu. P. Raizer: *JETP Lett.*, 7, 55 (1968).
24. N. G. Basov, V. A. Boiko, Y. P. Voinov, E. Ya. Kononov, S. L. Mandelshtam and G. V. Sklizkov: *JETP Lett.*, 5, 141 (1967); 6, 291 (1967).
25. W. I. Linlor: *Laser interaction and related plasma phenomenon*, Vol. I (Plenum Press, N.Y., 1971) p 173.

Table VI.1

Electron densities obtained from different CaI and CaII lines for air spectra (from Fig.VI.10)

Line (A)		Electron density (in cm^{-3})
CaII	3737	$5-7 \times 10^{18}$
	3179	5×10^{18}
CaI	4526	5×10^{16}
	3644	8×10^{16}
	4455	10^{18}
	4226	10^{19}

Table VI.2

a. Temperatures ($^{\circ}\text{K}$) at different distances from the target surface in a CaF_2 plasma (estimated from Fig. VI.13A and 13B by CaI/CaII line intensity ratio)

$\frac{\text{CaI}}{\text{CaII}} \left(\frac{\text{\AA}}{\text{\AA}} \right)$	Distance from target (mm)		
	1	2	4
$\frac{4445}{3737}$	11000	12500	9000
$\frac{4300}{3736}$	11000	13000	9250
$\frac{3637}{3706}$	11500	12000	8750
$\frac{4226}{3968}$	15500	14000	10000
$\frac{4445}{3158}$	10000	12500	8000
$\frac{4226}{3158}$	13000	15000	10500

b. Density and intensity at different distances from the target surface in a CaF_2 plasma for CaI and CaII lines (estimated from Fig. VI.13A and 13B)

4445(I)	$0.6 \times 10^{18} (404)$	$0.85 \times 10^{18} (531)$	$0.5 \times 10^{18} (760)$
3637(I)	$5 \times 10^{16} (58.5)$	$7.5 \times 10^{17} (218)$	$7.5 \times 10^{16} (142)$
4226(I)	$8.5 \times 10^{18} (204)$	$8.5 \times 10^{18} (312)$	$8.5 \times 10^{18} (525)$
4300(I)	(353)	(417)	(520)
3737(II)	$2.5 \times 10^{18} (148)$	$5 \times 10^{18} (430)$	$0.9 \times 10^{18} (51)$
3706(II)	$2 \times 10^{18} (84)$	$3.5 \times 10^{18} (280)$	$10^{18} (33)$
3968(II)	$6 \times 10^{18} (528)$	$6 \times 10^{19} (440)$	$1.5 \times 10^{19} (324)$
3158(II)	$3 \times 10^{18} (95)$	$8 \times 10^{18} (576)$	$10^{18} (29.5)$

Densities are in cm^{-3} . Intensities, in arbitrary units, are given in brackets.

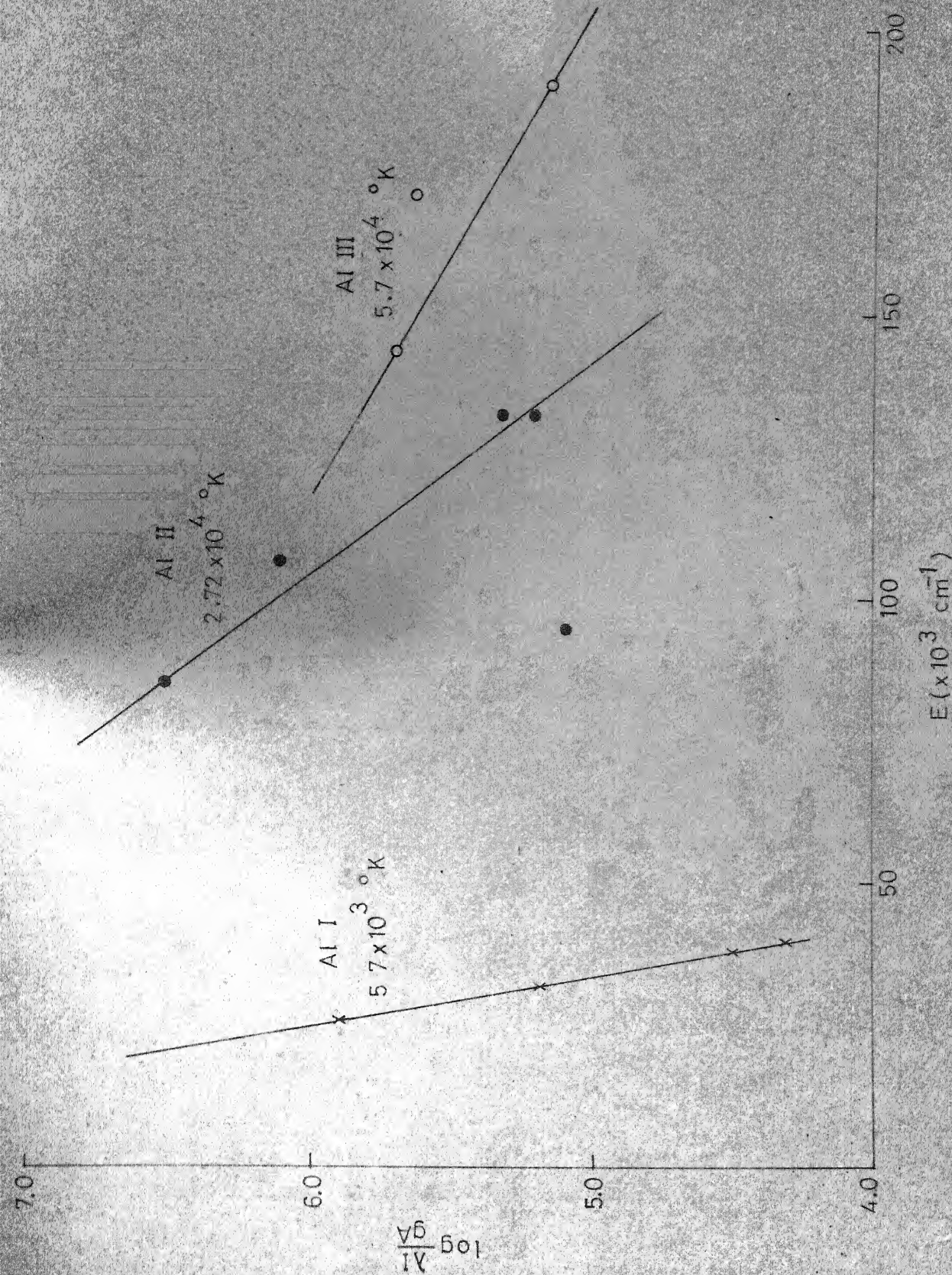


FIG. VI. 8 BOLTZMAN PLOT FOR ALUMINUM (SPECTRUM IN FIG. VI. 5 AND DENSITOMETER TRACE IN FIG. VI. 14.)

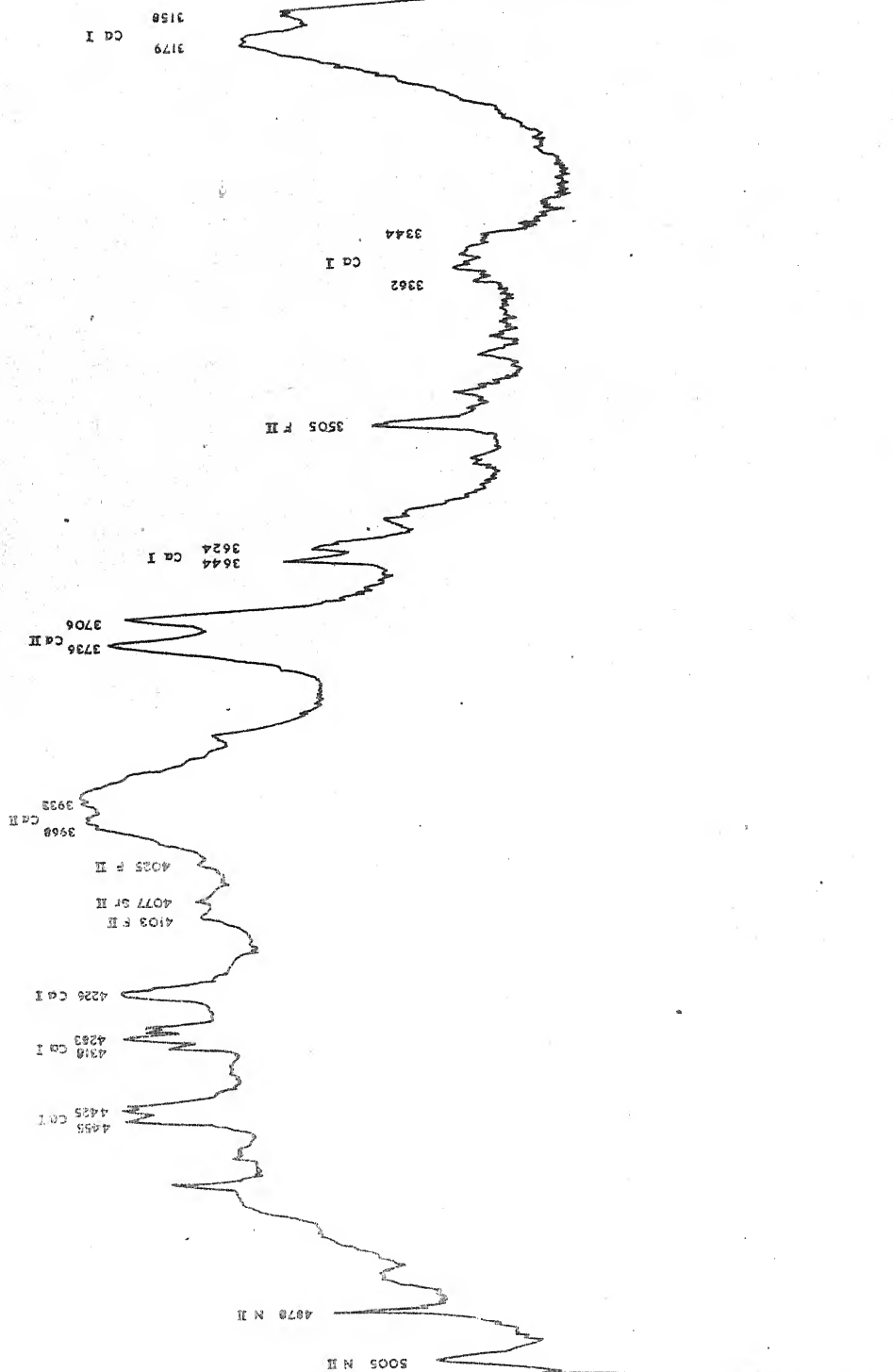


FIG. VI.9 DENSITOMETER TRACE SPECTRUM OF CaF_2 IN AIR (ALONG THE CENTRE)

4 mm

2 mm

 $x = 1 \text{ mm}$

100

4500

4450

4400

4350

4300

4250

4200

4150

4100

4050

4000

4050

4100

4150

4200

4250

4300

FIG. 12A DENSITOMETER TRACE SHOWING CO_2 IN AIR AT DISTANCES
1, 2 AND 4 mm FROM THE TARGET SURFACE (4220 - 4600 Å)

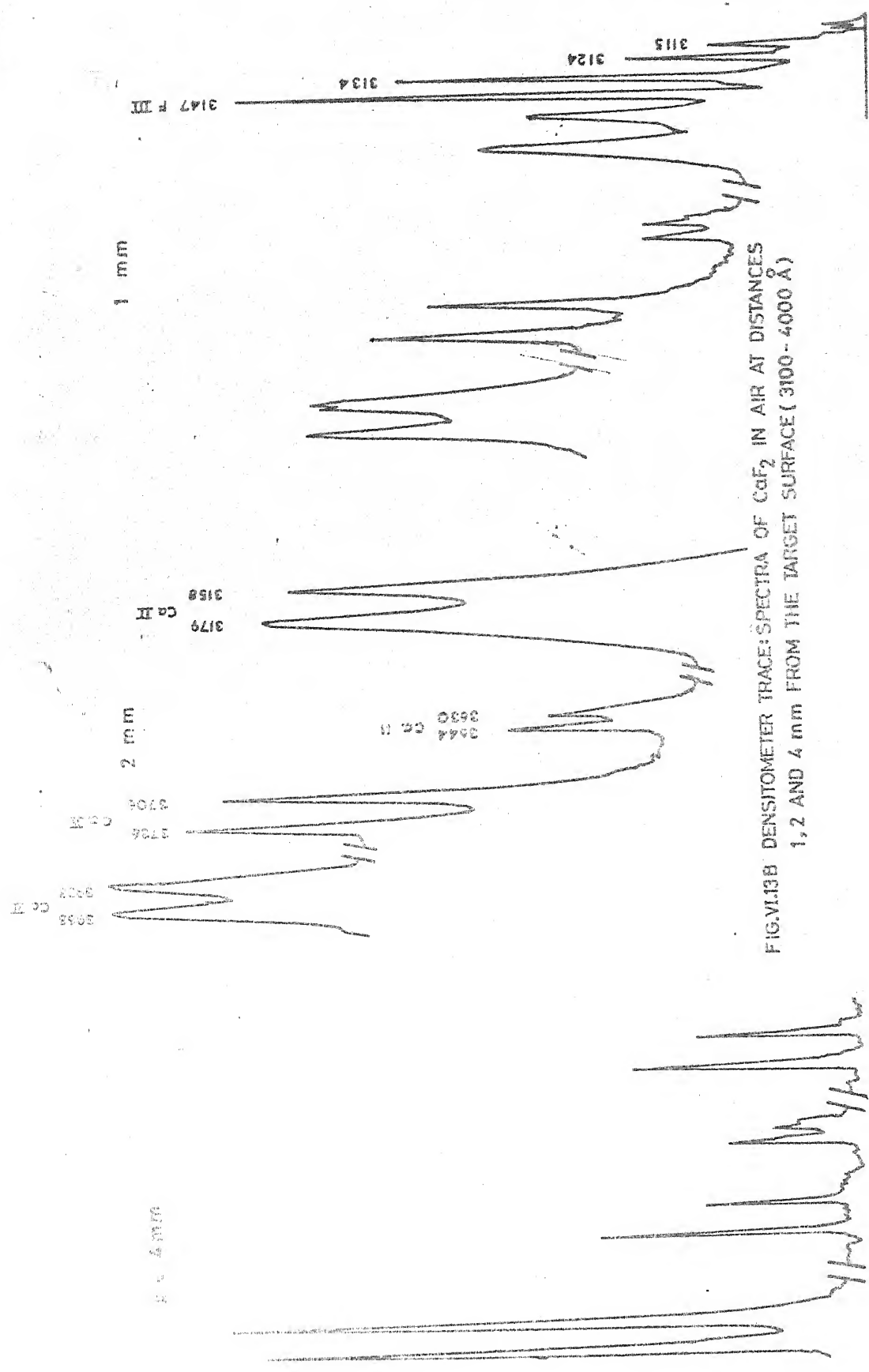


FIG. VI.13B DENSITOMETER TRACE SPECTRA OF CaF_2 IN AIR AT DISTANCES 1, 2 AND 4 mm FROM THE TARGET SURFACE (3100-4000 \AA)

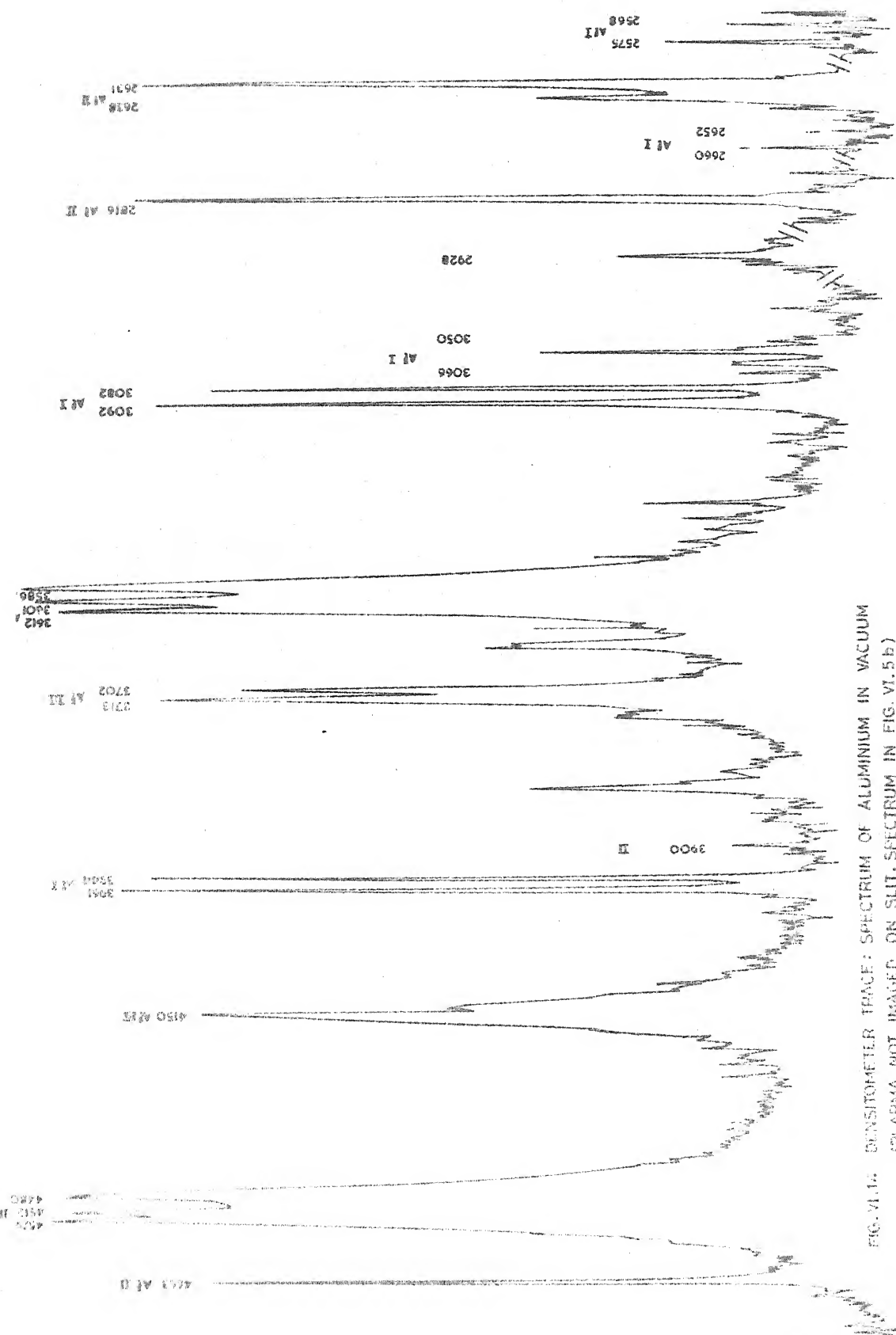
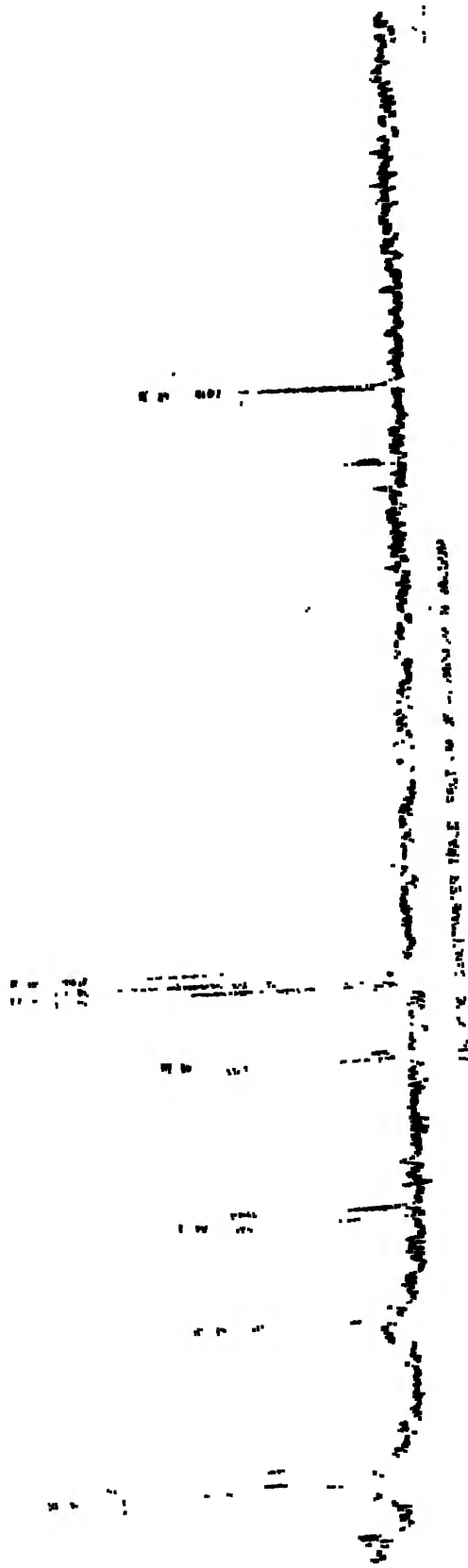


FIG. VI.1: DENSITOMETER TRACE: SPECTRUM OF ALUMINUM IN VACUUM
(PLASMA NOT IMAGED ON SLIT. SPECTRUM IN FIG. VI.5.b)



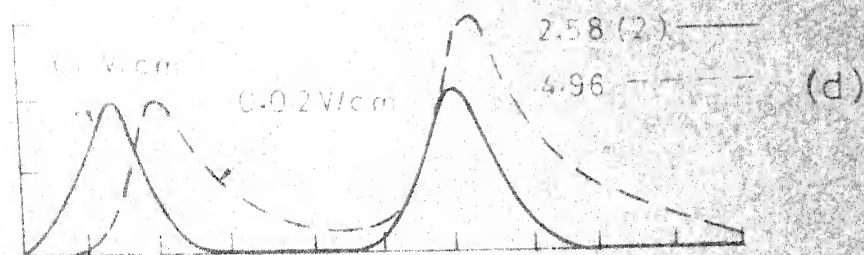
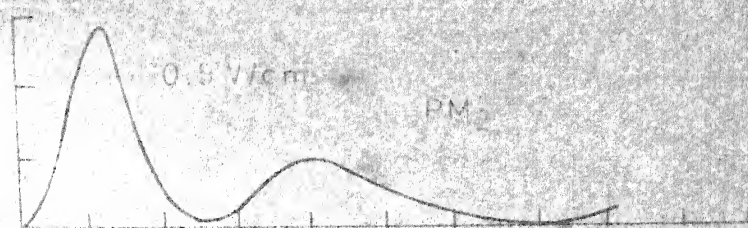
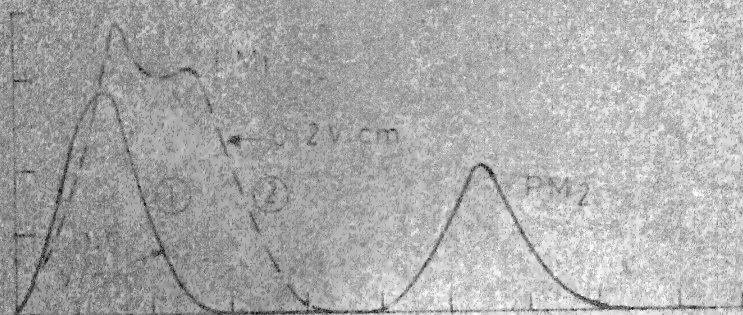
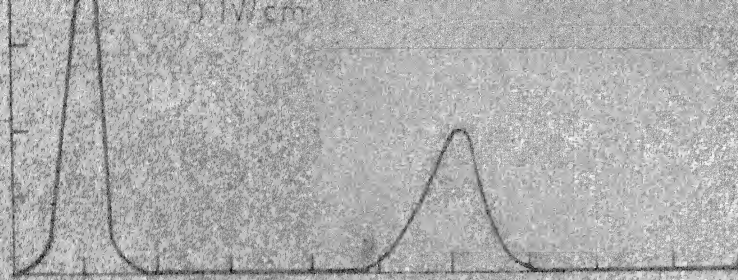


FIG VI.17 OSCILLOSCOPE TRACE(Visual) OF THE RUBY LASER PULSE MONITORED BY (a) PHOTO DIODE (b) (c) PHOTOMULTIPLIER (d) PLASMA EMISSION MONITORED BY PHOTODIODE THROUGH CORNING GLASS

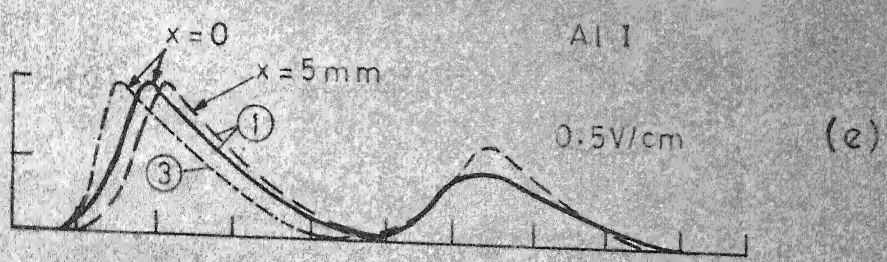
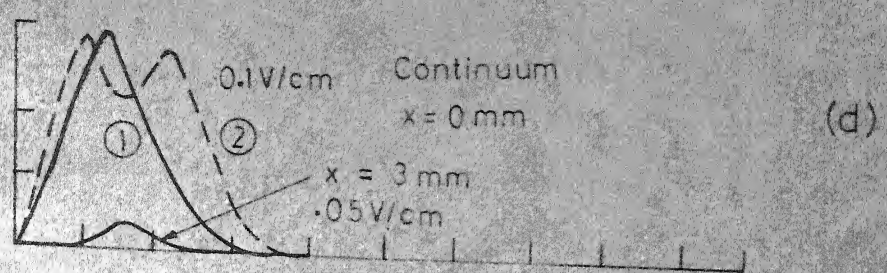
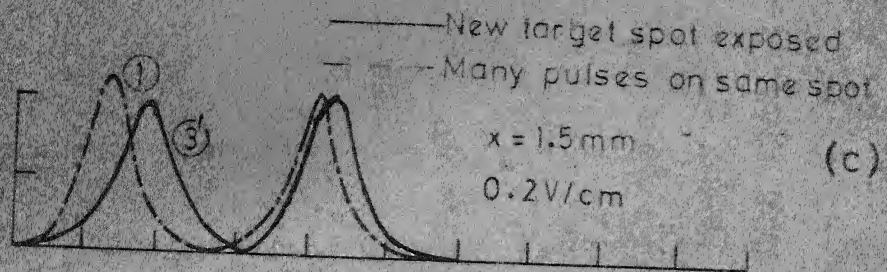
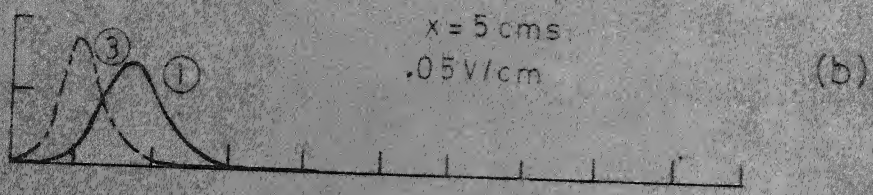
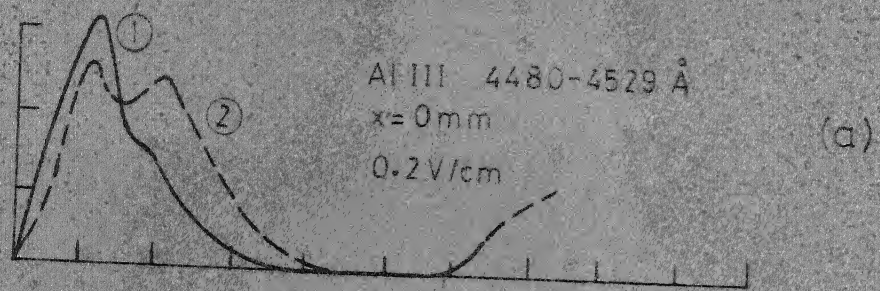


FIG. VI. OSCILLOSCOPE TRACE (VISUAL) FOR DIFFERENT LINES OF THE ALUMINIUM PLASMA EMISSION (TARGET IN AIR).
SOLID LINE (1) NORMAL PULSE
DOTTED LINE (2) TWIN PULSE STRUCTURE
CHAIN DOTTED LINE (3) PEAK ADVANCE AFTER SEVERAL PULSES ON SAME TARGET SPOT.

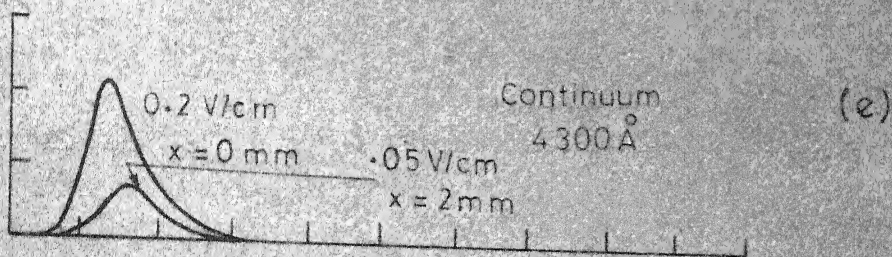
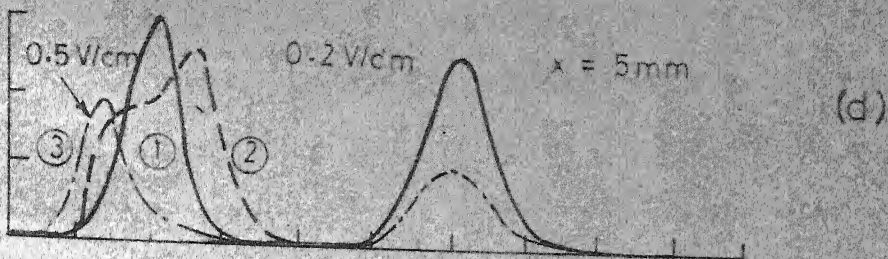
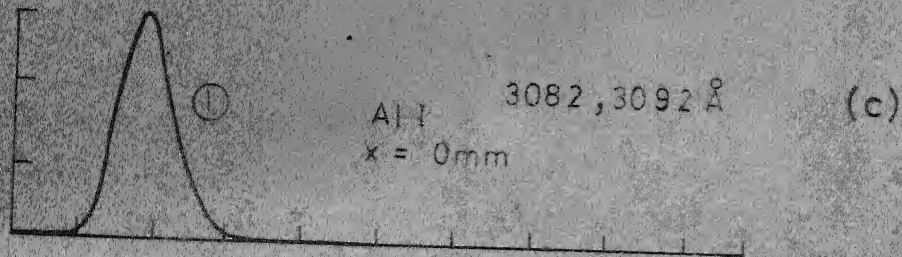
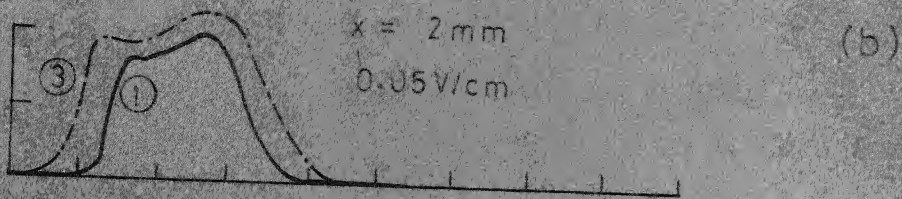
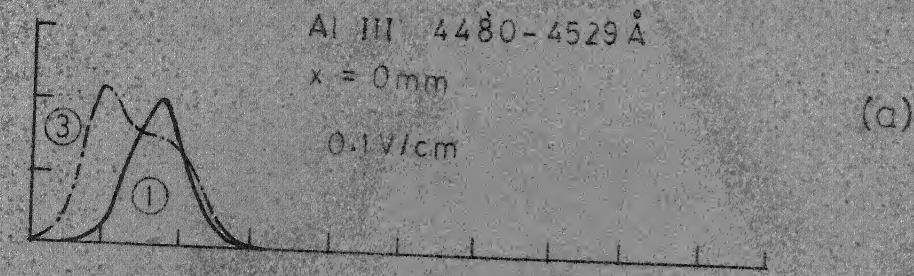


FIG. VI.19. OSCILLOSCOPE TRACE (VISUAL) FOR DIFFERENT LINES OF THE ALUMINIUM PLASMA EMISSION (TARGET IN VACUUM). SOLID LINE (1) NORMAL PULSE. DOTTED LINE (2) TWIN PULSE STRUCTURE. CHAIN DOTTED LINE (3) PEAK ADVANCE AFTER SEVERAL PULSES ON SAME TARGET SPOT.

Appendix-1

Interpolation procedure to obtain the constants in the modified Hartmann's formula:

$$n_{\lambda} = n_{\infty} + \frac{C}{(\lambda - \lambda^*)^{1.6}} \quad (\lambda \text{ and } \lambda^* \text{ in microns})$$

we will define:

$$\beta = \frac{1}{(\lambda - \lambda^*)^{1.6}}$$

and

$$\gamma = \frac{\beta_1 - \beta_2}{\beta_1 - \beta_3}$$

Where $\lambda_1, \lambda_2, \lambda_3$ are standard wave lengths such as for example 0.43583 (Hg), 0.65628 (H α) and 0.54607 (Hg) respectively.

Values of β for each of the three wave lengths 1, 2 and 3 are calculated for values of the constant λ^* from 0.07 to 0.15 in steps of 0.0005 or other suitable steps. For each λ^* , γ is calculated from the β values already calculated. From the given refractive index values n_1, n_2 and n_3 at the above three wave lengths we can obtain

$$\gamma_c = \frac{n_1 - n_2}{n_1 - n_3}$$

This γ_c is compared with the γ evaluated above for different λ^* and the value of λ^* is picked out for which $\gamma = \gamma_c$ (if necessary one could further interpolate around this λ^* with a finer step intervals. Also in case the λ^* corresponding to $\gamma = \gamma_c$ is beyond the considered range, we can recalculate the values with different range of values for λ^*).

With this value of λ^* values of β_1 , β_2 and β_3 are picked out corresponding to this λ^* and the constant C calculated from:

$$C = \frac{n_1 - n_2}{\beta_1 - \beta_2} \quad \text{or} \quad \frac{n_1 - n_3}{\beta_1 - \beta_3}$$

one can take the average value of the two C's.

Knowing λ^* and C, the remaining constant can be obtained from substituting in the Hartmann's formula

$$n_1 = n_{\infty} + C\beta_1$$

There are three such equations, each of which gives a value of n_1 which should tally within 0.00001. Again an average of the three n_1 values can be taken.

Using the calculated constant one can back-calculate the refractive indices at λ_1 , λ_2 and λ_3 or any of the standard wave length for which refractive index is known, to check the accuracies of the constants. Usually no further refinement is found necessary.

Using these three constants the refractive index at any other wave length, especially at the Raman shifted wave lengths, could be calculated.

A similar procedure is adopted for the data at another temperature.

B. Calculation of Thermal period

Let us define the following:

δn = change in refractive index per $^{\circ}\text{C}$

$\delta(\frac{\Delta k}{2})$ = change in $\frac{\Delta k}{2}$ per $^{\circ}\text{C}$

The refractive indices at the required Raman wave lengths are obtained by procedure A at the two temperatures 20°C and 25°C for which standard data are available. Assuming a linear variation with temperature in this range, we can calculate δn as $(n_{20} - n_{25})/5$.

Writing down Δk for the four-wave mixing process for the generation of second Stokes as $\omega_0 - 2\Delta$:

$$\begin{aligned}\Delta k &= k_0 + k_{-1} - k_{+1} - k_{-2} \\ &= \frac{1}{c} [n_0 \omega_0 + n_{-1}(\omega_0 - \Delta) - n_{+1}(\omega_0 + \Delta) - n_{-2}(\omega_0 - 2\Delta)]\end{aligned}$$

Where n_m are the refractive indices at the wave length of the m^{th} order SR wave. Further remembering that $\frac{f}{c}$ is the frequency in wave numbers (cm^{-1}) we have

$$\begin{aligned}\Delta k &= 2\pi [f_0^{\text{cm}^{-1}} (n_0 + n_{-1} - n_{+1} - n_{-2}) - \Delta^{\text{cm}^{-1}} (n_{-1} + n_{+1} - 2n_{-2})] \\ \delta(\frac{\Delta k}{2}) &= \pi [14400(\delta n_0 + \delta n_{-1} - \delta n_{+1} - \delta n_{-2}) - \Delta^{\text{cm}^{-1}} (\delta n_{-1} + \delta n_{+1} - 2\delta n_{-2})] \\ &= \pi X \text{ (say)}\end{aligned}$$

the thermal period P in $^{\circ}\text{C}$ is given by the condition

$$|\delta(\frac{\Delta k}{2})| PL = \pi$$

hence the product PL is the reciprocal of the quantity $|X|$ in the square bracket which is to be evaluated knowing the δn 's and Δ for the liquid.

Appendix 2

Time averaged work done per unit volume by a harmonic field at frequency ω on a dielectric medium is given by

$$W = \frac{1}{T} \int_0^T \bar{E} \frac{d\bar{P}}{dt} dt \quad (1)$$

where electric field \bar{E} and induced polarization \bar{P} are given by

$$\bar{E} = \frac{1}{2} [E \exp -i\omega t + c.c.]; \quad \bar{P} = \frac{1}{2} [P \exp -i\omega t + c.c.] \quad (2)$$

hence $W = -\frac{\omega}{2} \text{Im} (EP^*) = \frac{\omega}{2} \text{Im} (E^*P)$

since $P = \chi E = (\chi' + i\chi'') E$, we have $W = \frac{\omega}{2} \chi'' |E|^2$

for $\chi'' > 0$, $W > 0$ i.e. the harmonic field experiences loss

$\chi'' < 0$, $W < 0$ i.e. there is gain at frequency ω and the radiation field is amplified. i.e., Negative imaginary susceptibility corresponds to positive gain for the radiation field.

Note : If the time-dependence of \bar{E} and \bar{P} in eqn. (2) is:

defined as $\frac{1}{2} [E \exp i\omega t + c.c.]$ and $\frac{1}{2} [P \exp i\omega t + c.c.]$ respectively, then $\chi'' > 0$ corresponds to positive gain.

Appendix 3

Atomic Lines observed in the different plasma spectra, the excitation energies of the levels involved and other relevant data.

Line (Å)	Spectra Air Vac	Lower Level E_i (cm ⁻¹)	Upper Level E_k (cm ⁻¹)	Transition array	Multiplet	g_i	g_k	f_{ik}
CaI 5260.39	W	20335	39340	4s3d-3d(² D)4p ¹	3D-3P ⁰	3	5	0.0042
5261.7		20335	39335			3	3	0.062
5188.8	W	23652	42919	4s4p-4s(² S)5d	1P ⁰ -1D	3	5	0.27
4878.1	S	21850	42344	4s3d-4s(² S)4f	1D-1F ⁰	5	7	0.094
4685.2	W	23652	44990	4s4p-4s(² S)6d	1P ⁰ -1D	3	5	0.044
4585.8	S	20371	42171	4s3d-4s(² S)4f	3D-3F ⁰	7	9	0.093
4581.4		20349	42171		3D-3F ⁰	5	7	0.092
4526.9	m	21850	43933	4s3d-3d(² D)4p ¹	1D-1P ⁰	5	3	0.075
4456.6		15316	37748	4s4p-4s(² S)4d	3P ⁰ -3D	5	3	0.00437
4455.8	S	15316	37752			5	5	0.062
4454.7		15316	37757			5	7	0.357
4435.7	S	15210	37748		3P ⁰ -3D	3	3	0.105
4425.4	S	15158	37748			1	3	0.412
4355.0	m	21850	44805	4s3d-4s(² S)5f	1D-1F ⁰	5	7	0.074

Appendix 3 - Contd.

4318.6	S	m	15316	38465	4s4p-4p ²	3p ^o -3p	5	3	0.124
4307.7	S	m	15210	38418			3	1	0.185
4302.5	S	m	15316	38552			5	5	0.377
4298.9			15210	38465			3	3	0.129
4289.4			15158	38465			1	3	0.498
4283.0	S	m	15210	38552			3	5	0.199
4226.7	VS	S	0	23652	4s ² -4s(2S)4p	1s-1p ^o	1	3	1.75
4062.4	m	W							
3875.8	VW	-	20371	46165	4s3d-4s(2S)6f	3p ^o -3p ^o	7	9	0.023
3644.7	S	W	15316	42745	4s4p-4s(2S)5d	3p ^o -3D	5	5	0.0188
3644.4			15316	42747			5	7	0.099
3630.9	S	VW	15210	42743			3	3	0.0302
3630.7			15210	42745			3	5	0.098
3624.1	S	-	15158	42743			1	3	0.125
3487.6	m	-	15316	43981	4s4p-4s(2S)7s	3p ^o -3S	5	3	0.0085
3361.9	m	-	15316	45052	4s4p-4s(2S)6d	3p ^o -3D	5	7	0.053
3350.2	m/w	-	15210	45050			3	5	0.050
3180.5	m	S	15316	46748	4s4p-4s(2S)9s	3p ^o -3S	5	3	0.0026

Appendix 3 - Contd.

3136.0	W	-	15158	47036	4s4p-4s(² S)8d	³ P ^o - ³ D	1	3	0.018
3117.6	W	-	15316	47382	4s4p-4s(² S)10s	³ P ^o - ³ S	5	3	0.0015
3095.0	W	-							
3009.2	S	W	15316	48538	4s4p-3d ²	³ P ^o - ³ P	5	3	0.035
3006.8			15316	48564			5	5	0.101
3000.8			15210	48524			3	1	0.071
2999.6			15210	48538			3	3	0.0376
2997.3			15210	48564			3	5	0.054
2994.9	S	W	15158	48538			1	3	0.148
2721.6	W	-	0	36732	4s ² -4s(² S)5p	1s-1p ^o	1	3	9x10 ⁻⁴
2398.6	m	-	0	41679	4s ² -4s(² S)6p	1s-1p ^o	1	3	0.0433
<u>CaII</u>									
3933.6	VS	S	0	25192	4s-4p	2s-2p ^o	2	4	0.69
3968.5	VS	S	0	25414			2	4	0.69
3736.9	S	S	25414	52167	4p-5s	2p ^o -2s	4	2	0.173
3706.1	S	S	25192	52167			2	2	0.173
3179.3	S	S	25414	56859	4p-4d	2p ^o -2D	4	6	0.82
3158.8	S	S	25192	56839			2	4	0.91
2208.6	W		25414	70678	4p-6s	2p ^o -2s	4	2	0.0227

Appendix 3 - Contd.

CaIII

3537.7	-	W	243927	272185	4s ₄ -4p ₁₀
3372.6	-	W	242543	272185	4s ₅ -4p ₁₀
3119.6	-	VW	247693	279738	4s ₂ -4p ₆
3028.6	-	W	245608	278616	4s ₃ -4p ₇
2988.6	m	m	243927	277377	4s ₄ -4p ₈
2924.3	W	m	247693	281878	4s ₂ -4p ₃
2899.7	m	S	242543	277018	4s ₅ -4p ₉
2881.6	S	m	243927	278616	4s ₄ -4p ₇
2869.9	W	m	242543	277377	4s ₅ -4p ₈
2866.6	-	W	247693	282568	4s ₂ -4p ₂
2813.8	VW	W	245608	281136	4s ₃ -4p ₄
2791.6	VW	VW	243927	279738	4s ₄ -4p ₆
2704.8	W	VW	245608	282568	4s ₅ -4p ₂
2687.8	W	m	242543	279738	4s ₅ -4p ₆
2634.2	W	W	243927	281878	4s ₄ -4p ₃
2620.8	W	W	243927	282072	4s ₄ -4p ₅
2541.6	m	W	242343	281878	4s ₅ -4p ₃

FII

4446.9	-	W	232066	254547	$2p^3 3d-2p^3(^4S^o)4f$	$3D^o-3F$	15	21	0.97
4246.1	-	m	[231159]	[254703]		$5D^o-5F$	25	25	0.93
4119.2	-	W	211901	236170	$2p^3 3s^1-2p^3(^2D^o)3p^1$	$3D^o-3D$	3	3	0.34
4116.5	W	W	211888	236173			5	5	0.32
4109.1	S	W	211867	236196			7	7	0.40
4103.5		S	207705	232067	$2p^3 3p-2p^3(^4S^o)3d$	$3P-3D^o$	5	7	0.72
4025.5	m	S	182865	207700	$2p^3 3s-2p^3(^4S^o)3p$	$3S^o-3P$	3	3	0.30
3851.6	m	S	[176654]	[202610]		$5S^o-5P$	5	3	0.17
3849.9			[176654]	[202621]			5	5	0.28
3847.1	s	S	[176654]	[202641]			5	7	0.39
3602.8	-	m							
3541.8		W	211867	240093	$2p^3 3s^1-2p^3(^2D^o)3p^1$	$3D^o-3P$	7	5	0.23
3505.6	s	S	[202641]	[231158]	$2p^3 3p-2p^3(^4S^o)3d$	$5P-5D^o$	7	9	0.68
3503.1	m	S	[202621]	[231159]			5	7	0.491
3502.9			[202621]	[231160]			5	5	0.307
3501.4			[202610]	[231161]			3	1	0.175
3202.7	-	W	215070	246284	$2p^3 3s^1-2p^3(^2D^o)3p^1$	$1D^o-1D$	5	5	0.21
3059.9	-	W							

FII

3174.1	-	W	324874	356370	$2p^2 3s-2p^2(^3P)3p$	$2p-2D^0$	4	6	0.38
3154.4	-	W	384485	416178	$2p^2 3p^1-2p^2(^1D)3D^1$	$2p^0-2D$	4	6	0.309
3145.9		S	317238	349005	$2p^2 3s-2p^2(^3P)3p$	$4p-4D^0$	6	6	0.070
3134.2		S	316919	348815			4	4	0.12
3124.7		S	316707	348701			2	2	0.19
3124.4			317043	349040			12	20	0.40
3121.5		m	317238	349264			6	8	0.31
3115.6		s	316919	349005			4	6	0.25

ALI

3961.5	VS	S	112	25348	$3s^2 3p-3s^2(^1S)4s$	$2p-2S$	4	2	0.115
3944.0	VS	S	0	25348			2	2	0.115
3092.7	S	S	112	32437	$3s^2 3p-3s^2(^1S)3d$	$2p-2D$	4	6	0.158
3P82.1	S	S	0	32435			2	4	0.175
3066.3	S	W							
3064.3	S	W							
3059.9	S	W							
3057.1	S	m							

Appendix 3 - Contd.

3738.0	m	W	105468	132213	3s4p-3s(² S)6s	³ P ^o - ³ S	5	3	0.027
3655.0	-	W	105468	132820	3s4p-3s(² S)5d	³ P ^o - ³ D	5	7	0.077
3586.9	s	S							
2816.1	S	S	59850	95348	3s3p-3s(² S)4s	¹ P ^o - ¹ S	3	1	0.152
2669.1	m	-							
2631.5	VS	S							
<u>AlIII</u>									
4529.1	S	S	143712	165785	4p-4d	² P ^o - ² D	4	6	1.17
4512.5	S	S	143632	165787			2	4	1.31
3713.1	-	s	143712	170636	4p-5s	² P ^o - ² S	4	2	0.235
3702.1	-	s	143632	170636			2	2	0.235
3612.3	s	S	115957	143632	3d-4p	² D- ² P ^o	4	2	0.145
3601.6	s	S	115955	143712			6	4	0.174

The wave-lengths are taken from standard tables (Ref. 16) after identifying these lines in our spectra by means of the Cu-standard lines.

The data are reproduced from Ref.17 except that for CaIII which is reproduced from Ref. 19.

LIST OF PUBLICATIONS

Journals

1. Beam Characteristics of Ruby Optical Masers:
T. S. Jaseja, M. K. Dheer and D. Mathavan,
App. Opt., 4, 1643 (1965).
2. Secondary Stimulated Raman Emission in Liquids:
M. K. Dheer, D. Madhavan and T. S. Jaseja,
App. Phy. Lett., 8, 225 (1966).
3. Stimulated Raman Spectrum of Cyclohexane:
T.S. Jaseja, M. K. Dheer and D. Madhavan,
J. App. Phys., 37, 4996, 1966.
4. Nonlinear Effects of Raman Radiations:
D. Madhavan, M. K. Dheer and T. S. Jaseja,
App. Opt., 5, 1823 (1966).
5. SRS in H_2O and D_2O :
M. K. Dheer, D. Madhavan and D. Ramachandra Rao,
Chem. Phy. Lett., 32, 341 (1975).
6. Thermospectrum of SRS in Liquids:
D. Madhavan and D. Ramachandra Rao,
(Accepted for publication in Chem.Phy. Lett.)

Conference Proceedings

7. Thermospectrum of SRS in Liquids:
D. Madhavan and D. Ramachandra Rao,
Symposium on Solid State Physics and Nuclear Physics,
Dept. of Atomic Energy, India (held at Roorkee, India
Dec. 1969).
8. Spectroscopic Investigation of Laser-generated Plasma
from Solid Targets:
D. Madhavan and D. Ramachandra Rao,
7th National Conference on Lasers and Nonlinear Optics
Tashkent, USSR (May 1974).

9. Thermospectrum of SRS in Liquids:
D. Madhavan and D. Ramachandra Rao
 10. Laser Generated Plasma from Solid Targets:
D. Madhavan and D. Ramachandra Rao
 11. SRS in H_2O and D_2O :
M.K. Dheer, D. Madhavan and D. Ramachandra Rao.
- 9-11: Quantum and Opto-electronic Conference at BARC, Bombay, India (February 1974).